THE UNIVERSITY
of EDINBURGH

The Development of Metallosupramolecular Photoredox Catalysts

THE UNIVERSITY *of* EDINBURGH

David August

Thesis submitted for the degree of PhD

2016

Own Work Declaration

I declare that this thesis has been composed solely by myself and that it has not been submitted, in whole or in part, in any previous application for a degree. Except where states otherwise by reference or acknowledgment, the work presented is entirely my own.

_____

David August

Acknowledgements

Firstly, thank you to my PhD supervisor, Dr Paul Lusby, who has provided so much support over the last few years and has always been keen to discuss all of my results – good or bad. Thanks also for all of his help and advice in preparing me for a career in academia.

To the members of the Lusby group over the years: Oleg Chepelin, Paul Symmers, Dhassida Sooksawat, Matthew Edwards, William Grantham, Vicente Marti Centelles, Bec Spicer and Garima Sharma who have passed on their hard earned knowledge and made the lab such a great place to work. A special thank you to Michael Burke, who has started and finished his PhD alongside me and who without the last few years would have been considerably less enjoyable!

To Alberto Credi and Serena Silvi who offered me the chance to experience life and work in Bologna, the home of photochemistry. I will never forget the ice cream!

To Kirsten Zeitler at the Universität Leipzig who agreed to let me work in her lab for 2 months. It was a fantastic experience and I could not ask for a more friendly or inviting group.

The work in this thesis would not have been possible without the amazing efforts of Juraj Bella and Lorna Murray in the NMR department. They were always willing to help and provided much needed company throughout my many hours performing titrations.

Thanks also to Alexandra Slawin (St Andrews) and Gary Nichol (Edinburgh) who put so much effort into trying to get X-ray crystal structures from my temperamental samples.

To my parents Ryan and Julie for providing everything anyone could ask for over the last 27 years and instilling me with a love of science and chemistry from an early age. And to the rest of my family; Augusts, Chadwicks and Iversens alike, thank you for all of your help and support.

To all of my friends who are always there and continuously asking about my work. I will miss everyone in Edinburgh as I move onto new pastures down south but I hope to visit regularly.

And last but not least, to my incredible wife Nina. Chemistry was one of the many things that brought us together and continues to feature in many dinner time conversations. Thank you for all of her help and support over the last 8 years - I look forward to many more!

Lay Summary

Self-assembly allows the rapid formation of complex molecular systems, such as cages, through the use of weak interactions between nano-sized building blocks. These multi-component systems often possess unique properties not observed for conventional molecules and have potential applications in areas such as sensing, medicine and catalysis. In particular, cage like compounds can act as tiny containers capable of trapping and controlling the reactivity of smaller molecules, in a manner similar to the processes used by proteins within the human body. Another field of chemistry, called photoredox catalysis, has developed compounds capable of absorbing visible light from the sun or household lightbulbs and using the resultant energy to perform chemical reactions. This allows reactions to be performed without expensive heating that might otherwise destroy the fragile compounds involved.

This work details attempts to combine these two areas of chemistry to allow the strict control of individual reactions that can be performed using green and environmentally friendly conditions. Various methods are described in order to increase the stability of the cage systems, improve the trapping of smaller molecules within the cage compounds and assess the resultant reactions.

Abstract

Supramolecular chemistry allows the rapid formation of complex systems through self-assembly. These systems often possess unique properties not observed for conventional covalent constructs and have potential applications in areas such as sensing, drug delivery and catalysis. Metallosupramolecular container compounds have been shown to catalyse reactions with both regio- and stereo-selectivity in methods analogous to enzyme type catalysis. Separately, visible-light photoredox catalysis has recently gained considerable interest as an efficient, green and mild method for the rapid synthesis of many chemical compounds.

In order to combine the favourable properties of both supramolecular catalysis and visible-light photoredox catalysis, a number of photoredox active metallosupramolecular assemblies were designed, synthesised and analysed. Initial steps were taken to stabilise a known iridium-based M_6L_4 luminescent cage compound to allow guest encapsulation to take place. The incorporation of isocyanide donors as strong ligands improved the stability of model compounds but synthesis of an analogous three-dimensional assembly was unsuccessful. Instead, a "complex-as-ligand" approach was taken that allowed the straight-forward formation of Pd_2L_4 systems from a range of photoactive iridium complexes. Importantly, unlike many other photoactive systems, the complexation to palladium did not drastically affect the photoredox properties of the constituent iridium complexes. Multiple approaches were then taken to improve both the stability and guest binding properties of the photoactive assembly in an effort to achieve supramolecular photoredox catalysis. Utilising a model system, a general method was thus developed for enhancing the association constants of neutral guests in organic solvents by switching to large, non-coordinating counter ions that provided reduced competition for the internal binding site. In combination with this increased binding affinity, a range of guest properties were adjusted by association with the hydrogen bond donor environment of the internal cavity. The encapsulation of quinone based oxidants led to unexpected and novel reaction pathways not observed in the bulk phase. As such, this work represents a significant advancement in development of metallosupramolecular systems capable of regio- and stereo-selective photoredox catalysis.

Abbreviations

Compounds

ppy	2-Phenylpyridine
ppz	2-Phenylpyrazine
Phppy	2,5-Biphenylpyridine
dib	1,4-Diisocyanobenzene
emibipy	2,2’-Bi(4-ethynyl-1-methyl-imidazolyl)pyridine
TBAF	Tetrabutylammonium fluoride
PEG	Polyethyleneglycol

Solvents

DMSO	Dimethylsulfoxide
DCE	1,2-Dichloroethane
TCE	1,1,2,2-Tetrachloroethane
NMR	Nuclear Magnetic Resonance Spectroscopy
OTf	Trifluoromethanesulfonate

Techniques

MS	Mass spectrometry
MSMS	Tandem mass spectrometry
nESI	(nano) Electrospray ionisation
EI	Electron ionisation
NMR	Nuclear Magnetic Resonance Spectroscopy
DOSY	Diffusion Ordered Spectroscopy
EXSY	Exchange Spectroscopy
COSY	Correlation Spectroscopy
NOESY	Nuclear Overhauser Effect Spectroscopy
HSQC	Hetero-nuclear Single Quantum Coherence
HMBC	Hetero-nuclear Multiple Bond Coherence

Other

N/D	Not determined

Overview

Chapter 1 - Introduction: Combined Metallosupramolecular and Photoredox Catalysis

Chapter 2 - Stability of Ir_6L_4 Photoredox Active Metallosupramolecular Assemblies

Chapter 3 - A Complex-as-Ligand Approach to Metallosupramolecular Photoredox Catalysis

Chapter 4 - Solvophobic Guest Binding in Photoactive Pd_2L_4 Cages

Chapter 5 - Enhanced Guest Binding in Organic Solvents

Chapter 6 - Hydrogen Bond Donor Metallosupramolecular Catalysis

CHAPTER 1

Introduction:

Combined Metallosupramolecular and Photoredox Catalysis

Contents

1.1 Synopsis

Metallosupramolecular systems have shown interesting properties as “molecular flasks” that can isolate encapsulated compounds from the bulk phase and catalyse both regio- and stereo-selective reactions in an enzyme like manner. Separately, photoredox catalysis has shown great potential as a mild and environmentally friendly method for the production of complex organic compounds. This chapter aims to introduce the reader to these research areas and propose the general idea of combining both concepts to produce a single self-assembled system capable of regio- and stereo-selective catalysis in the presence of visible light.

1.2 Introduction

The idea of catalysis, whereby a substance increases the rate of a chemical reaction and yet itself remains unchanged, has transformed the way in which chemistry is performed. From the protein-based enzymes that perform thousands of different biochemical transformations within our cells to the metal hetero-catalysts that are used to produce millions of tons of fertilizers and fuels every day, catalysis plays an essential role in all aspects of human life. Without the incorporation of catalysts, these chemical processes would still take place but with reaction half-lives measured in years or even millennia. Indeed, some enzymes have been estimated to increase the rates of specific reactions by up to 10^{19} fold.[1]

Enzymes achieve these remarkable rate enhancements by binding substrates in specific conformations that favour reactivity. In addition, various functional groups are activated or stabilised by the proximity of amino acid side chains with specific properties.[2] In theory, if the transition states of a chemical process are known then an enzyme could be designed from scratch to specifically catalyse that chemical process. However, the vast array of intermolecular interactions that hold peptide chains together are too complex for rational *de novo* design at present.[3–5]

Supramolecular chemistry allows the self-assembly of large complex systems from relatively simple building blocks. These can be held together by a range of reversible interactions but the use of metal-ligand bonds provides the unique advantage of strict geometries and high strength. This allows, so called metallosupramolecular systems to be designed and synthesised successfully with a high degree of predictability in the resultant structure. Discrete metallosupramolecular structures often possess internal cavities that can bind and alter the properties of guest compounds and as such, can serve as synthetically achievable analogues of biological enzymes.

Even with efficient catalysis, many industrial processes still require high temperatures and harsh conditions to drive chemical processes. Photoredox catalysis offers a mild and environmentally friendly alternative whereby visible-light, even in the form of virtually limitless sunlight, can be used to drive reactions at room temperature. However, the formation of highly reactive species *in situ* means that stereo- and regio-selective photoredox catalysis remains challenging.

This chapter aims to familiarise the reader with the areas of metallosupramolecular catalysis and visible-light photoredox catalysis and introduce the concept of combining both methods

to form photoactive supramolecular assemblies capable of achieving regio- and stereo-specific photoredox catalysis.

1.3 Metallosupramolecular Catalysis

1.3.1 Introduction

One of the first examples of a discrete metallosupramolecular system was discovered unexpectedly as a result of investigations with Grignard reagents, malonic esters and oxalyl chloride.[6] The malonic esters and oxalyl chloride combined to form a dianionic bis-bidentate ligand (**3**) that then complexed the free magnesium ions (Scheme 1.1). The isolated Mg_4L_6 compound (**4**) was identified as a symmetrical tetrahedron by X-ray crystallography but the internal cavity was far too small for the system to display any of the host:guest chemistry that has become fundamental to the potential applications of metallosupramolecular cages.

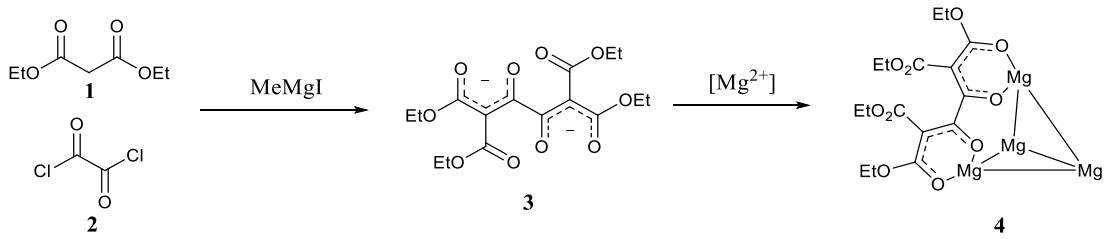

Scheme 1.1: Serendipitous discovery of a magnesium based Mg_4L_6 tetrahedron via formation of a dianionic bis-bidentate ligand.

This result was followed shortly by Fujita and co-workers who developed discrete two-dimensional palladium squares by capping the palladium centres with ethylene diamine to form 90° corner segments (**6**) (Scheme 1.2).[7] These Pd_4L_4 squares (**7**) were also used to demonstrate the first example of guest binding by a self-assembled metallosupramolecular system with a reported K_a of 750 M^{-1} for 1,3,5-trimethoxybenzene in water.

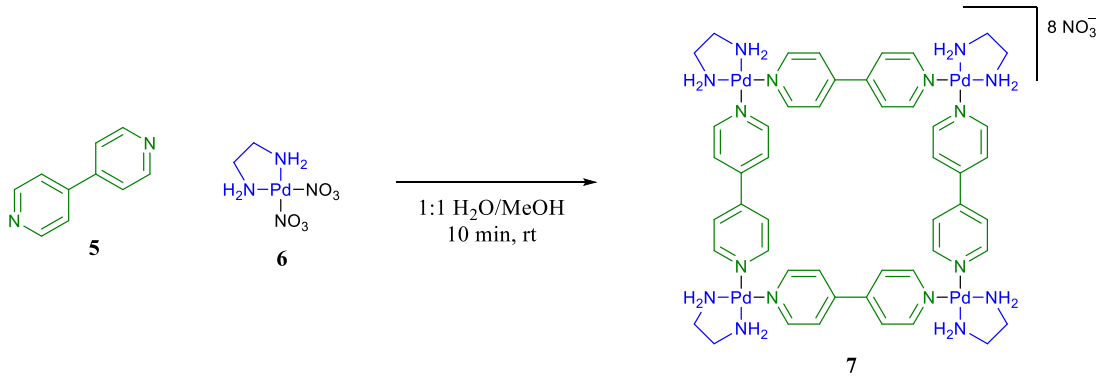

Scheme 1.2: Self-assembly of Pd_4L_4 squares from diamine capped palladium corner units.

A complementary series of organic soluble metallosupramolecular square compounds were also developed by Stang and co-workers using phosphine based capping ligands.[8–10] Labilisation of the metal-ligand interactions due to the strong *trans*-effect of phosphine ligands, also aided the formation of the corresponding platinum structures.

In 1995, Fujita and co-workers expanded upon their initial two-dimensional design and reported the synthesis of a Pd_6L_4 truncated tetrahedron (**8**) (Figure 1.1).[11] The structure was confirmed by X-ray crystallography of the adamantyl carboxylate salt and ^{1}H NMR studies showed significant interactions and slow binding between the host and carboxylate guests. Fujita and co-workers also highlighted the surprising thermodynamic stability of the assembled Pd_6L_4 cage. Rather than degrading into a complex mixture of partially coordinated species upon addition of excess ligand, the cage remained completely intact due to a high degree of cooperativity and highlights the thermodynamic stability required for the selective formation of discrete metallosupramolecular structures through self-assembly.

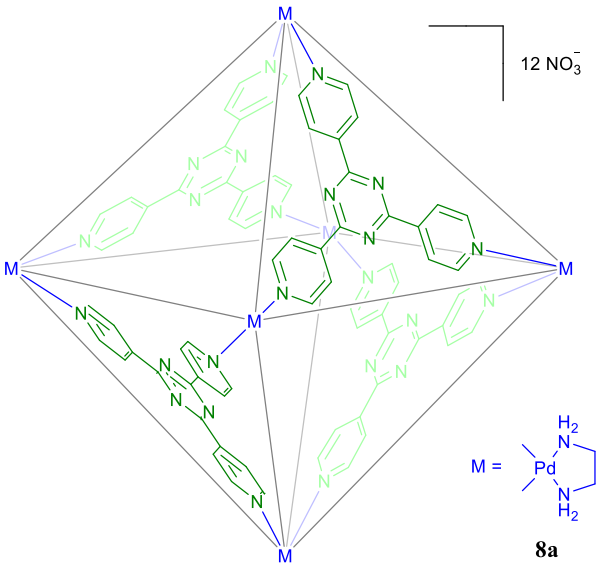

Figure 1.1: Structure of the Pd_6L_4 truncated tetrahedron self-assembled from diamine capped palladium.

Since then, the range of metallosupramolecular assemblies known has increased greatly, as has the variety. These systems often possess remarkable properties that make them ideal candidates for areas such as chemical sensing,[12–15] drug delivery[16,17] and catalysis (see later for specific examples), many of which rely on the interaction and isolation of guest compounds within the resultant internal cavities. For the remainder of this report, the focus shall remain on metallosupramolecular systems with defined internal cavities that display

precedent for catalysis either through alteration of guest properties, stoichiometric rate enhancements or even the rare few examples that have achieved true catalysis. It should be noted at this point that there are many alternative supramolecular systems that have also displayed catalytic activity, such as hydrogen bonded assemblies[18–21] or covalent macrocycles in the form of cyclodextrins,[22–34] cucurbiturils,[35–37] cyclophanes[38,39] and antibodies,[40] but, with the exception of a few specific examples, these organic systems are out with the scope of this work.

1.3.2 Stabilisation of Reactive Species

The first step in achieving supramolecular catalysis relies on the ability to change the physical properties of a substance by encapsulation within a supramolecular framework. In many cases, rather than enhancing the rate of reaction, such encapsulation leads to the stabilisation of the species in question due to isolation from the bulk phase. Ordinarily, compounds in solution will be surrounded by a mixture of solvent molecules, dissolved oxygen and other reactants. By isolating a species within a framework, they are prevented from interacting with anything other than the framework itself and are often held in much more rigid and unusual geometries that can physically prevent reactions that would otherwise occur.

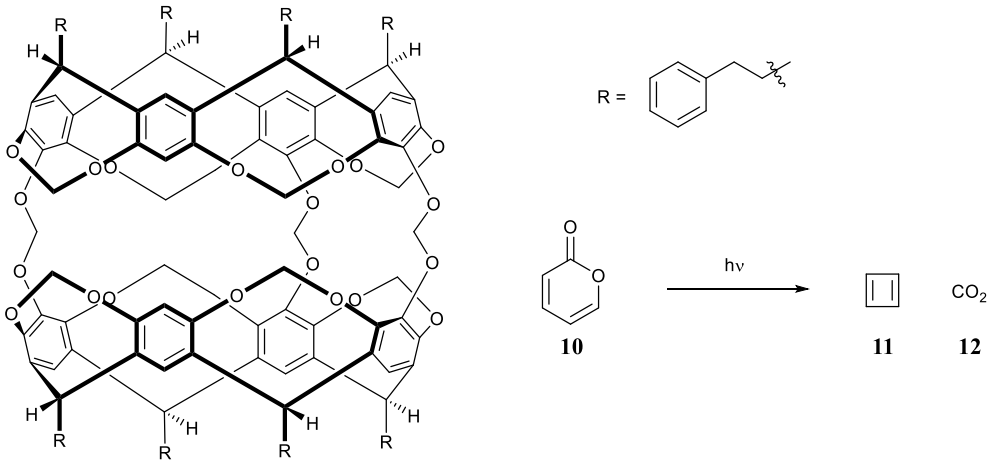

Figure 1.2: Structure of calixarene based hemicarcerand used for the encapsulation and stabilisation of in situ *generated cyclobutadiene.*

This concept was first identified by Cram and co-workers in 1991 with a calixarene based hemicarcerand (**9**) that was capable of binding and stabilising the highly reactive cyclobutadiene (Figure 1.2).[41] Irradiation of encapsulated α-pyrone (**10**) with UV-light

allowed the *in situ* preparation of cyclobutadiene (**11**) within the internal cavity where it remained stable in solution at room temperature under an inert atmosphere.

Perhaps the most prominent example of substrate stabilisation by a metallosupramolecular cage was given by Nitschke and co-workers who demonstrated the encapsulation and safe storage of white phosphorus within an Fe_4L_6 tetrahedron (**13**) (Figure 1.3).[42] Although the portals of the cage are large enough to allow the entry of O_2, the intermediate product formed from oxidation is too large to fit within the interior of the cage. Whilst encapsulated within the cage, P_4 can be stored in aqueous solution under air almost indefinitely but can be selectively released upon displacement with excess benzene.

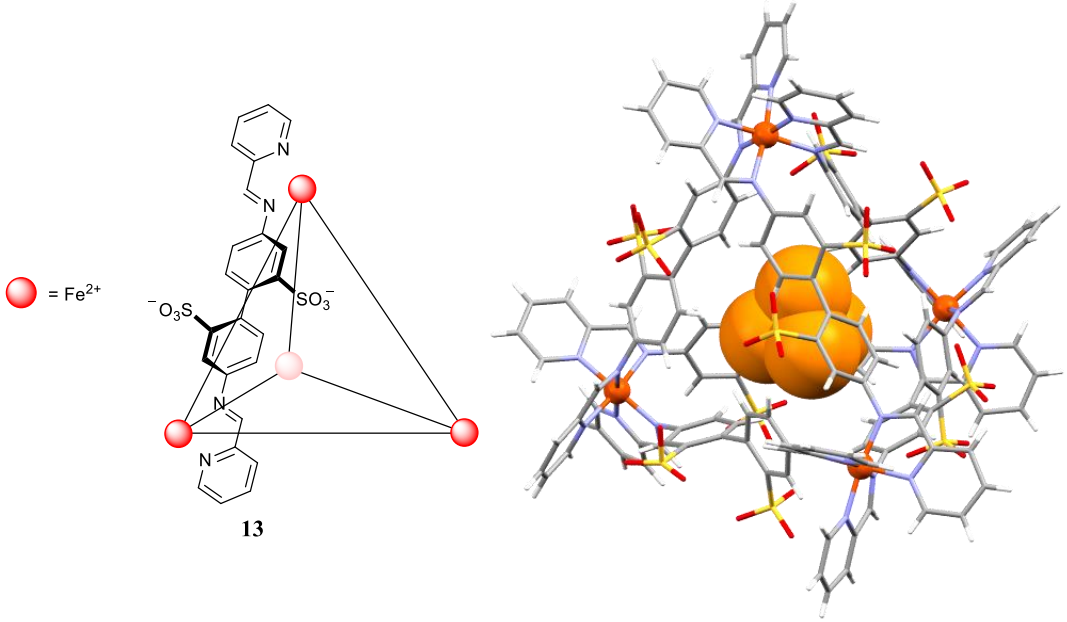

13

Figure 1.3: Chemical structure of water-soluble Fe_4L_6 metallosupramolecular cage and crystal structure of white phosphorus, P_4, bound within the internal cavity. For clarity, only one ligand is shown.

In a similar manner, cage **13** can be used to protect furan and prevent it undergoing Diels-Alder reactions with maleimide (**15**) (Scheme 1.3).[43] Again, steric confinement within the cage prevents any cyclisation and selective release with excess benzene as a competing guest allows the reaction to proceed.

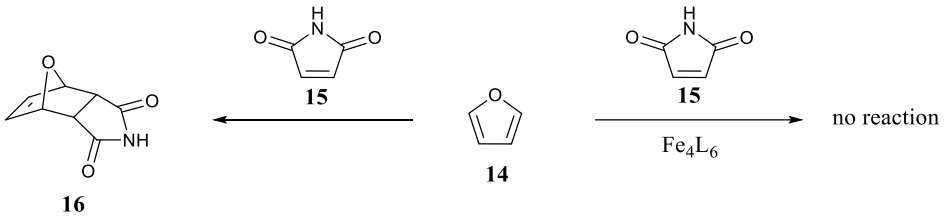

*Scheme 1.3: Diels-Alder reaction of furan and maleimide with and without the presence of cage **13**.*

Using a gallium based tetrahedral cage,[44] Raymond and co-workers showed that iminium cations could be stabilised within the highly anionic cavity (Figure 1.4).[45] By performing a competition experiment with a dynamic library of amines and ketones, the cage was shown to recognise slight structural variations in the iminium ions and preferentially bind the most ideal conformation. This highlights the enzyme-like ability of supramolecular containers to recognise specific molecular targets based on size and shape rather than the generic reactivity of common functional groups.

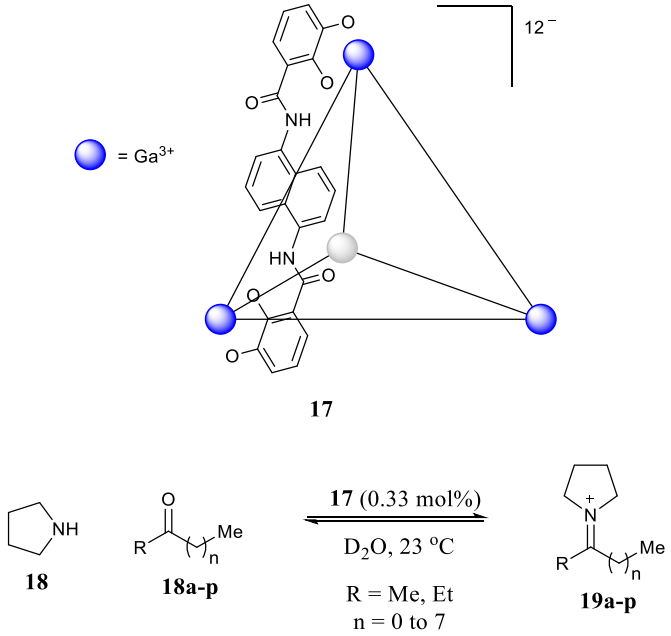

Figure 1.4: Structure of self-assembled anionic Ga_4L_6 cage (for clarity, only one ligand is shown) and stabilisation of encapsulated iminium ions.

More recently, metal complexes have also been stabilised within metallosupramolecular assemblies. Utilising cage **8**, Fujita and co-workers incorporated a di-ruthenium complex that ordinarily undergoes rapid rearrangement in solution to form an equilibrium mixture of conformational isomers (Scheme 1.4).[46] Within the cage interior, quantitative conversion to

the more unusual cis-bridged isomer was observed along with increased stability towards visible-light. The increase in photostability was thought to be due to strict steric confinement preventing the release of CO or splitting of the Ru-Ru bond whilst also increasing the rate of re-combination.

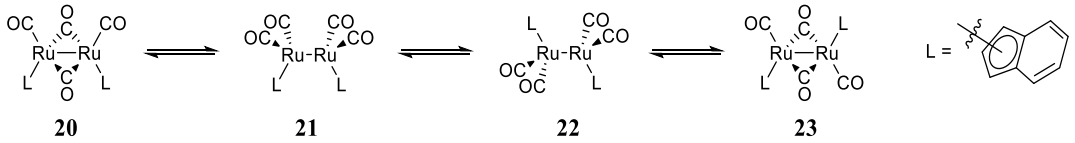

20 **21** **22** **23**

Scheme 1.4: Conformational isomers of di-ruthenium complex

Another example of enhanced photostability is given by the encapsulation of radical initiators within an anthracene based Pd_2L_4 system (**24**) developed by Yoshizawa and co-workers (Figure 1.5).[47] Ordinarily, irradiation with UV-light leads to the degradation of azobisisobutyronitrile (AIBN, **25a**) and the release of reactive radicals due to the high thermodynamic driving force provided by the release of N_2. This mechanism is not sterically demanding and thus the increased stability within the capsule is thought to arise from the high extinction coefficient of the anthracene ligands which prevents any UV absorption by the encapsulated guest. Even though encapsulated AIBN remained thermally unstable, the thermal stability of the structurally larger derivative (**25c**) was also improved, owing to the increased steric encumbrance which prevented even the slight elongation required for homolytic bond cleavage.

Rather than using extended π-systems for photon absorption, highly coloured ruthenium complexes have also been used to protect photosensitive compounds (**27-29**) from visible light by incorporating them into a supramolecular structure (Figure 1.6).[48] Although simple dissolution of the ruthenium complex offers some degree of protection from visible light in its own right, encapsulation of the guests within a $Pd_6(RuL_3)_8$ cage (**26**) increased the guest half-life still further.

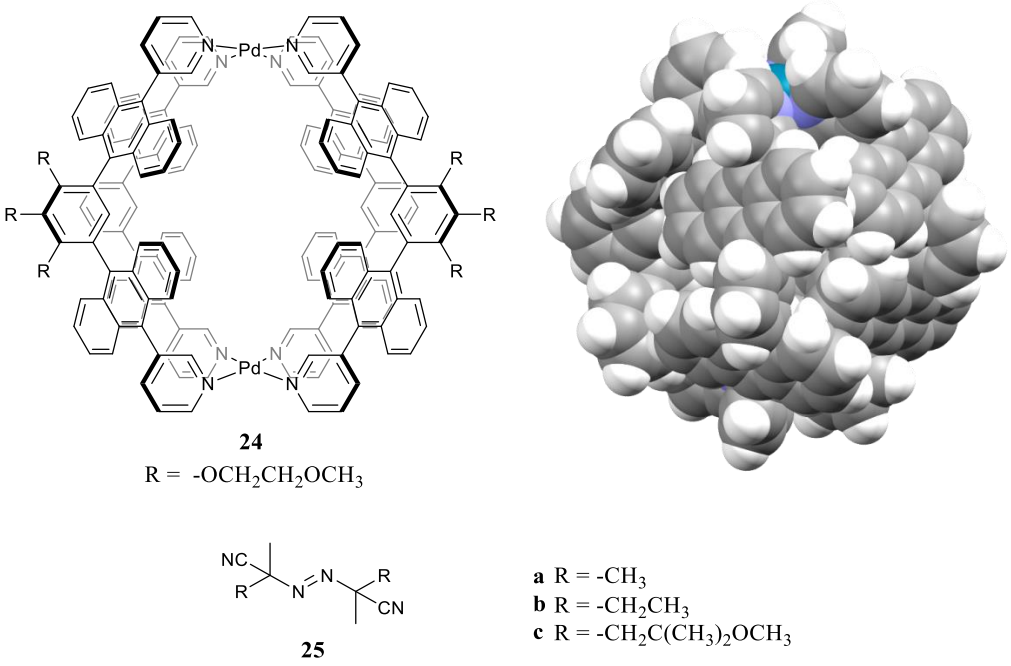

*Figure 1.5: Structure of Pd_2L_4 anthracene cage (**24**) and corresponding encapsulated radical initiators guests (**25a-c**).*

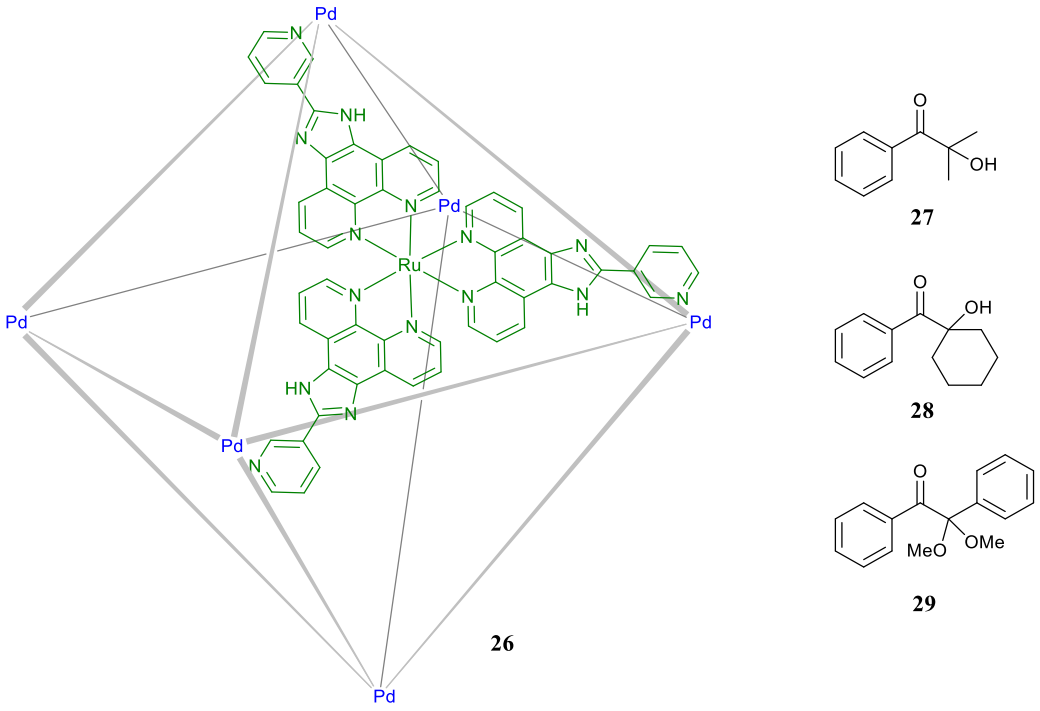

*Figure 1.6: Structure of ruthenium based Pd_6L_8 cage (**29**) and investigated photosensitive compounds (**27-29**). For clarity, only one ligand is shown.*

1.3.3 Regioselectivity & Unusual Reaction Pathways

Metallosupramolecular assemblies can drastically alter the properties of an encapsulated compound due to the restricted environment within the enclosed internal cavities. As such, these systems have been termed as "molecular flasks" in reference to their ability to encapsulate and contain individual reaction environments.[49] The restricted spatial confines can lead to alterations in the reaction pathways normally observed for solution based chemistry and give rise to unusual regio- or stereoselectivity.

After describing the synthesis of the metallosupramolecular Pd_6L_4 cage (**8**), Fujita and co-workers showed how the internal cavity could be used as a molecular-sized reaction container to control the products formed by polymerisation of trialkoxysilanes.[50] Under suitable conditions, trialkoxysilanes are well known to undergo rapid polymerisation to form extended siloxane networks.[51] When the trialkoxysilanes were reacted in the presence of Pd_6L_4 (**8**), polymerisation was prevented and instead, the trimer was isolated within the capsule cavity. The individual trialkoxysilane molecules were able to enter the interior of the cage through the open portals where they rapidly condensed to form a trimer that was subsequently irreversibly bound. In an extension of this work, a range of different metallosupramolecular tubes, bowls and cages were able to selectively produce the siloxane monomer, dimer and trimer respectively (Figure 1.7).[52]

The Pd_6L_4 truncated tetrahedron (**8**) described by Fujita has also been utilised as a molecular flask for a number of different reactions. The system was found to be a suitable host for a range of hydrophobic aromatic guests that bound in a 1:2 host:guest ratio. The dimerization of acenaphthylene or naphthoquinone (**32**) by activation with UV light usually results in a mixture of *syn* or *anti* products. The exact ratio of these products is often heavily influenced by the reaction conditions but a mixture is always obtained. However, when these compounds were bound within (**8a-b**) prior to irradiation, only the sterically less demanding *syn* adduct was formed (Scheme 1.5).[53] The physical space within the cage interior pre-arranged the guests into the *syn* conformation and prevented the formation of the extended *anti* conformer. The size selectivity of the system was shown to be even more specific by the dimerization of methyl acenaphthylene (**35**), where in a similar manner, only the head-to-tail *syn* conformer was observed (Scheme 1.6).[53]

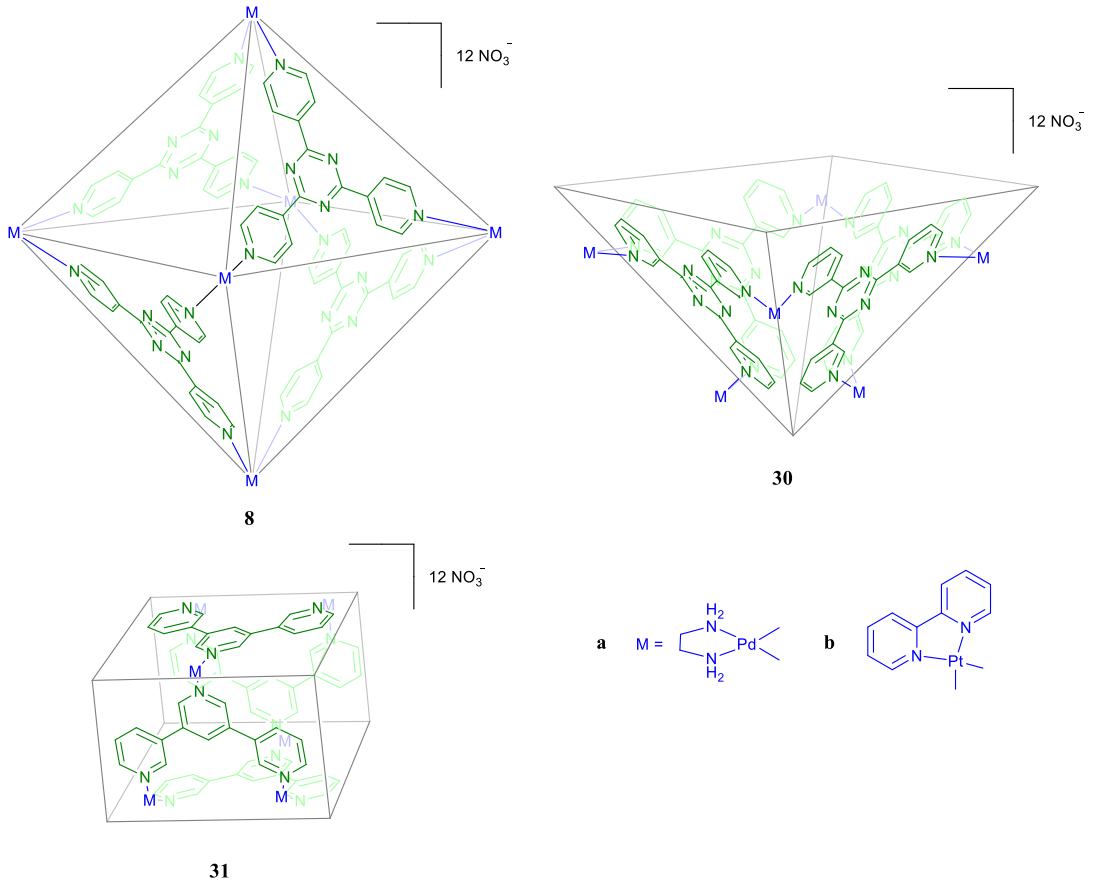

*Figure 1.7: Structures of the Pd_6L_4 truncated tetrahedron (**8**), Pd_6L_4 bowl (**30**) and Pd_6L_4 tube (**31**) used to selectively generate the trialkoxysilane trimer, dimer and monomer respectively.*

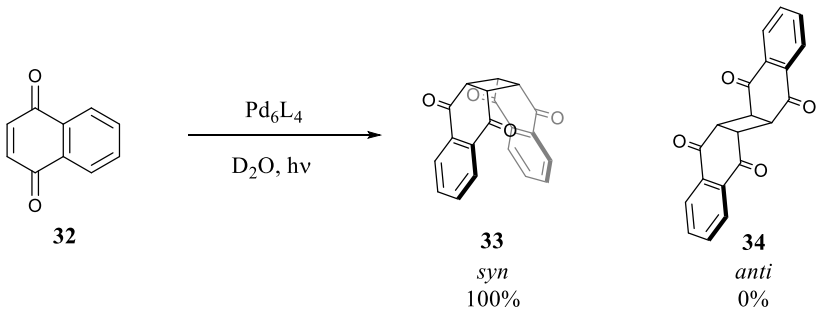

*Scheme 1.5: Selective dimerization of naphthaquinone within a Pd_6L_4 cage (**5**).*

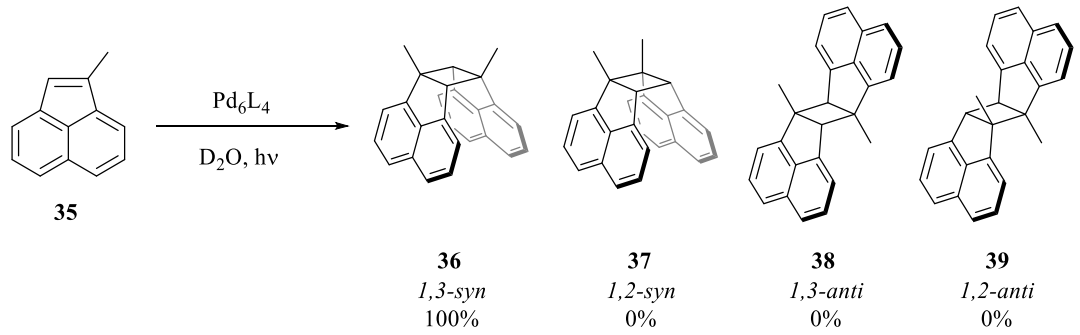

*Scheme 1.6: Selective dimerization of methyl acenaphthalene within a Pd_6L_4 cage (**8**).*

Steric confinement within the cavity of Pd_6L_4 could also alter the reaction pathways of organic radicals (Scheme 1.7).[54] *In situ* photoactivation of α-diketones (**40**) normally results in the formation of the cleaved aldehyde (**41**) but trapped within the cage cavity, the resultant radicals are held in proximity long enough to undergo a cyclisation reaction. Although different to the normal solution processes, the reaction was not clean and produced significant quantities of alternative by products. The authors suggest that the peroxy adduct (**43**) was formed due to the incomplete removal of oxygen and the hydroxy α-diketone (**44**) resulted from reaction with hydroxide radicals formed during the process.

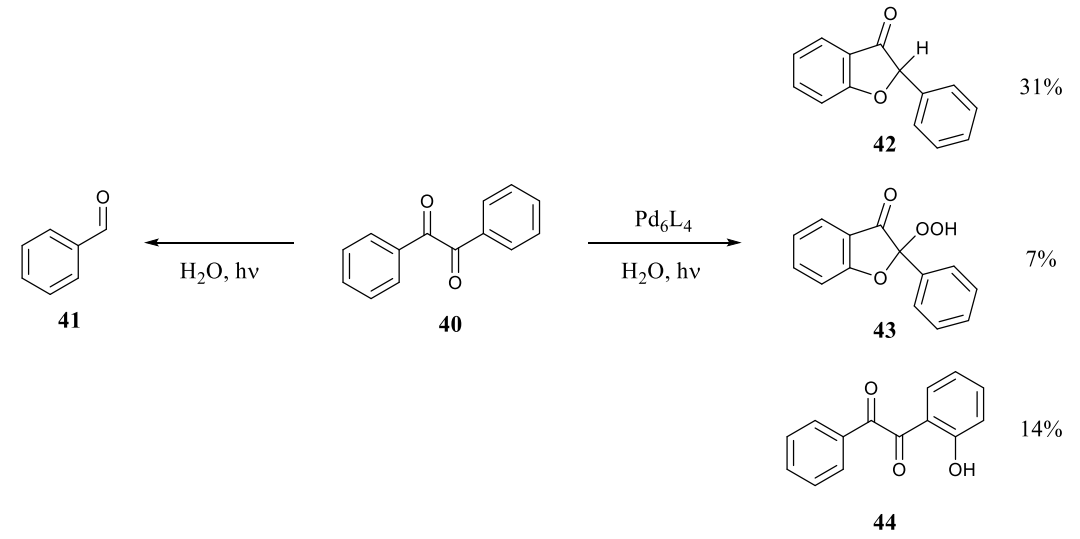

*Scheme 1.7: Photoactivation of α-diketones in solution and bound within Pd_6L_4 (**5**). Encapsulation prevents immediate formation of the aldehyde through hydrogen abstraction.*

In a similar fashion, an *o*-quinone (**45**) co-encapsulated with a toluene derivative (**46**) was shown to produce an unusual 1,4-adduct (**47**) upon UV irradiation of the reaction mixture (Scheme 1.8).[55] The authors propose that photoexcitation of the *o*-quinone leads to hydrogen

abstraction from the sterically confined toluene derivative to give a benzylic radical that consequently reacts to form the coupled product. This degree of selectivity in radical promoted reactions is very difficult to produce in solution due to the high reactivity of radical species. This can normally only be achieved by physically holding the substrates in fixed geometries as observed for many enzyme catalysed pathways.

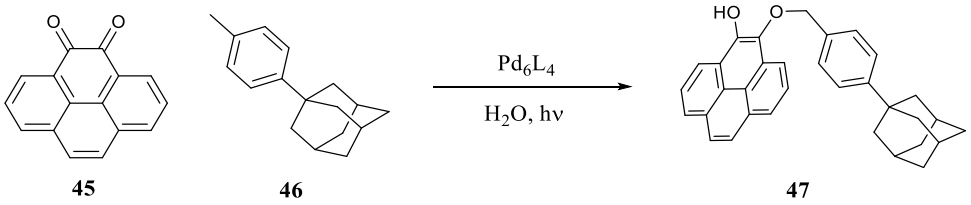

*Scheme 1.8: Selective redox coupling via a reactive radical intermediate mediated by cage **8**.*

By utilising the isolation and stabilisation properties of the cavity, substrates containing multiple reaction sites could be selectively protected by partial encapsulation. Nucleophilic substitution of allylic chlorides at the terminal position was enhanced by tethering the opposite end of the compound within the cage cavity using a large hydrophobic group (Scheme 1.10).[56] Although the reaction selectivity was still not ideal, presumably due to the equilibrium formed between the bound and unbound substrate, this demonstrates the principal of using cage systems as non-covalent protecting groups. The main advantage compared with conventional protecting groups is that the corresponding deprotection step is not required as the reaction products are simply isolated by extraction into organic solvents.

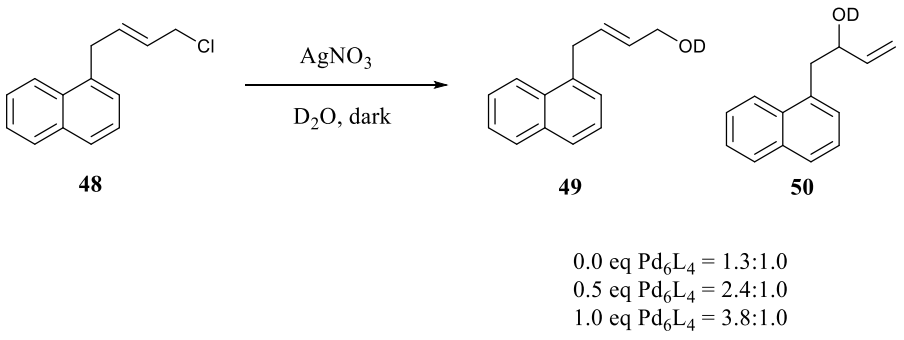

*Scheme 1.10: Regioselective protection of compounds through partial encapsulation within Pd_6L_4 **(8)**.*

Inspired by the photostability of diruthenium complexes within Pd_6L_4, Fujita and co-workers also demonstrated how this could be used to drive unusual reaction pathways. By irradiating an encapsulated diruthenium complex (**51**) in the presence of an alkyne, the normal Ru-Ru

bond dissociation was disfavoured and the resultant loss of CO allowed the subsequent formation and stabilisation of the alkyne complex (**52**) (Scheme 1.11).[57] This complex was unstable in the solution phase and immediately rearranged upon extraction (**53**). Interestingly, the importance of steric confinement and substrate specificity was again highlighted since the use of the less bulky but-2-yne allowed the immediate formation of the rearranged product even when isolated within the cage cavity.

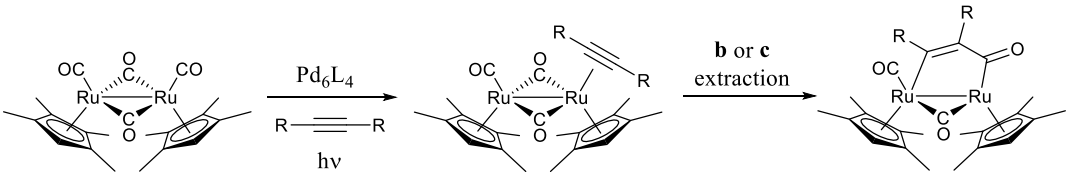

51 **52** **53**

a R = Me
b R = Et
c R = ^{n}Pr

*Scheme 1.11: The size-selective stabilisation and formation of a ruthenium alkyne complex within cage **5**.*

Regioselectivity often occurs within metallosupramolecular systems due to the physical restrictions placed on molecular geometry within the steric confines of the internal space; however, stereoselectivity can also be induced by incorporation of chiral building blocks within the cage structure. By switching the common ethylenediamine palladium corner piece for a range of chiral cyclohexyldiamine complexes, chiral assemblies were constructed based on the standard Pd_6L_4 framework (**54**) (Figure 1.8).[58] Despite the large distances between the internal guests and the external chiral groups, an enantiomeric excess of up to 50% was achieved upon the photoinduced [2+2] cycloaddition between 3-methylfluoranthene (**55**) and N-cyclohexylmaleimide (**56**) (Scheme 1.12). As with many previous examples, the reaction was completely regiospecific for the 4-5 position on the 3-methylfluoranthene, due to pre-organisation within the cage cavity.

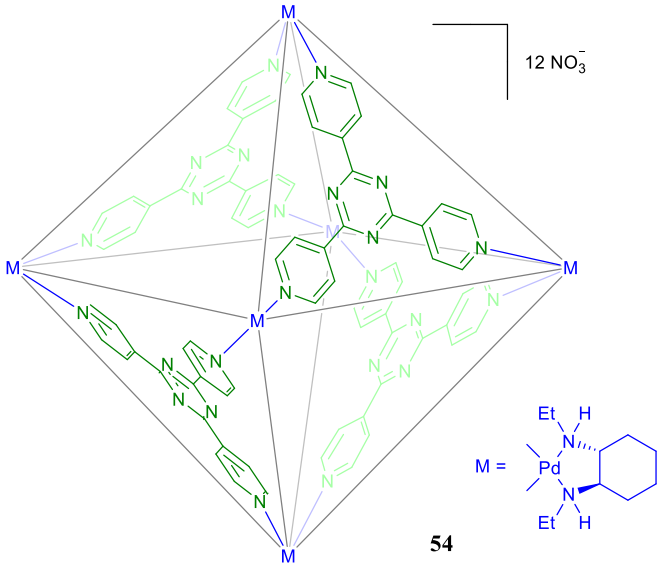

Figure 1.8: Structure of the Pd_6L_4 chiral analogue using an enantiopure palladium cyclohexyldiamine complex.

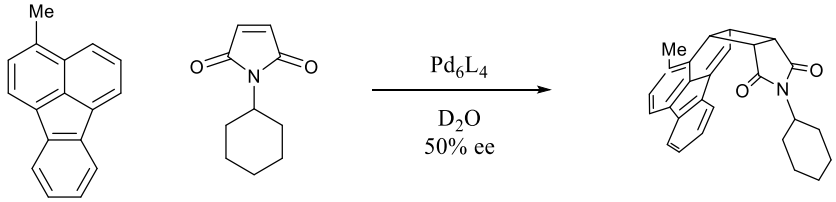

Scheme 1.12: Enantioselective and regioselective [2+2] cycloaddition reaction within the cavity of a chiral Pd_6L_4 analogue.

1.3.4 Stoichiometric Rate Enhancement

Since many metallosupramolecular systems are capable of drastically altering the physical properties of encapsulated guests, as well as protecting fragile compounds, they can also increase the reactivity of relatively inert substances. Increasing the rate of reaction is the first step in achieving catalysis and there are now a number of examples of metallosupramolecular induced stoichiometric rate enhancement.

The Fujita lab has been fundamental in the development of metallosupramolecular systems capable of reaction rate enhancement. The Pd_6L_4 system described earlier, along with a range of derivatives (**8a-d**) has been shown to enhance the reaction rates for a number of bimolecular reactions (Figure 1.9). A range of stable aromatic systems, not normally considered active dienes, were successfully utilised for Diels-Alder reactions with N-

cyclohexylmaleimide within the cavity of Pd_6L_4.[59–61] Due to the extended aromatic rings already present in the starting materials, the Diels-Alder reaction does not proceed in solution, even at elevated temperature.

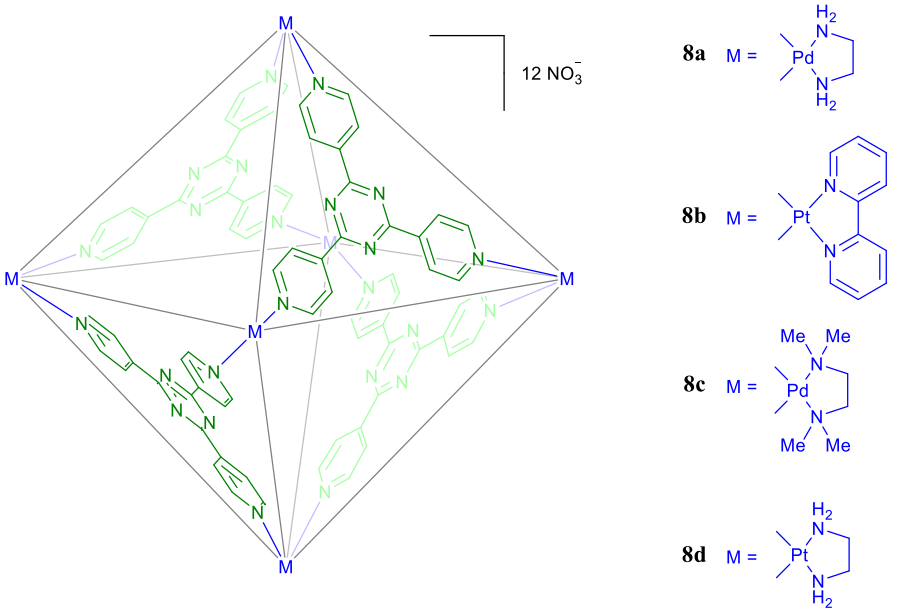

Figure 1.9: Structure of Pd_6L_4 structural analogues utilised for a range of Diels-Alder reactions.

Encapsulation within the cage brings the reagents within such proximity in a pre-organised state that the reaction activation barrier is lowered sufficiently enough to allow reaction at elevated temperatures. The Diels-Alder product formed from perylene was found to undergo rapid oxidation in air after extraction into $CDCl_3$ to rearomatize the π-system but interestingly, this did not occur with the encapsulated compound.[59] This is an unusual example of cage induced stability where neither the reagent (O_2) nor the potential product show any obvious steric reasons for unreactivity; however, the authors do not provide any further analysis.

As well as lowering the reaction activation barrier, the encapsulated transformations remained highly regiospecific with the ability to change the desired product using either thermal or photochemical activation.[60] Both aceanthrylene (**58**) and 1H-cyclopenta[l]phenanthrene (**59**) were shown to undergo either a photoinduced [2+2] or a thermally induced [2+4] cycloaddition with N-cyclohexylmaleimide (**60**) (Scheme 1.13). In each case, the process was not observed in solution and required encapsulation within Pd_4L_6 to proceed.

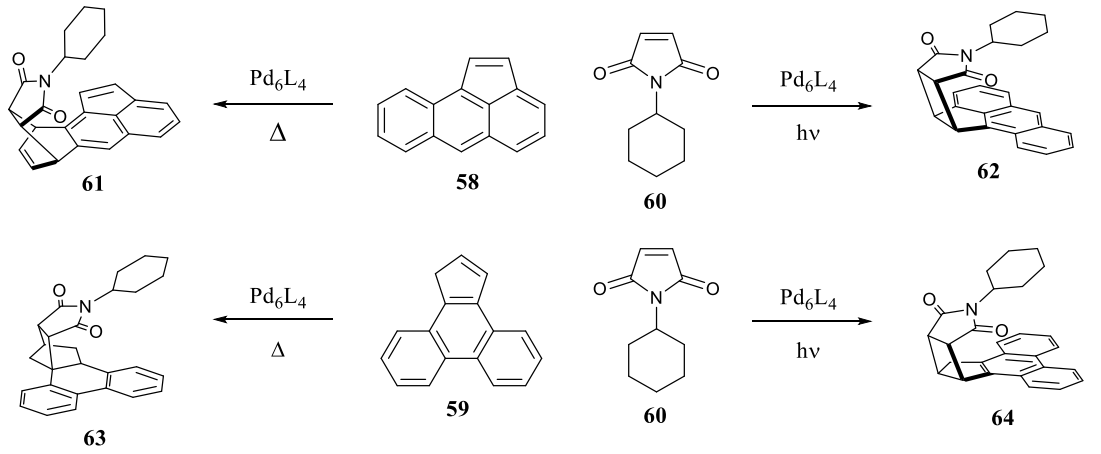

Scheme 1.13: Selective [2+2] and [2+4] cyclisation reactions of "inert" aromatic systems by encapsulation within Pd_6L_4.

1.3.5 Enhancing Conventional Metal Catalysts

Many catalysts suffer from various degradation pathways that reduce the catalytic efficiency over time and ultimately prevent the catalyst working indefinitely. As supramolecular capsules have been shown to significantly alter the properties of guests and protect them from reactive species, it could be envisaged that encapsulation of a catalytic species may lengthen its active lifetime. Indeed, as long the reaction can still take place within the cage cavity, the rate or regioselectivity may even be enhanced due to the steric confinement within the cage.

An early example of this approach was provided by Hupp and co-workers using a porphyrin based metallosupramolecular square (Figure1.10).[62] Encapsulation of a manganese porphyrin, **66**, within the Zn-porphyrin rhenium square, **65**, reduced degradation of the catalyst due to unwanted side reactions with other porphyrin species and increased the TON by tenfold for a styrene epoxidation reaction (Scheme 1.14). Further dilution to prevent intermolecular processes and increasing the binding affinity of the manganese porphyrin by switching to the tetradentate **67** resulted in a TON increase of up to 100-fold. Due to the steric confines of the porphyrin square, the system also displayed moderate substrate selectivity but enantioselectivity could not be induced using the chiral template **68**.

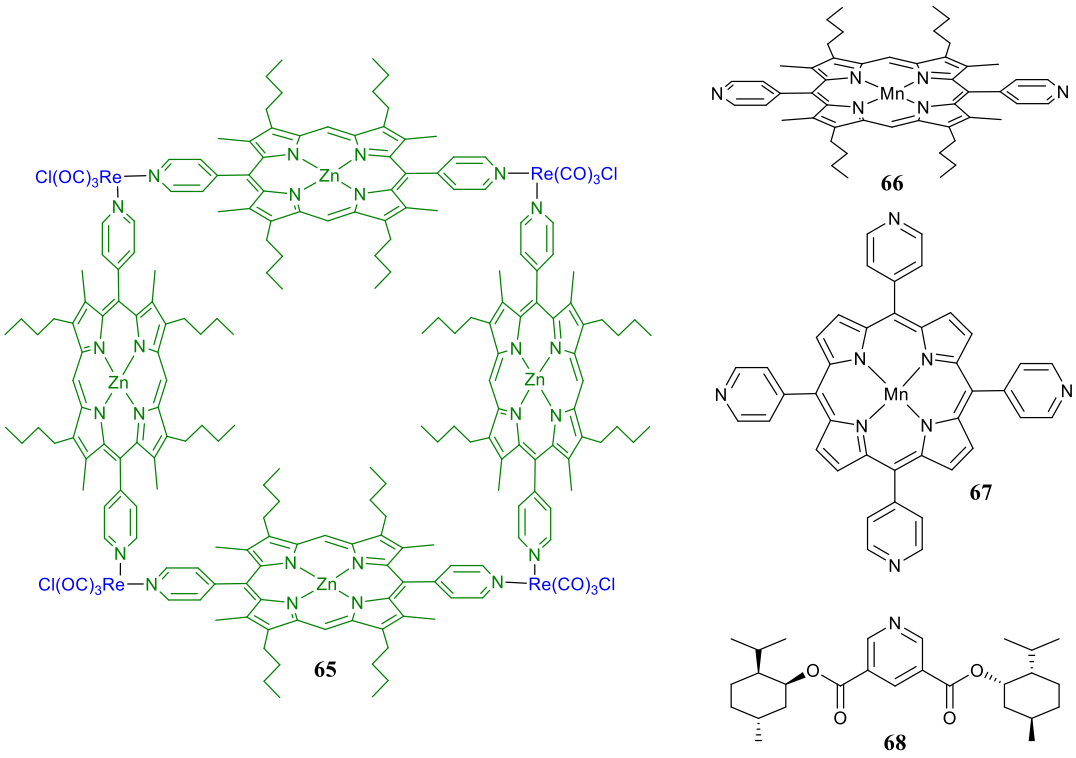

*Figure 1.10: Structure of Zn-porphyrin based rhenium square (**65**), Mn-porphyrin catalytic guests (**66** and **67**) and chiral co-catalyst (**68**).*

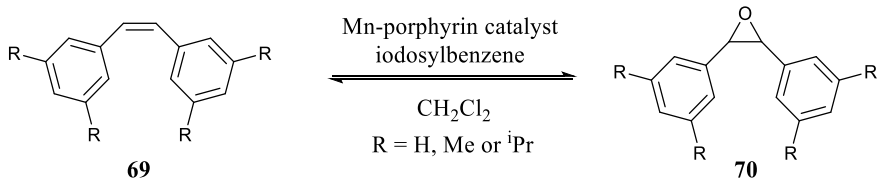

Scheme 1.14: Styrene epoxidation with encapsulated manganese porphyrin.

Raymond and co-workers also attempted catalyst stabilisation by encapsulation of a cationic rhodium complex, with well-known allylic alcohol isomerisation properties, within the cavity of a Ga_4L_6 anionic tetrahedron.[63] However, the activation of the catalyst with H_2 was found to slowly dissociate the activated complex from the cage. Reactions proceeded at the same rate as the solution-based processes for smaller substrates but reaction with sterically hindered substrates was completely prevented. Although this shows control of substrate selectivity, no evidence was given for improved catalytic rate or lifetime of the catalyst.

In a similar manner, Raymond and co-workers achieved enhanced catalysis by a fully encapsulated metal complex using a gold hydroalkoxylation species bound within the same Ga_4L_6 cage.[64] The combined supramolecular catalyst was shown to increase the reaction rate

and increase the yield from 11% to 48%. The use of a "blocking agent" (tetraethylphosphonium cation) also provided evidence that encapsulation of the gold complex was responsible for the rate enhancement rather than separate catalytic ability of the cage. The same encapsulated gold complex has also been shown to catalyse the cycloisomerisation of 1,6-enynes with partial protection of the intermediate from water resulting in a different product distribution to the uncatalysed solution process.[65]

Whilst the turn over number (TON) of the gold hydroalkoxylation process was limited to 67, a similar method using a ruthenium alcohol isomerisation catalyst provided a TON of 1070.[66] This increase from the solution process TON was attributed to protection of the ruthenium complex which is normally unstable under aqueous conditions. However, the rate of the reaction was slightly hindered by encapsulation.

Inclusion of dimethyl gold complexes (**71**) within the Ga_4L_6 cage gave a dramatic increase in the reductive elimination of ethane (Scheme 1.15).[67] A similar effect was observed for trimethyl iodo platinum complexes (**74**) in the presence of Ga_4L_6, with extraordinary rate enhancements of up to 1.9×10^7 observed. With some adjustments to the cage stability, this effect could be combined with a transmetallating agent, $SnMe_4$, to produce a catalytic C-C coupling system capable of rapid and efficient release of ethane due solely to the increased rate of reductive elimination promoted by encapsulation of the cationic intermediate within the cage internal cavity (Figures 1.11 and 1.12).

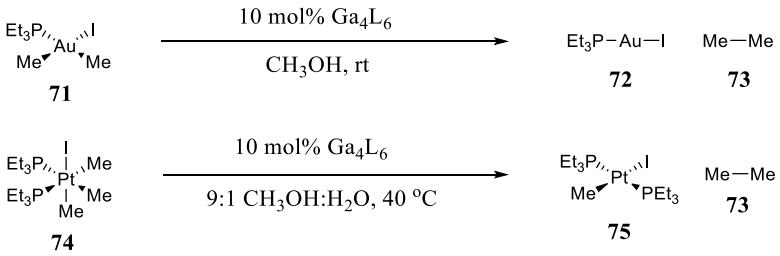

*Scheme 1.15: Conditions for the Ga_4L_6 (**8**) catalysed elimination of ethane from encapsulated metal complexes.*

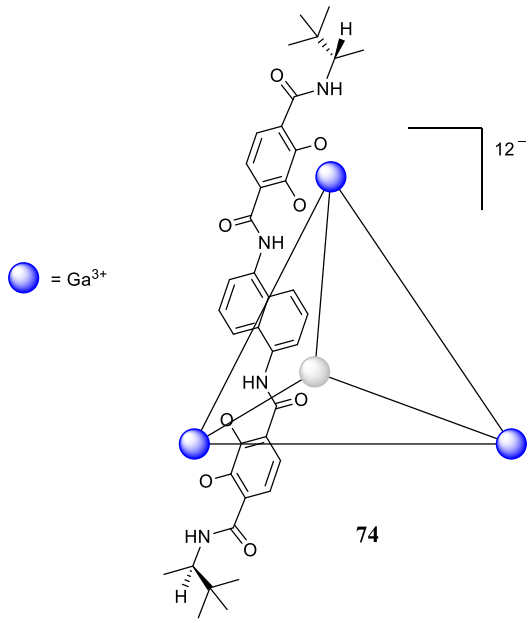

Figure 1.11: Modified structure of Ga_4L_6 used for the combined $Pt(PEt_3)_2Me_2$ and $SnMe_4$ reductive elimination cycle. The addition of amide capping groups improved the stability of the system to the presence of MeI. For clarity, only one ligand is shown.

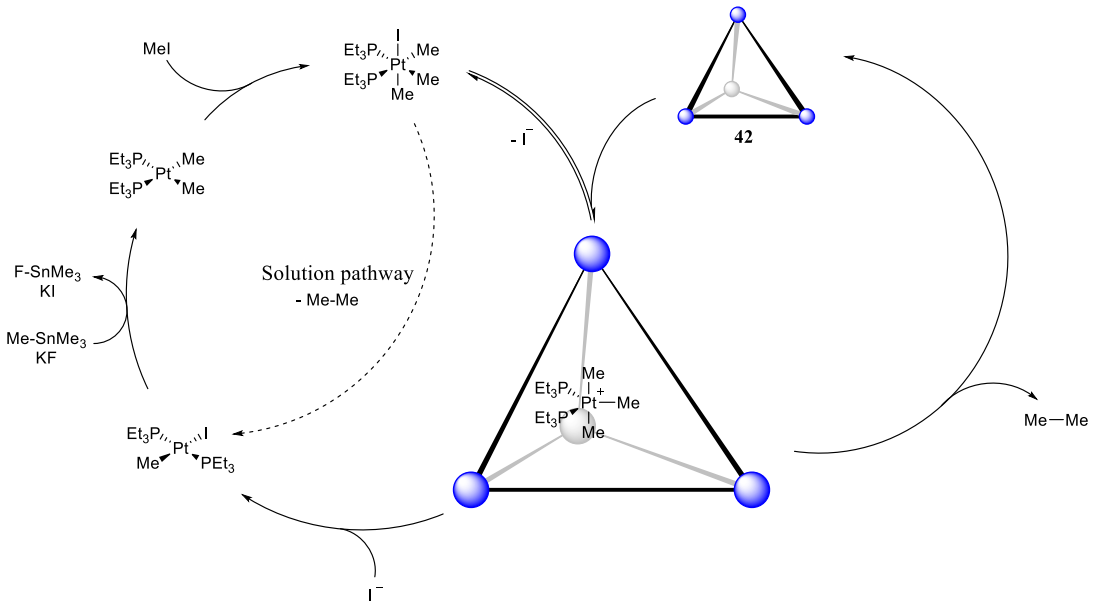

*Figure 1.12: Proposed catalytic cycle for the reductive elimination of ethane encapsulated within cage **74** coupled with a traditional transmetallation cycle.*

1.3.6 Catalytic Internal Cavities

Many of the previous examples of supramolecular rate enhancement involve the preorganisation of two substrates within a sterically confined cavity and thus, increase the effective molarity and reduce the entropic penalty towards reaction. However, as the resultant product is often a more favourable guest or too large to escape the internal cavity, the system cannot turn over and exhibit true catalysis. This product inhibition is a common problem for the design of metallosupramolecular catalysts and two main methods have been developed to solve this: stabilisation of a reactive intermediate rather than the final product or the addition of a secondary solution phase reaction that removes the product from the host:guest equilibrium.

The first reported true catalytic metallosupramolecular system based solely on the properties of the internal cavity was demonstrated by Raymond and co-workers with the Ga_4L_6 tetrahedron **17** (Scheme 1.16). The 3-aza-cope rearrangement was catalysed for a range of ammonium cations (**74**) with rate enhancements of up to 854 fold.[68] Since the resultant iminium cations (**75**) hydrolyse rapidly in solution to a non-binding aldehyde (**76**), the product of the rearrangement was removed from the host:guest equilibrium and thus, the system was able to turn over catalytically. Changing the solvent or the addition of KCl did not alter the rate of the catalyst-free rearrangement and thus, the rate enhancement was found to be due to preorganization of the substrate within the cage cavity rather than simply the hydrophobic environment or stabilisation of the positive charge. As such, the reaction was also found to be highly substrate specific, with only a relatively small subset of substrate variants showing reasonable rate enhancements. This enzyme-like catalysis also allowed the reaction to proceed enantioselectively with an enantiomeric excess of up to 78% reported using the homochiral Ga_4L_6 assembly.[69]

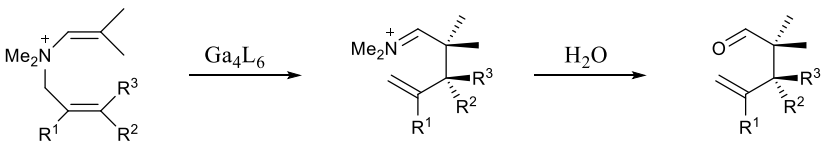

74 **75** **76**

*Scheme 1.16: Ga_4L_6 (**17**) catalysed 3-aza-cope rearrangement of ammonium cations followed by solution phase hydrolysis to the corresponding aldehyde.*

Further in-depth studies of the reaction mechanism showed that at pH 7, the hydrolysis was the rate limiting step.[70] Increasing the pH to allow hydroxide rather than water to function as

the nucleophile resulted in an increase in the reaction rate. More surprisingly, the reaction rate was also increased by the addition of ammonium cations. The iminium intermediate was found to have a strong ion pairing interaction with the outside of the cage which shielded the compound from hydrolysis due to strong anion-anion repulsion between the cage and hydroxide anions. The addition of "innocent" cations allowed competition for the external ion-pairing sites and increased the rate of release of the iminium intermediate into solution.

In a similar manner, orthoformates (**77**) were also efficiently hydrolysed by Ga_4L_6 (**17**) (Scheme 1.17). The anionic interior of the cage stabilises the protonated substrate to such a degree that the reaction takes place even at pH 11.[71–73] Importantly, only the very first step in the reaction pathway requires specific acid catalysis. Each of the following intermediates (**77**) can be either acid or base hydrolysed and every subsequent hydrolysis decreases the affinity of the resultant compound for the cage interior. The final hydrolysis step produces the anionic formate product (**79**) which, due to strong coulombic repulsion, prevents any binding and therefore any product inhibition. The deprotection of acetals was also carried out using an analogous method (Scheme 1.18).

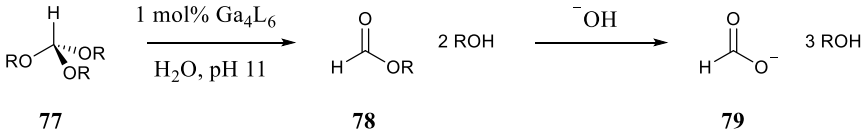

77 **78** **79**

*Scheme 1.17: Ga_4L_6 (**8**) catalysed orthoformate hydrolysis under basic conditions.*

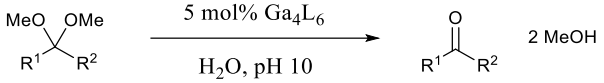

80 **81**

*Scheme 1.18: Ga_4L_6 (**8**) catalysed deprotection of acetals under basic conditions.*

Even more remarkable rate enhancements were then achieved utilising Ga_4L_6 (**17**) for the Nazarov cyclisation of 3,4,5-trimethylhepta-2,5-dien-4-ol (**82**), with the catalysed process proceeding up to 2.1 x 10^6 times faster than the solution based reaction (Scheme 1.19).[74] The authors attribute this to a combined stabilisation of the cationic intermediate and pre-organisation of the substrate into a reactive conformation, essentially combining the effects of the last two reported processes (3-aza-cope rearrangement and orthoformate hydrolysis). The initial product, pentamethylcyclopentadiene (**83**), strongly inhibited the reaction process due to competitive binding within the cage interior. This was overcome by the addition of maleimide which subsequently underwent a Diels-Alder reaction to form the bulky, non-

binding product (**84**). Further studies also elucidated that dihydrofulvene was formed from the other stereoisomers of **82** before rearrangement and trapping with maleimide, indicating high regioselectivity with respect to the deprotonation site.[75]

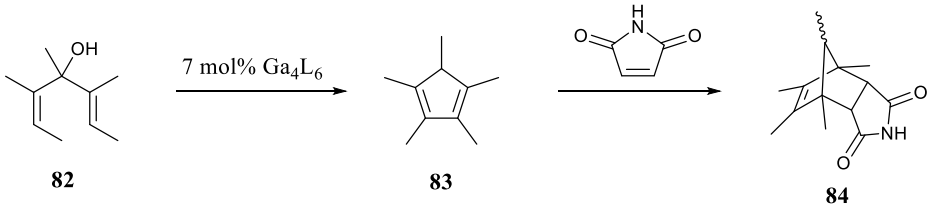

82 **83** **84**

*Scheme 1.19: Ga_4L_6 (**17**) catalysed Nazarov cyclisation. Product inhibition was prevented by a solution phase Diels-Alder reaction to form a bulky, non-binding product (**84**).*

The latest example of supramolecular catalysis from the Raymond group is the Ga_4L_6 (**17**) mediated Prins cyclisation of monoterpene derivatives (**86**) (Scheme 1.20). Protection of the reactive intermediates from nucleophilic H_2O resulted in the formation of a mixture of pulegol stereoisomers (**87**), rather than the *p*-menthane-3,8-diols (**85**) isolated from the aqueous solution process.[65,76] Utilising a chiral analogue of Ga_4L_6, this reaction also proceeded enantioselectively with an enantiomeric excess of up to 69% reported.[77] As with other catalytic reactions within the interior of Ga_4L_6, the stabilisation of the cationic conjugate acid is vital for the reaction rate enhancement.

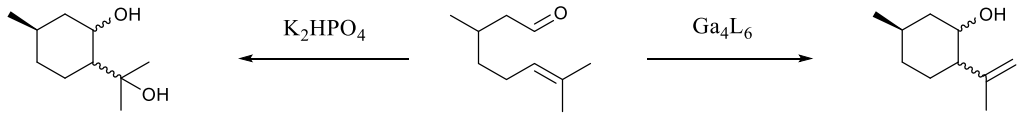

85 **86** **87**

*Scheme 1.20: Standard aqueous phase Prins cyclisation (left) versus the Ga_4L_6 (**8**) catalysed process (right).*

While the Fujita group was fundamental for the development of supramolecular rate enhancement, the Pd_6L_4 cage (**8a**) enhanced Diels-Alder reactions discussed previously have suffered from severe product inhibition that prevents catalytic turn over. This was first overcome by carrying out a bimolecular Diels-Alder reaction within a metallosupramolecular "bowl" (**30**) rather than the complete Pd_6L_4 cage (**8a**).[78] Heating encapsulated 9-hydroxy-methylanthrancene (**88**) and N-cyclohexylmaleimide (**60**) within cage **8a** led to the formation of the 1,4-Diels-Alder adduct (Scheme 1.21). However, as shown previously with a number of cyclisation reactions, the product remained trapped within the cavity and prevented any catalytic turn over. Repeating a similar reaction with N-

phenylphthalimide (**89**) using the Pd_6L_4 bowl (**30**), the catalyst loading could be reduced from stoichiometric quantities to 1 mol% and still maintain 100% conversion to the 9,10-Diels-Alder product (**90**). The authors rationalised this catalytic turn over by reasoning that both the reagent and intermediate could gain significant stabilisation within the bowl cavity through π-π interactions but the resultant bent conformation of the product would prevent this and allow release of the weakly bound compound.

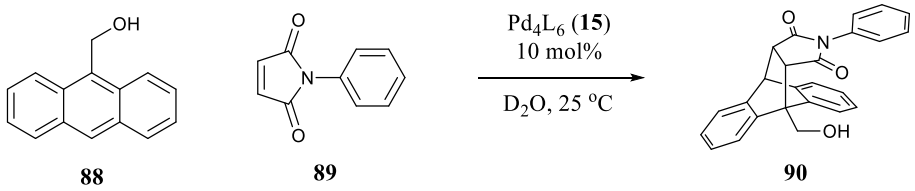

88 **89** **90**

*Scheme 1.21: A Diels-Alder reaction catalysed within a metallosupramolecular "bowl" (**15**).*

Rather than increasing the steric bulk of reactants to optimise the fit within the cage cavity, altering the capping ligands was shown to decrease the accessible volume of the Pd_4L_6 cage (Figure 1.13).[79] This reduction in cavity size allowed previously unattainable reaction rate enhancements for a number of smaller naphthalene based Diels-Alder reactions (Scheme 1.22). Despite strong product inhibition, these reactions proceeded slowly with catalytic quantities of Pd_4L_6 at high temperatures, presumably due to the slow release of the encapsulated product by metal-ligand dissociation.

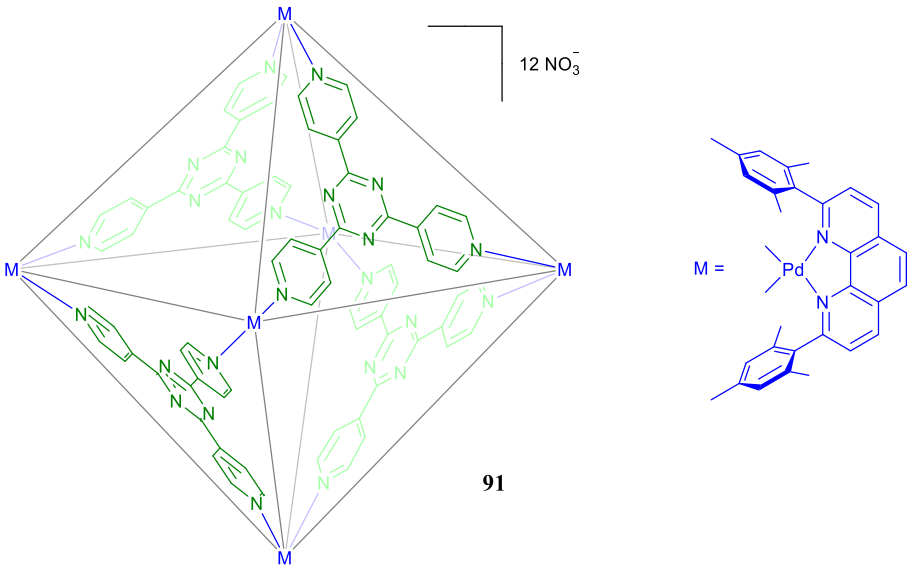

91

Figure 1.13: Modified structure of a Pd_6L_4 cage incorporating sterically crowded palladium corner pieces that restrict the volume of the internal cavity.

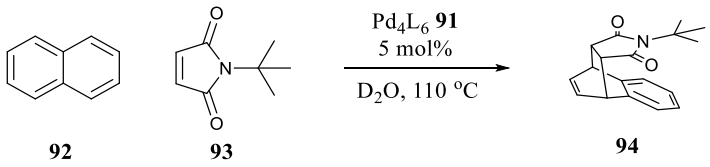

*Scheme 1.22: Restriction of the cage cavity volume (**91**) allows the catalysis of Diels-Alder reaction between smaller substrates.*

Stabilisation of an anionic intermediate allowed Pd_4L_6 (**8a**) to catalyse the Knoevenagel condensation of Meldrum's acid (**96**) with a range of aromatic aldehydes (**95**) (Scheme 1.23).[80] A similar reaction was also carried out in an analogous cage containing triimidazole ligands.[81] The resultant product (**97**) is sterically excluded from the cage cavity and the reaction proceeds catalytically. As such, this process can be seen as the anionic equivalent of Raymond and co-workers stabilisation of cationic intermediates.

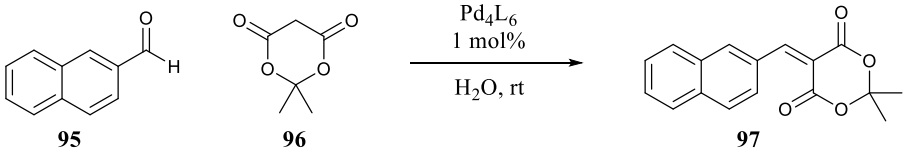

*Scheme 1.23: Knoevenagel reaction between bulky aromatic aldehydes (**95**) and Meldrum's acid (**96**) catalysed by cage **8a**.*

Ward and co-workers have recently reported catalysis of a Kemp elimination reaction using a Co_8L_{12} cube (Figure 1.14 and Scheme 1.24).[82] Under alkaline conditions, the Kemp elimination relies on nucleophilic attack of hydroxide anions and follows a first order relationship with respect to hydroxide concentration. In the presence of **98**, the reaction is efficiently catalysed and the rate becomes independent of the hydroxide concentration. The authors provide evidence that this is due to the binding of hydroxide anions within the cationic cage portals and the resultant dramatic increase in the effective molarity of hydroxide anions with respect to the bound substrate. When compared with the neutral solution process, rate enhancements of up to 6×10^6 were reported.

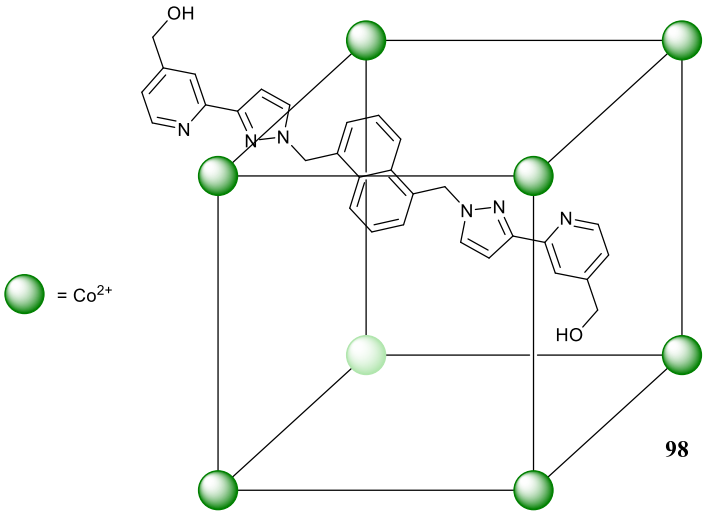

Figure 1.14: The structure of a self-assembled Co_8L_{12} cube. For clarity, only one ligand is shown.

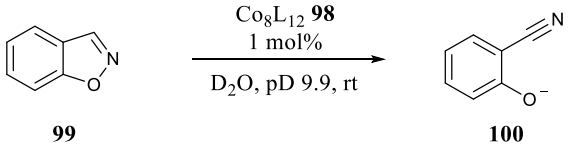

*Scheme 1.24: The Kemp elimination catalysed by encapsulation within cage **65**.*

Interestingly, the authors attribute the efficient catalytic turn over to the release of the weakly bound phenolate anion since, as discussed in additional publications, cage **98** displays a stronger affinity for neutral guests rather than charged compounds.[16] The authors suggest this is due to the much more favourable solvation of charged species in water overcoming the additional coulombic attraction between the cationic cage and the anionic guest. This is in direct contrast to the catalytic mechanism proposed by Raymond and co-workers using cage **17**, whereby cationic species are strongly stabilised within the anionic cage interior relative to the bulk aqueous phase. A simple explanation for this difference in activity is not available at this time but it does, once again, highlight the subtle balance of forces in play that gives rise to supramolecular catalysis and further studies on more systems are required for a complete understanding of catalytic metallosupramolecular structures.

1.3.7 Summary & Conclusions

Over the last two decades, metallosupramolecular containers have shown great promise as catalysts. Their ability to modulate the reactivity of encapsulated substrates and act as molecular reaction vessels gives them enzyme-like properties that, in theory, can be applied to almost any synthetic process. However, there still remains many significant hurdles in the realisation of metallosupramolecular catalysts as real world systems capable of working on an industrial scale.

Although examples of reaction rate enhancements have grown substantially, examples of true catalytic systems remain rare. While binding and altering the properties of guest compounds has proven relatively straight forward, promoting reactions can be challenging. Since cages tend to shield encapsulated compounds from the external environment, many of the examples described above rely either on the encapsulation of two compounds simultaneously or the promotion of a unimolecular reaction.

Even if a rate enhancement can be achieved, catalytic turnover is often prevented due to strong product inhibition, since the very stabilisation of the product that resulted in reaction catalysis also infers a greater binding strength for the resultant compound. A number of methods have been utilised to prevent this, including stabilisation of reaction intermediates and secondary, solution based reactions but these examples remain very few. Indeed, even for the many inspirational catalytic examples published by the Raymond group, the processes are all based on the same supramolecular structure and a very similar reaction pathway.

The highly selective enzyme-like ability of supramolecular systems can make it difficult to rationally screen reactions. The complex array of factors that govern whether a system will work cannot be easily predicted. Although the use of ligand-metal complexation has now made it relatively straight forward to design and self-assemble complex container compounds, the synthesis of a new system can still take months if not years. Once isolated and characterised, reaction screening can begin but since the addition of even a single methyl group to any individual substrate can have a drastic influence on the size specific reaction pathway, it can be very easy to miss potentially successful substrates. Many of these reactive substrates are also complex compounds in their own right and not commercially available and thus also require valuable time and effort to synthesize.

As such, there is still the need for the development of many more metallosupramolecular systems and the study of the subtle forces that give rise to catalysis rather than substrate protection.

1.4 Photoredox Catalysis

1.4.1 Introduction

As famously envisaged by Giacomo Ciamician as early as 1912,[83] sunlight provides a virtually unlimited supply of energy, that if harnessed, could easily provide all of humanities current energy needs. As well as direct transformation of light to electricity, the concept of using light to initiate otherwise unreactive chemical reactions has gained growing interest over the last century.

Since the discovery of photoinduced chemical reactions by Ciamician and Silber in 1908,[84] a huge range of useful organic transformations have been promoted by irradiation with high energy UV-light.[85–87] However, photoredox catalysis offers many advantages over conventional UV photocatalysis. The catalysts absorb visible light which means that reactions can be carried out under household fluorescent bulbs or indeed sunlight, rather than the expensive, high energy UV lamps required for conventional photocatalysis. In addition, irradiation of organic compounds with UV photons often leads to uncontrollable side reactions. Since many organic compounds do not absorb in the visible region, direct excitation is avoided and consequently, unwanted side reactions are reduced.

This section hopes to provide the reader with an introduction to the concepts and theory of photoredox catalysts and their applications in organic transformations. The area of photoredox catalysis is too vast to cover in this work in its entirety and thus, specific examples have been chosen to highlight key concepts and recent developments. For additional information, the readers are directed to a number of thorough and recent reviews published on the subject.[88–97]

1.4.2 Theory of Photoredox catalysis

The general principle involves the use of a photoredox catalyst capable of absorbing visible light to excite an electron to a higher energy state. This excited state possesses the unique property of being both a better reductant and a better oxidant than the ground state compound, due to the easier abstraction of the excited electron from a higher energy orbital or the easier replacement of an electron in the positive hole.

The redox potential of a photoredox catalyst can be further enhanced by the use of a sacrificial reductant or oxidant (Figure 1.16). The excited state allows the removal or gain of

an electron from a species with a relatively low redox potential; however, the resultant fully oxidised or reduced catalyst can then possess a higher redox potential than either the excited complex or the sacrificial quencher. The resultant strong oxidant or reductant can then be used to promote a range of organic transformations.

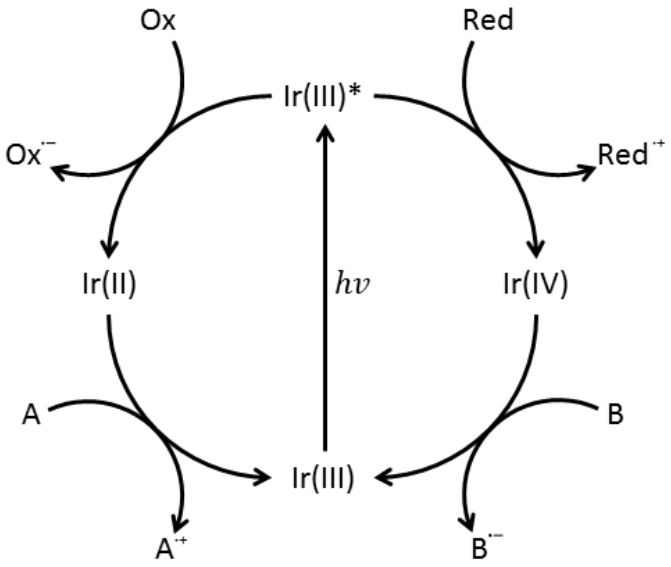

Figure 1.16: An example of a photoredox catalytic cycle based on an iridium complex. Excitation with a visible photon followed by efficient quenching generates either a strong oxidant or reductant capable of promoting a wide range of redox reactions.

1.4.3 Common Photoredox Catalysts

A photoredox catalyst, just like any other catalyst, must perform multiple turnovers while remaining unchanged itself at the end of the reaction process. Additionally, photoredox catalysts must be able to absorb photons to form stable, long-lived excited states that can then interact with substrates through single electron transfer (SET) pathways. In order for successful catalysis to occur, there must be two electron transfer steps: one initial reduction/oxidation to form the reactive species followed by back electron transfer to regenerate the catalyst.

A number of different photoredox catalysts have now been employed for use in visible-light catalysed chemical transformations (Figure 1.17 and Table 1.1). By far the most common is the ruthenium polypyridine complex $[Ru(bpy)_3]^{2+}$ (**101**) due to its strong reduction and

oxidation potentials, high extinction coefficient, long-lived excited state, and stability under most reaction conditions. Iridium cyclometallated complexes have also gained increasing popularity due to their increasingly strong reduction potentials. Organic photoredox catalysts have seen limited use in comparison, due to their lower redox potentials, but they have gained growing interest due to general benefits associated with non-reliance on precious metals such as reduced cost and lower toxicity.

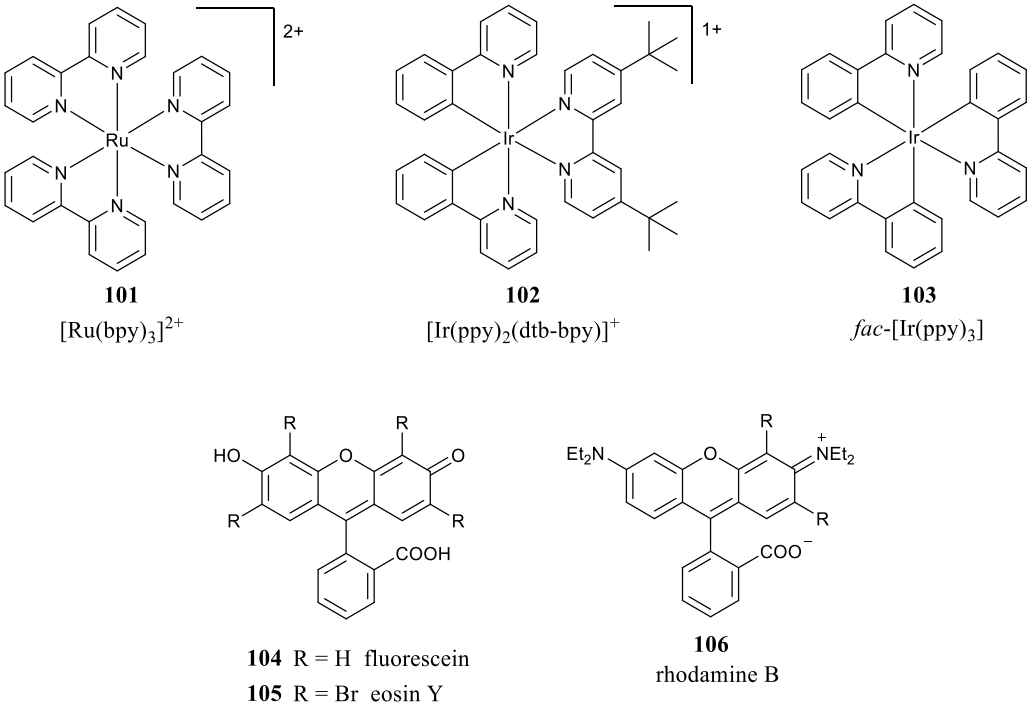

101 $[Ru(bpy)_3]^{2+}$

102 $[Ir(ppy)_2(dtb\text{-}bpy)]^{+}$

103 *fac*-$[Ir(ppy)_3]$

104 R = H fluorescein

105 R = Br eosin Y

106 rhodamine B

Figure 1.17: A range of common photoredox catalysts.

Table 1.1: Redox potentials for a range of common photoredox catalysts.

Compound	**$E_{1/2}$ M^+/M (V)**	**$E_{1/2}$ M/M^- (V)**
$[Ru(bpy)_3]$[98]	+1.29	-1.33
$[Ir(ppy)_2(dtb\text{-}bpy)]$[99]	+1.20	-1.51
fac-$[Ir(ppy)_3]$[100]	+0.69[a]	-2.32[a]
fluoroscein[101]	+0.70[b]	-1.22
eosin Y[101]	+0.78[b]	-1.06
rhodamine B[102]	+1.19[c]	-0.81[c]

a) converted from original measurement made in DMF vs Fc^+/Fc b) irreversible process c) converted from original measurement made in CH_2Cl_2 vs $Ag/AgNO_3$[103]

1.4.4 Synthetic Applications

Photoredox catalysis has been in common use since the 1950s but early work was dominated by the initiation of polymerisation reactions and the photo-splitting of water. Photoredox catalysis as a synthetically useful technique has only really gained momentum in the last few decades.

One of the first synthetically useful visible-light photoredox reactions was developed by Cano-Yelo and Deronzier (Scheme 1.25).[104] Excitation of $[Ru(bpy)_3]^{2+}$ led to the reduction of stilbene diazonium salts (**107**) and the subsequent release of nitrogen, cyclisation and back electron transfer to regenerate the catalyst gave phenanthrene derivatives (**108**) in quantitative yields. Utilising diazonium salts as effective oxidative quenchers also allowed the oxidation of benzylic alcohols to the corresponding aldehydes in the presence of collidine.[105]

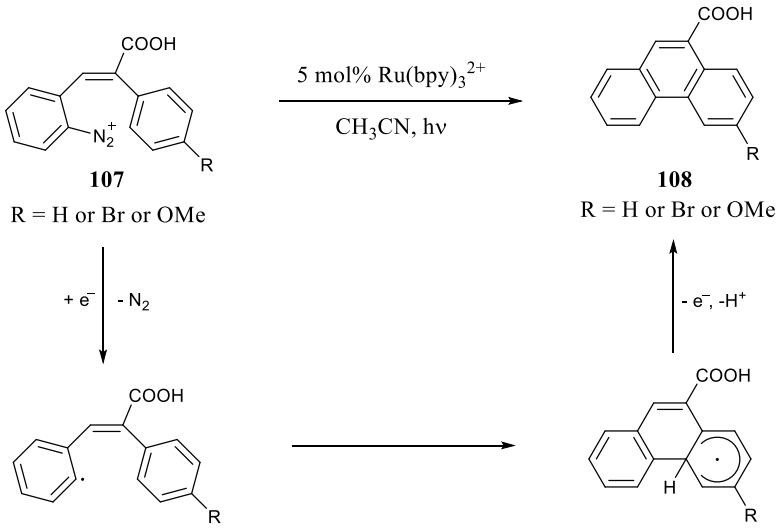

Scheme 1.25: Photoredox synthesis of phenanthrene derivatives from stilbene diazonium salts.

Stephenson and co-workers developed a visible-light photoredox catalysed system for reductive dehalogenation of organic compounds (Scheme 1.26).[106] This environmentally friendly and safe alternative to current methods is tolerant of many functional groups including organo-iodides. Reductive quenching of the catalyst by $^{i}Pr_2NEt$ gave the strong reductant $[Ru(bpy)_3]^{+}$ which consequently underwent SET to the organohalide (**109**). Subsequent release of the halide gave the alkyl radical which then readily abstracted a hydrogen atom from the amine radical cation. Addition of hydrogen atom donors such as

formic acid or Hantzsch ester (**111**) dramatically increased the isolated yield. The use of Iridium catalysts with very high reduction potentials also allowed the cleavage of organo-iodides.[107]

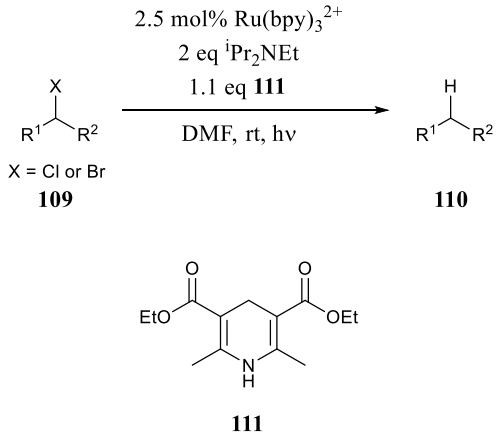

Scheme 1.26: Reductive dehalogenation of organohalides using visible-light photoredox catalysis.

The organic radical formed from reductive cleavage of the C-X bond is an incredibly reactive and versatile species and has since been utilised for a variety of C-C bond forming processes including trifluoromethylation,[108,109] benzylation,[110] alkylation,[111] glycosylisation[112] and the total synthesis of gliocladin C.[113] In addition, the reactive imine intermediates formed from reductive quenching of the photoexcited state by tertiary amines have also been utilised for a range of organic transformations including, but not limited to, phosphonylations, aza-Henry reactions, alkynylations, alkylations, arylations and cyanations.[114–123] The huge range of organic transformations described highlights the powerful synthetic utility of visible-light photoredox catalysis to generate highly reactive species under very mild conditions.

Yoon and co-workers developed a photoredox catalysed method for the [2+2] cycloaddition of tethered bis(enones) (**112**) (Scheme 1.27).[124] Irradiation with visible-light in the presence of $[Ru(bpy)_3]^{2+}$ and DIPEA produced the reduced catalyst that was then capable of reducing the enone to the radical anion. This initiated cyclisation of the tethered alkenes to form the cyclobutane product (**113**) in high yields and diastereomeric selectivity. $LiBF_4$ was required as an additive and the authors propose that it plays a dual role in increasing the solubility of the catalyst and as a Lewis acid for activation of the enone toward one-electron reduction.

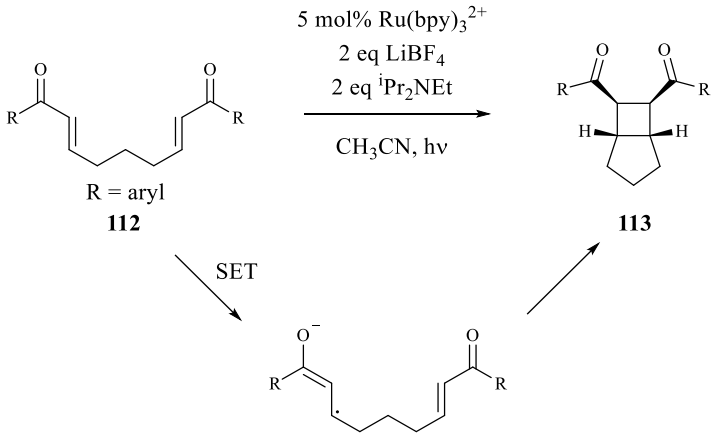

Scheme 1.27: [2+2] intramolecular cycloadditions initiated by electron transfer from the excited state $[Ru(bpy)_3]^{2+}$ to form the enone radical anion.

This work has since been expanded upon to allow the intermolecular cycloaddition of unsymmetrical enones[125] and the [3+2] cycloaddition of aryl cyclopropyl ketones (Scheme 1.28).[126] Substituting the Lewis acid for a Brønsted acid led to the formation of the 5-*exo*-trig product (**114**) through generation of a neutral radical intermediate as opposed to the previous radical anion.[127] This method of activation also had the additional benefit of increased reactivity towards previously unreactive alkyl substituted enones.

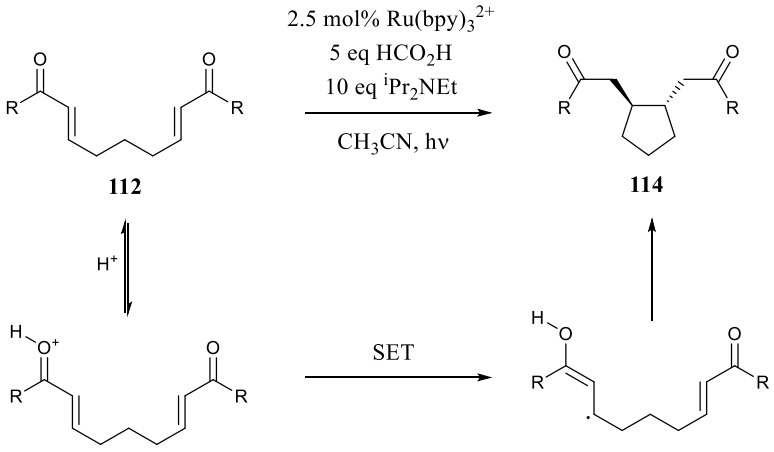

Scheme 1.28: Under Brønsted acidic conditions, protonation of the enone leads to the generation of the neutral radical which subsequently undergoes 5-exo-trig cyclisation.

Both the [2+2] cycloaddition and 5-*exo*-trig cyclisation can also be carried out under metal free conditions using the organic photoredox catalyst, eosin Y, and utilising a hydrogen bond donor catalyst in place of the Lewis acidic lithium cation.[128] However, unlike the

$[Ru(bpy)_3]^{2+}$ catalysed [2+2] cycloadditions, only the more thermodynamically stable *trans*-products could be isolated.

For all of the above cycloadditions, the photoredox process proceeds via the reductive quenching cycle whereby the reactive intermediate is generated by electron transfer from the reduced catalyst to the substrate. This reduction process relies on the use of an electron deficient alkene to allow the reaction to proceed which severely limits the reaction substrate scope. In order to facilitate the [2+2] cycloaddition of electron rich styrenes (**115**), Yoon and co-workers utilised methyl viologen as an oxidative quencher to promote the reaction via the radical cation (Scheme 1.29).[129]

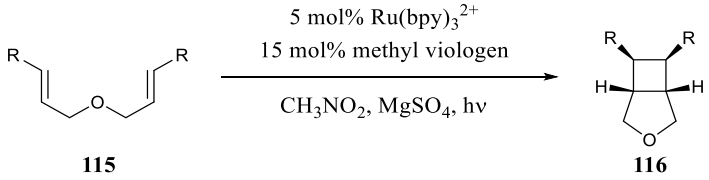

*Scheme 1.29: [2+2] cycloaddition of electron deficient tethered styrenes (**83**) catalysed by oxidative quenching of $[Ru(bpy)_3]^{2+}$.*

This oxidative process was then applied to photoredox promoted Diels-Alder reactions,[130] however, the authors report limited substrate scope and high catalyst loadings (Scheme 1.30). To prevent rapid back electron transfer from the viologen to the photocatalyst, $[Ru(bpz)_3]^{2+}$ was utilised as a stronger oxidative photocatalyst that possessed a high enough excited state potential (+1.4 V vs SCE) that direct oxidation of the substrate could be accomplished without the need for a sacrificial quencher.

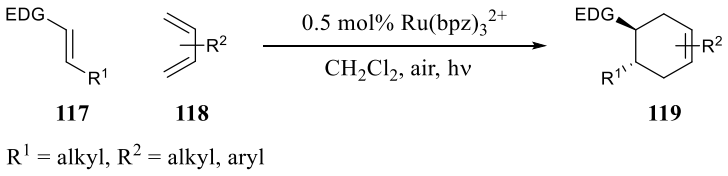

Scheme 1.30: Photoredox catalysed direct oxidation of electron rich alkenes to promote intermolecular Diels-Alder reactions.

Surprisingly, these highly oxidising conditions were unsuccessful for the corresponding intramolecular Diels-Alder due to substrate degradation and thus the reaction proceeded more efficiently with the original $[Ru(bpy)_3]^{2+}$/methyl viologen system.[131] This highlights the fine balance of redox potentials often required for successful photoredox catalytic systems

and thus, the continued generation of a wide variety of photocatalysts with easily tuneable properties is fundamental to the future development of the field.

Many of the processes described above utilise either Lewis or Brønsted base/acid catalysis to enhance the reactivity of substrates toward oxidation or reduction. An important development in this area was the merger of organocatalysis with photoredox catalysis by Macmillan and co-workers (Figure 1.18).[111] The incorporation of a chiral imidazolidinone organocatalyst to generate an enamine intermediate allows efficient chiral induction and enantioselectivity for the α-alkylation of aldehydes. Furthermore, like many photoredox catalysed processes, the reaction conditions are very mild and tolerant to a large range of substrates and functional groups.

As seen previously, the strongly reducing $[Ru(bpy)_3]^+$ species undergoes SET to the alkyl bromide followed by C-X bond cleavage to generate the reactive alkyl radical. However, rather than the addition of a sacrificial quencher, coupling of the enamine to the alkyl radical generates an α-amino radical species that reduces the excited state photocatalyst to form an iminium ion that rapidly hydrolyses to the α-alkylated aldehyde product. In this manner, both electron transfer steps associated with the photoredox catalyst are synthetically useful and remove the need for the stoichiometric addition of a sacrificial quencher.

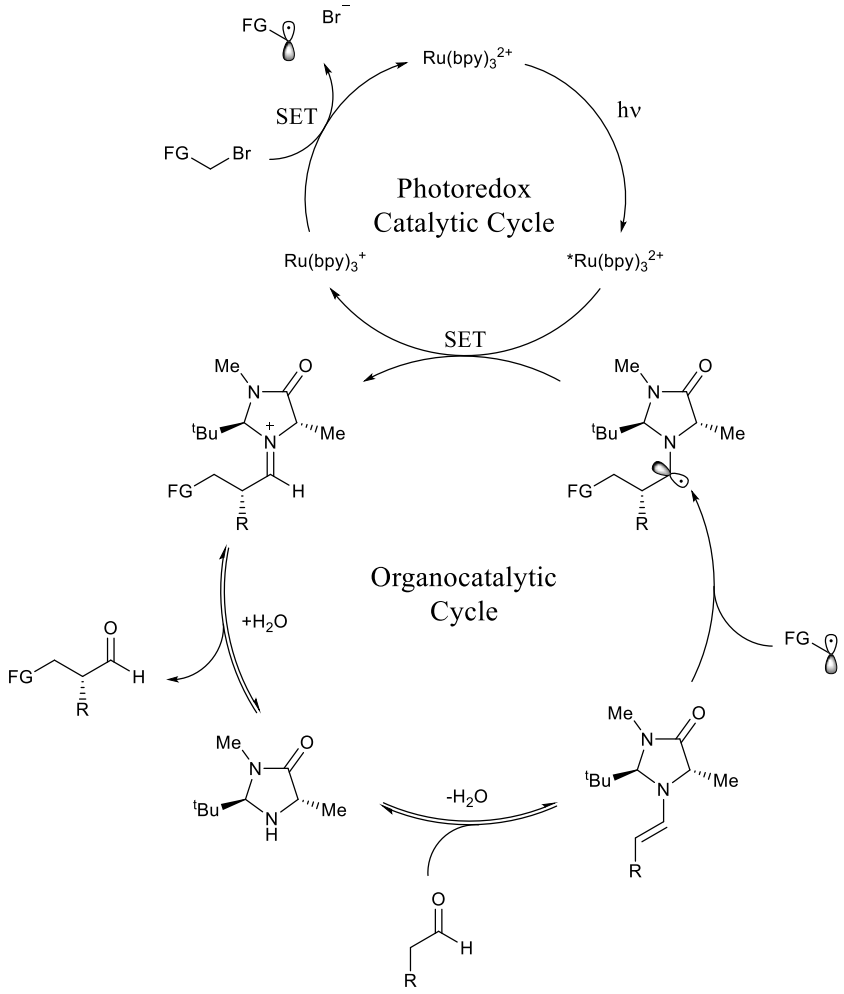

Figure 1.18: Combined organocatalytic and photoredox catalytic cycles for the asymmetric alkylation of aldehydes.

1.4.5 Summary & Conclusions

Photoredox catalysts has recently gained great interest as a mild and environmentally friendly method for the synthesis of a wide range of organic compounds. The ability to perform conventionally difficult organic transformations, such as carbon-carbon bond formations, at room temperature with little more than a common household lightbulb or sunlight has a certain chemical elegance associated with it. Moreover, the use of organic photocatalysts also completely removes the need for potentially toxic and expensive metal catalysts that are still widely used in industrial processes.

Despite this obvious synthetic usefulness, there remains a number of issues in the field. Examples of enantioselective or regioselective photoredox catalysis remain very rare since the generation of highly reactive radical species *in situ* can make it difficult to control the resultant bond formation process. Secondly, many compounds remain unreactive to photoredox catalysts due to their high oxidation and reduction potentials.

As discussed in section 1.3, metallosupramolecular cage compounds are capable of activating unreactive substrates and directly controlling both regio- and stereo-selectivity through confinement of reactive species within a well-defined internal cavity. As such, a combination of photoredox catalysis within the strict confines of a metallosupramolecular cavity could allow mild and environmentally friendly alternatives to currently unobtainable synthetic routes. The following chapters describe studies made to address this hypothesis and design systems capable of performing regio- and stereo-selective photoredox catalysis.

1.5 References

1 R. Wolfenden and M. J. Snider, *Acc. Chem. Res.*, 2001, **34**, 938–945.

2 R. A. Copeland, *Enzymes - A Practical Introduction to Structure, Mechanism, and Data Analysis*, 2000.

3 D. N. Woolfson, G. J. Bartlett, A. J. Burton, J. W. Heal, A. Niitsu, A. R. Thomson and C. W. Wood, *Curr. Opin. Struct. Biol.*, 2015, **33**, 16–26.

4 R. Guerois and M. López de la Paz, *Protein Design*, 2006.

5 F. Yu, V. M. Cangelosi, M. L. Zastrow, M. Tegoni, J. S. Plegaria, a. G. Tebo, C. S. Mocny, L. Ruckthong, H. Qayyum and V. L. Pecoraro, *Chem. Rev.*, 2014, **114**, 3495–578.

6 R. W. Saalfrank, A. Stark, K. Peters and H. G. von Schnering, *Angew. Chemie Int. Ed.*, 1988, **27**, 851–853.

7 M. Fujita, J. Yazaki and K. Ogura, *J. Am. Chem. Soc.*, 1990, **112**, 5645–5647.

8 P. J. Stang and D. H. Cao, *J. Am. Chem. Soc.*, 1994, **116**, 4981–4982.

9 P. J. Stang and B. Olenyuk, *Acc. Chem. Res.*, 1998, **30**, 502–518.

10 P. J. Stang, D. H. Cao, S. Saito and A. M. Arif, *J. Am. Chem. Soc.*, 1995, **117**, 6273–6283.

11 M. Fujita, D. Oguro, M. Miyazawa, H. Oka, K. Yamaguchi and K. Ogura, *Nature*, 1995, **378**, 469–471.

12 S. Tashiro, M. Tominaga, M. Kawano, B. Therrien, T. Ozeki and M. Fujita, *J. Am. Chem. Soc.*, 2005, **127**, 4546–4547.

13 H. Ahmad, B. W. Hazel, A. J. H. M. Meijer, J. A. Thomas and K. A. Wilkinson, *Chem. – A Eur. J.*, 2013, **19**, 5081–5087.

14 R. V Slone, D. I. Yoon, R. M. Calhoun and J. T. Hupp, *J. Am. Chem. Soc.*, 1995, **117**, 11813–11814.

15 A. Mishra, V. Vajpayee, H. Kim, M. H. Lee, H. Jung, M. Wang, P. J. Stang and K.-W. Chi, *Dalt. Trans.*, 2012, **41**, 1195–1201.

16 W. Cullen, S. Turega, C. A. Hunter and M. D. Ward, *Chem. Sci.*, 2015, **6**, 625–631.

17 J. E. M. Lewis, E. L. Gavey, S. a. Cameron and J. D. Crowley, *Chem. Sci.*, 2012, **3**, 778.

18 K. Tiefenbacher and Q. Zhang, *Nat. Chem.*, 2015, **7**, 197–202.

19 J. Kang, J. Santamaría, G. Hilmersson and J. Rebek, *J. Am. Chem. Soc.*, 1998, **120**, 7389–7390.

20 J. Kang and J. Rebek, *Nature*, 1997, **385**, 50–52.

21 T. M. Bräuer, Q. Zhang and K. Tiefenbacher, *Angew. Chemie Int. Ed.*, 2016, 1–5.

22 M. Bonchio, T. Carofiglio, F. Difuria and R. Fornasier, *J. Org. Chem.*, 1995, **60**, 5986–5988.

23 E. A. Kataev, M. Ramana Reddy, G. Niranjan Reddy, V. H. Reddy, C. Suresh Reddy and B. V. Subba Reddy, *New J. Chem.*, 2016, **40**, 1693–1697.

24 C. Ke, C. Yang, T. Mori, T. Wada, Y. Liu and Y. Inoue, *Angew. Chemie Int. Ed.*, 2009, **48**, 6675–6677.

25 V. P. Kumar, M. Narender, R. Sridhar, Y. V. D. Nageswar and K. R. Rao, *Synth. Commun.*, 2007, **37**, 4331–4336.

26 L. G. Marinescu and M. Bols, *Angew. Chemie Int. Ed.*, 2006, **45**, 4590–4593.

27 S. N. Murthy, B. Madhav, A. V. Kumar, K. R. Rao and Y. V. D. Nageswar, *Helv. Chim. Acta*, 2009, **92**, 2118–2124.

28 F. Ortega-Caballero, C. Rousseau, B. Christensen, T. E. Petersen and M. Bols, *J. Am. Chem. Soc.*, 2005, **127**, 3238–3239.

29 M. S. Reddy, B. Srinivas, R. Sridhar, M. Narender and K. R. Rao, *J. Mol. Catal. A Chem.*, 2006, **255**, 180–183.

30 S. B. Singh, K. Tiwari, P. K. Verma, M. Srivastava, K. P. Tiwari and J. Singh, *Supramol. Chem.*, 2013, **25**, 255–262.

31 R. Sridhar, B. Srinivas, K. Surendra, N. S. Krishnaveni and K. R. Rao, *Tetrahedron Lett.*, 2005, **46**, 8837–8839.

32 N. Srilakshmi Krishnaveni, K. Surendra, V. P. Pavan Kumar, B. Srinivas, C. Suresh Reddy and K. Rama Rao, *Tetrahedron Lett.*, 2005, **46**, 4299–4301.

33 K. Surendra, N. Srilakshmi Krishnaveni, A. Mahesh and K. Rama Rao, *J. Org. Chem.*, 2006, **71**, 2532–2534.

34 K. Surendra, N. S. Krishnaveni, R. Sridhar and K. R. Rao, *J. Org. Chem.*, 2006, **71**, 5819–5821.

35 H. Cong, T. Yamato, X. Feng and Z. Tao, *J. Mol. Catal. A Chem.*, 2012, **365**, 181–185.

36 W. L. Mock, T. a Irra, J. P. Wepsiec and M. Adhya, *J. Org. Chem.*, 1989, **54**, 5302–5308.

37 C. Klöck, R. N. Dsouza and W. M. Nau, *Org. Lett.*, 2009, **11**, 2595–2598.

38 F. Diederich and H. D. Lutter, *J. Am. Chem. Soc.*, 1989, **111**, 8438–8446.

39 L. Jimanez and F. Diederich, in *Tetrahedron Letters*, 1989, vol. 30, pp. 2759–2762.

40 E. Keinan, *Catalytic Antibodies*, 2005.

41 D. J. Cram, M. E. Tanner and R. Thomas, *Angew. Chemie Int. Ed.*, 1991, **30**, 1024–1027.

42 P. Mal, B. Breiner, K. Rissanen and J. R. Nitschke, *Science*, 2009, **324**, 1697–1699.

43 M. M. J. Smulders and J. R. Nitschke, *Chem. Sci.*, 2012, **3**, 785–788.

44 D. L. Caulder, C. Brückner, R. E. Powers, S. König, T. N. Parac, J. A. Leary and K. N. Raymond, *J. Am. Chem. Soc.*, 2001, **123**, 8923–8938.

45 V. M. Dong, D. Fiedler, B. Carl, R. G. Bergman and K. N. Raymond, *J. Am. Chem. Soc.*, 2006, **128**, 14464–14465.

46 S. Horiuchi, T. Murase and M. Fujita, *J. Am. Chem. Soc.*, 2011, **133**, 12445–12447.

47 M. Yamashina, Y. Sei, M. Akita and M. Yoshizawa, *Nat. Commun.*, 2014, **5**, 1–7.

48 K. Li, L.-Y. Zhang, C. Yan, S.-C. Wei, M. Pan, L. Zhang and C.-Y. Su, *J. Am. Chem. Soc.*, 2014, **136**, 4456–4459.

49 M. Yoshizawa, J. K. Klosterman and M. Fujita, *Angew. Chemie Int. Ed.*, 2009, **48**, 3418–3438.

50 M. Yoshizawa, T. Kusukawa, M. Fujita and K. Yamaguchi, *J. Am. Chem. Soc.*, 2000, **122**, 6311–6312.

51 R. Baney, M. Itoh, a Sakakibara and T. Suzuki, *Chem. Rev.*, 1995, 1409–1430.

52 M. Yoshizawa, T. Kusukawa, M. Fujita, S. Sakamoto and K. Yamaguchi, *J. Am. Chem. Soc.*, 2001, **123**, 10454–10459.

53 M. Yoshizawa, Y. Takeyama, T. Kusukawa and M. Fujita, *Angew. Chemie Int. Ed.*, 2002, **41**, 1347–1349.

54 T. Furusawa, M. Kawano and M. Fujita, *Angew. Chemie Int. Ed.*, 2007, **46**, 5717–5719.

55 T. Yamaguchi and M. Fujita, *Angew. Chemie Int. Ed.*, 2008, **47**, 2067–2069.

56 Y. Kohyama, T. Murase and M. Fujita, *Chem. Commun.*, 2012, **48**, 7811–7813.

57 S. Horiuchi, T. Murase and M. Fujita, *Angew. Chemie Int. Ed.*, 2012, **51**, 12029–12031.

58 Y. Nishioka, T. Yamaguchi, M. Kawano and M. Fujita, *J. Am. Chem. Soc.*, 2008, **130**, 8160–8161.

59 Y. Nishioka, T. Yamaguchi, M. Yoshizawa and M. Fujita, *J. Am. Chem. Soc.*, 2007, **129**, 7000–7001.

60 S. Horiuchi, Y. Nishioka, T. Murase and M. Fujita, *Chem. Commun.*, 2010, **46**, 3460–3462.

61 S. Horiuchi, T. Murase and M. Fujita, *Chem. – An Asian J.*, 2011, **6**, 1839–1847.

62 M. L. Merlau, M. del Pilar Mejia, S. T. Nguyen and J. T. Hupp, *Angew. Chemie Int. Ed.*, 2001, **40**, 4239–4242.

63 D. H. Leung, R. G. Bergman and K. N. Raymond, *J. Am. Chem. Soc.*, 2007, **129**, 2746–2747.

64 Z. J. Wang, C. J. Brown, R. G. Bergman, K. N. Raymond and F. D. Toste, *J. Am. Chem. Soc.*, 2011, **133**, 7358–7360.

65 W. M. Hart-Cooper, K. N. Clary, F. D. Toste, R. G. Bergman and K. N. Raymond, *J. Am. Chem. Soc.*, 2012, **134**, 17873–17876.

66 C. J. Brown, G. M. Miller, M. W. Johnson, R. G. Bergman and K. N. Raymond, *J. Am. Chem. Soc.*, 2011, 11964–11966.

67 D. M. Kaphan, M. D. Levin, R. G. Bergman, K. N. Raymond and F. D. Toste, *Science*, 2015, **350**, 1235–1238.

68 D. Fiedler, R. G. Bergman and K. N. Raymond, *Angew. Chemie Int. Ed.*, 2004, **43**, 6748–6751.

69 C. J. Brown, R. G. Bergman and K. N. Raymond, *J. Am. Chem. Soc.*, 2009, **131**, 17530–17531.

70 D. Fiedler, H. van Halbeek, R. G. Bergman and K. N. Raymond, *J. Am. Chem. Soc.*, 2006, **128**, 10240–10252.

71 M. D. Pluth, R. G. Bergman and K. N. Raymond, *Science*, 2007, **316**, 85–88.

72 M. D. Pluth, R. G. Bergman and K. N. Raymond, *J. Am. Chem. Soc.*, 2008, **130**, 11423–11429.

73 M. D. Pluth, R. G. Bergman and K. N. Raymond, *Acc. Chem. Res.*, 2009, **42**, 1650–1659.

74 C. J. Hastings, M. D. Pluth, R. G. Bergman and K. N. Raymond, *J. Am. Chem. Soc.*, 2010, **132**, 6938–6940.

75 C. J. Hastings, M. P. Backlund, R. G. Bergman and K. N. Raymond, *Angew. Chemie Int. Ed.*, 2011, **50**, 10570–10573.

76 W. M. Hart-Cooper, C. Zhao, R. M. Triano, P. Yaghoubi, H. L. Ozores, K. N. Burford, F. D. Toste, R. G. Bergman and K. N. Raymond, *Chem. Sci.*, 2015, **6**, 1383–1393.

77 C. Zhao, Q. F. Sun, W. M. Hart-Cooper, A. G. Dipasquale, F. D. Toste, R. G. Bergman and K. N. Raymond, *J. Am. Chem. Soc.*, 2013, **135**, 18802–18805.

78 M. Yoshizawa, M. Tamura and M. Fujita, *Science*, 2006, **312**, 251–254.

79 Y. Fang, T. Murase and M. Fujita, *Chem. Lett.*, 2015, **44**, 1095–1097.

80 T. Murase, Y. Nishijima and M. Fujita, *J. Am. Chem. Soc.*, 2011, **134**, 162–164.

81 D. Samanta, S. Mukherjee, Y. P. Patil and P. S. Mukherjee, *Chem. – A Eur. J.*, 2012, **18**, 12322–12329.

82 W. Cullen, M. C. Misuraca, C. A. Hunter, N. H. Williams and M. D. Ward, *Nat. Chem.*, 2016, **8**, 231–236.

83 G. Ciamician, *Science*, 1912, **36**, 385–394.

84 G. Ciamician and P. Silber, *Berichte der Dtsch. Chem. Gesellschaft*, 1908, **41**, 1928–1935.

85 J. Iriondo-Alberdi and M. F. Greaney, *European J. Org. Chem.*, 2007, 4801–4815.

86 S. Poplata, A. Tröster, Y.-Q. Zou and T. Bach, *Chem. Rev.*, 2016.

87 D. De Keukeleire and S. L. He, *Chem. Rev.*, 1993, **93**, 359–380.

88 J. M. R. Narayanam and C. R. J. Stephenson, *Chem. Soc. Rev.*, 2011, **40**, 102–113.

89 C. K. Prier, D. A. Rankic and D. W. C. MacMillan, *Chem. Rev.*, 2013.

90 J. W. Tucker and C. R. J. Stephenson, *J. Org. Chem.*, 2012, **77**, 1617–1622.

91 K. Zeitler, *Angew. Chemie Int. Ed.*, 2009, **48**, 9785–9789.

92 T. P. Yoon, M. a Ischay and J. Du, *Nat. Chem.*, 2010, **2**, 527–532.

93 Y. Xi, H. Yi and A. Lei, *Org. Biomol. Chem.*, 2013, **11**, 2387–2403.

94 F. Teplý, *Collect. Czechoslov. Chem. Commun.*, 2011, **76**, 859–917.

95 D. A. Nicewicz and T. M. Nguyen, *ACS Catal.*, 2014, **4**, 355–360.

96 T. Koike and M. Akita, *Inorg. Chem. Front.*, 2014, **1**, 562–576.

97 S. Fukuzumi and K. Ohkubo, *Org. Biomol. Chem.*, 2014, **12**, 6059–71.

98 B. P. Sullivan and J. K. Nagle, 1979 *J. Am. Chem. Soc.*, 1979, **101**, 4815–4824.

99 J. D. Slinker, A. A. Gorodetsky, M. S. Lowry, J. Wang, S. Parker, R. Rohl, S. Bernhard and G. G. Malliaras, *J. Am. Chem. Soc.*, 2004, **126**, 2763–2767.

100 A. B. Tamayo, B. D. Alleyne, P. I. Djurovich, S. Lamansky, I. Tsyba, N. N. Ho, R. Bau and M. E. Thompson, *J. Am. Chem. Soc.*, 2003, **125**, 7377–7387.

101 T. Lazarides, T. McCormick, P. Du, G. Luo, B. Lindley and R. Eisenberg, *J. Am. Chem. Soc.*, 2009, **131**, 9192–9194.

102 X. Cui, J. Zhao, Z. Lou, S. Li, H. Wu and K.-L. Han, *J. Org. Chem.*, 2014.

103 V. V. Pavlishchuk and A. W. Addison, *Inorganica Chim. Acta*, 2000, **298**, 97–102.

104 H. Cano-Yelo and A. Deronzier, *J. Chem. Soc. Perkin Trans. II*, 1984, 1093–1098.

105 H. Cano-Yelo and A. Deronzier, *Tetrahedron Lett.*, 1984, **25**, 5517–5520.

106 J. M. R. Narayanam, J. W. Tucker and C. R. J. Stephenson, *J. Am. Chem. Soc.*, 2009, **131**, 8756–8757.

107 J. D. Nguyen, E. M. D'Amato, J. M. R. Narayanam and C. R. J. Stephenson, *Nat Chem*, 2012, **4**, 854–859.

108 N. Iqbal, J. Jung, S. Park and E. J. Cho, *Angew. Chemie Int. Ed.*, 2014, **53**, 539–542.

109 D. A. Nagib, M. E. Scott and D. W. C. MacMillan, *J. Am. Chem. Soc.*, 2009, **131**, 10875–10877.

110 H.-W. Shih, M. N. Vander Wal, R. L. Grange and D. W. C. MacMillan, *J. Am. Chem. Soc.*, 2010, **132**, 13600–13603.

111 D. A. Nicewicz and D. W. C. Macmillan, *Science*, 2008, **105**.

112 R. S. Andrews, J. J. Becker and M. R. Gagné, *Angew. Chemie Int. Ed.*, 2010, **49**, 7274–7276.

113 L. Furst, J. M. R. Narayanam and C. R. J. Stephenson, *Angew. Chemie Int. Ed.*, 2011, **50**, 9655–9659.

114 M. Rueping, S. Zhu and R. M. Koenigs, *Chem. Commun.*, 2011, **47**, 8679–8681.

115 A. G. Condie, J. C. González-Gómez and C. R. J. Stephenson, *J. Am. Chem. Soc.*, 2010, **132**, 1464–1465.

116 D. B. Freeman, L. Furst, A. G. Condie and R. J. Corey, *Org. Lett.*, 2012, **14**, 94–97.

117 D. P. Hari and B. König, *Org. Lett.*, 2011, **13**, 3852–3855.

118 Y. Pan, C. W. Kee, L. Chen and C.-H. Tan, *Green Chem.*, 2011, **13**, 2682–2685.

119 Q. Liu, Y. N. Li, H. H. Zhang, B. Chen, C. H. Tung and L. Z. Wu, *Chem. - A Eur. J.*, 2012, **18**, 620–627.

120 M. Rueping, C. Vila, R. M. Koenigs, K. Poscharny and D. C. Fabry, *Chem. Commun.*, 2011, **47**, 2360–2362.

121 Z. Q. Wang, M. Hu, X. C. Huang, L. B. Gong, Y. X. Xie and J. H. Li, *J. Org. Chem.*, 2012, **77**, 8705–8711.

122 S. Zhu and M. Rueping, *Chem. Commun.*, 2012, **48**, 11960–11962.

123 J. Xuan, Y. Cheng, J. An, L.-Q. Lu, X.-X. Zhang and W.-J. Xiao, *Chem. Commun.*, 2011, **47**, 8337–8339.

124 M. A. Ischay, M. E. Anzovino, J. Du and T. P. Yoon, *J. Am. Chem. Soc.*, 2008, **130**, 12886–12887.

125 J. Du and T. P. Yoon, *J. Am. Chem. Soc.*, 2009, **131**, 14604–14605.

126 Z. Lu, M. Shen and T. P. Yoon, *J. Am. Chem. Soc.*, 2011, **133**, 1162–1164.

127 J. Du, L. R. Espelt, I. a. Guzei and T. P. Yoon, *Chem. Sci.*, 2011, **2**, 2115.

128 M. Neumann and K. Zeitler, *Chem. - A Eur. J.*, 2013, **19**, 6950–6955.

129 M. A. Ischay, Z. Lu and T. P. Yoon, *J. Am. Chem. Soc.*, 2010, **132**, 8572–8574.

130 S. Lin, A. Ischay Michael, G. Fry Charles and P. Yoon Tehshik, *J Am Chem Soc*, 2011, **133**, 19350–19353.

131 S. Lin, C. E. Padilla, M. A. Ischay and T. P. Yoon, *Tetrahedron Lett.*, 2012, **53**, 3073–3076.

CHAPTER 2

Stability of Ir_6L_4 Photoredox Active Metallosupramolecular Assemblies

Contents

2.1 Synopsis

Previous attempts in combining metallosupramolecular catalysis and photoredox catalysis led to the synthesis of an Ir_6L_4 truncated tetrahedron by Lusby and co-workers; however, this system was unsuitable for encapsulation of neutral guests due to the required templation by bound anions. This work describes attempts to stabilise the Ir_6L_4 structure by alteration of either the cyclometallated or bridging ligands. Switching 2-phenylpyridine for 2-phenylpyrazine disrupted the structure and reduced the solution stability still further. Investigations with isocyanides as bridging ligands showed great promise in the formation of two-dimensional homo- and hetero-leptic iridium architectures but the synthesis of the corresponding three-dimensional architectures could not be achieved due to ligand instability. Therefore, iridium was found to be unsuitable as a structural element in the synthesis of metallosupramolecular cages and alternative methods were explored in the following chapters.

2.2 Introduction

As discussed throughout Chapter 1, supramolecular assemblies possess a wide range of properties that make them excellent candidates for stereo- or regio-selective catalysis. Photoredox catalysis is also an emerging field in chemistry whereby synthetic reactions that normally require harsh or complex conditions can be carried out at room temperature using nothing more than visible light and an appropriate photocatalyst. In this way, potentially delicate functional groups can be protected that would otherwise degrade at high temperatures or under UV irradiation.

In order to try and combine the beneficial properties of both supramolecular and photoredox catalysts, Lusby and co-workers previously developed a M_6L_4 assembly (**120**·6X) that incorporated photoactive 2-phenyl pyridine (ppy) iridium moieties into the structure (Figure 2.1).[1] Using 1,3,5-tricyanobenzene as a bridging ligand, the $Ir(ppy)_2$ sub-units were held together in a truncated tetrahedron with an internal cavity volume of approx. 500 $Å^3$. Assembly into a rigid three-dimensional structure also led to an increase in the luminescent quantum yield due to loss of non-radiative decay pathways. In comparison, simple mononuclear complexes with ancillary nitrile ligands are completely non-emissive in solution.

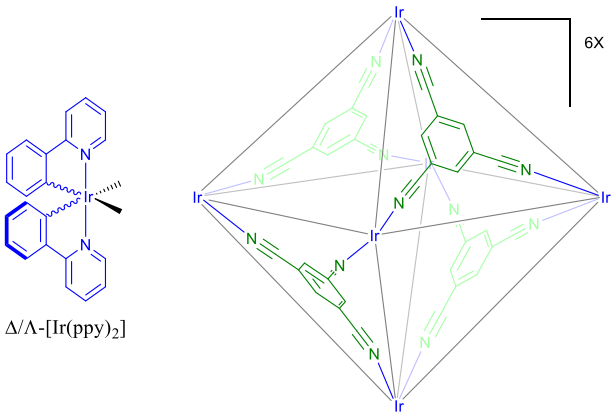

*Figure 2.1: Structure of Ir_6L_4 cage (**120**·6X) developed by Lusby and co-workers.*[1]

Despite the initial success of producing enantiopure luminescent cage structures, any attempt at binding neutral organic guests or carrying out photocatalysis on encapsulated substrates was unsuccessful due to the inherent instability of the cage structure without the templating

effect of four encapsulated counter ions. Although a range of different counter anions could be bound within the cavity (OTf, PF_6, BF_4 or ClO_4), any attempt to replace the ions with a neutral guest was unsuccessful and the addition of larger counter anions resulted in the formation of different molecular species. In order to improve the structural stability of the assembly to allow supramolecular catalysis to take place, significant modifications were required. The following chapter focuses on further investigations into the mechanism of counter ion templation and alternative methods for stabilising the cage structure.

2.3 Counter Anion Dependency

2.3.1 Introduction

The Ir_6L_4 system (**120**·6X) described by Lusby and co-workers showed a number of interesting properties, including enhanced luminescence, but the cage structure depended entirely on the presence of encapsulated anions.[1] Any attempt to replace these encapsulated anions with a neutral guest was unsuccessful, presumably due to strong competition for the internal binding sites driven by coulombic attraction between the anions and cationic cage. In addition, attempts to synthesise an "empty" cage, by self-assembly in the presence of large bulky anions (eg. NTf_2), were also unsuccessful.

The stability of the cage system was found to be anion dependent with the cage half-life following the trend OTf > PF_6 > ClO_4 > BF_4. Although templation of the cage assembly was thought to occur via encapsulation of 4 anions, guest exchange experiments showed that PF_6 had a stronger association constant than OTf for the cage internal cavity. Thus, binding strength alone could not explain the trend in cage stability.

2.3.2 Rate of Ligand Dissociation

One possible explanation for the reported variation in cage stability was that coordination of the counter ions to the iridium centres created a competition pathway for the iridium coordination sites. Direct competition between the counter ions and the nitrile ligands would increase the dissociation rate of the nitrile ligands and reduce the overall stability of the cage structure.

In order to examine the counter-ion effect on the rate of ligand dissociation, a series of iridium bis-nitrile complexes (**121**·X) were prepared as model compounds (Scheme 2.1). 4-Fluorobenzonitrile (F-PhCN, **123**) was chosen as an appropriate model ligand due to a similar benzonitrile binding motif. The fluorine provided an additional spectroscopic handle for measuring the system properties through ^{19}F NMR spectroscopy. The electron withdrawing effect of fluorine substitution could reduce the ligand binding strength but, since variation of the counter ion was the key comparison, this should not affect the experimental outcome.

The model compounds were prepared using a similar method to the synthesis of **120**·6OTf whereby [(Ir(ppy)$_2$Cl)$_2$] was treated with AgX (X = OTf, PF_6, BF_4 or ClO_4) to remove the chloride anions followed by addition of the nitrile ligand. Isolation of the compounds was carried out by precipitation from CH_2Cl_2 with Et_2O; however, the high solubility of the compounds in CH_2Cl_2, coupled with the small reaction scale, made isolation of the complexes in high yields difficult.

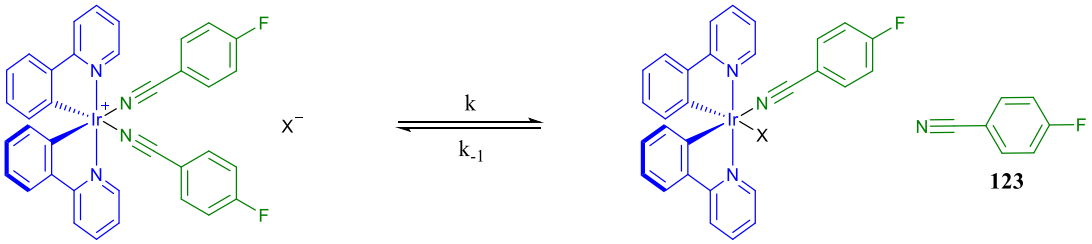

121·X
X = OTf, PF_6, ClO_4, BF_4

122·X

Scheme 2.1: Bis-(4-fluorobenzonitrile) complexes used as a model compounds for studying the effects of anions (X) on the rate of ligand dissociation.

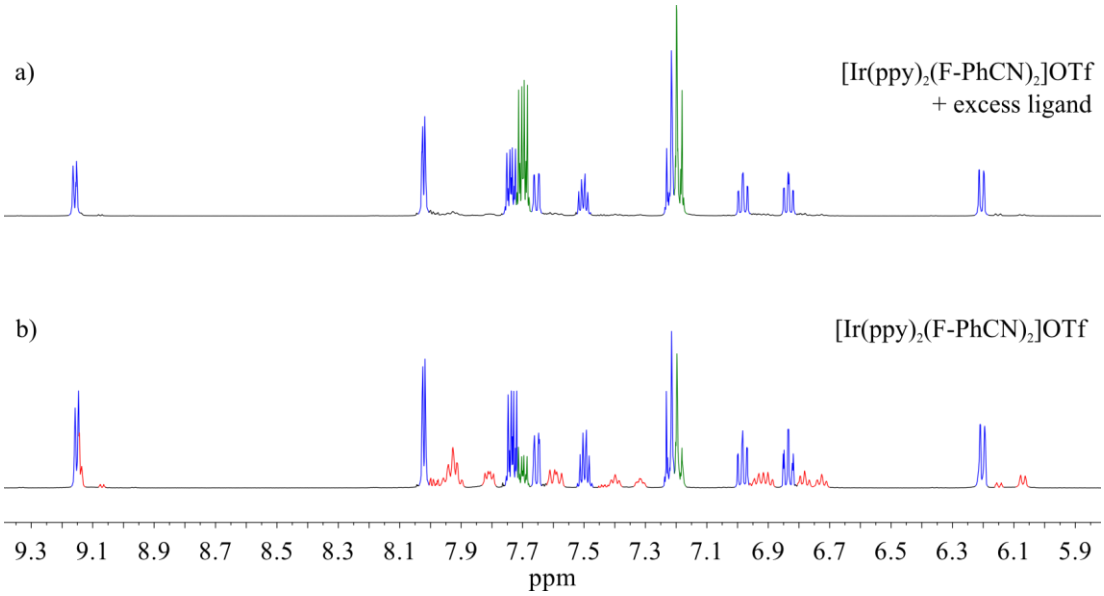

*Figure 2.2: ^{1}H NMR spectroscopy (500 MHz, CD_2Cl_2, 300 K) of **121**·OTf a) with excess ligand and b) as an equilibrium mixture of intact and partially dissociated species. Peaks corresponding to the bis(nitrile) species [IrL$_2$(F-PhCN)$_2$] (blue), mono(nitrile) [IrL$_2$(F-PhCN)OTf] (red) and free F-PhCN (green) are coloured accordingly.*

Initial NMR experiments of the isolated compounds showed that due to the relatively weak binding strength of the monodentate nitrile ligand, dissolution of the isolated complexes in CH_2Cl_2 or $C_2H_2Cl_4$ leads to an equilibrium mixture of the intact di-substituted complex (**121**), a mono-substituted complex (**122**) and free ligand (**123**) (Figure 2.2). The addition of excess ligand drives the equilibrium towards the fully intact complex and this method was used to determine the spectroscopic assignments for each of the compounds.

The ^{19}F NMR spectra of the equilibrium mixtures showed a similar distribution of species that could be driven towards the intact di-substituted complex by the addition of excess ligand. Interestingly, the peak associated with the OTf counter ion also showed a distribution of species due to complexation with the free binding site on the iridium (Figure 2.3). This shows the propensity of the counter ions, rather than solvent, to occupy the free binding site on the iridium centre and provides evidence that strong competition by the counter ions for the binding sites could therefore lead to increased dissociation of the nitrile ligands.

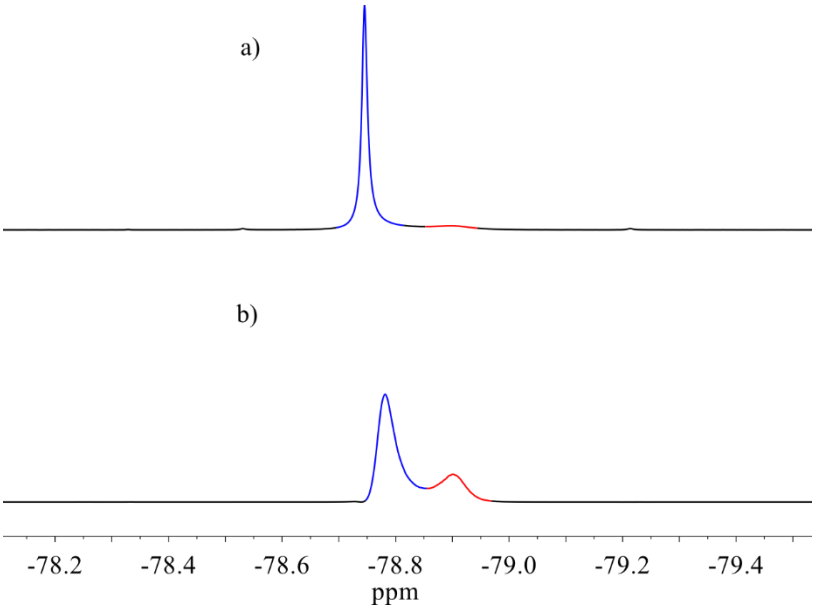

*Figure 2.3: Partial ^{19}F NMR spectrum (471 MHz, CD_2Cl_2, 300 K) of **121**·OTf as a) a sample with excess ligand showing almost complete dissociation of the OTf anion and b) an equilibrium mixture of coordinated (red) and free (blue) OTf.*

Since formation of the equilibrium mixture was rapid (the sample was completely equilibrated within 5 minutes) but exchange between the bound and free ligand was slow on an NMR timescale, ^{19}F EXSY was used to measure the exchange parameters (Figure 2.4). ^{19}F EXSY of the equilibrium mixture gave a series of cross peaks between the signals

associated with the 4-fluorobenzonitrile in various states of complexation. As with other techniques, **121** was observed along with both **122** and **123**.

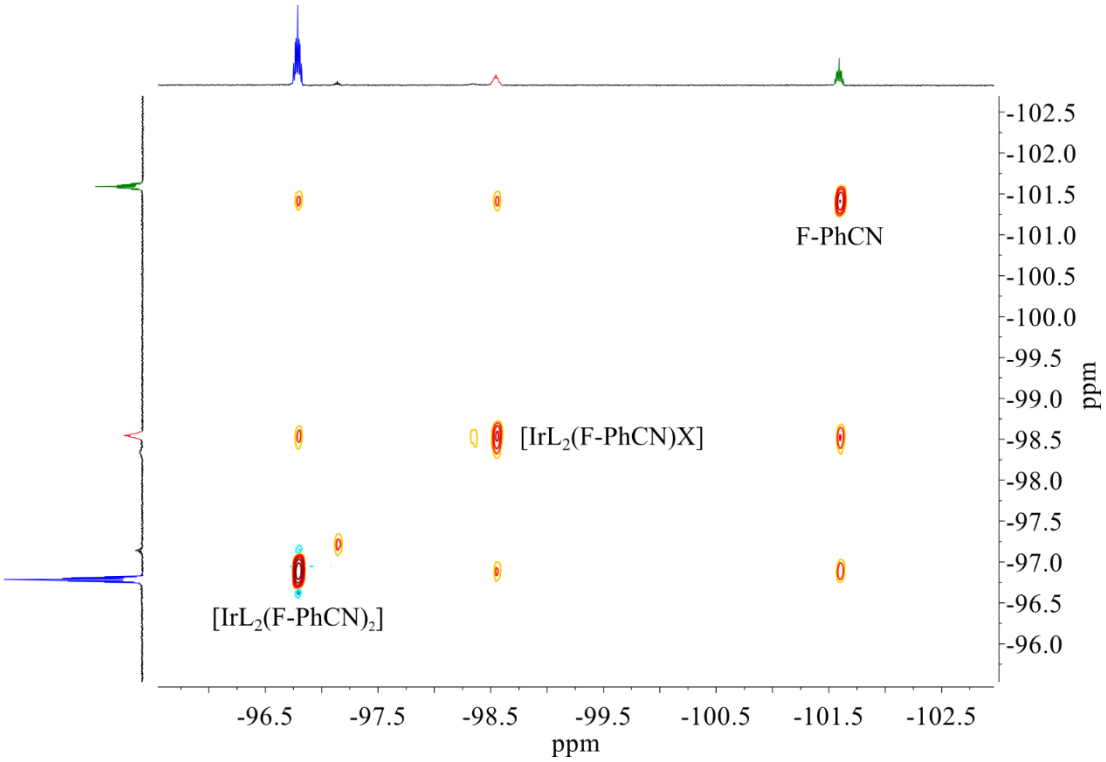

Figure 2.4: Example ^{19}F EXSY (376 MHz, $C_2D_2Cl_4$, 300 K) spectrum where L = a cyclometallated ligand, X = complexed solvent or counter ion and F-PhCN = complexed 4-fluorobenzonitrile. Peaks corresponding to the di-complexed species [IrL_2(F-PhCN)$_2$] (blue), mono-complexed [IrL_2(F-PhCN)X] (red) and uncomplexed F-PhCN (green).

For each complex, EXSY spectra were taken over a range of mixing times and plotted versus the peak ratios. In order to reduce complications arising from multiple cross peaks, the experiments were carried out in the presence of 10 equivalents of 4-fluorobenzonitrile in order to minimise the quantity of **122** in solution. The gradient of the straight line plot gives the reciprocal of the rate constant ($1/k$) which can be converted to the observed rate constant (k_{obs}) (see experimental for details). The corresponding rates of association/dissociation display very little variation with different associated counter ions and for these model systems, the rate of ligand dissociation is completely independent of the associated counter ion (Table 2.1).

Table 2.1: Rate of ligand dissociation in relation to the associated counter ion.

Compound	Gradient	k_{obs} (s^{-1})	$G^{\ddagger}$ ($kJmol^{-1}$)
2·OTf	0.0512	9.766	67.34
2·PF_6	0.0394	12.690	66.69
2·BF_4	0.0510	9.804	67.33
2·ClO_4	0.0376	13.298	66.57

Since ligand dissociation rate is not responsible for the relative stability of **1**.6X, alternative explanations were required. Further work by O. Chepelin showed that the counter ion dependent cage stability varied in accordance with the relative electrostatic potentials of the counter ions.[2] Increasing the electrostatic potential destabilises the encapsulated arrangement of anions due to coulombic repulsion and reduces the effectiveness of anion templation.

2.4 Phenylpyrazole variants

2.4.1 Introduction

Based on earlier experiments by O. Chepelin on iridium macrocycles, 2-phenylpyrazole (ppz) was found to enhance the strength of the metal-ligand interaction *cis* to the nitrogen when compared with 2-phenylpyridine (ppy).[2] This was explained by greater electron withdrawal from the phenyl ring leading to a weaker Ir-C bond which consequently increased the iridium-nitrile interaction through the *trans*-effect. Thus, it was surmised that incorporation of $Ir(ppz)_2$ moieties rather than $Ir(ppy)_2$ could lead to an analogous Ir_6L_4 structure (**124**·6X) with enhanced stability (Figure 2.5).

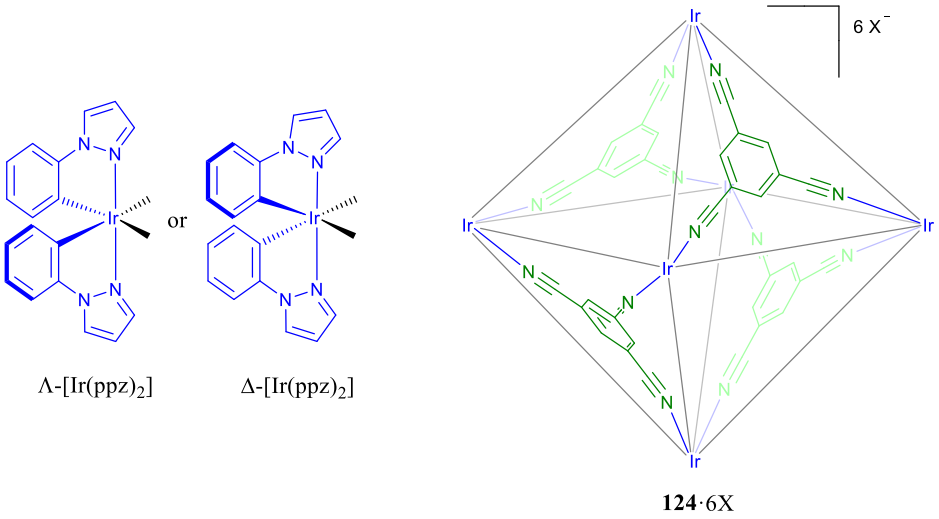

Figure 2.5: Proposed structure of the ppz substituted Ir_6L_4 truncated tetrahedron.

2.4.1 Quantification of Ligand Strength

Before carrying out the difficult resolution of enantiomers required for the synthesis of **124**·6OTf, a series of experiments were designed to quantify the relative ligand binding strengths and confirm that ppz did indeed strengthen the iridium-nitrile interaction.

In a similar manner to the experiments described in section 2.3, the corresponding ppy and ppz bis-(4-fluorobenzonitrile) complexes were synthesised. The ppz derivative (**125**·OTf) showed similar solution properties to **121**·OTf and rapidly dissociated upon dissolution in CH_2Cl_2 or TCE to form an equilibrium mixture of intact and partially dissociated species (Scheme 2.2). Rather than the time consuming experiments carried out previously where the

mixing time was varied, a single EXSY spectrum was recorded for each sample and the observed rate constant calculated directly from the cross peak ratios.

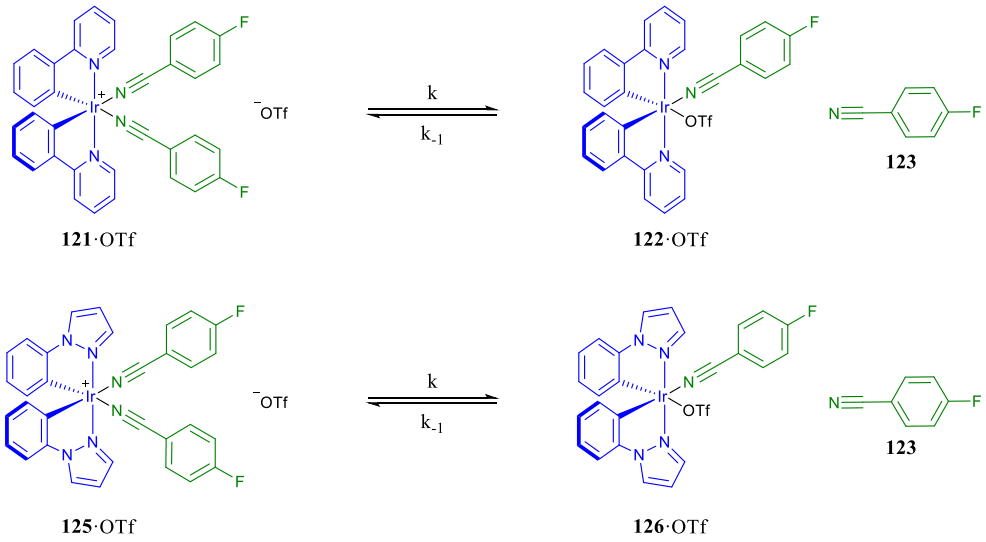

Scheme 2.2: Bis-(4-fluorobenzonitrile) complexes used as model compounds for studying the effect of ppz versus ppy on the rate of ligand dissociation.

Comparison of the values showed that **125**·OTf displays a slightly slower dissociation of the complexed 4-fluorobenzonitrile and consequently a higher activation barrier when compared with **121**·OTf under identical conditions (Table 2.1).

Table 2.1: Rate of nitrile dissociation in relation to the cyclometalled ligand.

Compound	r	k_{obs} (s^{-1})	$G^{\ddagger}$ ($kJmol^{-1}$)
121·OTf	12.605	0.159	77.54
125·OTf	37.418	0.053	80.24

Although the stability of **125**·OTf was only marginally better than **121**·OTf, incorporation of ppz into the cage structure could lead to a significant increase in the overall cage stability due to the combined decrease in the rate of dissociation for 16 metal-ligand interactions.

2.4.2 Separation of Ir(ppz)$_2$ Enantiomers

Previous analysis of **120**·6OTf showed that the iridium stereochemistry had a drastic impact on the complexity of the ^{1}H NMR.[1] The racemic sample constituted a complex mixture of cage systems containing a statistical mixture of different enantiomeric centres. In order to simplify the system for analysis, the homochiral variant was assembled from enantiopure [(Ir(ppy)$_2$Cl)$_2$] prepared using serine as a chiral resolving agent.

124·6OTf could be expected to form the same complex mixture of diasteromers and thus, enatiomerically pure [(Ir(ppz)$_2$Cl)$_2$] (**127**) was required for the formation of homochiral **124**·6OTf. *rac*-[Ir(ppz)$_2$D-Serine] (**128**) was prepared based on the literature procedures describing the original synthesis of enantiopure [(Ir(ppy)$_2$Cl)$_2$] (Scheme 2.3). However, unlike the previously investigated [Ir(ppy)$_2$Serine] compounds, separation of the Λ/Δ-[Ir(ppy)$_2$D-Serine] diasteromers did not require silica chromatography and instead, the diastereomers could be separated based on solubility alone. Partial dissolution in CH_2Cl_2 followed by filtration gave a solution containing the single diasteromer Δ-**128**, confirmed by ^{1}H NMR spectroscopy. After separation, enantiopure **127** could be reconstituted by the dissolution of **128** in CH_3OH and the addition of concentrated $HCl_{(aq)}$. Unfortunately, the opposite enantiomer could not be obtained from the solid residue and instead, the process was repeated with L-Serine.

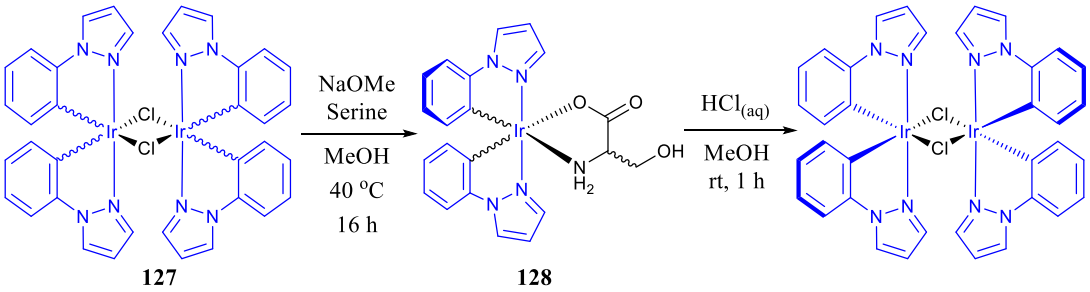

Scheme 2.3: Synthesis and separation of serine diasteromers to give enantiopure Λ/Δ-[(Ir(ppz)$_2$Cl)$_2$].

Due to the difference in separation methods, the chirality of **127** could not be assumed based on the enantiomers obtained using [(Ir(ppy)$_2$Cl)$_2$]. Instead, the chirality of **128** was confirmed through X-ray crystallography of the assembled cage **124**·6OTf (see section 2.4.3).

2.4.3 Synthesis of Phenylpyrazole Ir_6L_4 Assembly

Following the successful separation of Λ-**127** & Δ-**127**, **124**·6OTf was prepared in an analogous manner to the parent compound **120**·6OTf. First of all, **127** was treated with AgOTf and filtered to remove the competing chloride ligands and provide the OTf counter ions required for templation of the cage structure. 1,3,5-tricyanobenzene (tcb, **129**) was then charged and the mixture stirred at room temperature until a yellow precipitate was formed (Scheme 2.4).

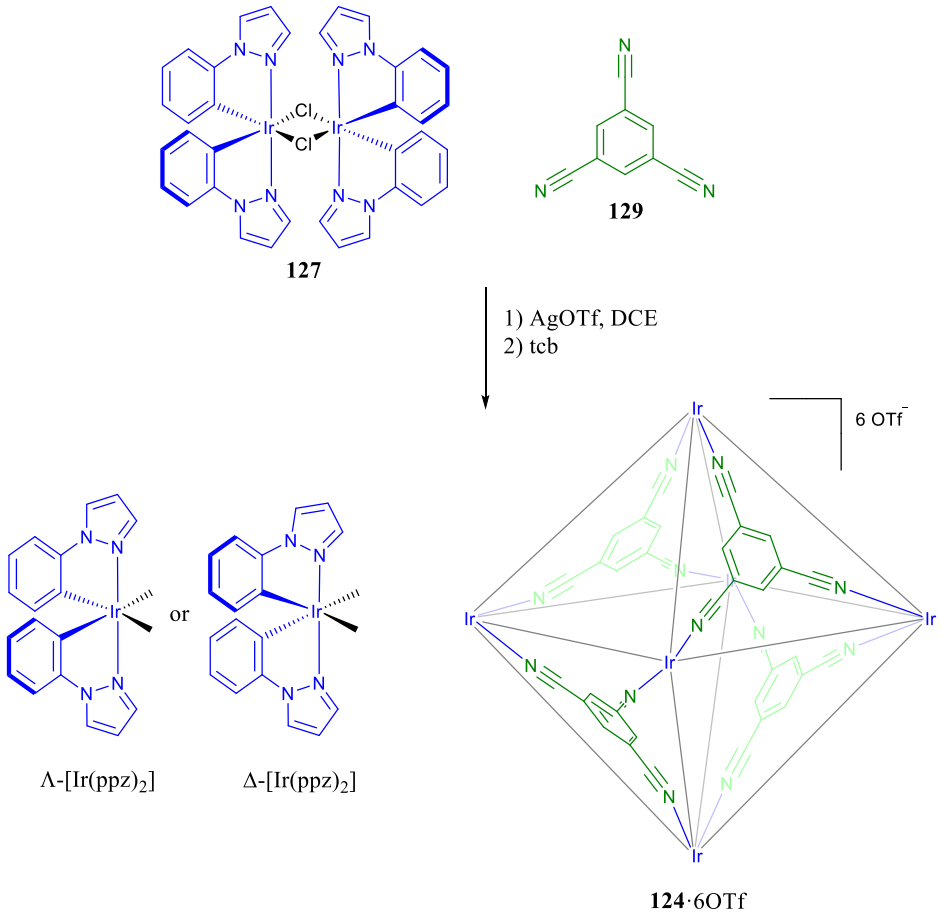

*Scheme 2.4: Synthesis of [(Ir(ppz)$_2$)$_6$(tcb)$_4$]6OTf (**5**·6OTf). The compound was prepared separately with both Δ & Λ enantiomers of the starting [(Ir(ppz)$_2$Cl)$_2$].*

NMR analysis in TCE showed the characteristic peak shifts observed upon metal-ligand complexation whilst the structure remained completely symmetric (Figure 2.6). DOSY NMR confirmed a significant increase in the hydrodynamic radius from 8.8 Å to 14.3 Å which is in direct agreement with the 14.3 Å radius recorded for the original **120**·6OTf system.[1] X-ray

quality crystals were prepared by slow diffusion of benzene into a saturated solution of **124**·6OTf in TCE. Only partial resolution of the diffraction data was achieved but the expected truncated tetrahedral structure was clearly visible and OTf counter anions were detected within the cage interior (Figure 2.22).

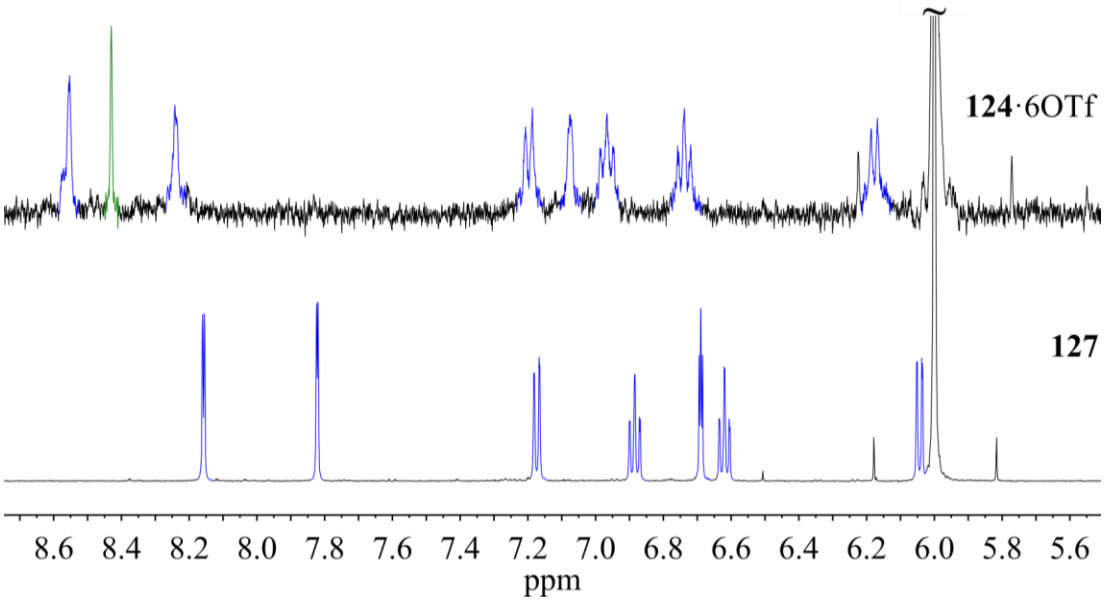

*Figure 2.6: ^{1}H NMR (500 MHz, $C_2D_2Cl_4$, 300 K) comparison of **127** versus **124**·6OTf. Strong downfield shifts were observed for all proton signals consistent with ligand complexation.*

As observed for **120**·6OTf, the ^{19}F NMR spectrum showed two partially overlapping peaks corresponding to free and encapsulated OTf. However, both peaks were heavily broadened due to chemical exchange. VT experiments at reduced temperatures allowed the complete resolution of the peaks and showed that coalescence occurred just above room temperature.

All of characterisation data agreed with the formation of an Ir_6L_4 truncated tetrahedron in solution. Many similarities were observed when comparing **124**·6OTf to **120**·6OTf, including downfield chemical shifts, an identical hydrodynamic radius and encapsulation of OTf counter anions.

2.4.4 Stability of Phenylpyrazole System

In order to assess the stability of **124**·6OTf, a scrambling experiment was carried out in which the enantiomerically pure samples were combined and the resultant rearrangement to a statistical mixture was monitored by ^{1}H NMR spectroscopy (Figure 2.7). The results were compared with a similar experiment carried out on **120**·6OTf by O. Chepelin. Since the resultant rearrangement generates a complex mixture, the singlet corresponding to the symmetrical ligand was chosen as the best analytical probe due to the ease of integration and obvious splitting. However, since a portion of the statistical mixture remains an enantiopure cage even after complete rearrangement, the exponential decay functions do not tend to zero. In addition, **120**·6OTf contains overlapping peaks such that the integral does not diminish as far as expected and thus, the exponential decay functions were fitted based on the final minimum area. Due to the complex aromatic region, integration was referenced versus the grease peak.

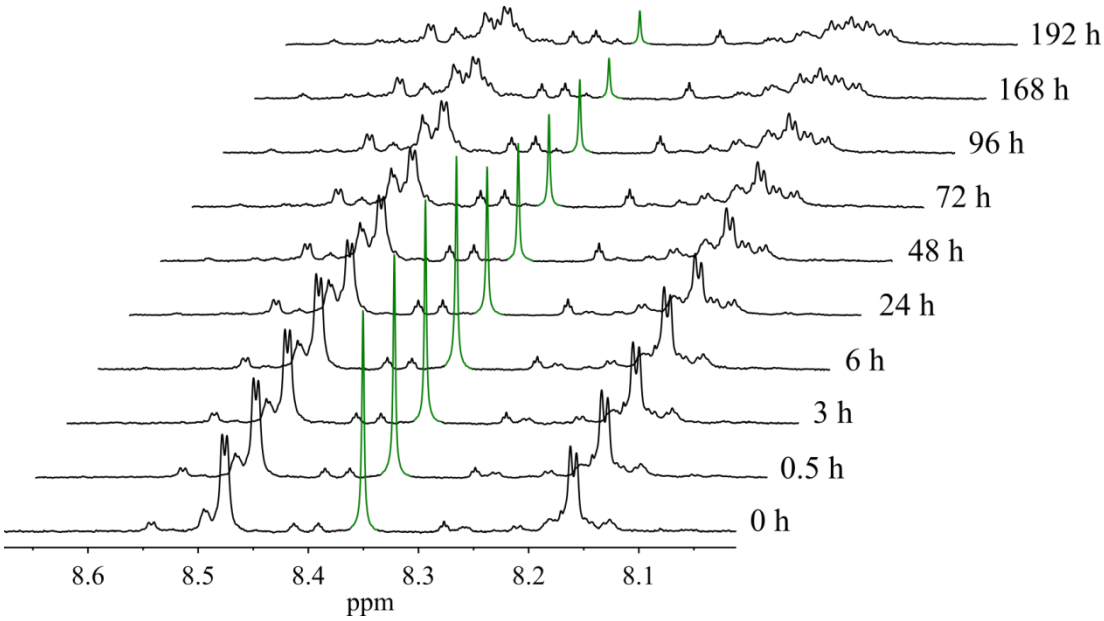

Figure 2.7: Partial ^{1}H NMR spectra (500 MHz, CD_3CN, 300 K) showing slow rearrangement of the enantiomerically pure cage systems to the complex statistical mixture. The symmetrical 1,3,5-tricyanobenzene peak (green) gradually reduced as the system was desymmetrised.

Despite early experiments lending evidence towards 2-phenylpyrazole strengthening the iridium-nitrile interaction compared to 2-phenylpyridine (Section 2.4.1), the stability of the corresponding Ir_6L_4 cage was reduced from a half-life of 56 h for **120**·6OTf to 39 h for

124·6OTf. Since mono-nuclear studies indicated a stronger metal-nitrile interaction for the ppz derivatives, it seems likely that the reduced stability of **124**·6OTf is due to structural effects from the self-assembly of a large supramolecular species. The smaller ppz ligands do not show any obvious steric clash between adjacent iridium groups; however, the smaller size does result in an increase in cage portal size. This may explain the faster rate of exchange between bound and free OTf anions as demonstrated by the peak coalescence in the ^{19}F NMR spectrum for **124**·6OTf compared with the slow binding observed for **120**·6OTf. Interestingly, even at low temperatures, integration of the relevant ^{19}F NMR signals suggests that a higher proportion of the OTf anions remain unbound at equilibrium rather than the distinct 4 encapsulated anions observed for **124**·6OTf. Therefore, it seems likely that the reduced stability of **124**·6OTf is due to weaker templation of the cage structure by the encapsulated anions, despite any marginal increases in the iridium-nitrile binding strength.

Whilst the reduced stability of **124**·6OTf could potentially be altered by incorporation of different anions, the dominating factor in cage formation and stability is still the presence of encapsulated anions. Any subtle increase in metal-nitrile bond strength by variation of the cyclometallated ligands is unlikely to offset the need for efficient templation by encapsulated anions.

2.5 Homoleptic Iridium Isocyanide Architectures

2.5.1 Introduction

In an effort to further increase the metal-ligand bond strength, isocyanides were proposed as a replacement to the nitrile functional groups already employed. Isocyanides show much stronger binding affinities for metals, both being better σ-donors and π-acceptors than the corresponding nitriles, such that they even rival carbon monoxide in binding strength.[3] Assuming the metal-ligand interactions would still be reversible at elevated temperatures to allow self-assembly, any supramolecular species formed would then be stabilised at room temperature through kinetic trapping.

Although isocyanide and cyanide based supramolecular structures have been reported previously,[4–7] very few examples exist where the bridging units consist of solely metal-isocyanide linkages.[8,9] Since the metal-isocyanide interactions are usually kinetically inert, they are often used to incorporate functionality into systems assembled from other more labile interactions.[10] Direct addition of diisocyanides to metals often results in the rapid formation of coordination polymers.[11–18] Successful synthesis of iridium based isocyanide supramolecular structures therefore relies on the iridium-isocyanide interaction attaining an element of reversibility at high temperatures.

Since the direct isocyanide analogue of **129**, 1,3,5-triisocyanobenzene (**130**), was unknown in the literature, the commercially available 1,4-diisocyanobenzene (**131**) was initially chosen as a model compound to investigate the feasibility of isocyanides as self-assembly components (Figure 2.8).

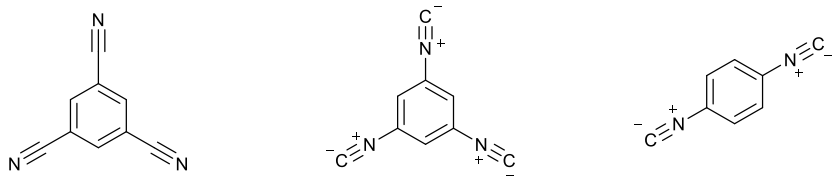

129 **130** **131**

*Figure 2.8: Comparison of 1,3,5-tricyanobenzene (**129**) versus the envisaged stronger binder, 1,3,5-triisocyanobenzene (**130**) and commercially available 1,4-diisocyanobenzene (**131**).*

2.5.1 Synthesis

Using **131** as a model compound, the synthesis of a two-dimensional structures was attempted using conditions based on those used for the original synthesis of **120**·6OTf. $[(Ir(ppy)_2Cl)_2]$ and **131** were stirred in TCE and AgOTf was charged to aid the replacement of the chloride with loosely coordinated OTf anions. Since the ligands were expected to bind irreversibly at room temperature, the mixture was refluxed in order to increase the rate of the iridium-isocyanide dissociation and promote the self-assembly and rearrangement to the thermodynamic product.

After cooling and filtering through Celite, analysis of the crude reaction mixture by ^{1}H NMR spectroscopy showed a complex aromatic region where each of the original 2-phenylpyridine signals had been split into a range of different environments. DOSY NMR indicated that the peaks all belonged to similar sized species with a radius of approximately 10.4 Å. This increase in hydrodynamic radius from the starting material (8.8 Å) suggested that complexation had occurred but the formation of well-defined supramolecular species was still uncertain.

Mass spectrometry of the crude mixture confirmed the presence of several different two-dimensional species. Although additional fragments were observed, the major peaks corresponded to predicted $[(Ir(ppy)_2)_n(dib)_n]$nOTf structures with n = 3,4 or 5. Since the majority of the peaks contained equal numbers of $Ir(ppy)_2$ groups and ligand **131**, the structures for n = 3,4 or 5 were assigned as the cyclised triangle, square and pentagon respectively (Figure 2.9). Although alternative non-cyclised structures were also possible, the formation of coordination polymers would be expected to give a more random distribution of peaks and produce chains of increasing length until irreversible precipitation occurred.

Three-dimensional metallosupramolecular assemblies often form well-defined discrete species with the overall configuration dictated by the highly directional transition metal-ligand bonds. However, in two-dimensional assemblies each metal forms only two structural bridges with neighbouring metal centres and thus a greater degree of structural flexibility is observed. Since the ideal bond angle of octahedral Ir(III) is close to 90^o, the expected macrocyclic structure with linear ligands is that of a square but the slight structural flexibility afforded by the metal centre and ligand backbone accommodates the formation of both the triangle and the pentagon. Although these strained structures would be expected to be

slightly less thermodynamically stable due to ring strain, the small energy barriers are easily overcome, particularly at elevated temperatures. Similar effects have been observed previously with palladium based two-dimensional assemblies.[19,20]

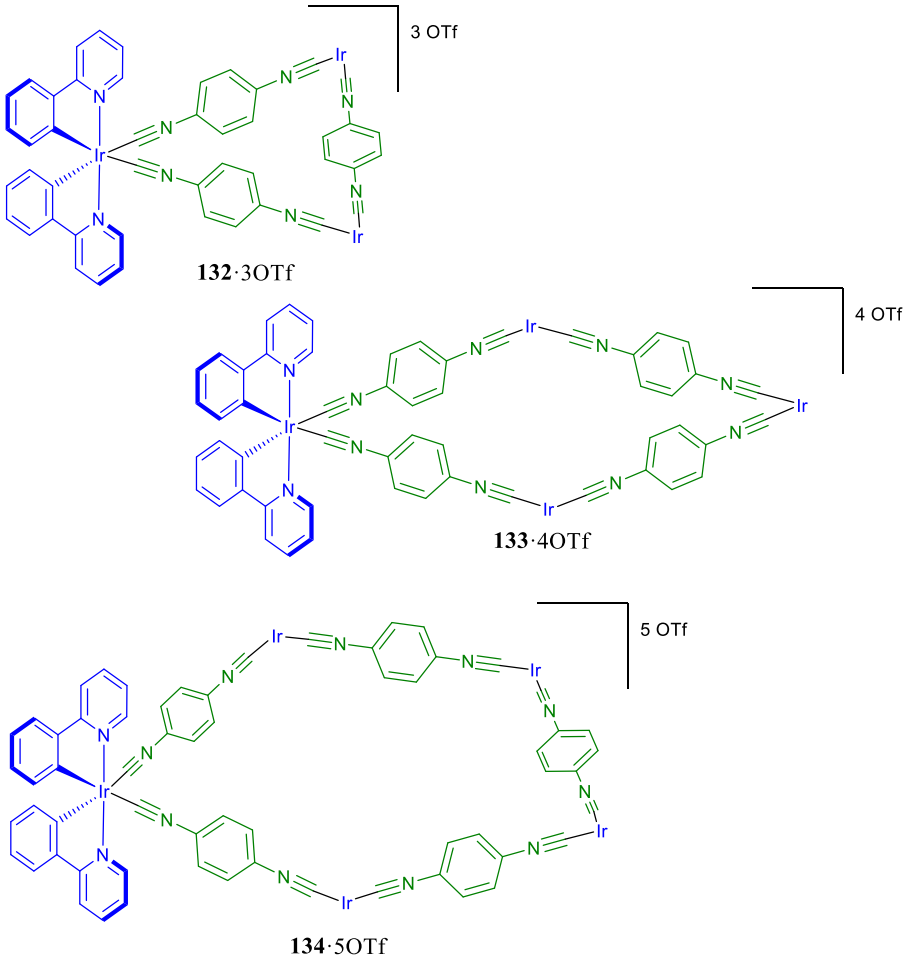

Figure 2.9: Predicted structures for [(Ir(ppy)$_2$)$_n$(dib)$_n$]nOTf where n = 3, 4 or 5.

2.5.2 Purification

Since the reaction conditions could not differentiate between the similar cyclised products, further purification was required to isolate and confirm their chemical composition. Due to the strong metal-isocyanide interactions, the assembled structures were found to be stable on silica and individual species could be separated using a solvent gradient method starting with 100% CH_2Cl_2 progressing to 10% CH_3OH in CH_2Cl_2.

The products display green/blue fluorescence under UV light and this was used to monitor the progress of the column. The different species were visible as more intense bands but due

to compound smearing and staining of the silica, these bands became less visible as the column progressed. In addition, the charged nature of the iridium complexes resulted in significant product loss on the column. Despite these difficulties, both **132**·3OTf and **133**·4OTf were isolated pure and fully characterised by NMR spectroscopy and nESI-MS.

Since the relative chemical environments and symmetry for each of the structures are so similar, the ^{1}H NMR spectra are also very difficult to differentiate (Figure 2.10). The only noticeable variation is due to slight shifts in the peak positions, particularly apparent for the singlet signal associated with the bridging 1,4-diisocyanobenzene ligand. However, DOSY confirmed that the isolated **132**·3OTf and **133**·4OTf had hydrodynamic radii of 8.4 Å and 9.0 Å respectively. nESI-MS confirmed the structural composition of the isolated species and matched with the previous analysis of the crude reaction mixture (Figures 2.27-2.32).

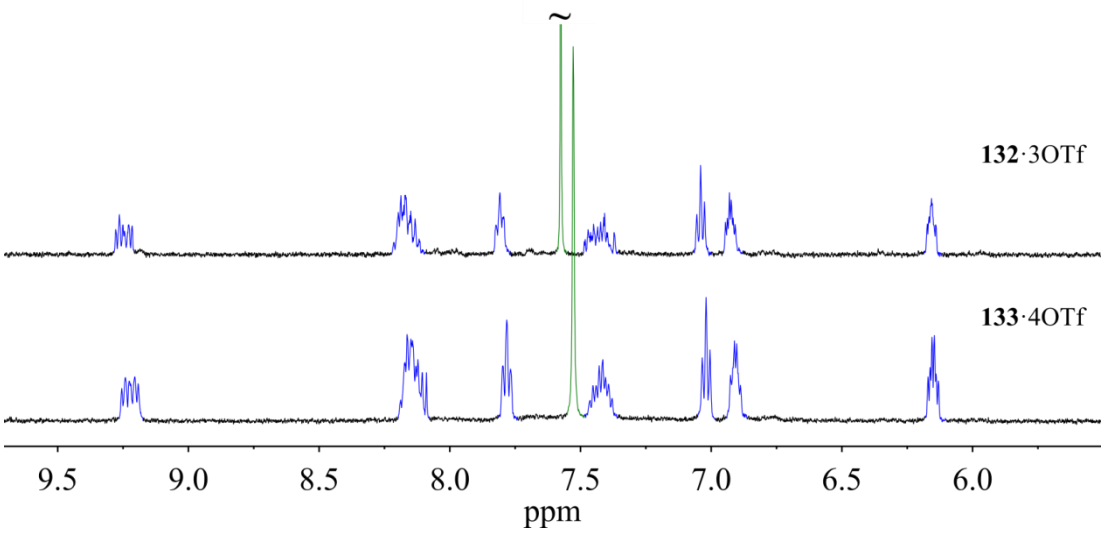

Figure 2.10: ^{1}H NMR (500 MHz, CD_3CN, 300 K) comparison of isolated rac-*[(Ir(ppy)$_2$)n(dib)$_n$]nOTf where n = 3 (**132**·3OTf) and n = 4 (**133**·4OTf).*

Despite purification and confirmation of the molecular structure by NMR and nESI-MS, both samples still showed extensive splitting patterns in the ^{1}H NMR spectra. This complex splitting was thought to be due to the formation of a mixture of diastereomers as observed for the Ir_6L_4 cage systems discussed in section 2.3-2.4.

To confirm this hypothesis, the synthesis was repeated with enantiopure Λ-[(Ir(ppy)$_2$Cl)$_2$]. Importantly, the cyclometallated ligands are completely inert even in refluxing TCE, as demonstrated by the need for very high temperatures (ca. 240 ºC) required for the

rearrangement of *mer*-Ir(ppy)$_3$ to *fac*-Ir(ppy)$_3$,[21,22] such that the synthesis could be carried out without racemisation of the iridium centres. Due to the smaller scale, only the [(Ir(ppy)$_2$)$_3$(dib)$_3$]3OTf triangle could be isolated pure in usable yields. DOSY and nESI-MS confirmed that the size and molecular formula were identical to the analogous racemic compound, however, the ^{1}H NMR spectrum was drastically simplified to give only the expected ^{1}H-^{1}H coupling patterns confirming that the complex spectrum observed in the racemic samples was due solely to the formation of a mixture of diastereomers (Figure 2.11).

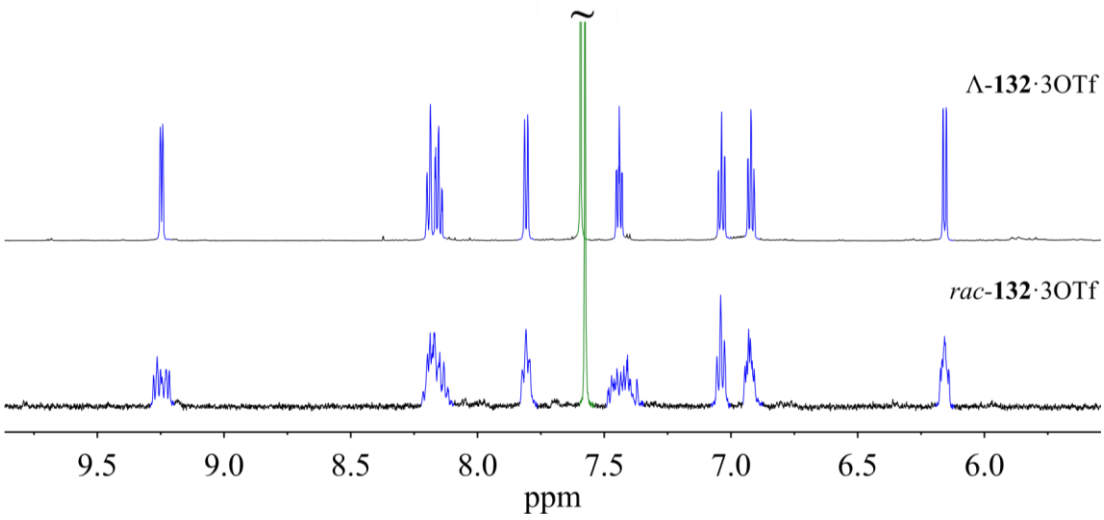

Figure 2.11: ^{1}H NMR (500 MHz, CD$_3$CN, 300 K) Comparison of rac-***132**·3OTf and Λ-**132**·3OTf showing loss of signal complexity due to a mixture of diastereomers.*

2.5.3 Stability of Two-dimensional Isocyanide systems

In order to assess the stability of the isolated isocyanide systems, a scrambling experiment was carried out by the addition of a competing ligand. 2,6-Dimethylphenylisocyanide was chosen as an appropriate competitor due to a similar mode to **131** and commercial availability.

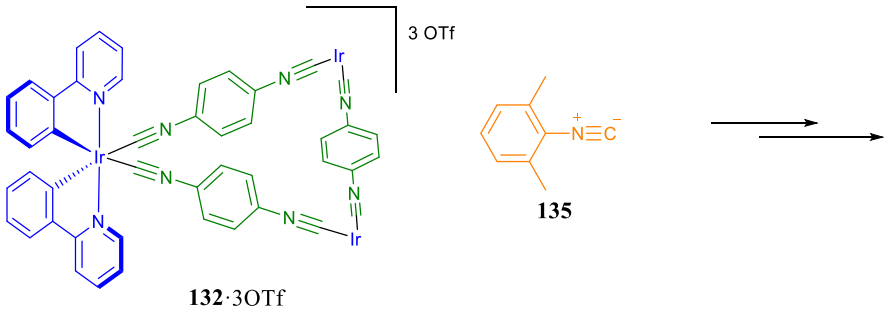

*Scheme 2.5: Addition of a 2,6-dimethylphenylisocyanide as a competing ligand for analysis of the structural stability of Λ-**132**·3OTf.*

Successive heating at high temperatures over the course of several weeks produced only a very small quantity of the scrambled products (Figure 2.12). Given that complete scrambling of **120**·6OTf occurs at room temperature in only a few days, even without the presence of a competing ligand and that dissolution in CH_3CN results in immediate disassembly of the cage structure, the isocyanide ligands show a remarkable increase in stability.

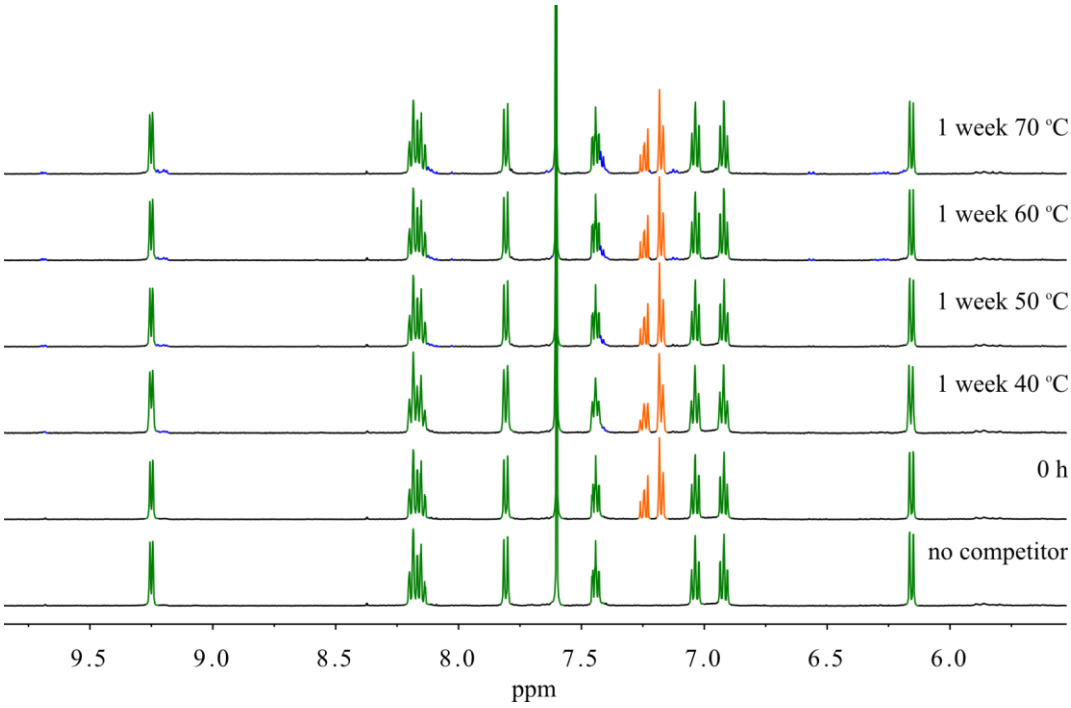

*Figure 2.12: ^{1}H NMR (500 MHz, CD_3CN, 300 K) of successive heating of Λ-**13**·3OTf (green) in the presence of **16** (3 equivalents, orange) resulted in the very slow appearance of the scrambled species (blue).*

2.6 Heteroleptic Iridium Isocyanide Architectures

2.6.1 Introduction

Self-assembly presents a powerful method for the synthesis of large complex molecules from simple starting materials. However, the combination of multiple ligands to form heteroleptic architectures remains challenging as self-assembly often leads to a complex mixture of different species. This can be overcome by using a step-wise assembly process where certain interactions can be sequentially favoured.[23] Hupp and co-workers have previously developed a range of luminescent square compounds based on the stepwise synthesis of rhenium complexes.[24,25] The initial complexation of a bridging ligand to rhenium produces a dinuclear complex that can be isolated and purified by column chromatography. Removal of the remaining chloride anions by treatment with AgOTf allows the complexation of a second linear bidentate ligand to form a range of molecular square compounds. This selective square formation could be applied to the synthesis of iridium-isocyanide structures to produce heteroleptic luminescent architectures.

2.6.2 Synthesis

While refluxing in TCE (146 ºC) completely labilises all of the iridium-isocyanide interactions as demonstrated by the formation of the homoleptic architectures described in section 2.5, specific interactions can be favoured at lower temperatures. The most common synthetic starting material for iridium complexes is the bridged chloride dimer, $[(Ir(C\hat{}N)_2Cl)]_2$. The bridging chloride complex could be selectively split by the addition of 1 equivalent of **131** (Scheme 2.6). Since the bridging interactions significantly weaken the Ir-Cl bond, the initial displacement of the chloride occurs rapidly. Once the chloride is bound to only a single iridium centre, the Ir-Cl interaction is strengthened and any additional displacement requires high temperatures. The resultant diisocyanide bridged compound (**137**) can be isolated and purified to yield a non-fluorescent yellow/green solid suitable as a synthetic "edge" piece for the formation of the luminescent heteroleptic architectures.

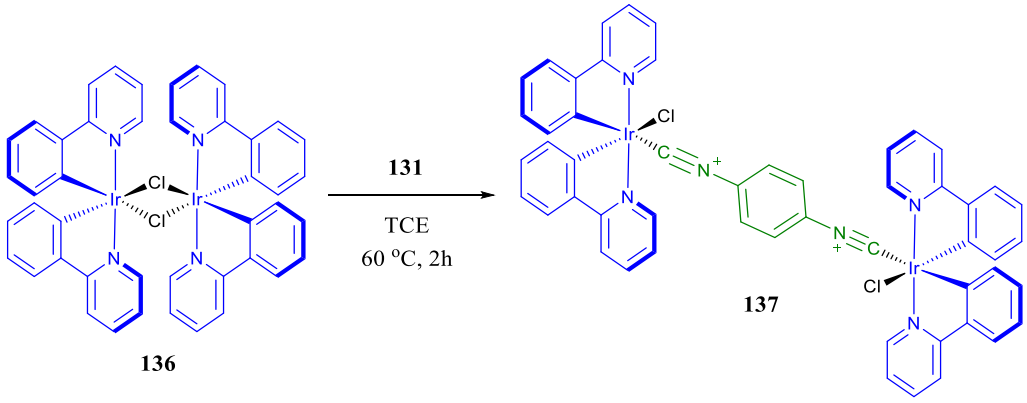

*Scheme 2.6: Synthesis of isocyanide bridged iridium dimer (**137**) by selective cleavage of the bridging chloride bonds.*

Similar diisocyanide bridged complexes have been prepared previously using ruthenium bipyridine/terpyridine compounds.[26–30] Whilst these systems often possess interesting photophysical and redox properties, they do not contain easily removable ligands that can be utilised for stepwise synthesis of supramolecular structures.

For the second step in the synthesis, rather than use excessively high temperatures that could lead to breakdown products, **137** was treated with AgOTf to replace the tightly bound chloride ligands with weakly interacting OTf. Addition of a different linear bidentate ligand, such as 4,4'-bipyridine, then led to the formation of a symmetric heteroleptic rectangle in a similar manner to that described by Hupp and co-workers (Scheme 2.7).[24]

Although switching to weaker bipyridine ligands potentially reduces the overall stability of the compound, this method represents a unique way of rapidly constructing a wide array of heteroleptic architectures from simple starting materials. In theory, any linear bis-bidentate ligand could be used for formation of the square allowing easy modulation of the chemical and photophysical properties. The step-wise synthetic pathway also selectively generates the square rather than alternative molecular structures. As discussed in section 2.5, synthesis of the corresponding homoleptic isocyanide architectures results in a complex mixture of products but selective formation of **138** results in a much cleaner self-assembly process.

Interestingly, the formation of the homoleptic 4,4'-bipyridine analogue of **133** could not be accomplished even at elevated temperatures. A similar observation was made by Lusby and co-workers upon initial attempts to synthesise an iridium analogue of the Pd_6L_4 truncated tetrahedron described by Fujita and co-workers, where L = tripyridyltriazine. The authors

suggest that the 45º dihedral angle favoured by the pyridine sub-units due to steric constraints, heavily disfavours the formation of rigid frameworks. In this sense, this method also provides a way of incorporating ligands that would otherwise struggle to form homoleptic supramolecular assemblies.

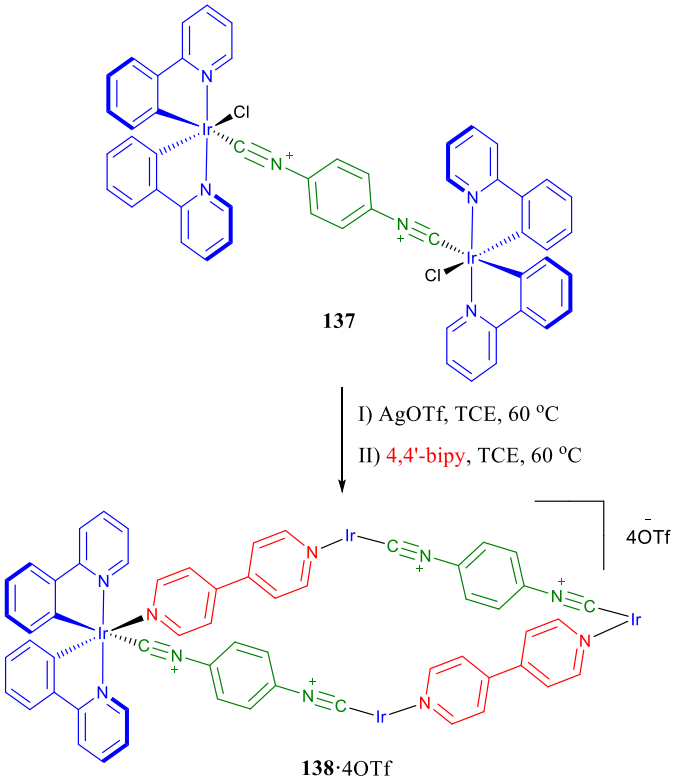

Scheme 2.7: Synthesis of heteroleptic iridium rectangle, ***138****·4OTf, from the isocyanide "edge" piece,* ***137****.*

2.7 Three-dimensional Isocyanide Architectures

2.7.1 Introduction

The strong metal-isocyanide interaction was found to be labile at elevated temperatures, allowing the reversible bond formation required for the self-assembly process. Importantly, when cooled to room temperature, the bonds remained stable for long periods of time allowing the assembled luminescent structures to remain stable in solution for months at a time, even in the presence of competing ligands. However, these model two-dimensional systems were too open to expect any strict guest confinement that is fundamental for regio- and stereo-selective supramolecular catalysis.

In order to generate the isocyanide variant of the three-dimensional **120**·6OTf, 1,3,5-isocyanobenzene was required to replace the 1,3,5-tricyanobenzene used in the original synthesis. In addition, three-dimensional heteroleptic systems could also be envisaged incorporating isocyanide panels joined with 4,4'-bipyridine linkers (Figure 2.13).

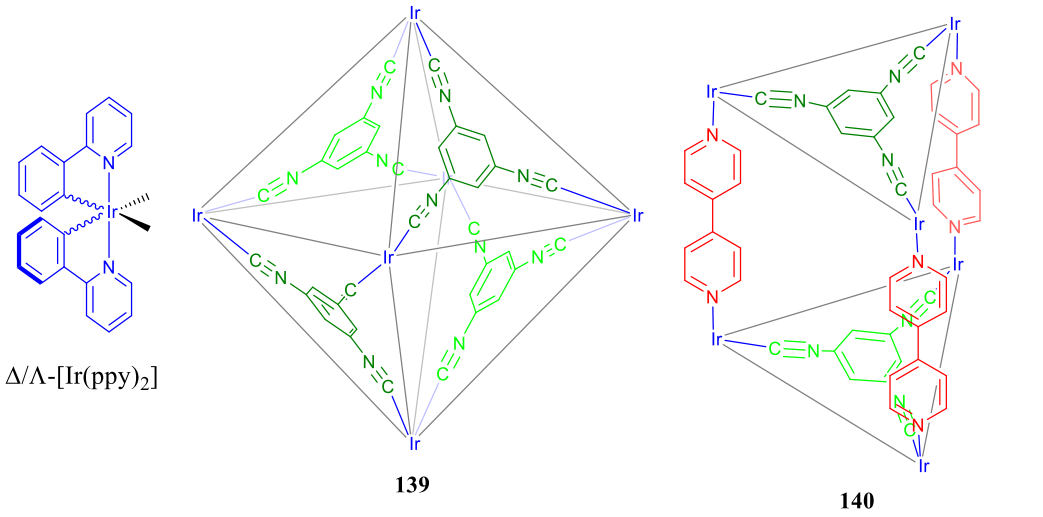

*Figure 2.13: Proposed structures of potential homoleptic (**139**) and heteroleptic (**140**) three-dimensional isocyanide based iridium supramolecular architectures.*

2.7.2 Synthesis

Synthesis of the 1,3,5-isocyanobenzene was carried out using 1,3,5-triaminobenzene as the starting material. This was prepared using literature methods by hydrogenation of the commercially available 3,5-dinitroaniline (Scheme 2.8).

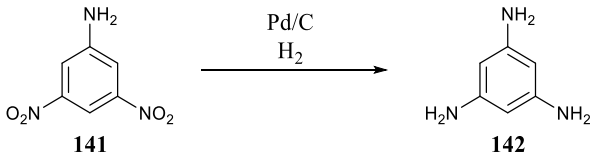

141 **142**

Scheme 2.8: Synthesis of 1,3,5-triaminobenzene.

Conversion of the amino groups to isocyanides was attempted using the Hofmann carbylamine reaction (Scheme 2.9). The reactive species, dichlorocarbene, was generated *in situ* by the addition of a strong base to chloroform. Although this reaction was known for aniline, there was no literature evidence for the formation of 1,3,5-triisocyanobenzene.

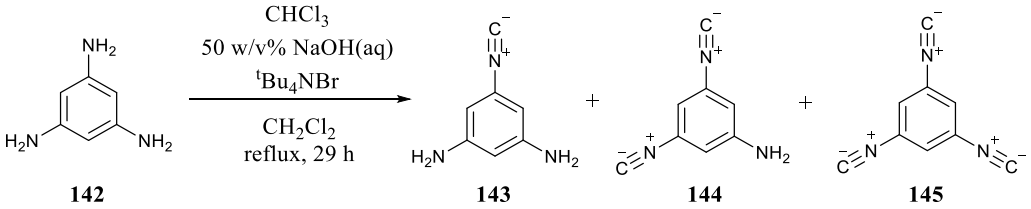

142 **143** **144** **145**

*Scheme 2.9: Synthesis of 1,3,5-triisocyanobenzene (**145**) and the structures of the observed mono- (**143**) and di-substituted (**144**) intermediates and product.*

TLC analysis of the reaction mixture showed the slow generation of new species, with multiple spots observed indicative of the expected **143**, **144** and **145**. ^{1}H NMR analysis of the reaction mixture after 29 h showed a mixture of the starting material, product and intermediates. Due to limited number of proton peaks and thus information associated with each species, they were identified primarily by chemical shift and relative peak integrations for the unsymmetrical intermediates (Figure 2.14). However, extended heating did not lead to any further conversion to the final product and instead, all of the peaks slowly diminished. Any attempt to optimise the reaction conditions or purify and isolate the compound by column chromatography was unsuccessful as the product appeared to rapidly degrade on silica, potentially due to acid hydrolysis.

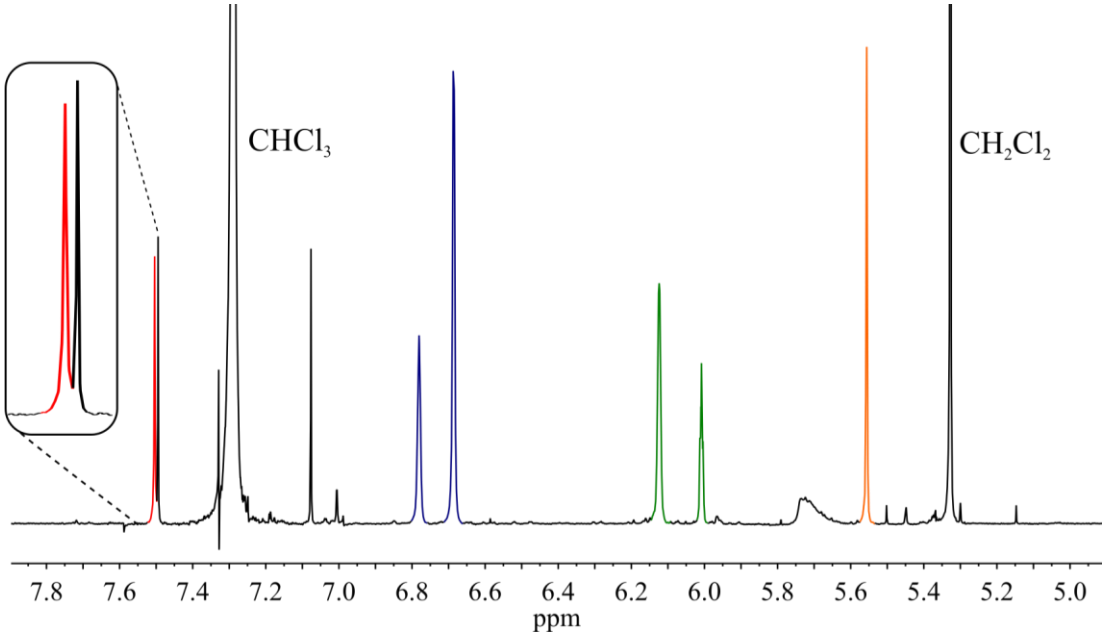

Figure 2.14: ^{1}H NMR (500 MHz, $CDCl_3$, 300 K) of crude products from the formation of ***145****. The tri- (red), di- (blue) and mono-isocyanide (green) are all observed along with the starting material, 1,3,5-triaminobenzene (orange).*

Storage of the crude reaction samples at room temperature also led to the rapid degradation of the isocyanide compounds and the loss of the relevant peaks from the aromatic region. The apparent instability of the 1,3,5-triisocyanobenzene made it impossible to isolate or purify a usable amount for further studies. As such, alternative systems were explored for generating photoactive metallosupramolecular structures.

2.8 Summary & Conclusions

The photoactive iridium-based supramolecular system, **120**·6OTf, developed by Lusby and co-workers relies on templation by encapsulated counter anions. Attempts have been made to stabilise the structure so that an "empty" cavity could be obtained to allow the encapsulation of neutral guest molecules and the development of supramolecular photoredox catalysis.

The iridium-nitrile bond strength was found to be completely independent of the associated counter ions, and thus the counter ion dependent stability of **120**·6OTf was thought to arise from differences in the templating ability. Separate work by O.Chepelin showed that the resultant cage stability followed a direct correlation with the differences in electrostatic repulsion between the encapsulated anions.[2]

Alteration of the cyclometallated ligand from 2-phenylpyridine to 2-phenylpyrazole was shown to produce a measurable enhancement in the iridium-nitrile bond strength based on mononuclear studies. However, the corresponding cage compound, **124**·6OTf, was less stable than the parent compound, **120**·6OTf, due to more rapid exchange of the encapsulated OTf anions.

In order to further strengthen the iridium-ligand interactions, isocyanides were explored as supramolecular building blocks. Self-assembly of two-dimensional homoleptic assemblies was accomplished at elevated temperatures and the resultant compounds displayed a remarkable increase in stability compared with similar nitrile systems. In addition, a step-wise synthetic approach to the formation of heteroleptic iridium assemblies was developed allowing the selective incorporation of alternative binding groups.

Despite the room temperature stability of two-dimensional iridium isocyanide assemblies, attempts to synthesise the 1,3,5-triisocyanobenzene ligand, required for formation of the direct structural analogue of **120**·6OTf, were unsuccessful due to the inherent instability of 1,3,5-triisocyanobenzene.

Isocyanide iridium compounds show great promise as synthetically useful building blocks for generating stable luminescent supramolecular assemblies. However, due to synthetic difficulties the remainder of this work will focus on alternative methods of incorporating photoredox active building blocks into the structures of well-defined and stable supramolecular coordination compounds.

2.9 Experimental

2.9.1 General Information

Unless stated otherwise, all reagents and solvents were purchased from Alfa Aesar, VWR or Sigma Aldrich and used without further purification. Column chromatography was carried out using Geduran Si60 (40-63 µm) as the stationary phase and TLC was performed on precoated Kieselgel 60 plates (0.20 mm thick, $60F_{254}$. Merck, Germany) and observed under UV light at 254 nm or 365 nm. All reactions were carried out under air, unless stated otherwise. 1,3,5-Tricarboxamidobenzene,[31] 1,3,5-tricyanobenzene,[32] 1,3,5-triaminobenzene[33] were prepared according to literature procedures. *rac*-$[(Ir(ppz)_2Cl)_2]$ was prepared by O. Chepelin.

All ^{1}H, ^{13}C and ^{19}F NMR spectra were recorded on either a 500 MHz Bruker AV III equipped with a DCH cryo-probe (Ava500), a 500 MHz Bruker AV IIIHD equipped with a Prodigy cryo-probe (Pro500), a 600 MHz Bruker AV IIIHD equipped with a TCI cryo-probe (Ava600) or a 400 MHz Bruker AV III equipped with BBFO+ probe (Ava400) at a constant temperature of 300 K. All DOSY experiments were performed either on the Ava400 or the Ava500 using bipolar gradient pulses for diffusion with two spoil gradients (ledbpg2s.compensated) pulse sequence. The sequence was carried out under automated conditions where the duration of the magnetic field pulse gradient (δ) was 1.5 ms and the diffusion time (Δ) was 100 ms. Typically in each PFG NMR experiment, a series of 16 spectra on 32 K data points were collected and the eddy current delay (Te) was set to 5 ms in all experiments. The pulse gradients (g) were incremented from 2 to 95% of the maximum gradient strength in a linear ramp. The temperature was set and controlled at 300 K with an air flow of 400 l h^{-1} in order to avoid any temperature fluctuations due to sample heating during the magnetic field pulse gradients. The data was processed using Bruker Topspin 3.2. Chemical shifts are reported in parts per million. Coupling constants (J) are reported in hertz (Hz). Standard abbreviations indicating multiplicity were used as follows: m = multiplet, q = quartet, t = triplet, d = doublet, s = singlet, bs = broad singlet. Where required, peak assignments were confirmed through a range of two-dimensional techniques including, COSY, NOESY, HSQC and HMBC. All analysis was performed with MestReNova, Version 10.0.0.

MS of the cage compounds was performed on a Synapt G2 (Waters., Manchester, UK) mass spectrometer or a Q-ToF (Micromass UK Ltd), using a nano-electrospray ionization source (ESI), controlled using Masslynx v4.1 software. All of the scans in the experimental are for positive ions. The samples were dissolved in acetonitrile or TCE at 50 µM. Prior to analysis, instruments were calibrated using a solution of sodium iodide (2 mg/mL) in 50:50 water:isopropanol. Capillary voltages were adjusted between 1.5 and 2.5 kV to optimize spray quality, while the sampling cone and the extraction cone voltage were minimised to reduce breakdown of the assemblies. Source temperature was set between 60-120 °C. The data was analysed using MassLynx v4.1 and Origin 2015. Predicted isotopic distributions were calculated using Molecular Weight Calculator Version 6.49.

2.9.2 Analysis of Supramolecular Assemblies

Many fundamental analytical approaches remain exactly the same for studying supramolecular systems as they do for standard covalent molecules. However, due to the inherent dynamic nature of many supramolecular species, they possess some unique challenges when it comes to proving their exact composition and existence. A number of these challenges will be discussed here as they are relevant to the entirety of this work and are often underplayed in many publications.

X-ray Crystallography

X-ray crystallography is now established as a fundamental tool in the elucidation of chemical structures. The ability to get the fixed coordinates of the constituent atoms can remove almost any doubt as to the correct chemical structure for all but the most challenging compounds. This allows the identification of systems that would normally be very difficult to distinguish, for example, the reliable assignment of chiral centres.

The only major drawback to X-ray crystallography is the difficulty in preparing high quality crystalline samples. This is particularly difficult for supramolecular systems since many contain large cavity spaces filled either with disordered solvent molecules or bound counter ions. Coupled with the inherent reversibility of the bonding interactions, this makes high quality crystalline samples of supramolecular systems difficult to prepare and particularly prone to irreparable damage through solvent loss.

Despite the practical difficulties, X-ray crystallography has be used extensively in the study of supramolecular systems with many being characterised based purely on their solid state structures. However, caution should be taken when describing the solution properties of discrete, supramolecular systems with reversible interactions based solely on their solid state structures. While covalent linkages can be reasonably assumed to remain the same in both the solid and the solution states, reversible interactions such as metal-ligand coordination or hydrogen bonding can alter significantly. As such, systems that may show well defined cavities in the solid state may dissociate upon dissolution to give either smaller cavities, individual components without any defined cavity at all or a mixture of the above. Therefore, any discrete supramolecular system analysed by X-ray crystallography must be compared with solution based data before jumping to conclusions about any solution based processes such as guest inclusion or homogenous catalysis.

Exchange Spectroscopy (EXSY)

Nuclear magnetic spectroscopy (NMR) is an invaluable tool for probing the solution state properties of molecular compounds. The range of techniques and applications are far too numerous to be discussed in totality, however, a number of specialist techniques have been developed that are used extensively throughout this work and may be unfamiliar to many chemists.

The Nuclear Overhauser Effect is commonly used in the form of NOESY spectra for determining correlation between nuclei close in space. If the experiment is performed quantitatively, this can also be used to measure the exchange of chemical species such as metal-ligand complexation or host-guest interactions. For a simple, two species exchange system, the intensity of the observed cross peaks can be related to the observed rate constant, k, by the following relationship:[34]

$$k = \frac{1}{\tau_m} \times \ln \frac{r+1}{r-1}$$

$$r = \frac{(I_{AA} + I_{BB})}{(I_{AB} + I_{BA})}$$

$$I_{AA}\ \&\ I_{BB} = diagonal\ peak\ intensities$$

$$I_{AB}\ \&\ I_{BA} = cross - peak\ intensities$$

$$\tau_m = mixing\ time\ in\ s$$

Assuming that the system is at equilibrium then the observed rate constant can be assumed to be equal to both the forward and reverse processes as given by:

$$A + B \underset{k_{-1}}{\overset{k_1}{\rightleftharpoons}} AB$$

$$k = k_1 + k_{-1} = 2 \times k_{obs} \quad (k_1 = k_{-1} = k_{obs})$$

By repeating measurements with a variety of different mixing times, τ_m, a more accurate value for k_{obs} can be obtained by plotting a graph of $\ln((r+1/(r-1))$ versus τ_m to give a straight line with slope $1/k$.[35] Direct information about the activation barrier can then be obtained using the Eyring equation:[36]

$$\Delta G^{\ddagger} = -RT \ln \frac{k_{obs} h}{k_B T}$$

$$(R = 1.9872\ cal\ K^{-1}\ mol^{-1}, k_B = 3.30 \times 10^{-24}\ cal\ K^{-1}, h = 1.58 \times 10^{-34}\ cal\ s)$$

Thus, EXSY NMR provides a unique tool for providing quantitative information about equilibrium processes that are slow on the NMR timescale.

Diffusion Ordered Spectroscopy (DOSY)

Diffusion within NMR tubes can often lead to complications in many experiments but it can also be utilised to probe the size of molecular species based on their rate of diffusion through a particular solvent. Diffusion ordered spectroscopy (DOSY) is carried out by creating a gradient within the magnetic field by applying a specific radio frequency pulse. A second inverse pulse can then be used to realign the nuclei. Theoretically, if there was zero time between the two pulses, the obtained spectra would be identical to the original. However, if a time delay is included, diffusion within the sample tube misaligns the molecules with respect to the initial pulse. As a result, when the inverse pulse is applied, each signal is reduced in strength based on the distance the species has moved in solution. If the experiment is repeated with a number of different gradient strengths, an exponential decay function can be applied to the decrease in peak intensity to give the diffusion constant, D.

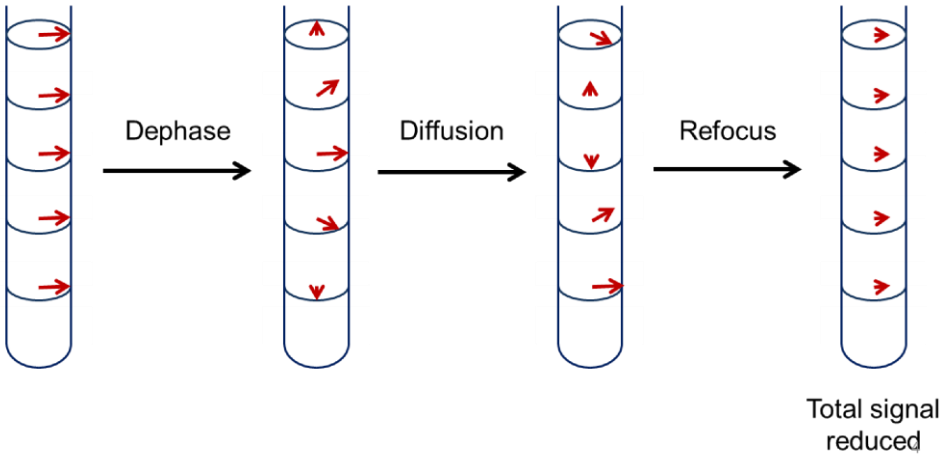

Figure 15: Graphical representation of the effects of diffusion on the dephasing and refocusing of nuclear spins.

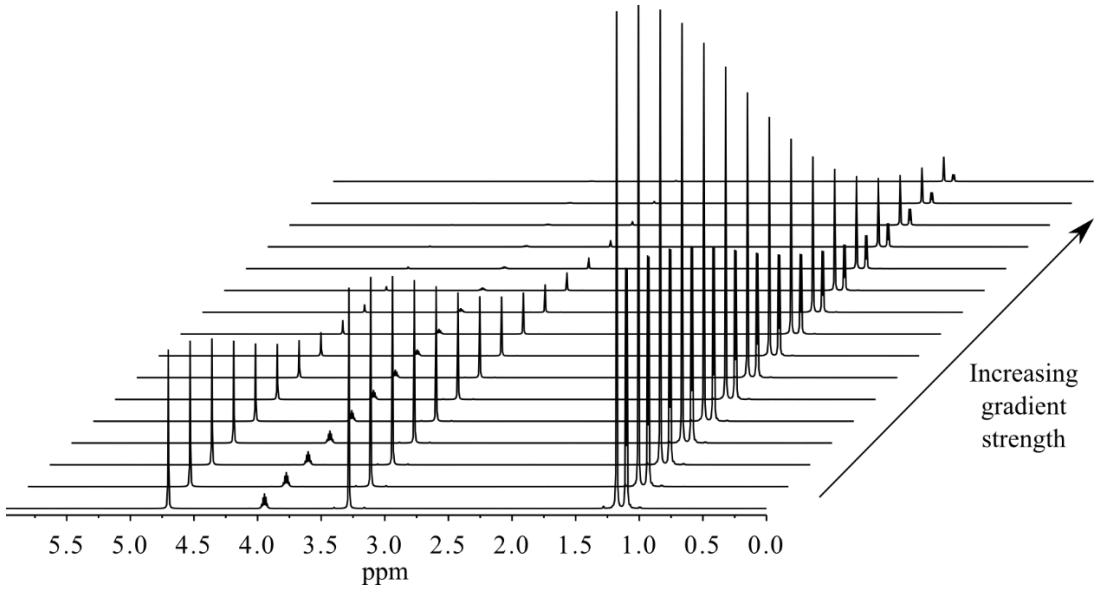

Figure 16: An example stack plot of ^{1}H NMR spectra illustrating the relative decrease in signal intensity as the applied gradient strength is increased.

The diffusion constant can then be used to calculate the hydrodynamic radius, r_s, for the species in question based on the Stokes-Einstein equation:

$$D = \frac{k_B T}{6\pi\eta r_s}$$

$$\eta = solvent\ viscosity$$

It should be noted that hydrodynamic radius includes the solvation shell surrounding the compound and assumes a spherical shape. Thus, the calculated radius may not agree exactly with predicted space filling models and will vary with different solvents. Nevertheless, by direct comparison, DOSY can be used to tell the difference between large supramolecular species and their constituent parts. For example, many metallosupramolecular assemblies possess high degrees of symmetry which means the ^{1}H NMR spectrum of the intact assembly can be nearly identical to the ^{1}H NMR of the free ligands. The only observable changes are usually small peak shifts due to metal complexation. However, the calculated hydrodynamic radius obtained from DOSY will show a dramatic increase in size providing substantial evidence that an assembly is formed and remains intact in solution.

In addition, many self-assembled systems can also generate a statistical mixture of species with non-identical ^{1}H NMR spectra, often as a result of chirality. These mixtures generate incredibly complex ^{1}H NMR spectra due both to the number of species and the lack of symmetry, which makes conventional analysis near impossible. DOSY NMR can distinguish if the complex ^{1}H NMR is due purely to a statistical distribution of identically sized assemblies or whether the solution contains a large number of unrelated species.

2.9.3 Synthetic Procedures

121 - $[Ir(ppy)_2(F\text{-}PhCN)_2]X$

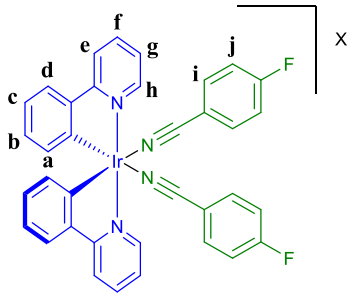

General Procedure:

$[(Ir(ppy)_2Cl)_2]$ (63.6 mg, 0.059 mmol) and AgX (30.0 mg, 0.117 mmol) were dissolved in DCE (30 mL) and stirred in the dark at room temperature for 2 h. The resultant mixture was filtered through celite and concentrated under reduced pressure. 4-Fluorobenzonitrile (31.2 mg, 0.258 mmol) was charged and stirred overnight in a darkened flask. The product was precipitated with Et_2O, filtered and washed with Et_2O to yield a yellow/green solid

*All NMR peak data abstracted from solutions containing excess free ligand.

X = OTf (39.6 mg, 50%). ^{1}H NMR (500 MHz, CD_2Cl_2) δ 9.16 (ddd, *J* = 5.8, 1.2 Hz, 2H, H_h), 8.05 – 7.99 (m, 4H, $H_{e,f}$), 7.76 – 7.72 (m, 4H, H_j), 7.65 (ddd, *J* = 7.8, 1.4, 0.5 Hz, 2H, H_d), 7.53 – 7.48 (m, 4H, H_g), 7.24 – 7.20 (m, 4H, H_i), 6.98 (ddd, *J* = 7.7, 7.3, 1.2 Hz, 2H, H_c), 6.83 (ddd, *J* = 7.5, 1.3 Hz, 2H, H_b), 6.21 (ddd, *J* = 7.7, 1.2, 0.5 Hz, 2H, H_a). ^{13}C NMR (126 MHz, CD_2Cl_2) δ 167.68 , 166.77 (d, *J* = 259.4 Hz), 151.42, 144.68, 143.84, 139.47, 136.95 (d, *J* = 10.0 Hz), 131.86, 130.59, 124.86, 124.40, 123.62, 120.36, 119.66, 117.88 (d, *J* = 23.0 Hz), 106.46 (d, *J* = 3.5 Hz). ^{19}F NMR (471 MHz, CD_2Cl_2) δ -78.75, -99.05 – -99.26 (m). *m/z* (HR-ESI): 501.09700 (predicted $[Ir(ppy)_2]^+$ = 501.09374), complete ligand dissociation observed in CH_3OH under MS conditions.

X = PF_6 (29.6 mg, 30%). ^{1}H NMR (500 MHz, CD_2Cl_2) δ 9.13 (ddd, *J* = 5.7, 1.2 Hz, 2H, H_h), 8.04 – 8.00 (m, 4H, $H_{e,f}$), 7.73 – 7.67 (m, 4H, H_j), 7.65 (dd, *J* = 7.9, 1.1 Hz, 2H, H_d), 7.51 – 7.45 (m, 2H, H_g), 7.24 – 7.17 (m, 4H, H_i), 6.98 (ddd, *J* = 7.8, 7.3, 1.2 Hz, 2H, H_c), 6.83 (ddd, *J* = 7.5, 1.4 Hz, 2H, H_b), 6.21 (ddd, *J* = 7.6, 1.2, 0.5 Hz, 2H, H_a). ^{13}C NMR (126 MHz, CD_2Cl_2) δ 167.69, 166.77 (d, J = 259.3 Hz), 151.33, 144.68, 143.83, 139.48, 136.85 (d, J = 10.0 Hz), 131.85, 130.60, 124.86, 124.34, 123.62, 120.36, 119.64, 118.56, 117.89 (d, J =

23.0 Hz), 106.46 (d, J = 3.5 Hz). ^{19}F NMR (471 MHz, CD_2Cl_2) δ -72.80 (d, *J* = 711.0 Hz), -99.05 – -99.18 (m). *m/z* (HR-ESI): 501.09380 (predicted $[Ir(ppy)_2]^+$ = 501.09374), complete ligand dissociation observed in CH_3OH under MS conditions.

X = BF_4 (12.7 mg, 14%). ^{1}H NMR (500 MHz, CD_2Cl_2) δ 9.16 (ddd, *J* = 5.8, 1.2 Hz, 2H, H_h), 8.05 – 7.97 (m, 4H. $H_{e,f}$), 7.77 – 7.67 (m, 4H, H_j), 7.65 (dd, *J* = 7.7, 1.3 Hz, 2H, H_d), 7.53 – 7.44 (m, 2H, H_g), 7.24 – 7.13 (m, 4H, H_i), 6.98 (ddd, *J* = 7.5, 1.2 Hz, 2H, H_c), 6.83 (ddd, *J* = 7.5, 1.4 Hz, 2H, H_b), 6.21 (dd, *J* = 7.6, 1.3 Hz, 2H, H_a). ^{13}C NMR (126 MHz, CD_2Cl_2) δ 167.67, 166.75 (d, *J* = 259.4 Hz), 151.45, 144.70, 143.89, 139.44, 136.93 (d, *J* = 10.0 Hz), 131.86, 130.57, 124.84, 124.35, 123.59, 120.32, 119.62, 117.85 (d, *J* = 23.0 Hz), 106.51 (d, *J* = 3.6 Hz). ^{19}F NMR (471 MHz, CD_2Cl_2) δ -99.19 – -99.30 (m), -152.25 (^{10}B), -152.30 (^{11}B). *m/z* (HR-ESI): 501.09350 (predicted $[Ir(ppy)_2]^+$ = 501.09374), complete ligand dissociation observed in CH_3OH under MS conditions.

X = ClO_4 (4.9 mg, 5%). ^{1}H NMR (500 MHz, CD_2Cl_2) δ 9.16 (ddd, *J* = 5.8, 1.2 Hz, 2H, H_h), 8.06 – 7.99 (m, 4H, $H_{e,f}$), 7.77 – 7.72 (m, 4H, H_j), 7.65 (dd, *J* = 7.8, 1.3 Hz, 2H, H_d), 7.52 – 7.47 (m, 2H, H_g), 7.25 – 7.17 (m, 4H, H_i), 6.98 (ddd, *J* = 7.5, 1.2 Hz, 2H, H_c), 6.83 (ddd, *J* = 7.5, 1.4 Hz, 2H, H_b), 6.21 (dd, *J* = 7.7, 1.1 Hz, 2H, H_a). ^{13}C NMR (126 MHz, CD_2Cl_2) δ 167.68, 166.76 (d, *J* = 259.4 Hz), 151.48, 144.69, 143.90, 139.44, 136.96 (d, *J* = 9.9 Hz), 131.87, 130.59, 124.85, 124.36, 123.60, 120.33, 119.63, 117.87 (d, *J* = 23.0 Hz), 106.53 (d, *J* = 3.6 Hz). ^{19}F NMR (471 MHz, CD_2Cl_2) δ -99.11 – -99.29 (m). *m/z* (HR-ESI): 501.09540 (predicted $[Ir(ppy)_2]^+$ = 501.09374), complete ligand dissociation observed in CH_3OH under MS conditions.

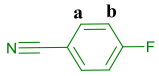

For reference only:

^{1}H NMR (500 MHz, CD_2Cl_2) δ 7.74 – 7.66 (m, 2H, H_b), 7.23 – 7.16 (m, 2H, H_a). ^{13}C NMR (126 MHz, CD_2Cl_2) δ 165.61 (d, *J* = 255.7 Hz), 135.33 (d, *J* = 9.5 Hz), 118.55, 117.31 (d, *J* = 22.9 Hz), 109.21 (d, *J* = 3.5 Hz). ^{19}F NMR (471 MHz, CD_2Cl_2) δ -103.52 – -103.68 (m).

125 - $[Ir(ppz)_2(F\text{-}PhCN)_2]OTf$

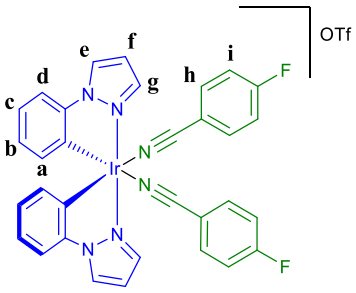

$[(Ir(ppz)_2Cl)_2]$ (60.8 mg, 0.059 mmol) and AgOTf (30.3 mg, 0.118 mmol) were dissolved in DCE (30 mL) and stirred in the dark at room temperature for 2 h. The resultant mixture was filtered through celite and concentrated under reduced pressure. 4-Fluorobenzonitrile (62.1 mg, 0.513 mmol) was charged and stirred overnight in a darkened flask. The product was precipitated with Et_2O, filtered and washed with Et_2O to yield a white solid (51.3 mg, 60%). ^{1}H NMR (500 MHz, CD_2Cl_2) δ 8.26 (dd, *J* = 3.0, 0.7 Hz, 2H, H_e), 8.19 (dd, *J* = 2.3, 0.7 Hz, 2H, H_g), 7.80 – 7.75 (m, 4H, H_i), 7.29 (dd, *J* = 7.9, 1.2 Hz, 2H, H_d), 7.27 – 7.22 (m, 4H, H_h), 7.00 (ddd, *J* = 7.9, 7.4, 1.3 Hz, 2H, H_c), 6.89 (dd, *J* = 2.9, 2.3 Hz, 2H, H_f), 6.81 – 6.75 (m, 2H, H_b), 6.18 (dd, *J* = 7.6, 1.0 Hz, 2H, H_a). ^{13}C NMR (126 MHz, CD_2Cl_2) δ 166.84 (d, *J* = 259.5 Hz), 143.45, 140.58, 136.97 (d, *J* = 10.0 Hz), 133.58, 127.90, 126.75, 125.91, 124.36, 119.35, 117.95 (d, *J* = 23.0 Hz), 112.03, 109.24, 106.31 (d, *J* = 3.5 Hz). ^{19}F NMR (471 MHz, CD_2Cl_2) δ -78.77, -98.83 – -99.09 (m), -103.46 – -103.70 (m). *m/z* (HR-ESI): 479.08650 (predicted $[Ir(ppz)_2]^+$ = 479.08424), complete ligand dissociation observed in CH_3OH.

Separation of Δ/Λ-$[(Ir(ppz)_2Cl)_2]$

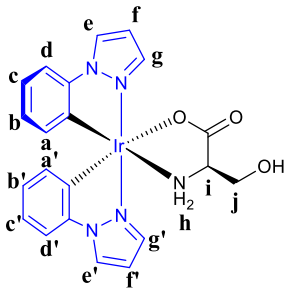

rac-$[(Ir(ppz)_2Cl)_2]$ (245.7 mg, 0.239 mmol), D-Serine (65.2 mg, 0.620 mmol) and NaOMe (32.6 mg, 0.603 mmol) were partially dissolved in CH_3OH (25 mL). The mixture was stirred at 40 ºC for 5 h. The solvent was removed under reduced pressure and crude product partially dissolved in CH_2Cl_2 (25 mL). The mixture was filtered and the solvent removed

from the filtrate under reduced pressure to yield a white solid (64.7 mg, 23%). ^{1}H NMR (500 MHz, CD_3OD) δ 8.54 (d, *J* = 2.9 Hz, 1H, $H_{e'}$), 8.50 (d, *J* = 2.9 Hz, 1H, H_e), 8.16 (dd, *J* = 2.3, 0.6 Hz, 1H, H_g), 7.85 (dd, *J* = 2.2, 0.7 Hz, 1H, $H_{g'}$), 7.38 – 7.34 (m, 2H, $H_{d,d'}$), 6.88 – 6.79 (m, 4H, $H_{c,c',f,f'}$), 6.64 – 6.56 (m, 2H, $H_{b,b'}$), 6.24 (dd, *J* = 7.6, 1.3 Hz, 1H, $H_{a'}$), 6.15 (dd, *J* = 7.5, 1.3 Hz, 1H, H_a), 5.37 – 5.26 (m, 2H, H_h), 4.04 – 3.95 (m, 1H, H_j), 3.76 – 3.69 (m, 2H, $H_{i,j}$). *H_j CH_2 protons split into two different environments, confirmed by HSQC. ^{13}C NMR (126 MHz, CD_3OD) δ 185.26, 145.51, 145.29, 140.61, 139.20, 135.28, 135.22, 134.10, 128.24, 128.18, 126.63, 126.36, 126.14, 122.76, 122.29, 111.92, 111.85, 108.70, 108.48, 64.83, 59.46. *m/z* (HR-ESI): 606.10890 (predicted $[M+Na]^+$ = 606.10878), 1189.23080 (predicted $[2M+Na]^+$ = 1189.22887).

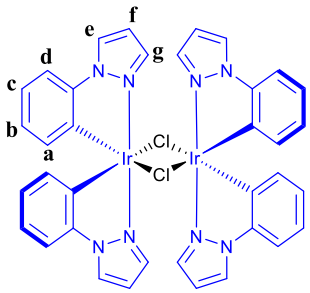

Δ/Λ-$[Ir(ppz)_2$(D-Serine)] (63.7 mg, 0.109 mmol) was dissolved in CH_3OH (16 mL). $HCl_{(aq)}$ (37 w/v%, 1 mL) was charged dropwise and the solution stirred at room temperature for 1 h. The resultant precipitate was filtered and washed with CH_3OH. The solid was redissolved in CH_2Cl_2, filtered and the solvent removed under vacuum to yield a white solid (49.8 mg, 89%). ^{1}H NMR (500 MHz, CD_2Cl_2) δ 8.21 (d, *J* = 2.9 Hz, 4H, H_g), 7.83 (d, *J* = 2.2 Hz, 4H, H_e), 7.20 (dd, *J* = 7.9, 1.2 Hz, 4H, H_d), 6.89 – 6.81 (m, 4H, H_c), 6.73 – 6.66 (m, 4H, H_f), 6.61 – 6.56 (m, 4H, H_b), 5.96 (dd, *J* = 7.7, 1.3 Hz, 4H, H_a). ^{13}C NMR (126 MHz, CD_2Cl_2) δ 143.69, 141.04, 133.02, 127.93, 126.98, 125.76, 122.48, 111.16, 107.26. DOSY NMR (500 MHz, $C_2D_2Cl_4$) –logD = 9.77 Hydrodynamic radius = 8.8 Å. *m/z* (HR-ESI): 479.08450 (predicted $[Ir(ppz)_2]^+$ = 479.08424)

Δ/Λ-124·6OTf - [(Ir(ppz)$_2$)$_6$(tcb)$_4$]6OTf

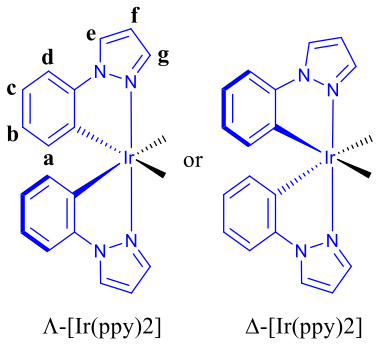

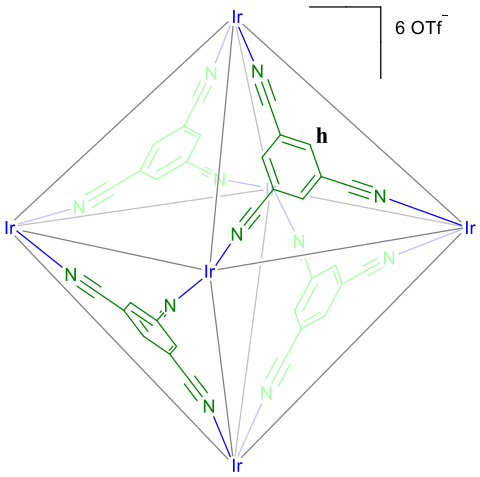

Δ/Λ-[(Ir(ppz)$_2$Cl)$_2$] (25.6 mg, 0.025 mmol) and AgOTf (12.8 mg, 0.050 mmol) were dissolved in DCE (10 mL) and stirred in the dark at room temperature for 2 h. The resultant mixture was filtered through celite and concentrated under reduced pressure. 1,3,5-Tricyanobenzene (2.5 mg, 0.016 mmol) was charged and the resultant precipitate was filtered and washed with the minimum volume of DCE and Et_2O to give a yellow solid (8.7 mg, 42 %). ^{1}H NMR (500 MHz, $C_2D_2Cl_4$) δ 8.56 (d, *J* = 2.4 Hz, 12H, H_g), 8.43 (s, 12H, H_h), 8.24 (d, *J* = 2.8 Hz, 12H, H_e), 7.20 (d, *J* = 8.2 Hz, 12H, H_d), 7.08 (d, *J* = 2.6 Hz, 12H, H_f), 6.97 (dd, *J* = 7.9 Hz, 12H, H_c), 6.74 (dd, *J* = 7.5 Hz, 12H, H_b), 6.18 (d, *J* = 7.6 Hz, 12H, H_a). ^{13}C NMR not obtained due to low signal strength. ^{19}F NMR (376 MHz, $C_2D_2Cl_4$) δ -77.74, -78.72. Signals very broad due to chemical exchange. DOSY NMR (500 MHz, $C_2D_2Cl_4$) – logD = 9.98 Hydrodynamic radius = 14.3 Å.

[(Ir(ppy)$_2$)$_n$(dib)$_n$]nOTf

[(Ir(ppy)$_2$Cl)$_2$] (25.2 mg, 0.024 mmol), 1,4-diisocyanobenzene (6.0 mg, 0.047 mmol) and AgOTf (12.1 mg, 0.047 mmol) were partially dissolved in TCE and heated at 100 ºC in a darkened flask for 3 days. The solvent was removed under vacuum and the crude products purified by silica chromatography using 100% CH_2Cl_2 to 90% CH_2Cl_2/10% CH_3OH.

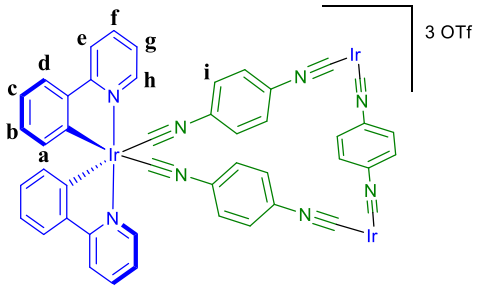

rac-132·3OTf - [(Ir(ppy)$_2$)$_3$(dib)$_3$]4OTf

^{1}H NMR (500 MHz, CD_3CN) δ 9.32 – 9.17 (m, 6H, H_h), 8.25 – 8.09 (m, 12H, $H_{e,f}$), 7.87 – 7.77 (m, 6H, H_d), 7.58 (s, 12H, H_i), 7.50 – 7.33 (m, 6H, H_g), 7.07 – 7.00 (m, 6H, H_c), 6.97 – 6.87 (m, 6H, H_b), 6.19 – 6.11 (m, 6H, H_a). *^{13}C NMR too complex for analysis. ^{19}F NMR (376 MHz, CD_3CN) δ -79.31. DOSY NMR (500 MHz, CD_3CN) –logD = 9.15 Hydrodynamic radius = 8.4 Å.

Δ/Λ-*132·3OTf* - [(Ir(ppy)$_2$)$_3$(dib)$_3$]4OTf

^{1}H NMR (601 MHz, CD_3CN) δ 9.25 (ddd, *J* = 5.7, 1.5, 0.8 Hz, 6H, H_h), 8.21 – 8.11 (m, 12H, $H_{e,f}$), 7.81 (dd, *J* = 7.8, 1.2 Hz, 6H, H_d), 7.59 (s, 12H, H_i), 7.44 (ddd, *J* = 7.3, 5.7, 1.7 Hz, 6H, H_g), 7.07 – 7.00 (m, 6H, H_c), 6.97 – 6.89 (m, 6H, H_b), 6.16 (dd, *J* = 7.7, 1.1 Hz, 6H, H_a). ^{13}C NMR (126 MHz, CD_3CN) δ 168.10, 155.50, 153.18, 145.45, 140.50, 136.19, 131.43, 131.38, 129.58, 128.72, 125.87, 125.70, 125.04, 121.97. ^{19}F NMR (376 MHz, CD_3CN) δ -79.25. DOSY NMR (500 MHz, CD_3CN) –logD = 9.15 Hydrodynamic radius = 8.4 Å.

rac-133·4OTf - [(Ir(ppy)$_2$)$_4$(dib)$_4$]4OTf

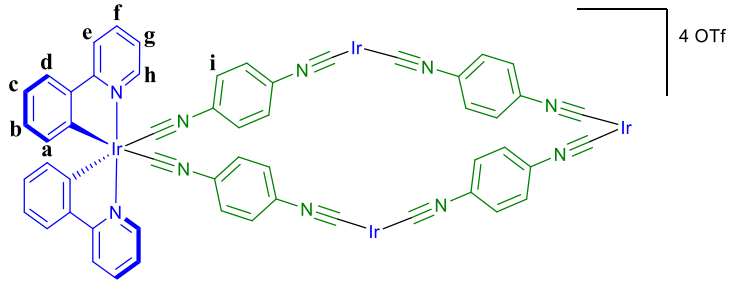

^{1}H NMR (500 MHz, CD_3CN) δ 9.31 – 9.16 (m, 8H), 8.20 – 8.07 (m, 16H), 7.82 – 7.75 (m, 8H), 7.53 (s, 16H), 7.49 – 7.36 (m, 8H), 7.07 – 6.98 (m, 8H), 6.95 – 6.86 (m, 8H), 6.21 – 6.10 (m, 8H). *^{13}C NMR too complex for analysis. ^{19}F NMR (376 MHz, CD_3CN) δ -79.32. DOSY NMR (500 MHz, CD_3CN) –logD = 9.18 Hydrodynamic radius = 9.0 Å.

137 - $[(Ir(ppy)_2)_2(dib)Cl_2]$

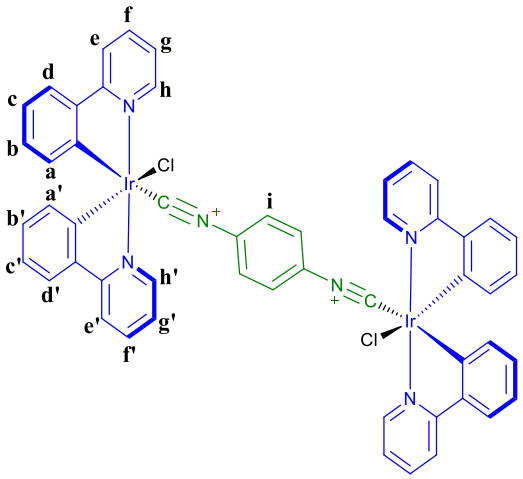

$[(Ir(ppy)_2Cl)_2]$ (59.2 mg, 0.055 mmol) and 1,4-phenyldiisocyanide (7.1 mg, 0.055 mmol) were dissolved in TCE (20 mL) and stirred at 60 ºC for 2 h. The solution was concentrated under reduced pressure and the product was precipitated with Et_2O, filtered and washed with Et_2O to yield a bright yellow solid (63.2 mg, 95%). ^{1}H NMR (601 MHz, CD_2Cl_2) δ 9.85 (ddd, *J* = 5.9, 1.6, 0.8 Hz, 2H, $H_{h'}$), 9.16 (ddd, *J* = 5.8, 1.6, 0.8 Hz, 2H, H_h), 7.98 – 7.92 (m, 4H, $H_{e,e'}$), 7.92 – 7.85 (m, 4H, $H_{f,f'}$), 7.67 – 7.59 (m, 4H, $H_{d,d'}$), 7.33 (ddd, *J* = 7.3, 5.9, 1.6 Hz, 2H, $H_{g'}$), 7.26 (s, 4H, H_i), 7.22 (ddd, *J* = 7.4, 5.7, 1.6 Hz, 2H, H_g), 6.97 – 6.89 (m, 4H, $H_{c,c'}$), 6.88 – 6.82 (m, 2H, $H_{b'}$), 6.82 – 6.75 (m, 2H, H_b), 6.40 (dd, *J* = 7.7, 0.8 Hz, 2H, $H_{a'}$), 6.03 (dd, *J* = 7.6, 1.3 Hz, 2H, H_a). Unable to confirm identity of unsymmetrical 2-phenylpyridine protons in relation to isocyanide ligand. ^{13}C NMR (126 MHz, CD_2Cl_2) δ 168.53, 167.87, 165.56, 153.90, 152.10, 145.04, 143.93, 143.87, 138.27, 138.08, 131.55, 130.80*, 130.80*, 130.34, 128.50, 124.66, 124.62, 124.00, 123.48, 123.17, 122.48, 120.55, 119.68, 74.89. *HSQC confirms two carbon atoms at identical ppm. DOSY NMR (500 MHz, CD_2Cl_2) –logD = 9.11 Hydrodynamic radius = 7.6 Å.

rac-138·4OTf - $[(Ir(ppy)_2)_4(dib)_2(bipy)_2]4OTf$

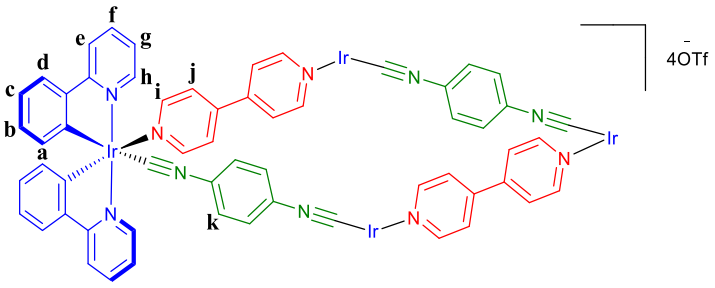

$[(Ir(ppy)_2)_2(dib)Cl_2]$ (12.2 mg, 0.010 mmol) and AgOTf (5.2 mg, 0.020 mmol) were dissolved in CH_2Cl_2 (20 mL). The solution was sonicated for 1 h in a darkened flask and a fine white precipitate was formed. 4,4'-Bipyridine (1.6 mg, 0.010 mmol) was charged and the mixture was filtered through celite. The yellow filtrate was heated at 60 ºC for 16 h and concentrated under reduced pressure. The product was precipitated with Et_2O, filtered and washed with Et_2O to yield an orange solid. ^1H & ^{13}C NMR too complex for analysis. ^{19}F NMR (376 MHz, CD_2Cl_2) δ -78.67. DOSY NMR (500 MHz, CD_2Cl_2) –logD = 9.29 Hydrodynamic radius = 10.3 Å.

145 - 1,3,5-triisocyanobenzene

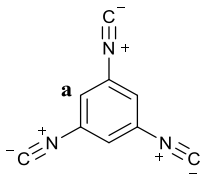

1,3,5-triaminobenzene (164.9 mg) was dissolved in CH_2Cl_2 (6.2 mL). 50 w/v% $NaOH_{(aq)}$ (3.1 mL) and $^tBu_4NBr$ (4.6 mg) were charged. Chloroform (0.5 mL) was charged slowly and the mixture was heated at reflux for 29 h. ^1H-NMR indicated the formation of the mono-, di- and triisocyanobenzene analogues. The organic layer was separated and washed with H_2O (2 x 20 mL) and brine (20 mL). The organic layer was dried with $MgSO_4$ and the solvent was removed under reduced pressure. Attempted purification was carried out by column chromatography with CH_2Cl_2 as the mobile phase. Product not isolated. ^1H NMR (500 MHz, $CDCl_3$) δ 7.50 (s, 3H H_a).

2.9.4 Counter Ion Induced Ligand Dissociation

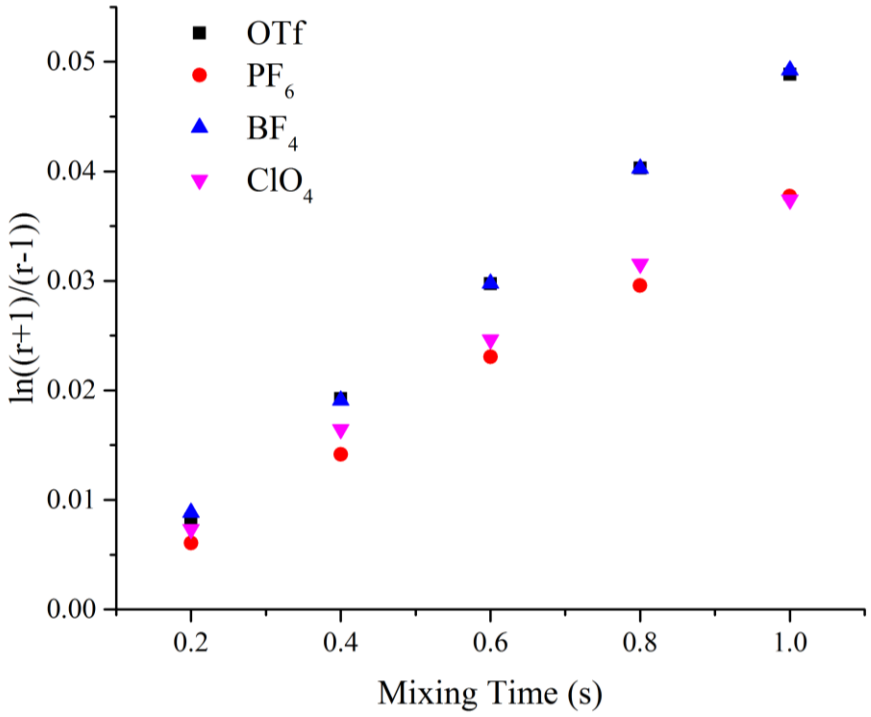

*Figure 2.17: Mixing time versus peak ratio for **121**·X with a range of different counter ions analysed by ^{19}F EXSY (471 MHz, $C_2D_2Cl_4$, 300 K).*

For each counter ion, a linear fit was applied and the gradient calculated to give $1/k$. Further experimental values were calculated as detailed in Section 2.9.2.

Table 2.3: The rate of ligand dissociation in relation to the associated counter ion.

Compound	Gradient	k_{obs} (s^{-1})	$G^{\ddagger}$ ($kJmol^{-1}$)
121·OTf	0.0512	9.766	67.34
121·PF_6	0.0394	12.690	66.69
121·BF_4	0.0510	9.804	67.33
121·ClO_4	0.0376	13.298	66.57

2.9.5 Quantification of Ligand Dissociation Barriers

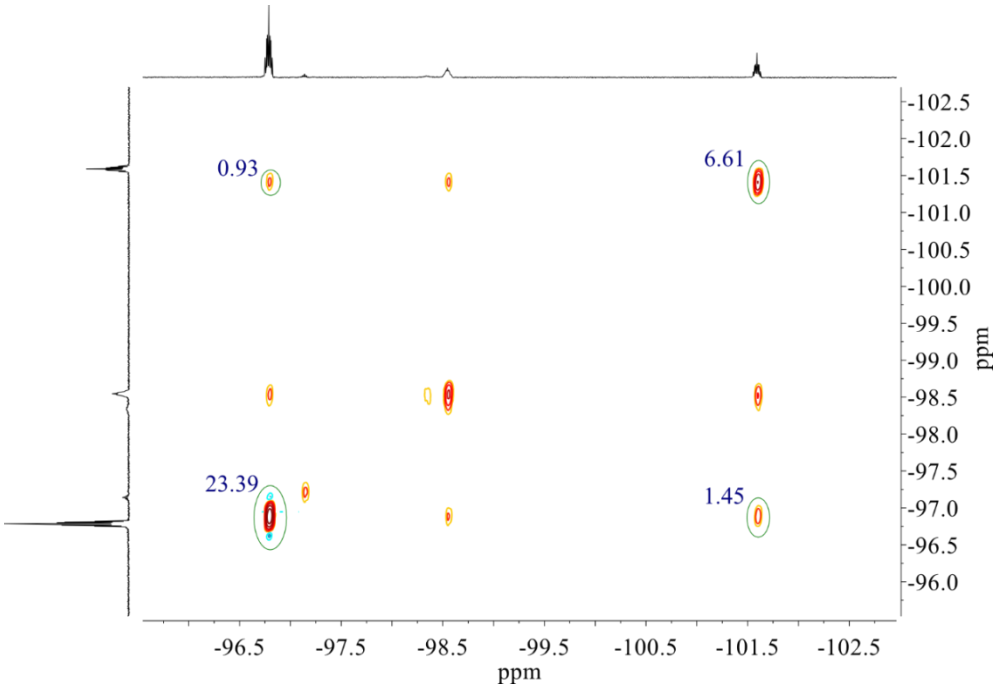

*Figure 2.18: ^{19}F EXSY (376 MHz, $C_2D_2Cl_4$, 300 K) of **121**·OTf showing peak integrals.*

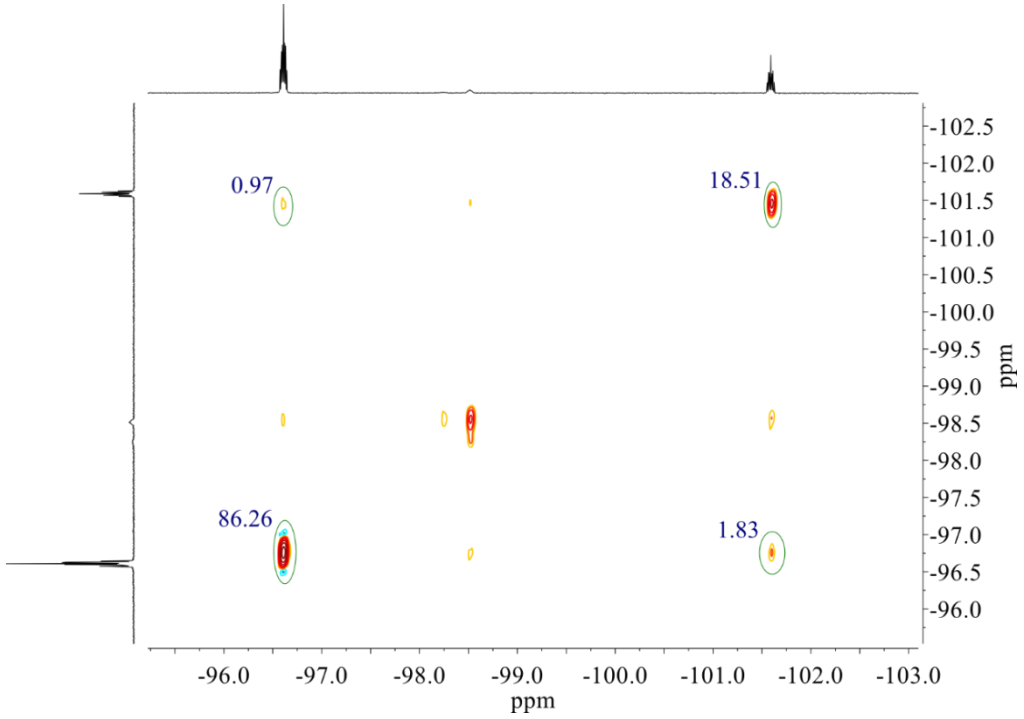

*Figure 2.19: ^{19}F EXSY (376 MHz, $C_2D_2Cl_4$, 300 K) of **125**·OTf showing peak integrals.*

2.9.6 Purification of Enantiopure $[(Ir(ppz)_2Cl)_2]$

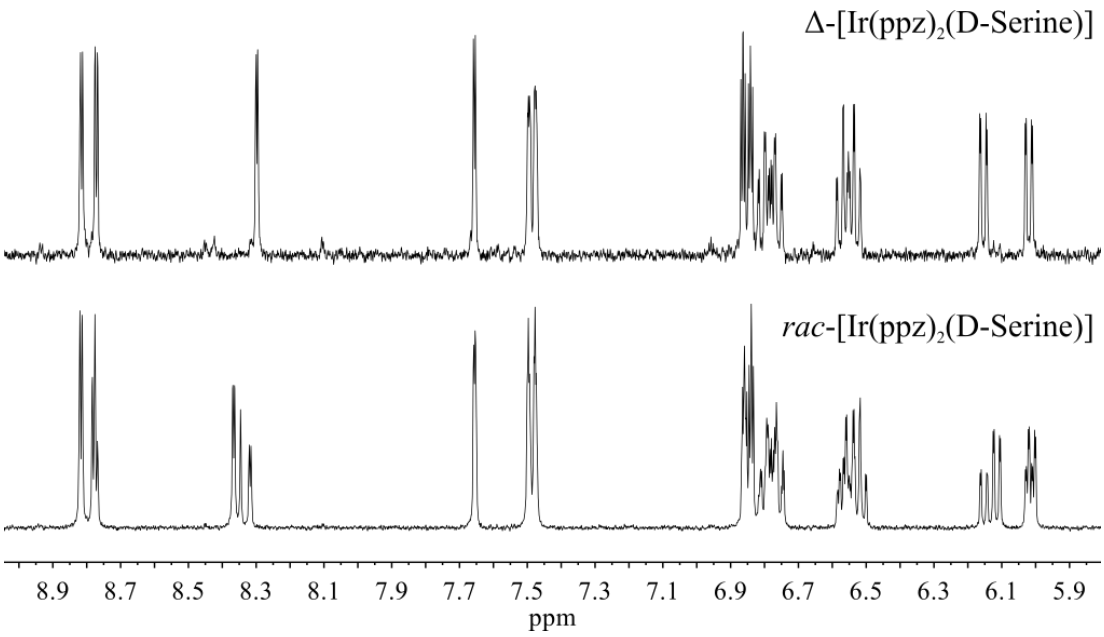

Figure 2.20: ^{1}H NMR (400 MHz, d_6-DMSO, 300 K) showing aromatic region of $[Ir(ppz)_2$(D-Serine)] and formation of diasteromers upon complexation of D-Serine to racemic mixture and isolation of a single diastereomer.

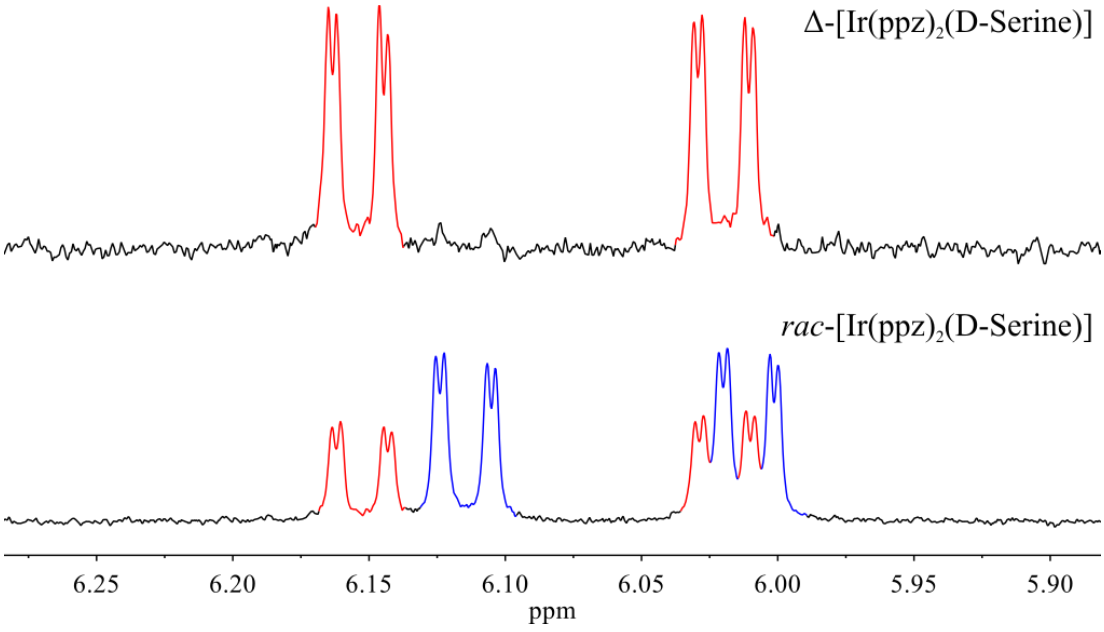

Figure 1.21: Expanded region of ^{1}H NMR (400 MHz, d_6-DMSO, 300 K) showing isolation of a single diastereomer of $[Ir(ppz)_2$(D-Serine)] from a mixture of Δ (red) and Λ (blue) isomers.

2.9.7 Crystal Structure of Δ-124·6OTf

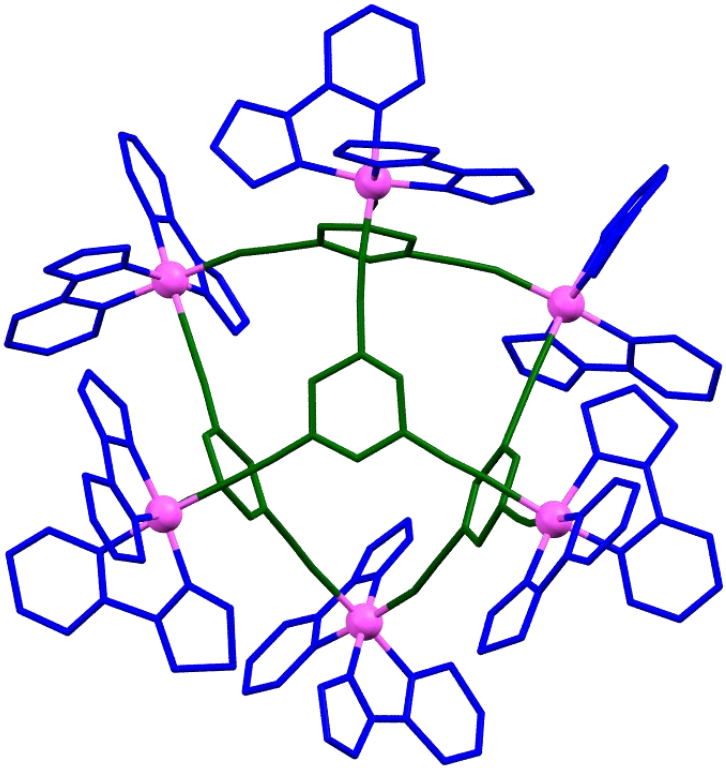

*Figure 2.22: Partially resolved crystal structure of Δ-**124**·6OTf confirming cage structure and chirality.*

X-ray quality crystals were grown using slow diffusion of benzene into a TCE solution. All structural characterisation was performed by Prof Alexandra M Z Slawin (The University of St Andrews). All of the structural data was collected using a Rigaku Saturn diffractometer (MM007 high-flux RA/MoKa radiation, confocal optic) at 93 K. All data collection employed narrow frames (0.3-1.0) to obtain at least a full hemisphere of data. Intensities were corrected for Lorentz polarisation and absorption effects (multiple equivalent reflections). The structure was solved by direct methods. Non-hydrogen atoms were refined anisotropically with C-H protons being refined in riding geometries (SHELXTL) against F^2. Structural refinement could only be partially resolved but the general cage structure and chirality could be confirmed.

*Table 2.4: Crystallographic details and parameters for Δ-**124**·6OTf.*

Identifier	DAPL1N
Empirical formula	$C_{150}H_{96}F_{18}Ir_6N_{36}O_{18}S_6$
Formula weight	4378.29
Temperature	93(1) K
Wavelength	0.71075 Å
Crystal system	Primitive Monoclinic
Space group	$P2_1$
Unit cell dimensions	a = 17.773(5) Å α = 90°
	b = 34.303(9) Å β = 95.828(4)°
	c = 19.085(5) Å γ = 90°
Volume	11575(5) $Å^3$
Z	2
Density (calculated)	1.256 g cm^{-3}
Absorption coefficient	3.565 mm^{-1}
F(000)	4224
Crystal size	0.100 x 0.100 x 0.020 mm
Theta range for data collection	1.60 to 25.42°
Index ranges	-21<=h<=21, -41<=k<=41, -22<=l<=22
Reflections collected	117344
Independent reflections	42060 [R(int) = 0.0757]
Completeness to theta = 25.42°	99.2%
Absorption correction	Multiscan
Max. and min. transmission	0.931 and 0.690
Refinement method	Full-matrix least-squares on F^2
Data / restraints / parameters	42060 / 1 / 819
Goodness-of-fit on F^2	1.561
Final R indices [I>2sigma(I)]	R1 = 0.1684
R indices (all data)	wR2 = 0.4363
Absolute structure parameter	0.089(18)
Largest diff. peak and hole	6.420 and -2.540 e^- $Å^{-3}$

2.9.8 Confirmation of Δ-124·6OTf Stereochemistry

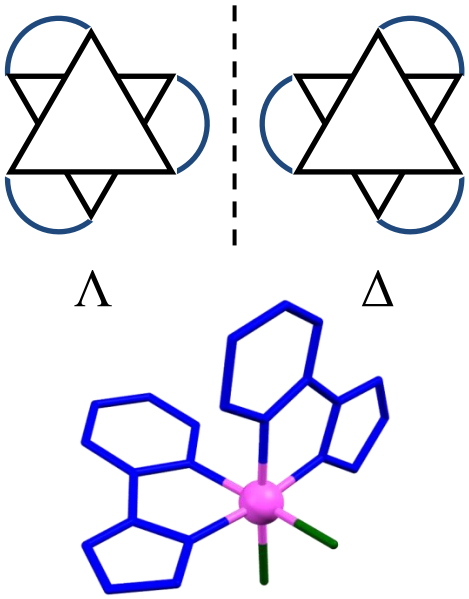

*Figure 2.23: Assignment of absolute configuration based on partially resolved X-ray crystal structure of Δ-**124**·6OTf.*[37]

2.9.9 Variable Temperature NMR of Anion Encapsulation

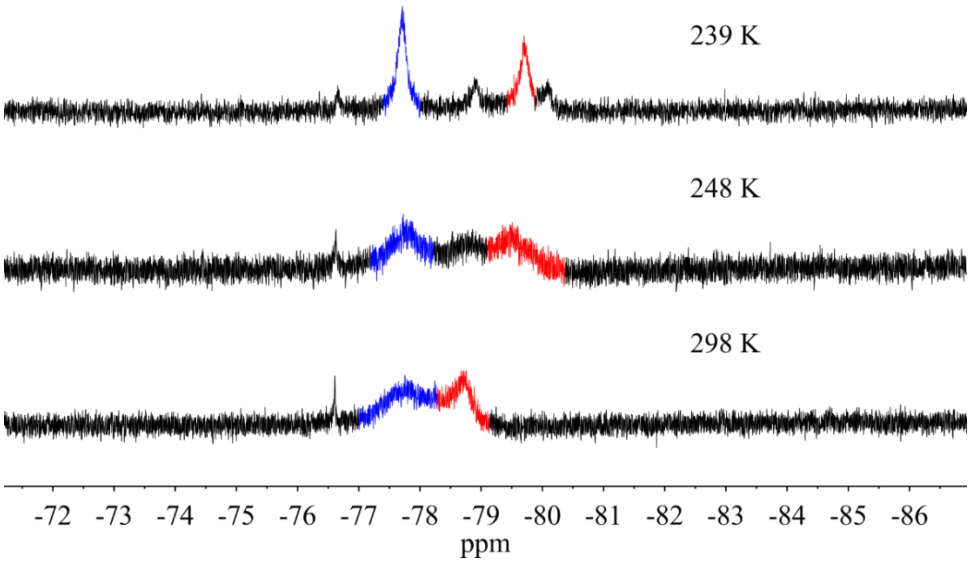

Figure 2.24: Variable temperature ^{19}F NMR (376 MHz, $C_2D_2Cl_4$) showing partial coalescence at room temperature of the signals corresponding to encapsulated (red) and free OTf (blue).

2.9.10 Stability of 124·6OTf versus 120·6OTf

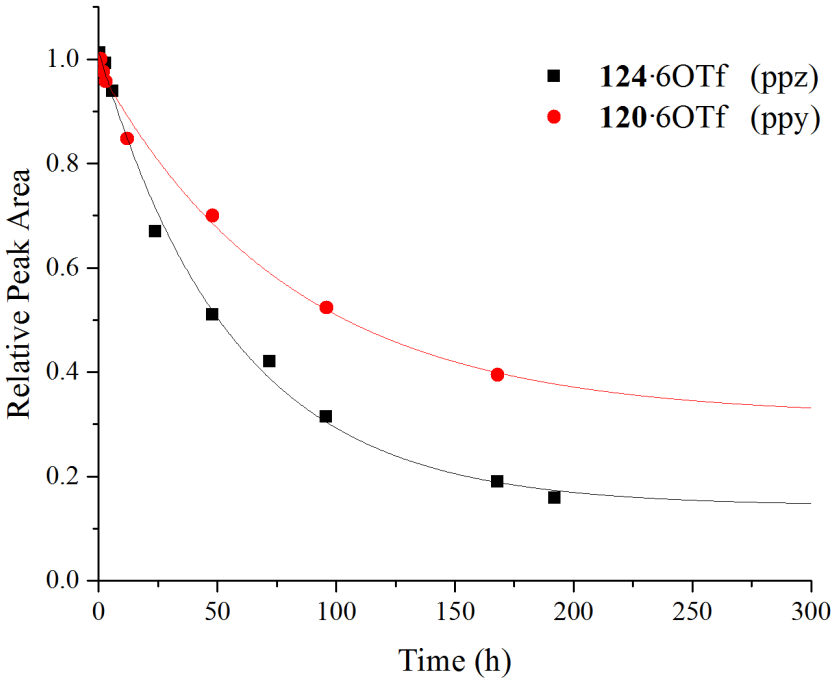

Figure 2.25: Stability of Ir_6L_4 systems assessed by ^1H NMR (500 MHz, $C_2D_2Cl_4$, 300 K) scrambling experiments. The percentage scrambling was monitored by integration of the 1,3,5-tricyanobenzene signal.

An exponential fit was applied and the corresponding half-lives calculated using the following expression:

$$y = y_0 + A_1 e^{\left(-\frac{(x)}{t_1}\right)}$$

$$half - life = t_1 \ln(2)$$

The value of y_0 was used to take into account the observation that the peak area did not trend to zero due to a statistical quantity of enantiopure material in the scrambled mixture and, in the case of **120**·6OTf, the presence of overlapping signals.

Table 2.5: Calculated values for exponential decay functions

Compound	Ligand	Mean lifetime, t_1 (h)	Half-life (h)
124·6OTf	2-phenypyrazole (ppz)	56.7 ± 4.6	39
120·6OTf	2-phenylpyridine (ppy)	80.9 ± 17.9	56

2.9.11 Formation of Two-Dimensional Isocyanide Structures

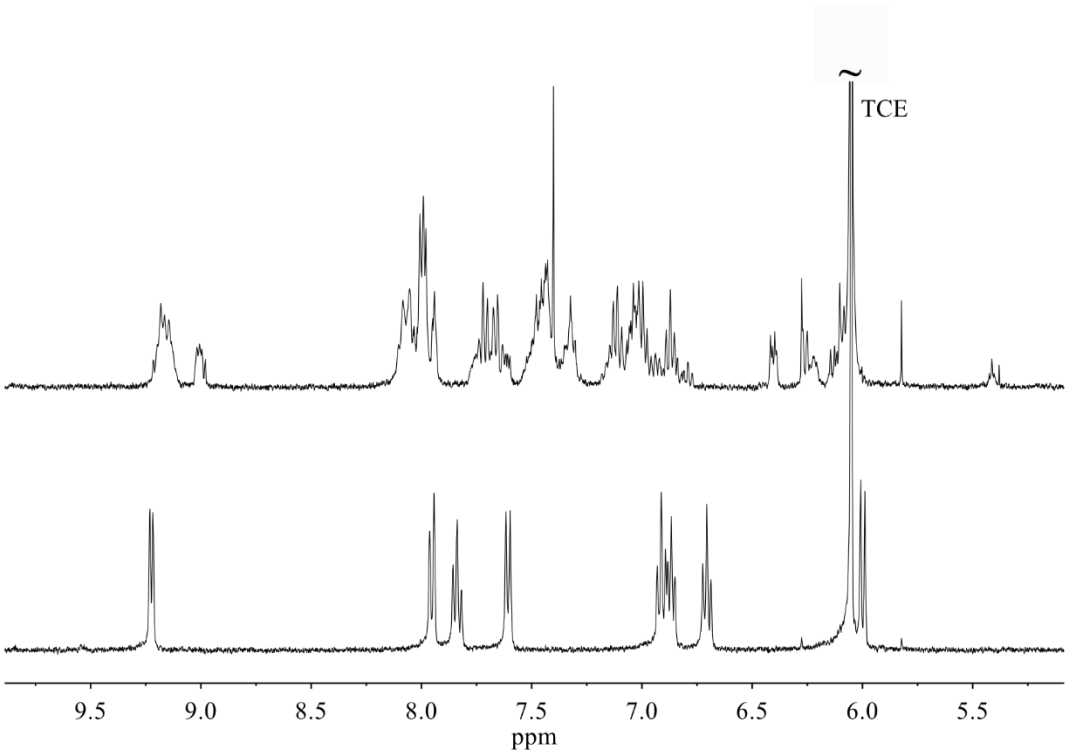

Figure 2.26: ^{1}H NMR (500 MHz, $C_2D_2Cl_4$, 300 K) of a statistical mixture of two-dimensional assemblies (top) formed from the self-assembly of rac-*[(Ir(ppy)$_2$Cl)$_2$] (bottom) with 1,4-diisocyanobenzene.*

2.9.12 Mass Spectrometry of Homoleptic Isocyanide Systems

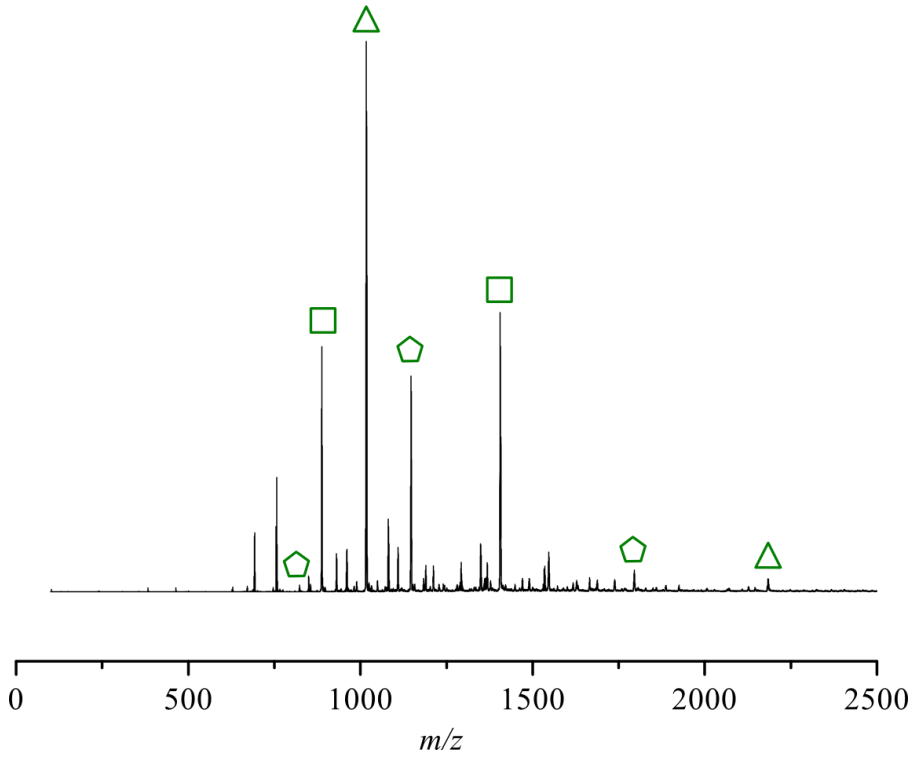

Figure 2.27: Mass spectrum of [(Ir(ppy)$_2$)$_n$(dib)$_n$]nOTf crude mixture. Major peaks are identified as the triangle, square or pentagon where n = 3,4 or 5 respectively.

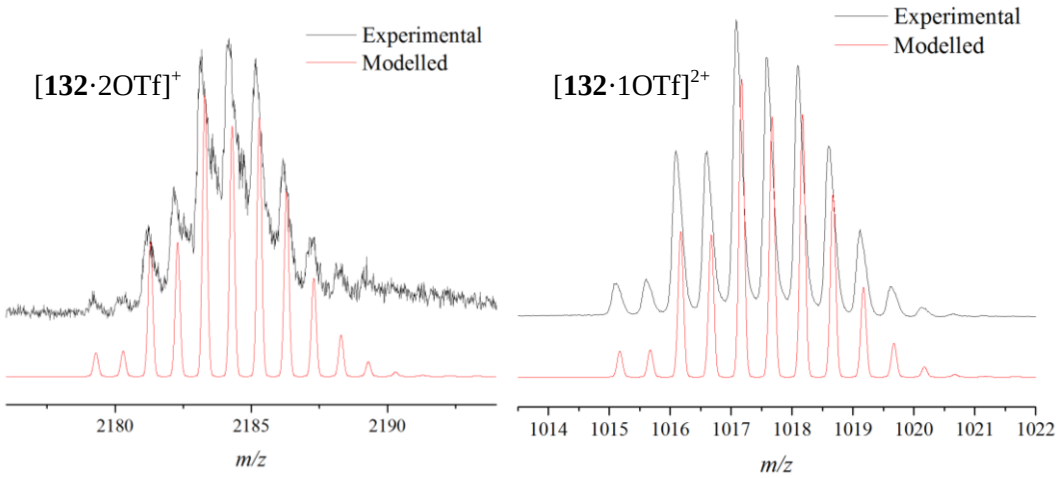

*Figure 2.28: Experimental peaks (black) from crude mixture identified as **132**·3OTf shown versus modelled isotopic distribution (red).*

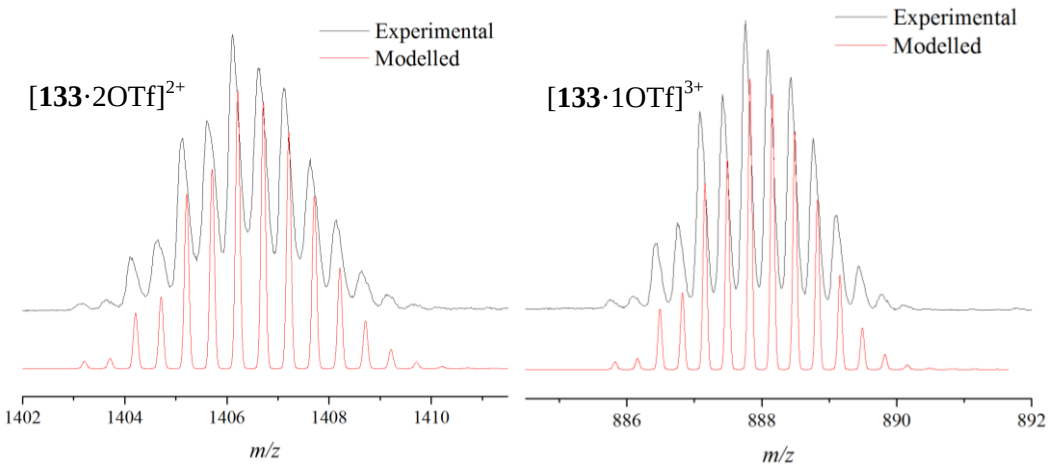

*Figure 2.29: Experimental peaks (black) from crude mixture identified as **133**·4OTf shown versus modelled isotopic distribution (red).*

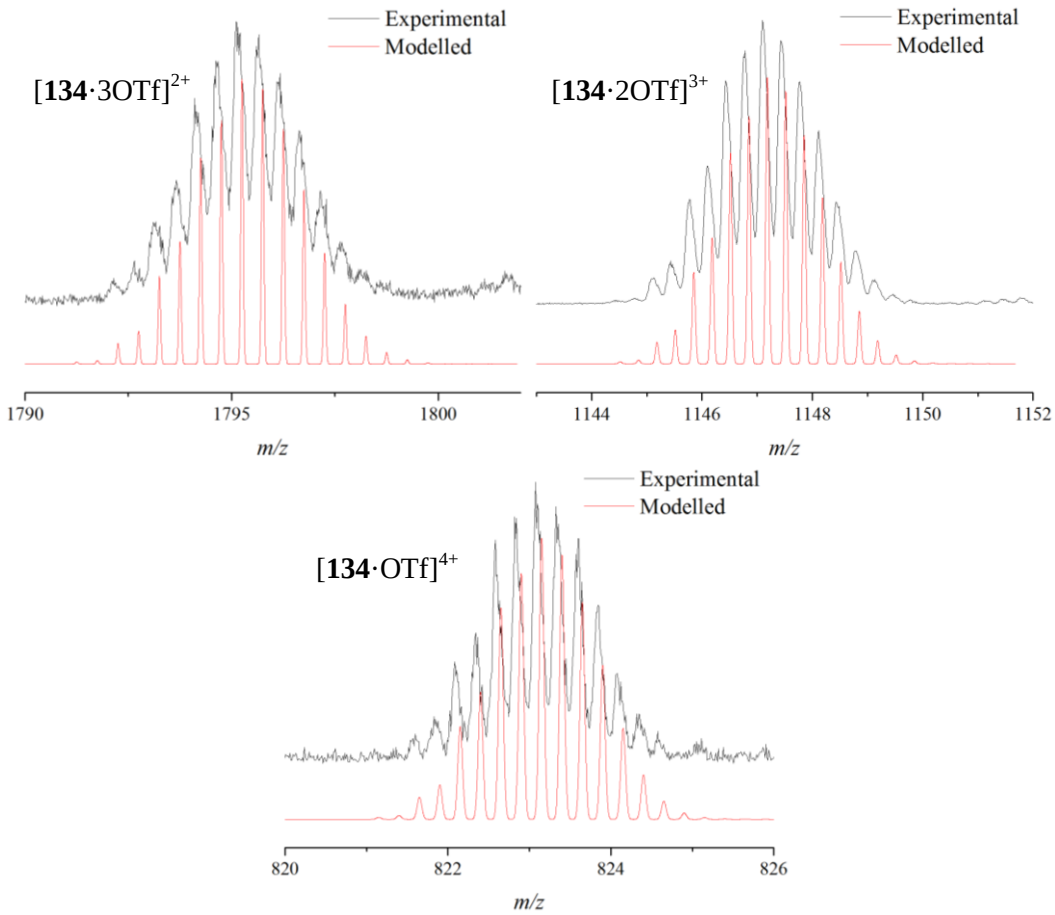

*Figure 2.30: Experimental peaks (black) from crude mixture identified as **134**·5OTf shown versus modelled isotopic distribution (red).*

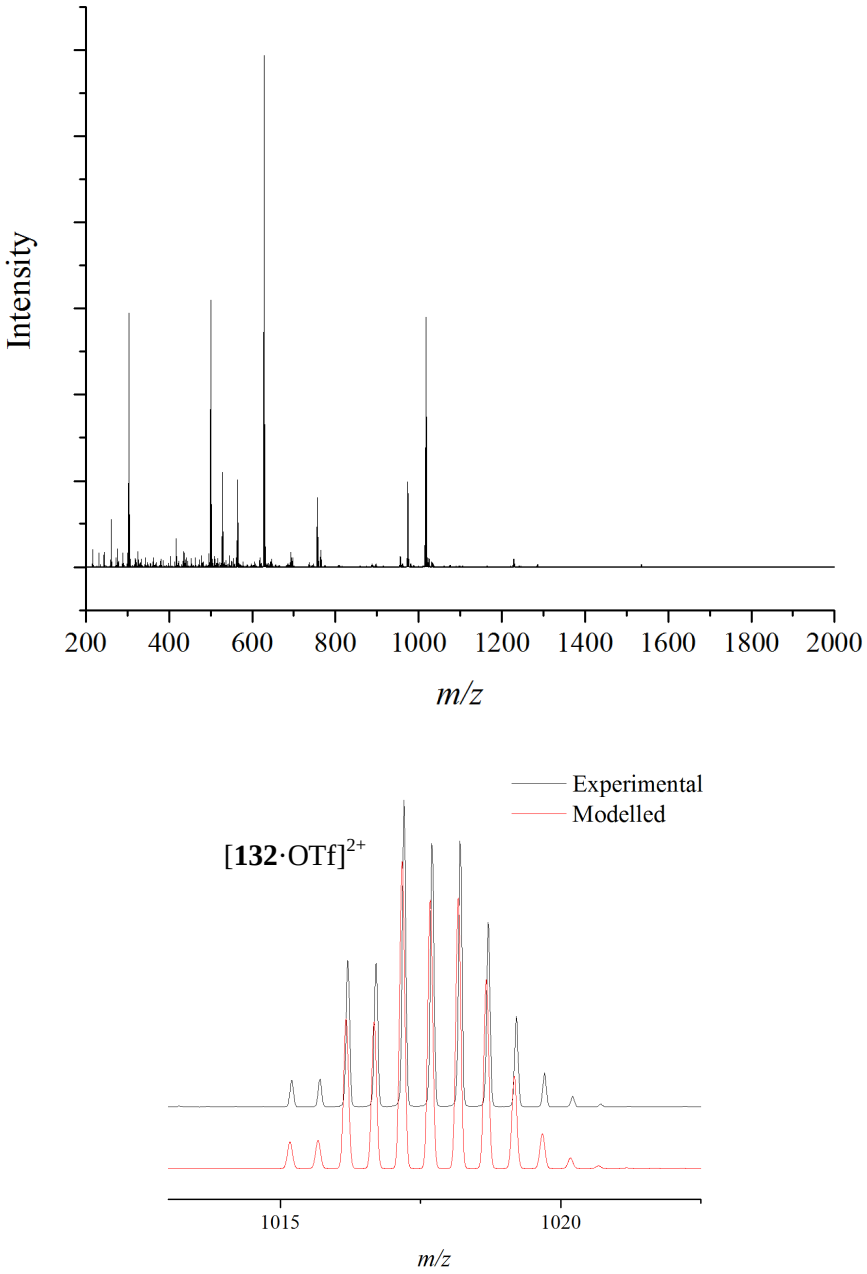

Figure 2.31: nESI-MS of the isolated rac-***132***·3OTf *triangle. The molecular ion peak is shown with experimental (black) versus the modelled isotopic distribution (red).*

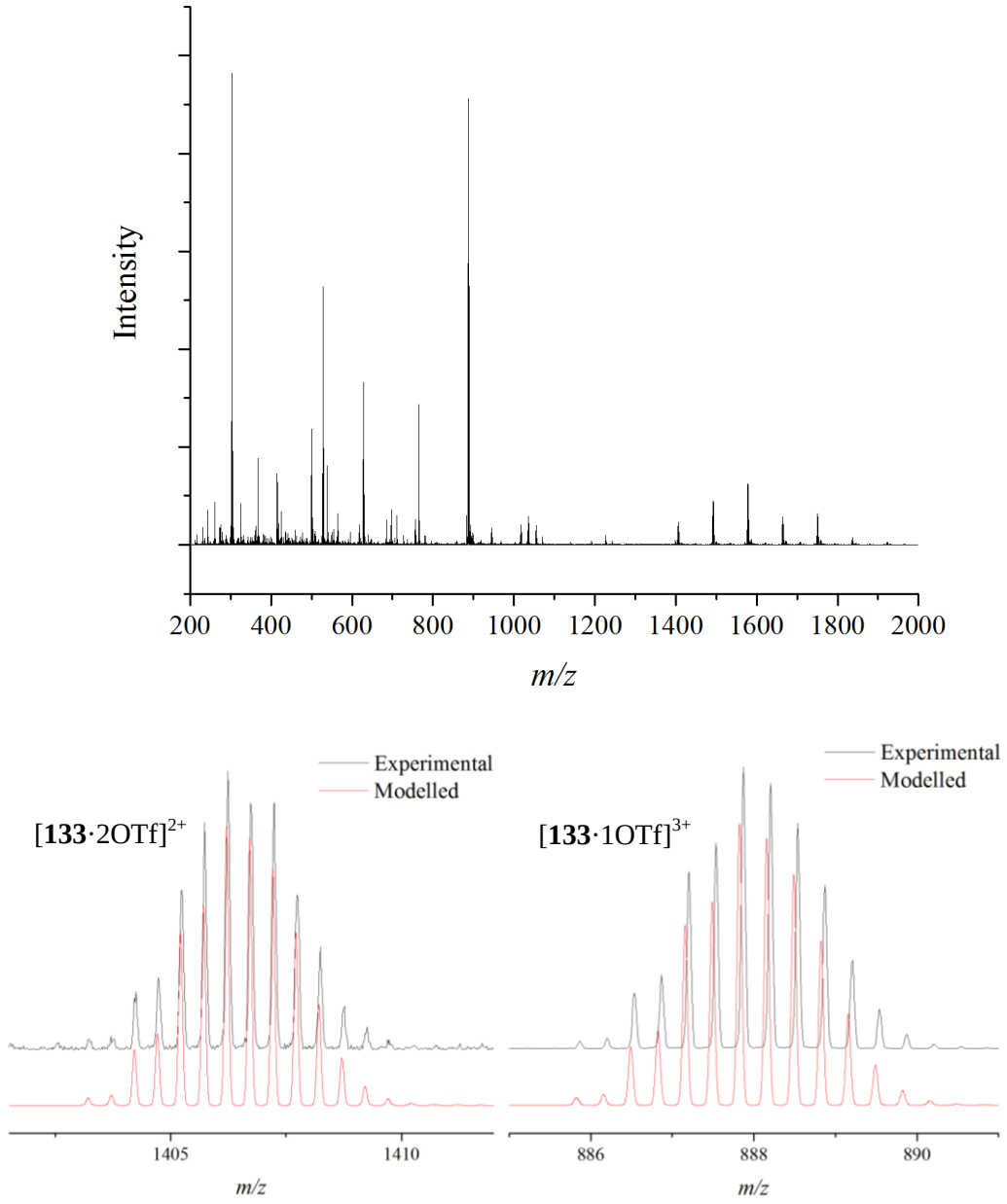

Figure 2.32: nESI-MS of the isolated rac-***133***·*4OTf square. Molecular ion peaks are shown with experimental (black) versus the modelled isotopic distribution (red).*

2.9.13 Mass Spectrometry of Heteroleptic Isocyanide Systems

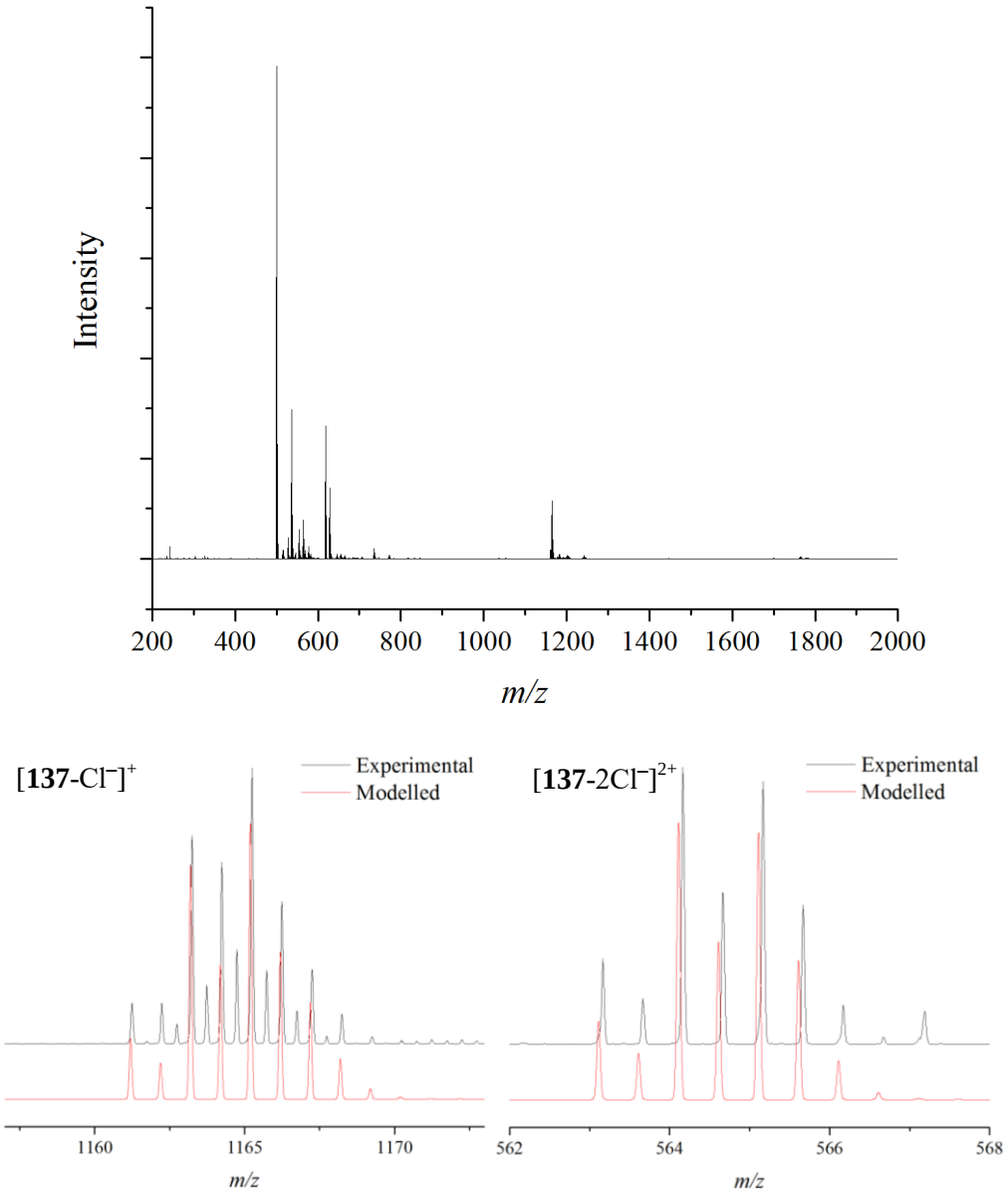

Figure 2.33: nESI-MS of the isocyanide "edge" piece, ***137****. Molecular ion peaks are shown with experimental (black) versus the modelled isotopic distribution (red). The +2 molecular ion shows a propensity to dimerise to form the chloro-bridged macrocycle resulting in a +2 species at m/z = 1165.*

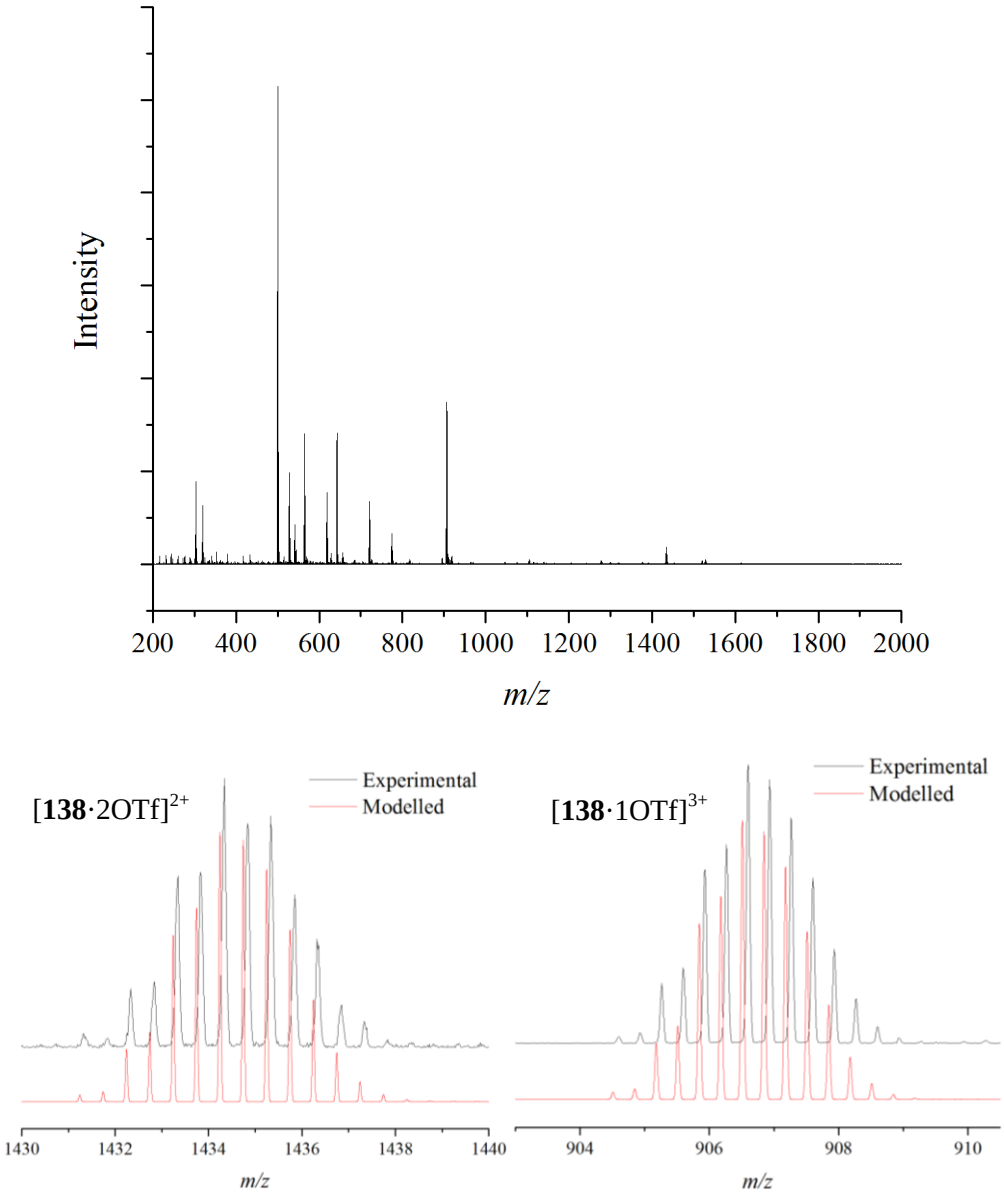

*Figure 2.34: nESI-MS of **138**·4OTf rectangle. Molecular ion peaks are shown with experimental (black) versus the modelled isotopic distribution (red).*

2.10 References

1 O. Chepelin, J. Ujma, X. Wu, A. M. Z. Slawin, M. B. Pitak, S. J. Coles, J. Michel, A. C. Jones, P. E. Barran and P. J. Lusby, *J. Am. Chem. Soc.*, 2012, **134**, 19334–19337.

2 O. Chepelin, The University of Edinburgh, 2013.

3 J. Wang, G. Li, Q. S. Li, Y. Xie and R. B. King, *Polyhedron*, 2012, **47**, 165–172.

4 E. Baranoff, E. Orselli, L. Allouche, D. Di Censo, R. Scopelliti, M. Grätzel and M. K. Nazeeruddin, *Chem. Commun.*, 2011, **47**, 2799–2801.

5 J. R. Farrell, C. A. Mirkin, S. R. Evanston, L. M. Liable-sands and A. L. Rheingold, *J. Am. Chem. Soc.*, 1998, **120**, 11834.

6 M. S. M. Iii, M. V Ovchinnikov, C. A. Mirkin, L. N. Zakharov and A. L. Rheingold, 2003, **42**, 6851–6858.

7 P. C. Lin, H. Y. Chen, P. Y. Chen, M. H. Chiang, M. Y. Chiang, T. S. Kuo and S. C. N. Hsu, *Inorg. Chem.*, 2011, **50**, 10825–10834.

8 P. Espinet, K. Soulantica, J. P. H. Charmant and a. G. Orpen, *Chem. Commun.*, 2000, **3**, 915–916.

9 K. Mann, M. DiPierro and T. Gill, *J. Am. Chem. Soc.*, 1980, **3965**, 3965–3967.

10 A. Mayr and J. Guo, *Inorg. Chem.*, 1999, **38**, 921–928.

11 A. Guitard, A. Mari, A. L. Beauchamp, Y. Dartiguenave and M. Dartiguenave, *Inorg. Chem.*, 1983, **8**, 1603–1606.

12 J. F. Bérubé, K. Gagnon, D. Fortin, A. Decken and P. D. Harvey, *Inorg. Chem.*, 2006, **45**, 2812–2823.

13 D. Fortin, M. Drouin and P. D. Harvey, *Inorg. Chem.*, 2000, **39**, 2758–2769.

14 M. J. Irwin, G. C. Jia, N. C. Payne and R. J. Puddephatt, *Organometallics*, 1996, **15**, 51–57.

15 M. Irwin, J. Vittal and R. Puddephatt, *Organometallics*, 1997, **16**, 3541–3547.

16 H. Schubert and L. Wesemann, *Organometallics*, 2010, **29**, 4906–4913.

17 A. Weber, T. S. Ertel, U. Reinöhl, M. Feth, H. Bertagnolli, M. Leuze and M. Hanack, *Eur. J. Inorg. Chem.*, 2001, **2001**, 679–684.

18 T. Tanase, E. Goto, R. A. Begum, M. Hamaguchi, S. Zhan, M. Iida and K. Sakai, *Organometallics*, 2004, **23**, 5975–5988.

19 S. B. Lee, S. Hwang, D. S. Chung, H. Yun and J. I. Hong, *Tetrahedron Lett.*, 1998, **39**, 873–876.

20 M. Fujita, O. Sasaki, T. Mitsuhashi, T. Fujita, J. Yazaki, K. Yamaguchi and K. Ogura, *Chem. Commun.*, 1996, **20**, 1535.

21 A. B. Tamayo, B. D. Alleyne, P. I. Djurovich, S. Lamansky, I. Tsyba, N. N. Ho, R. Bau and M. E. Thompson, *J. Am. Chem. Soc.*, 2003, **125**, 7377–7387.

22 K. Ono, M. Joho, K. Saito, M. Tomura, Y. Matsushita, S. Naka, H. Okada and H. Onnagawa, *Eur. J. Inorg. Chem.*, 2006, 3676–3683.

23 O. Chepelin, J. Ujma, P. E. Barran and P. J. Lusby, *Angew. Chemie Int. Ed.*, 2012, **51**, 4194–4197.

24 K. D. Benkstein, J. T. Hupp and C. L. Stern, *Inorg. Chem.*, 1998, **37**, 5404–5405.

25 P. H. Dinolfo, M. E. Williams, C. L. Stern and J. T. Hupp, *J. Am. Chem. Soc.*, 2004, **126**, 12989–13001.

26 J. L. Bear, B. Han, Z. Wu, E. Van Caemelbecke and K. M. Kadish, *Inorg. Chem.*, 2001, **40**, 2275–2281.

27 S. Coco, C. Cordovilla, P. Espinet, J. Martín-Álvarez and P. Muñoz, *Inorg. Chem.*, 2006, **45**, 10180–10187.

28 M. C. Irwin, L. M. Rendina, J. J. Vittal and R. J. Puddephatt, *J. Chem. Soc., Chem. Commun.*, 1996, 1281–1282.

29 C. Ko, A. W. Cheung and S. Yiu, *Polyhedron*, 2015, **86**, 17–23.

30 T. J. Wu, C. S. Chen, W. Y. Yeh, T. S. Kuo and G. H. Lee, *Inorganica Chim. Acta*, 2010, **363**, 2553–2560.

31 F. L. Weitl and K. N. Raymond, *J. Am. Chem. Soc.*, 1979, **101**, 2728–2731.

32 A. S. Bailey, B. R. Henn and J. M. Langdon, *Tetrahedron*, 1963, **19**, 161–167.

33 M. J. Jeong, J. H. Park, C. Lee and J. Y. Chang, *Org. Lett.*, 2006, **8**, 2221–2224.

34 C. L. Perrin and T. J. Dwyer, *Chem Rev*, 1990, **6**, 935–967.

35 D. Zuccaccia, L. Pirondini, R. Pinalli, E. Dalcanale and A. Macchioni, *J. Am. Chem. Soc.*, 2005, **127**, 7025–7032.

36 M. L. H. Green, L. L. Wong and A. Sella, *Organometallics*, 1992, **11**, 2660–2668.

37 C. E. Housecroft and A. G. Sharpe, *Inorganic Chemistry*, 2001.

CHAPTER 3

A Complex-as-Ligand Approach to Metallosupramolecular Photoredox Catalysis

Contents

3.1 Synopsis

Due to the difficulties in preparing photoactive assemblies utilising iridium as a structural component, a complex-as-ligand method was developed to allow the preparation of a photoredox active Pd_2L_4 type system. The assembled structure could be isolated as a stable solid and readily formed a discrete supramolecular system in solution at concentrations above 10 μM. Importantly, the beneficial photophysical properties of the iridium complex were maintained in the self-assembled cage despite the presence of the heavy Pd^{II} ions. Initial guest binding studies in 1:1 CD_3CN/D_2O showed that a range of neutral organic guests could be encapsulated using the hydrophobic effect and the cage could successfully function as a photocatalyst. However, regio-selective catalysis was unsuccessful, potentially due to the relatively low affinity for guests and the resultant competition with the bulk phase reaction.

3.2 Introduction

As discussed in Chapter 1, photoactive coordination capsules show great promise in combining the beneficial properties of both visible-light photoredox catalysis and that of stereo- or regio-selective supramolecular catalysis. The most commonly used photoredox catalysts are polypyridyl ruthenium complexes or cyclometallated iridium complexes due to their suitable photochemical properties such as high extinction coefficients, long-lived excited states, solution stability and high redox potentials.[1–9] Previous attempts at directly incorporating iridium as a structural component into the assembly of a coordination capsule were successful in producing a photoactive coordination cage.[10] Indeed, the cooperative binding actually enhanced the luminescent behaviour with respect to structurally similar mononuclear complexes. However, the structure was found to be inherently unstable towards the encapsulation of neutral organic molecules due to the requirement for the cage to encapsulate four templating counter ions. Upon removal of these counter ions, or replacement with bulky non-templating anions, the cage rapidly disassembled into the constituent monomeric parts. Attempts to stabilise this structure are discussed in chapter 2. As an alternative method for developing a stable cage system that incorporated an iridium photosensitiser, a complex-as-ligand approach was envisaged by which a cyclometallated iridium complex with additional donor sites could be assembled into a coordination capsule using an alternative metal linker.

Many examples of the complex-as-ligand approach already exist whereby kinetically inert metal complexes can be used in the stepwise synthesis of heterometallic supramolecular assemblies.[11–21] Indeed, examples are also present where luminescent building blocks have been used to create two-dimensional photoactive metallosupramolecular assemblies (see chapter 2).[22–26] However, although many of these systems display an affinity for binding ions,[22,24] host:guest chemistry with neutral organic molecules is limited and the macrocycles often lack the three-dimensional confines required for strict regio- or stereo-selective supramolecular catalysis. As such, a novel M_2L_4 iridium functionalised system was designed, synthesised and investigated for synthetically useful guest binding and photoredox properties.

3.3 Design & Synthesis of "Complex-as-Ligand" Systems

3.3.1 Ligand Synthesis

Iridium was chosen as the photocatalytic centre due to its ideal photophysical properties and the ease in which ancillary ligands could be attached when compared with analagous ruthenium polypyridyl chemistry. A complex was designed based on the common cyclometallated iridium bis-(2-phenylpyridine) moiety ($Ir(ppy)_2N\hat{}N$) where the ancillary ligand was altered to incorporate additional metal binding sites (Figure 3.1). Pyridine is commonly used as a metal-binding site in coordination chemistry but incorporation of 3- or 4-substituted pyridines would lead to an incorrect binding angle for the formation of a Pd_2L_4 system. Instead, imidazole groups were incorporated to improve the bite angle towards the required 180º. The remaining slight offset could then be accommodated by bond rotation along the alkyne bridge.

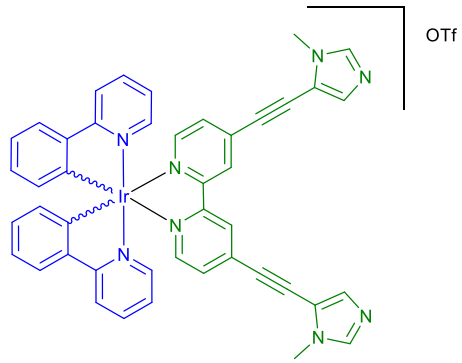

146·OTf

Figure 3.1: Structure of proposed iridium complex containing additional imidazole metal binding sites.

The ancillary ligand (**149**) was prepared in a single step from the commercially available 4,4'-dibromo-2,2'-bipyridine and ethynyl-1H-methylimidazole based on a copper-free Sonagashira coupling (Scheme 3.1).[27]

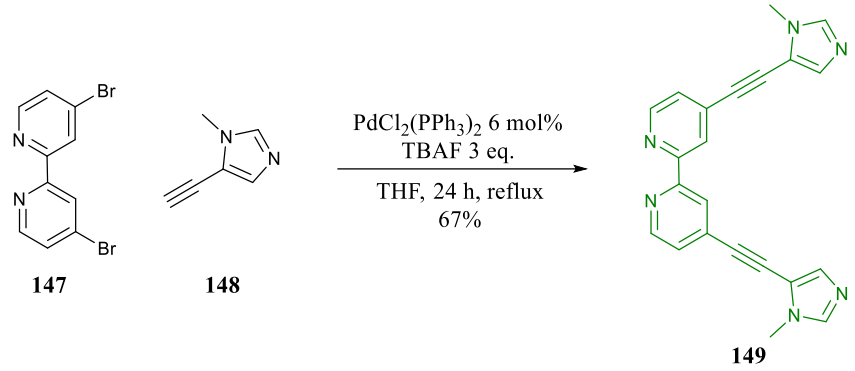

*Scheme 3.1: Synthesis of bis-4,4'-(ethynylmethylimidazole)-2,2'-bipyridine (**4**).*

Complexation of the ancillary ligand (**149**) was accomplished by heating the ligand and $[(Ir(ppy)_2Cl)_2]$ in ethylene glycol at 150 °C for 24 h (Scheme 3.2). The reaction was found to be air sensitive and thorough degassing of the solution under high vacuum was required before heating. Unlike other more mild methods for complexation of the ancillary ligand,[28–31] high temperatures were required to allow rearrangement of any imidazole bound intermediates to the thermodynamically most stable bidentate bipyridine complex. Direct substitution of the chloride ions rather than removal via precipitation with silver improved the solubility of the resultant complex throughout the reaction and allowed purification of the final product by precipitation with KOTf from the aqueous solution.

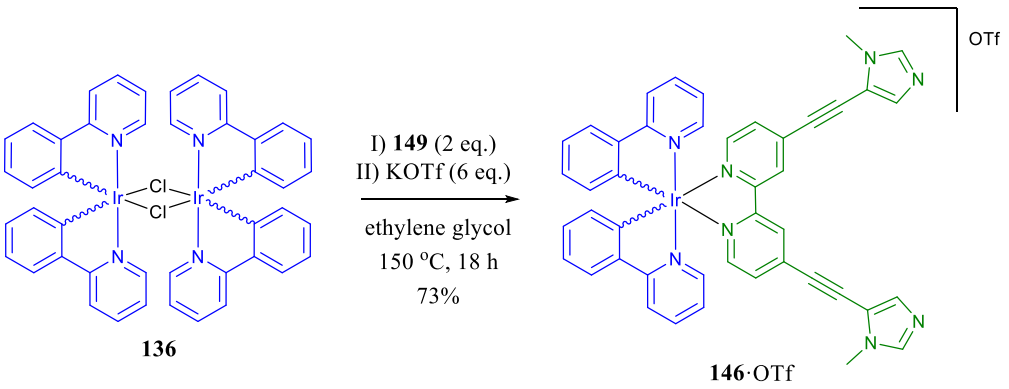

*Scheme 3.2: Complexation of **149** to iridium. Elevated temperatures were required to allow rearrangement to the stable bipyridine bidentate complex.*

For many of the reactions, the isolated precipitate was clean and required no further purification. When this was not the case, purification of the complex was achieved by silica chromatography running a gradient of 0 to 10% CH_3OH in CH_2Cl_2. The complex was fully characterised by NMR spectroscopy and mass spectrometry. X-ray quality crystals were

grown by slow evaporation of a 1:1 water:acetonitrile solution of Pd_2L_4 (**151**·8OTf) (see section 3.7.11 for further details). The obtained structure was consistent with the formation of the intended cyclometallated iridium complex, **146**·OTf (Figure 3.2). Interestingly, the imidazole groups are oriented with the N-donor sites pointing outwards in the solid state. However, this was expected to solely due to packing effects and free rotation along the alkyne bridge should allow rotation into a favourable binding geometry in solution.

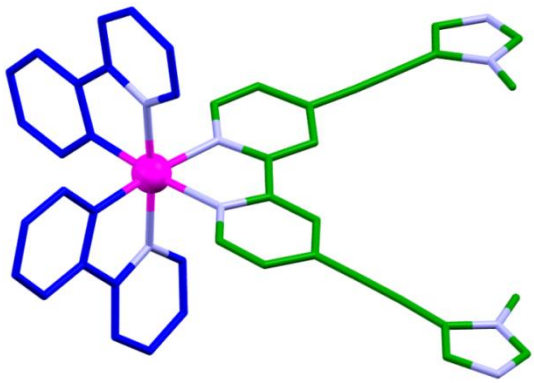

*Figure 3.2: Crystal structure of **146**. Hydrogen atoms, solvent and counter ions are removed for clarity. Atoms coloured pink – Ir, light blue – N, green – C (ancillary ligand), dark blue – C (cyclometallated ligand).*

3.3.2 Cage Assembly – Zinc

In order to facilitate guest binding within the cage, a 6-coordinate transition metal was chosen for the cage assembly with the aim of forming an M_2L_4 assembly that contained metal centres with free coordination sites. This could potentially provide a driving force for the binding of guests containing weak metal-binding sites such as nitriles. The Lewis acidity of the metal ions could also favour the formation of radical anions by single electron transfer (SET) from the photoexcited iridium complexes. The cationic cage structure would also further stabilise the radical anion intermediates allowing the rapid formation of the cyclised products (Figure 3.3 and 3.4).

Zinc was initially chosen as an appropriate 6-coordinate transition metal. The full outer shell of the Zn^{2+} was also thought to be advantageous towards preventing quenching of the iridium excited state through electron transfer.[32]

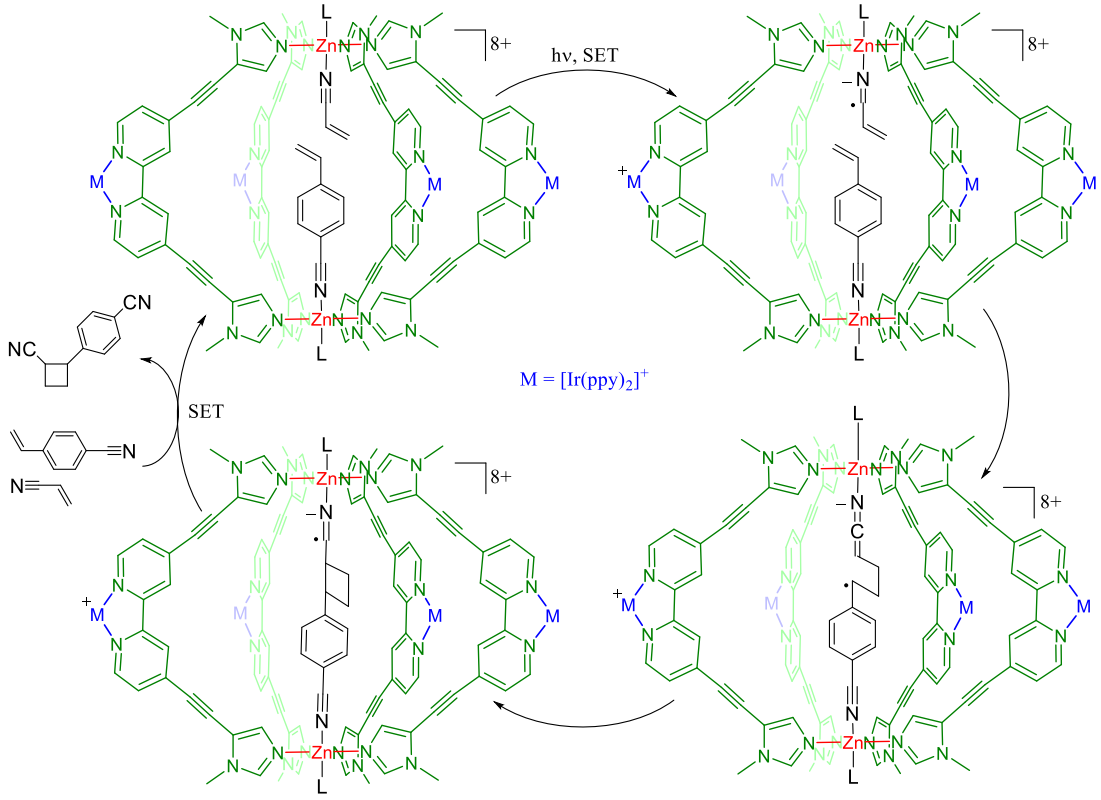

Figure 3.3: A proposed photoredox catalytic cycle for the 2+2 cycloaddition of metal-ligand bound substrates within an iridium functionalised Pd_2L_4 cage.

Addition of $Zn(OTf)_2$ 0.5 eq. resulted in significant ^1H NMR peak shifts for both the methyl imidazole protons and the bipyridine proton held within the inner cavity (Figure 3.5). The spectrum remained simple, indicating a symmetrical structure rather than the complex spectra associated with mixed species or the dramatically broadened spectra observed for polymerisation. Further evidence for cage formation was obtained from DOSY NMR which showed a change from a 6.6 Å radius to a single species with a radius of 11.3 Å.

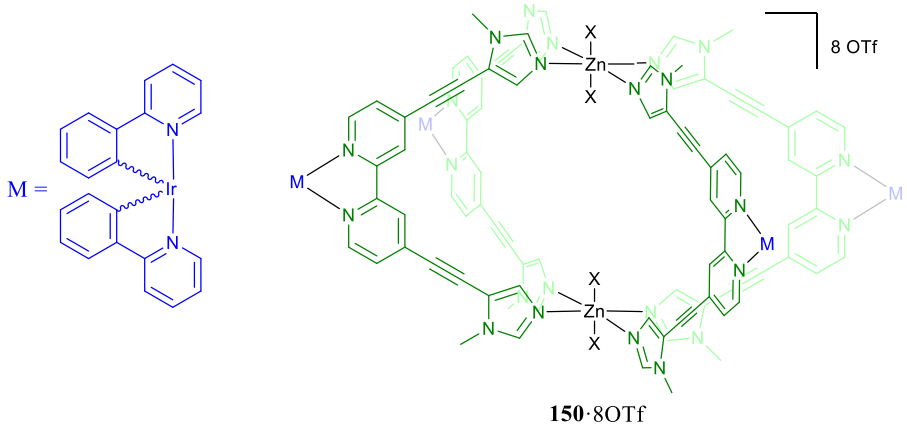

150·8OTf

*Figure 3.4: Structure of the intended Zn_2L_4 cage self-assembled from **146**·OTf. Axial sites on the zinc centres are most likely occupied by solvent molecules or weakly coordinated counter ions.*

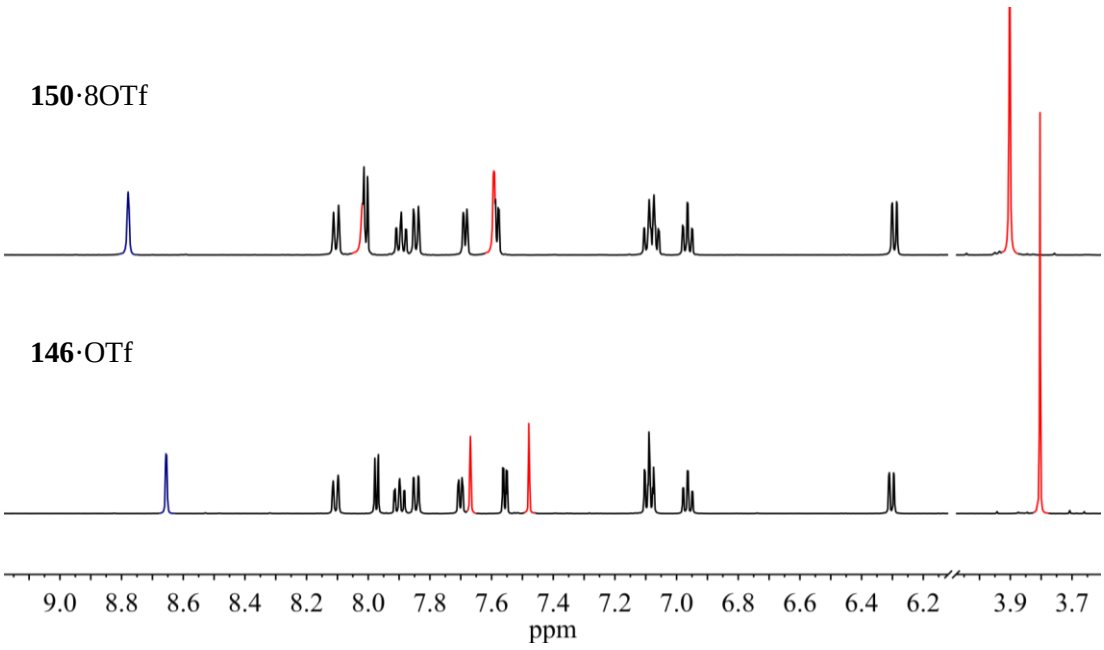

Figure 3.5: Comparison of ^1H NMR spectra (500 MHz, CD_3CN, 300 K) for the mono-nuclear complex and the Zn_2L_4 cage. The methyl imidazole protons (red) and the inner bipyridine proton (blue) show the most pronounced shifts upon complexation with zinc.

Although NMR spectroscopy suggested the formation of large symmetrical species, titration experiments showed that complexation of zinc and the formation of any higher order species was in fast exchange on the NMR timescale (Figure 3.6). As a consequence of this, the peak positions were highly dependent on the concentration of zinc present and the addition of excess Zn^{2+} (>0.5 eq.) resulted in the partial return of the peaks to their original positions.

The weak metal-ligand interactions also made it impossible to detect the intact Zn_2L_4 species using ESI-MS.

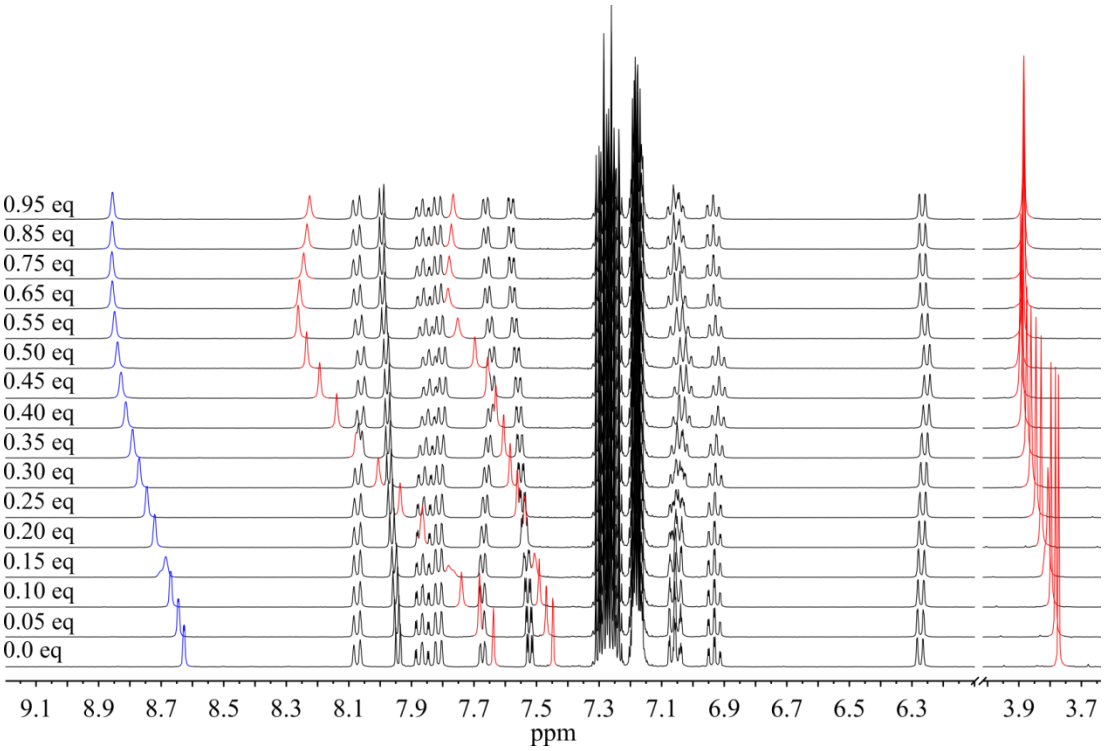

*Figure 3.6: ^{1}H NMR (400 MHz, CD_3CN, 300 K) titration of $ZnOTf_2$ into an 8 mM solution of **1**·OTf. The inner ortho-pyridyl (blue) and imidazole (red) protons show the greatest change in local environment. 1,2-Difluorobenzene was added as an internal ^{1}H/^{19}F standard.*

Due to the highly dynamic nature of the resultant zinc assembly, the exact speciation present in solution was difficult to interpret since any desymmetrisation of the structure could not be observed. In addition, guest binding within the intact assembly was difficult to assess since any observed peak shifts could also be attributed to changes in the cage speciation. To avoid these complications, alternative metal-linkers were considered for the formation of a more stable and consistent supramolecular system.

3.3.3 Cage Assembly – Palladium

In order to assemble a more stable structure, square planar palladium was chosen as an alternative 2nd row transition metal linker (Figure 3.7). Upon the addition of $Pd(CH_3CN)_4 \cdot 2OTf$ (0.5 eq.) to **146**·OTf in CH_3CN at room temperature, the formation of a large assembly was observed. In comparison with **150**·8OTf, a similar change in proton environments was observed, with the methyl imidazole protons and the internal bipyridine proton peaks showing the largest change in ppm. However, the ^1H NMR spectrum showed additional splitting patterns visible throughout the spectrum but most easily observed in the formation of a triplet-like 1:2:1 signal distribution for the CH_3 group (Figure 3.8).

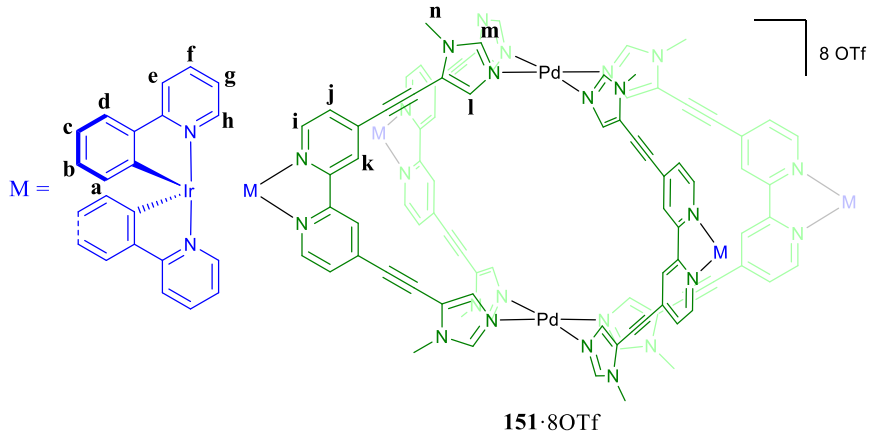

151·8OTf

*Figure 3.7: Structure of the intended Pd_2L_4 cage self-assembled from **146**·OTf.*

DOSY NMR showed exactly the same increase in size from 6.6 Å to 11.3 Å as observed for **150**·8OTf and confirmed that all of the signals belonged to species of a similar size. Although it was unlikely that this "splitting" was due to conventional proton coupling, since it was not observed in the parent complex, ^1H NMR experiments were carried out at different field strengths to confirm this hypothesis (Figure 3.9). As no change was observed in the position of the additional peaks, the 1:2:1 peak pattern was attributed to different proton environments. Pureshift NMR experiments also confirmed this observation since multiple peaks were still observed after all proton-proton coupling interactions were removed.

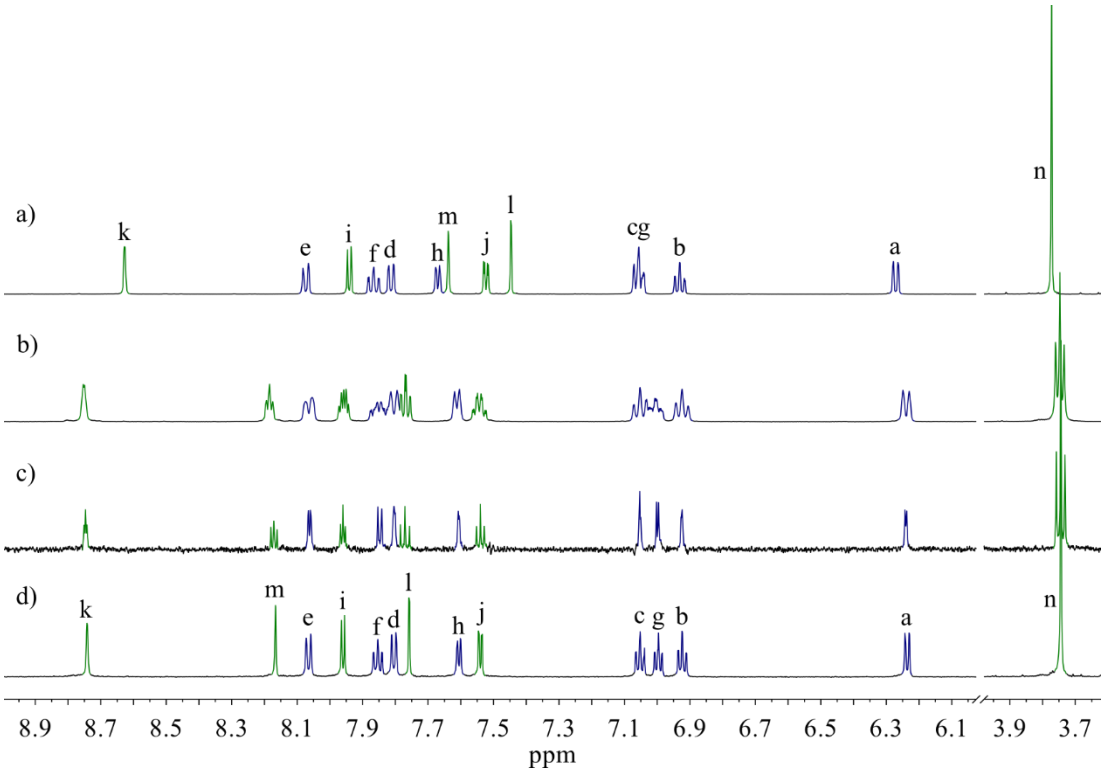

Figure 3.8: Comparison of ^{1}*H NMR spectra (500 MHz,* CD_3CN*, 300 K) for a)* ***146***·*OTf b)* rac-***151***·*8OTf c) pureshift analysis of* rac-***151***·*8OTf and d) enantiopure Δ-****151****·8OTf. Peak labels refer to those shown in Figure 3.7.*

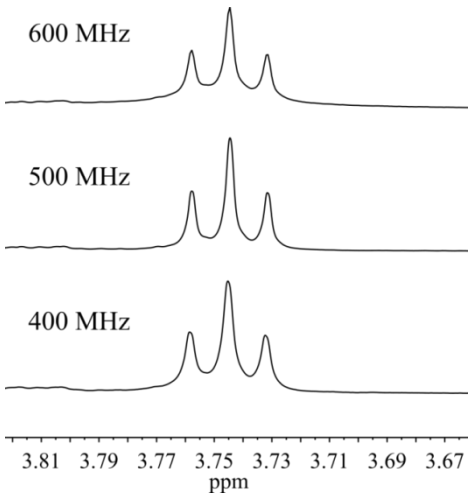

Figure 3.9: ^{1}*H NMR (*CD_3CN*, 300 K) of* rac-***151***·*8OTf showing the* CH_3 *peaks at different magnetic field strengths. As no change in the peak positions was observed, the 1:2:1 structure is due to multiple species containing similar proton environments.*

Using separation techniques developed previously by the group,[10] Δ- or Λ-$(Ir(ppy)_2Cl)_2$ was used to prepare enantiopure samples of **146**·OTf. As expected, the ^{1}H NMR remained identical for the mononuclear complex, **146**·OTf, but upon formation of the cage assembly by the addition of $Pd(CH_3CN)_4$·2OTf (0.5 eq), no additional signals were observed. Confirmation of successful preparation of enantiopure Λ/Δ-**146**·OTf and Λ/Δ-**151**·8OTf was also provided by circular dichroism (Section 3.7.7).

One explanation for the observed peak patterns is that the inherent chirality of the iridium complex creates a mixture of diastereomers when assembled into a Pd_2L_4 cage. Since **146**·OTf exists as a racemic mixture of Δ and Λ stereoisomers, this would give rise to a series of structures containing a statistical mixture of chiral centres. For a number of sites equal to n, with a 50:50 probability between two states, Λ or Δ, 2^n different combinations are possible (Figure 3.10). For **151**·8OTf containing 4 different chiral centres, this gives rise to $2^4 = 16$ possible arrangements. Due to the cyclic nature of the system, many of these possible combinations are chemically identical and instead four different possible configurations (A, B, C, and D) are perceived and populated according to their statistical likely hood (2, 8, 4 and 2 respectively). An explanation for the 1:2:1 triplet splitting based on this model would be to assume that configurations A and D produce identical spectra. However, analysis of enantiopure Δ- or Λ-**151**·8OTf shows that the larger central peak in the triplet, rather than the predicted smaller side peak, corresponds to configuration A.

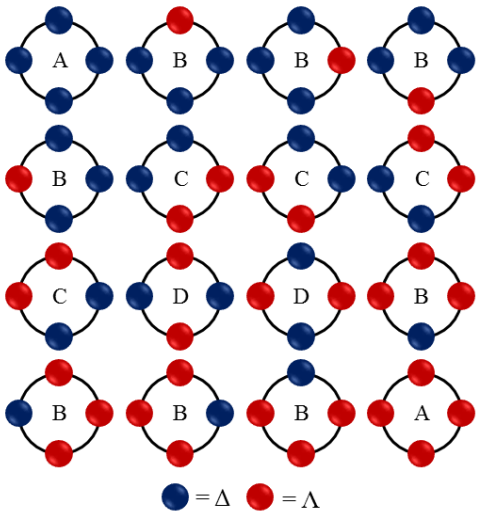

Figure 3.10: Statistical distribution of iridium chiral centres in a sample of rac-***151***·8OTf.

Instead, the peak position can be rationalised based on the configuration of the neighbouring groups, i.e. the local chemical environment. For an individual iridium centre (Λ), there are four possible configurations based on the chirality of the neighbouring iridium centres (Figure 3.11). Depending on the relative orientations of these groups, each 2-phenylpyridine ligand on the central iridium complex can either be in an open, enclosed or semi-enclosed environment. The semi-enclosed environments occur when the central iridium complex is next to two centres with the same symmetry as each other (i.e. ΛΛΛ and ΔΛΔ), while the configurations with two centres of opposite symmetry produce an equal mixture of open and closed environments. This results in desymmetrisation of the system along the horizontal plane for the ΔΛΛ/ΛΛΔ configurations and leads to two different peaks in the ^{1}H NMR spectrum. Along with the singlet signal from the ΛΛΛ/ΔΛΔ configurations, this gives a 1:2:1 ratio of chemical environments with the most populated environment corresponding to that observed for the homochiral variant.

Additional evidence for the existence of the cage assembly was obtained by ESI-MS and identical spectra were obtained for both the racemic and enantiopure mixtures (Figure 3.26). X-ray quality crystals could not be obtained by any conventional methods. Crystals were obtained by slow diffusion of diisopropylether into an acetonitrile solution but data of sufficient quality could not be obtained even with a synchrotron radiation source. Crystallisation by evaporation from a 1:1 mixture of CH_3CN and H_2O gave the disassembled mononuclear complex **146**·OTf.

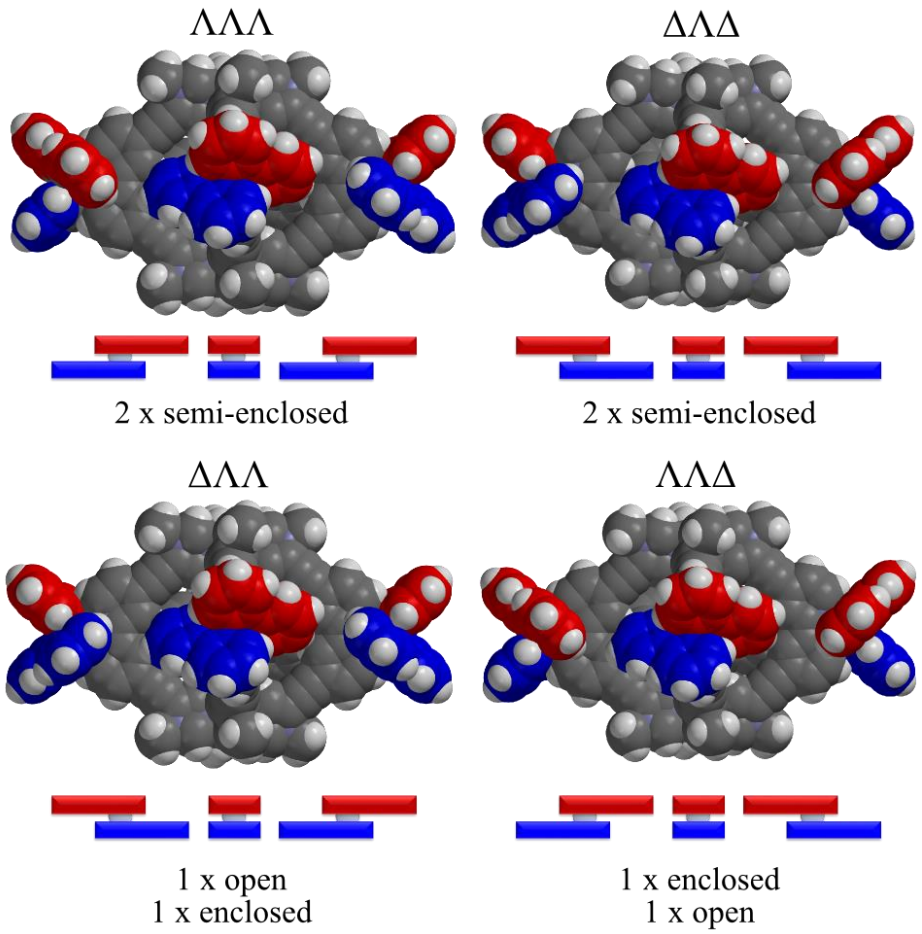

Figure 3.11: Comparison of the four possible configurations for a single iridium centre and direct neighbours. Top (red) and bottom (blue) environments are considered independently. Assuming the local environment is dominated by the relative orientations of the neighbouring two chiral centres, this produces a 1:2:1 mixture of chemical environments observed by ^{1}H NMR.

3.4 System Properties

3.4.1 Stability

As discussed in Chapter 2, the stability of the previous Ir_6L_4 luminescent supramolecular system was highly dependent on the encapsulated counter anions.[10] Removal of these anions, in order to encapsulate guest compounds, led to the rapid disassembly of the cage structure. In comparison, **151**·8OTf showed no obvious signs of anion templation or anion dependent stability. ^{19}F NMR spectroscopy of **151**·8OTf in CD_3CN shows only a single peak corresponding to free OTf (measured versus saturated KOTf in CD_3CN) and ESI-MS analysis gave a mixture of charged species.

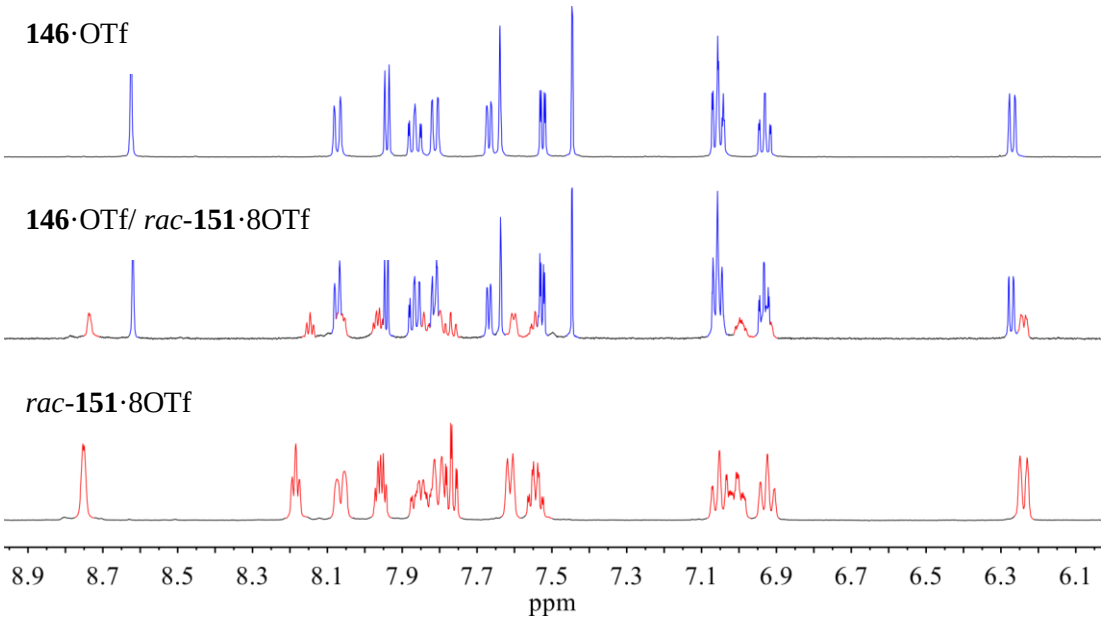

*Figure 3.12: ^{1}H NMR (500 MHz, CD_3CN, 300 K) of **146**·OTf, **151**·8OTf and comparison with a stable mixture of both obtained by the addition of $Pd(CH_3CN)_4$·2OTf (0.25 eq.) to a solution of **146**·OTf.*

151·8OTf was found to be stable for months in CD_3CN with no sign of disassembly or photobleaching. Unlike **150**·8OTf, stable mixtures of **146**·OTf and **151**·8OTf could also be prepared and identified without the formation of partially assembled structures by the addition of <0.5 eq. Pd^{2+} (Figure 3.12). Although ligand exchange was slow on the ^{1}H NMR timescale, the dynamic nature of the system was demonstrated by performing a scrambling experiment by mixing Λ and Δ-**151**·8OTf in a 1:1 ratio in CH_3CN and monitoring the

formation of the complex mixture observed for *rac*-**151**·8OTf (Figure 3.13). The half-life was calculated as 132 h and shows that the enantiopure assemblies are not significantly more thermodynamically stable than any of the alternative mixed chirality systems.

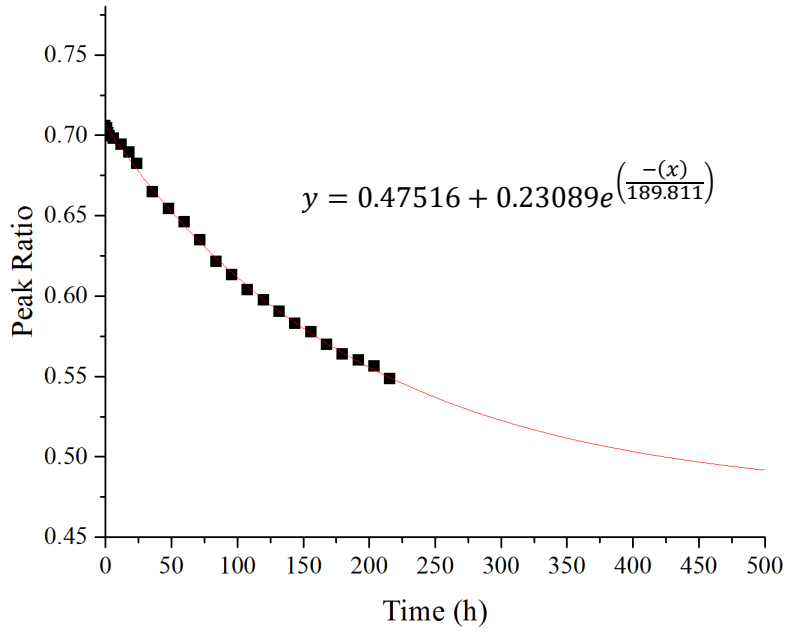

*Figure 3.13: Δ/Λ-**151**·8OTf scrambling experiment in CD_3CN at room temperature. The proportion of scrambling was measured by the ratio of the central triplet peak to the total peak area for the methyl imidazole proton signal. The fitted exponential decay (red) gives a mean lifetime of 190 h and a corresponding half-life of 132 h.*

Dilution experiments showed that the system was stable at concentrations above approximately 10 μM; however, further dilution resulted in disassembly of the structure to produce predominantly free complex (Figure 3.14). Similar observations were made using UV/Vis and thus, all experiments, including photophysical investigations, were carried out at concentrations greater than or equal to 10 μM.

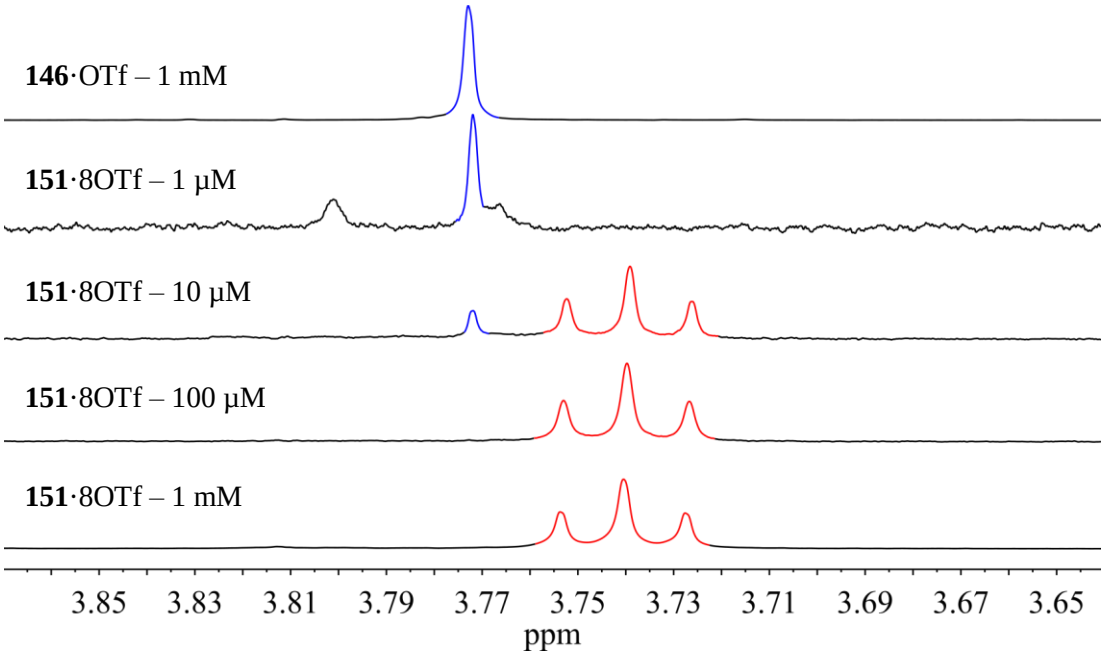

*Figure 3.14: Stability of **151**·8OTf under dilute conditions investigated by ^{1}H NMR (600 MHz, CD_3CN, 300 K). Disassembly of the cage (red) to primarily **146**·OTf (blue) begins at concentrations below approximately 10 µM and complete disassembly is observed below 1 µM.*

Although still inherently dynamic in nature, the selective formation of **151**·8OTf in the presence of excess **146**·OTf shows that the assembled cage only undergoes slow exchange on an NMR timescale and suggests that **151**·8OTf is significantly more stable than any of the other transient partially assembled structures. As a result, **151**·8OTf exists as a well-defined discrete metallosupramolecular assembly in solution at concentrations above 10 µM.

3.4.2 Photophysical & Electrochemical Properties

The photophysical properties of substances can be highly dependent on their surrounding environments.[33–39] Metallosupramolecular systems usually involve the complexation of ligand building blocks with transition metal ions to self-assemble large symmetrical structures. However, heavy metals ions can effectively quench any beneficial emissive properties due to the unpaired electrons present in the outer orbitals and/or the so called "heavy metal effect" whereby heavy atoms promote non-emissive inter-system-crossing (ISC).[40]

A large range of transition-metal based luminescent supramolecular assemblies have been reported in literature with many using luminescent building blocks self-assembled using metal ions.[22,23,32,41,42] However, other examples exist where highly luminescent compounds are efficiently quenched during self-assembly.[43] These examples can be difficult to assess since luminescence is deemed a favourable property, and as such, any systems that show strong quenching upon self-assembly are often discussed based on other properties.[16,44] In some cases, severe quenching can only be assumed based on the lack of reported emissive data for systems that contain inherently emissive building blocks.[45] In addition, care should be taken when supramolecular systems are initially shown to have identical photophysical properties to their individual sub-units. As described in section 3.4.1 and chapter 5, supramolecular assemblies often disassemble under the dilute conditions[46] required for fluorescence spectroscopy which could lead to incorrect assignment of the system properties. Thus, dilution experiments should always be carried out to assess the system stability under photophysical experimental conditions.[32]

For those that do retain their luminescent properties, a large proportion use the photoactive metal components in a structural role.[10,47–54] In this way, no additional, non-emissive metal centres are required and the systems retain their useful photophysical properties, and indeed, self-assembly can even lead to an enhancement in quantum yields due to the loss of non-emissive relaxation pathways afforded by the rigid supramolecular framework.[10] However, the use of photoactive metal centres as the structural components severely limits potential variation and can lead to difficulties in balancing the favourable photophysical properties with system stability.

Heteroleptic cyclometallated iridium complexes have gained great research interest over the last decade due to their important photophysical properties and use in OLEDs. As such, the

theory describing their photophysical properties is well developed. Unlike common first-row transition metal complexes, absorption is dominated by metal to ligand charge transfer (MLCT) and ligand centred (LC) transitions (Figure 3.15). The strong ligand field splitting, due to the presence of cyclometalled carbon donor atoms, results in a very large energy gap between the occupied t_{2g} orbitals and the empty e_g orbitals that prevents any transitions due to UV/visible light. MLCT is responsible for the broad, low-energy transitions that give many iridium complexes their bright colours. Higher energy π-π* transitions are also observed as sharper bands in the UV region. In addition, a weak absorption band is often observed stretching far into the visible region that corresponds to low-energy spin forbidden ^{3}MLCT transitions that become partially allowed due to strong spin-orbit coupling with iridium.

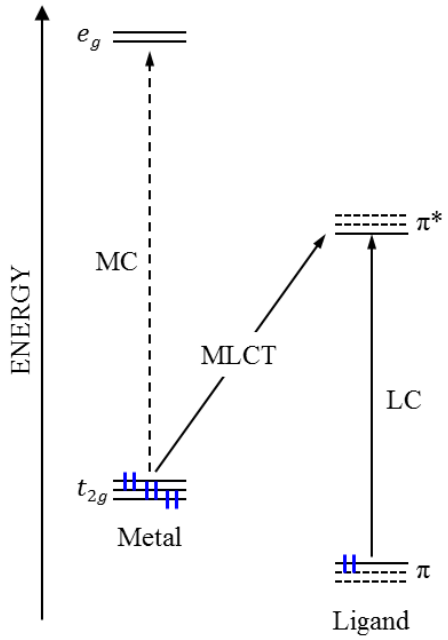

Figure 3.15: A simplified orbital energy diagram showing the observed low-energy metal to ligand charge transfer (MLCT) and high-energy ligand centred (LC) transitions observed for heteroleptic Ir(III) complexes. The strong ligand field splitting due to the cyclometallated ligands means the metal centred (MC) transitions are too high in energy to be observed in the UV/Vis spectrum.

Rapid thermal relaxation of the excited states followed by radiative decay to any of the ground vibrational states often gives a series of well-ordered emission bands for fluorescent organic compounds (Figure 3.16). However, for most cyclometallated iridium complexes, inter-system-crossing (ISC) to lower energy triplet states leads to emission from a mixture of

^{3}MLCT and ^{1}MLCT states, resulting in a broad emission band with a large Stokes-shift. The relatively long life-time of these MLCT states, along with the high redox potentials, make iridium complexes favourable candidates for photoredox catalysis.

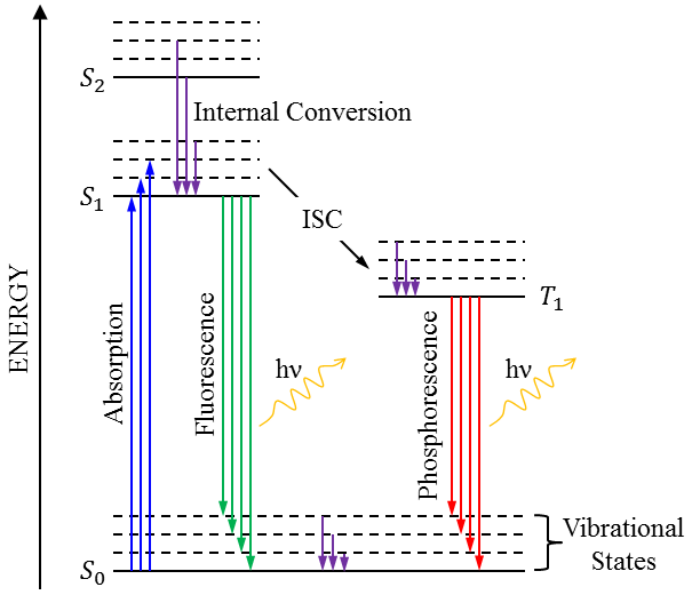

Figure 3.16: Jablonski diagram detailing possible transitions leading to luminescence.

The absorbance of the mononuclear complex and assembled cage showed similarities but with some noticeable differences (Figure 3.17). The weak spin-forbidden transitions remain almost identical but the broad band associated with MLCT spin-allowed transitions decreases in intensity. In addition, an intensity increase is observed for a sharp absorption band at 317 nm. Titration of $Pd(CH_3CN)_4 \cdot 2OTf$ into **146**·OTf whilst maintaining a constant concentration of **146**·OTf confirmed these observations (Figure 3.18).

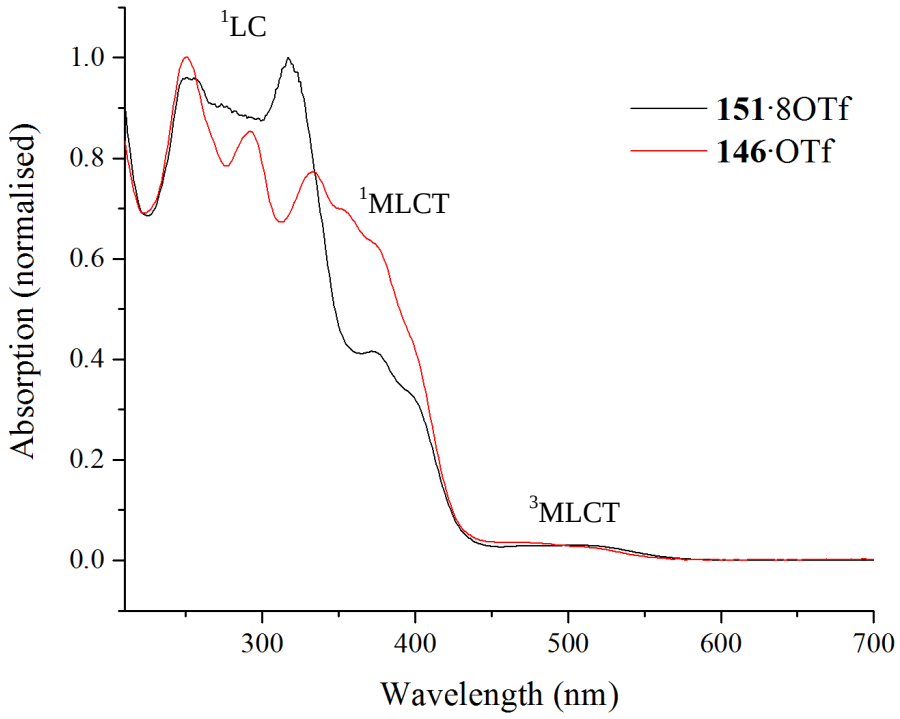

*Figure 3.17: Comparison of absorption spectra (100 µM in CH_3CN) for **151**·OTf (black) and **146**·8OTf (red).*

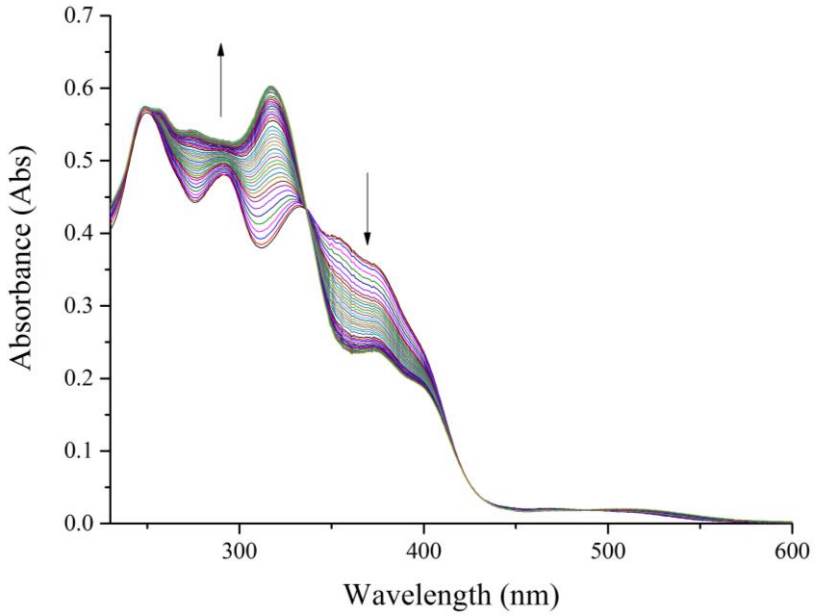

*Figure 3.18: Change in absorption upon addition of $Pd(CH_3CN)_4$·2OTf to **146**·OTf in CH_3CN.*

Self-assembly of **151**·8OTf resulted in a small red-shift of the emission spectrum (Figure 3.19). Although emission was more intense for equal concentrations of **146**·OTf and **151**·8OTf in acetonitrile, this was as a result of **151**·8OTf containing four photoactive iridium centres and quantum yield actually decreased upon self-assembly. A similar reduction in the luminescent lifetime was also observed. This slight reduction in quantum yield and lifetime can be attributed to the heavy atom effect arising from complexation with palladium but importantly, complete quenching of the photoexcited state was not observed.

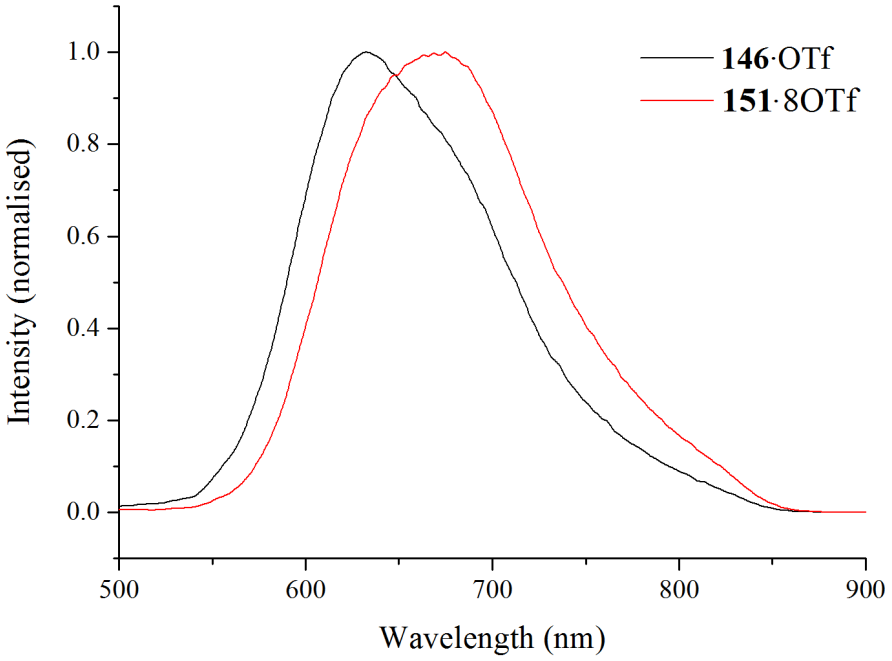

*Figure 3.19: Comparison of emission spectra (100 µM in CH_3CN) for **146**·OTf (black) and **151**·8OTf (red).*

Frozen glass experiments were carried out in a 1:1 mixture of CH_2Cl_2 and CH_3OH and compared with room temperature observations made under identical solvent conditions (Figure 3.20). As expected, at 77 K the emission of both **146**·OTf and **151**·8OTf was significantly blue-shifted and sharpened due to the removal of thermally occupied vibrational states and the lifetimes increased to 5210.57 ns and 3917.94 ns respectively. No significant difference was observed between the behaviour of **146**·OTf and **151**·8OTf suggesting that the formation of a rigid cage structure did not significantly reduce the occupancy of thermally excited vibrational states.

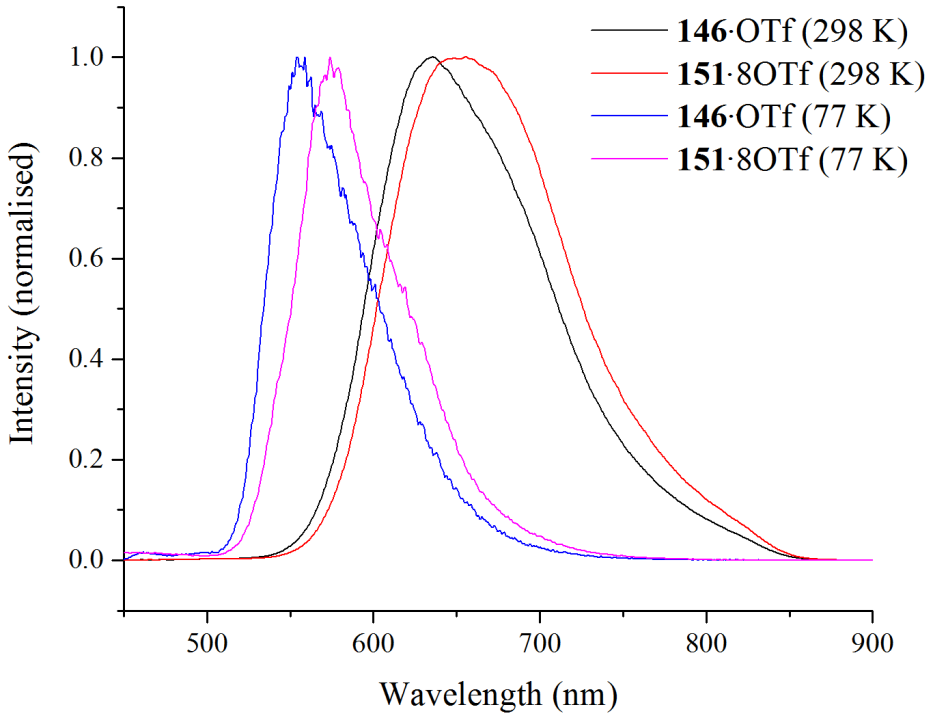

*Figure 3.20: Emission of **146**·OTf and **151**·8OTf in a mixture of 1:1 CH_2Cl_2 and CH_3OH at both room temperature and as a frozen glass at 77 K.*

To ascertain the relative energy levels of **146**·OTf and **151**·8OTf, electrochemistry was performed in CH_3CN, using tetraethylammonium hexafluorophosphate as the electrolyte (Table 3.1). All measurements were carried out with a glassy carbon working electrode, a platinum counter electrode and a Ag/Ag^+ quasi-reference electrode using ferrocene as an internal standard.

*Table 3.1: Comparison of key photophysical and electrochemical properties of compounds **1** and **7** versus commonly used photoredox catalysts.*

Compound	λ_{em} (nm)	Lifetime (ns)	Quantum Yield (%)[a]	$E_{1/2}$ M/M^- (V)	$E_{1/2}$ M^+/M (V)
146	632	84	9.1	-1.52	0.89
151	675	60	6.1	-1.51	0.94
$Ru(bpy)_3$	615	153	9.5	-1.71	0.91
$Ir(ppy)_2(dtbbpy)$	581	557[a]	27.1	-1.80	0.91

Measurements made in CH_3CN in air. Redox potentials measured in CH_3CN/TBA versus Ag/Ag^+ and reported versus Fc/Fc^+ a) degassed in acetonitrile b) literature values were converted from measurements vs SCE.[55]

Comparison of **146**·OTf and **151**·8OTf with commonly used ruthenium and iridium photoredox catalysts also highlights their similarity and the lack of photoquenching by complexation with Pd^{II}. However, whilst the oxidation potential remains almost identical, the reduction potential is significantly reduced with respect to $Ir(ppy)_2(dtbbpy)$ as a result of the structural differences between the ancillary ligands. The LUMO of most iridium complexes is situated primarily on the ancillary ligand whilst the HOMO resides on the metal centre.[56] The addition of the alkyne bridged imidazole groups to the ancillary ligand appears to significantly stabilise the LUMO, resulting in a reduced HOMO-LUMO gap and an easier ligand centred reduction process.

Despite this, the redox potentials remain largely unaffected by complexation to palladium and the formation of **151**·8OTf providing evidence that any electron withdrawal by the electropositive metal does not affect the LUMO situated on the ancillary ligand. However, the emission wavelength is strongly red shifted suggesting that ^{3}MLCT states are stabilised by complexation to palladium.

Whilst the formation of **151**·8OTf and complexation with palladium slightly alters the photophysical and electrochemical properties of the iridium centre, the supramolecular system still maintains the fundamental attributes required for effective photoredox catalysis.

3.4.4 Guest Binding

Encapsulation of neutral guest compounds within the interior of **151**·8OTf was deemed essential for any stereo- or regio-selective supramolecular catalysis to be achieved. As four-coordinate palladium was used as the structural metal in the cage synthesis, rather than six-coordinate zinc, ligand metal interactions could not be used to provide a driving force for the binding of substrates. Instead, it was envisaged that the hydrophobic effect could be used to drive the encapsulation of neutral organic guests within the hydrophobic interior of the **151**·8OTf. Consequently, a series of hydrophobic aromatic guests were screened by direct addition to a solution of **151**·8OTf in 1:1 D_2O:CD_3CN (1 mM) followed by monitoring any change in the ^{1}H NMR peak shifts (Figure 3.21 and 3.22). Evidence for binding was given by peak shifts for both **151**·8OTf and the guest compound with respect to the free components under identical conditions. Further evidence was obtained by specific peak movements, for instance, the peaks corresponding to the imidazole and the internal bipyridine were shielded relative to the empty cage due to the expected π-CH interactions.

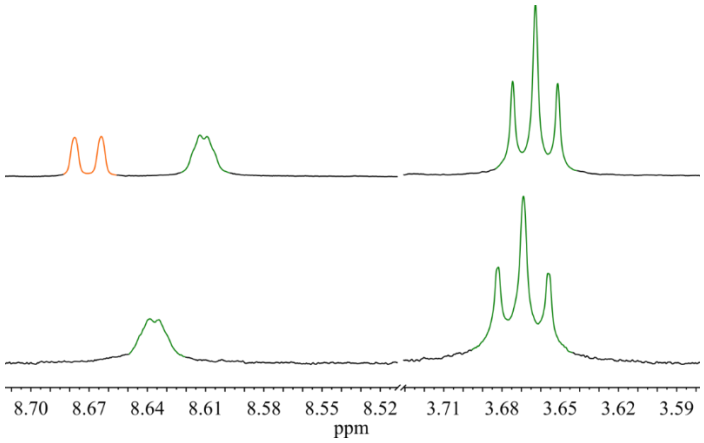

*Figure 3.21: Expanded view of ^{1}H NMR (400 MHz, 1:1 D_2O/CD_3CN, 300 K) spectra before (bottom) and after (top) the addition of phenanthrene (orange) to a solution of **151**·8OTf (green).*

For those guests that showed measurable peak shifts, ^{1}H NMR titrations were carried out to quantify the binding strength. In addition to the neutral guests, potassium trifluoronapthylborane (**G**^{30}) was also examined to investigate any increased association due to coulombic attraction between the negative charge and the positive cage (Figure 3.23). Despite the overall charge, **G**^{30} is water insoluble and can act as a hydrophobic guest with an additional coulombic interaction that is not cancelled out by efficient solvation. The

concentration of potassium trifluoronapthylborane could not be taken beyond 8 equivalents with respect to **151**·8OTf as precipitation of the trifluoronaphthyl borane salt of the cage occurred.

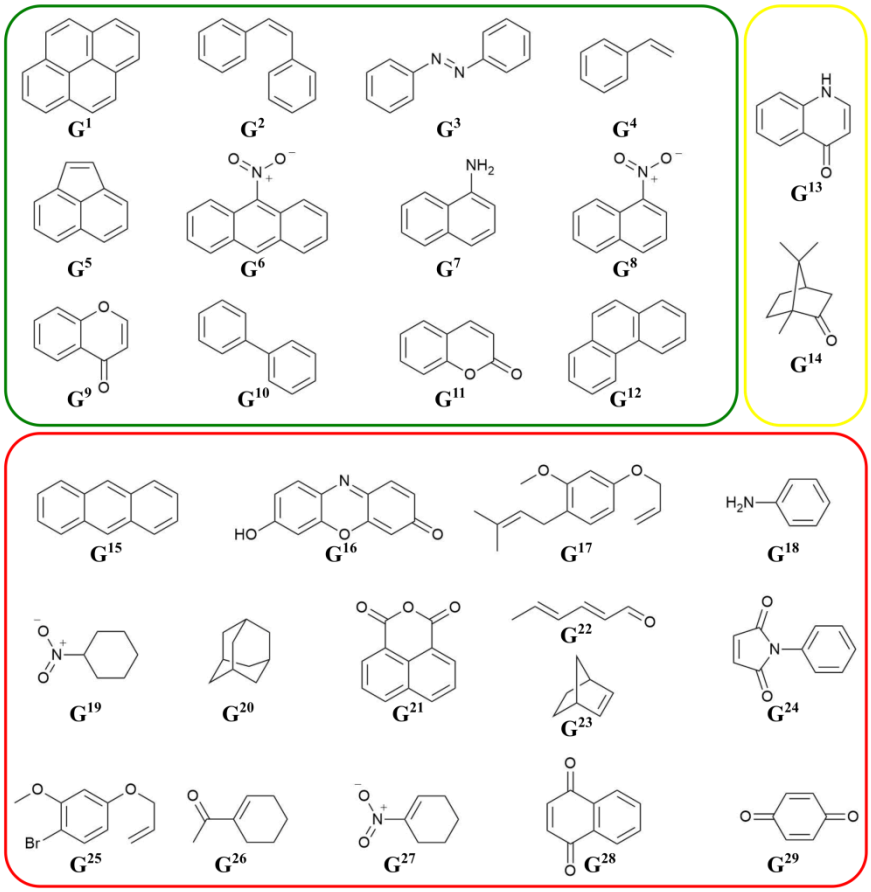

*Figure 3.22: A list of the neutral compounds screened for guest binding in **151**·8OTf. Guests either displayed obvious peak shifts (green), very small shifts (yellow) or no change (red) by ^{1}H NMR spectroscopy.*

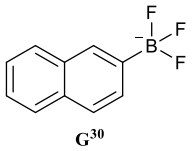

Figure 3.23: The structure of the anionic guest potassium trifluoro-2-napthalenylborane.

*Table 3.2: Calculated binding constants for a range of organic guests within **151**·8OTf.*

Compound	Name	Ka (M^{-1})	Error
G^{2}	*cis*-stilbene	40	±15
G^{12}	phenanthrene	257	±33
G^{30}	potassium trifluoro-2-napthalenylborane	429	±73

In summary, the photophysical properties of the self-assembled cage, **151**·8OTf, remain very similar to those observed for the mononuclear iridium complex, **146**·OTf, despite the potential quenching effects of complexation with palladium. The solubility of **151**·8OTf in a 1:1 mixture of H_2O/CH_3CN was utilised to drive encapsulation of neutral hydrophobic guests with binding constants of up to 257 M^{-1} reported. Guest encapsulation could be further strengthened by using hydrophobic anions to increase the host:guest interaction through coulombic attraction. As such, the complex-as-ligand design allows the rapid formation of photoredox active metallosupramolecular compounds that display promising guest binding properties and **151**·8OTf remains a good candidate for achieving combined supramolecular and photoredox catalysis.

3.5 Photoredox Catalysis

Having successfully prepared **151**·8OTf and confirmed the system stability and favourable photoredox properties, a series of photocatalytic processes were tested using **151**·8OTf as the photocatalyst in 1:1 D_2O/CH_3CN.

3.5.1 Isomerisation of Stilbene & Azobenzene

Heating stilbene to temperatures well in excess of 200 °C results in equilibration to a mixture of the *cis* and *trans* isomers with the *trans*-isomer heavily favoured.[57] As well as direct excitation,[58] *cis*-stilbene can be prepared from *trans*-stilbene through photoredox catalysis through formation of a radical cation intermediate.[59,60] Similar treatment of *trans*-stilbene with **151**·8OTf followed by irradiation with visible light resulted in isomerisation to 85 % *cis*-stilbene after 16 h (Scheme 3.3). However, further irradiation gave no additional increase in the proportion of *cis*-stilbene present. No isomerisation was observed without the presence of **151**·8OTf and direct comparison of the equilibrium position under the same solvent conditions was not possible due to the high temperatures required to allow thermal isomerisation.

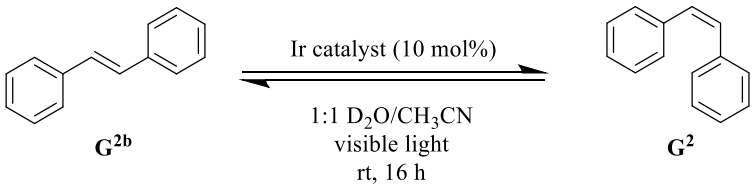

Scheme 3.3: Interconversion of trans/cis-*stilbene in the presence of* ***146****·OTf or* ***151****·8OTf under visible light.*

Interestingly, the oxidation potentials reported for *trans*-/*cis*-stilbene (1.09 V/1.20 V versus Fc/Fc^+) suggests that the reaction cannot proceed via a radical cation intermediate since the predicted oxidation potentials of the iridium excited states are not sufficient to allow single electron transfer (Table 3.3). Instead, the reaction must rely on direct energy transfer from **151**·8OTf to the substrate.

Table 3.3: Comparison of one-electron oxidation potentials for cis/trans-*stilbene as well as the mononuclear and supramolecular photocatalysts.*

Compound	$E_{1/2}$ M^{+}/M (V)	$E_{1/2}$ M^{*}/M^{-1} (V)
trans-stilbene	1.09[a]	-
cis-stilbene	1.20[a]	-
146·OTf	0.89	0.44[b]
151·8OTf	0.94	0.33[b]

Redox potentials recorded in CH_3CN/TBA versus Fc/Fc^{+}. a) converted from SCE to Fc/Fc^{+} [55] b) calculated from zero-zero excitation energy approximated based on emission wavelength.[4]

Similarly, azobenzene is well known to undergo *trans-cis* isomerisation upon irradiation with different wavelengths of light.[58] Irradiation with UV light (approx. 317 nm) leads to π-π* excitation that results in rearrangement from the *cis* to *trans* isomer, while irradiation with blue light (approx. 439 nm) gives n-π* excitation to give the opposite *trans* to *cis* rearrangement. Thus, under visible light in solution, azobenzene exists solely as the *trans*-isomer.

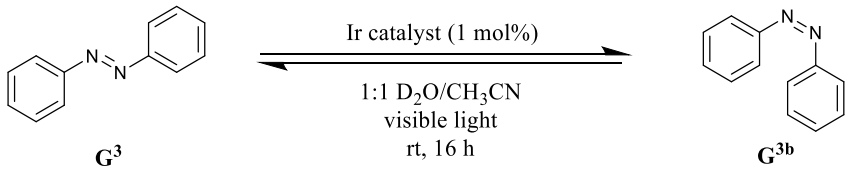

G³ **G^3b**

*Scheme 3.4: Interconversion of trans/cis-azobenzene in the presence of **1**·OTf or **7**·8OTf under visible light.*

The addition of **151**·OTf to a solution of *trans*-azobenzene in a 1:1 mixture of D_2O/CD_3CN led to partial conversion to *cis*-azobenzene upon irradiation with visible light for 16 h (Scheme 3.4 and Figure 3.24). The *trans* to *cis* ratio after 16 h irradiation was 3:1 but no further change was detected after additional irradiation over 72 h, suggesting that the system had reached a steady state equilibrium.

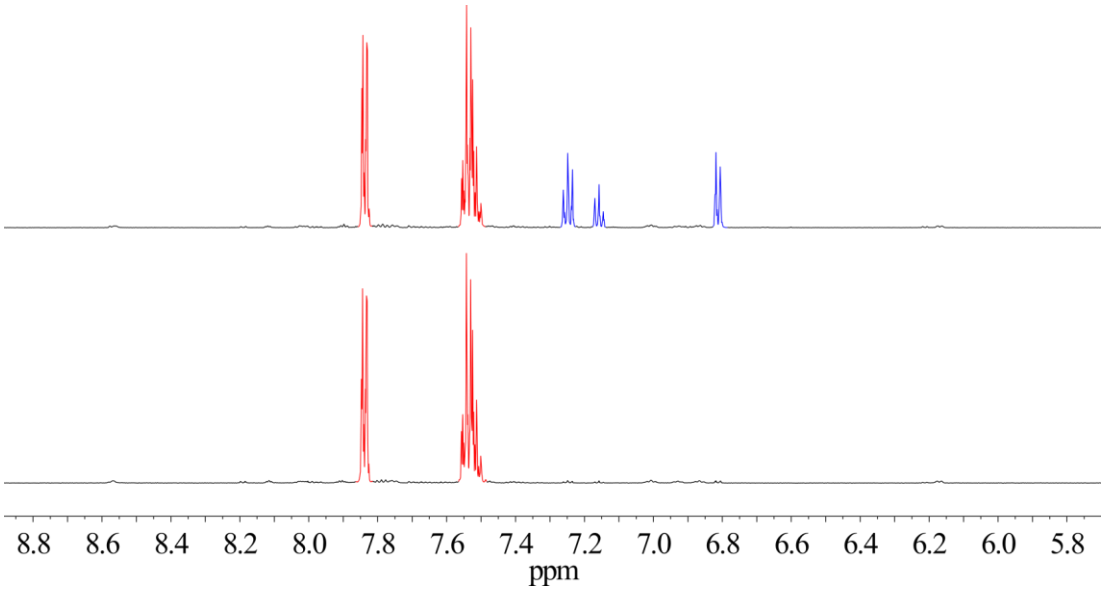

Figure 3.24: ^{1}H NMR (500 MHz, 1:1 D_2O/CD_3CN, 300 K) of trans-*azobenzene (red) and* cis-*azobenzene (blue) with **151**·8OTf before (bottom) and after (top) irradiation with visible light. Peaks corresponding to **151**·8OTf are not clearly visible due to the catalytic quantities required (1 mol%).*

Despite ^{1}H NMR evidence for host:guest interactions between **151**·8OTf and $\mathbf{G^2}$/$\mathbf{G^3}$, no difference in either the reaction rate or the equilibrium position was observed upon irradiation with **146**·OTf suggesting that either the bulk phase process was dominant and/or any guest binding was too weak to influence the conformational outcome of the isomerisation process.

3.5.2 Acenaphthylene

The dimerisation of acenaphthylene by irradiation with UV light can give either the *syn* or *anti* conformation. The preference for either *syn* or *anti* is highly dependent on the surrounding environment.[61] Fujita and co-workers demonstrated that inclusion of acenaphthylene within a Pd_6L_4 cage to form a 2:1 host:guest complex before irradiation with UV light resulted in a 100% conversion to the *syn* conformer (Scheme 3.5).[62,63] Formation of the extended *anti* conformation was physically impossible within the steric confinement of the cage cavity. However, this process still required the use of a high power mercury UV lamp in order for the dimerization to proceed. A similar process was also observed by Ramamurthy and co-workers using Eosin Y as a photosensitiser with either Fujita's Pd_6L_4 cage, a fully organic container compound or water-soluble dendrimers.[64–66]

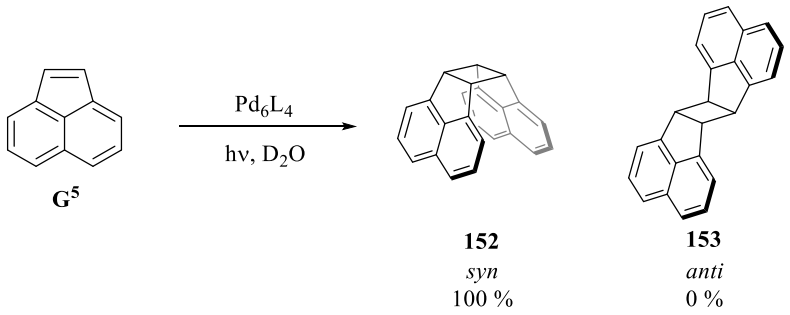

Scheme 3.5: Selective photocatalytic dimerisation of acenaphthylene within a Pd_6L_4 metallosupramolecular cage.[62,63]

146·OTf was found to efficiently catalyse the dimerization process in the presence of visible light (Scheme 3.6). Since a sacrificial quencher was not required, the reaction mechanism was thought to proceed via either the radical cation from reductive quenching of the iridium excited state or by the excitation of acenaphthylene through direct energy transfer from the photocatalyst. As expected, the solution phase process, without the presence of an internal cavity, gave a mixture of the *syn* and *anti*-conformations.

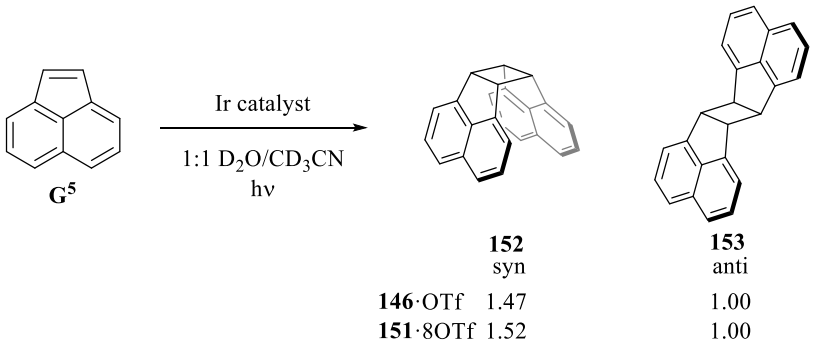

*Scheme 3.6: Visible-light photocatalytic dimerisation of acenaphthylene using **146**·OTf and **151**·8OTf and the relative ratios of the* syn*:*anti *dimer produced.*

Unfortunately, when the reaction was repeated with **151**·8OTf, no significant difference was observed in the product distribution or the rate of reaction. Simple modelling and examination of the binding constants for similar guests suggests that encapsulation follows a 1:1 binding model. Furthermore, if 2:1 binding could occur, the relatively low binding constants observed suggest that even with a stoichiometric catalyst loading, the percentage of guest encapsulated in a 2:1 ratio would be very low. Since no significant rate enhancement was observed, the bulk phase background reaction would dominate and significantly reduce any conformational specificity provided by the internal cavity. Despite the lack of

conformational selectivity, this process does provide evidence that the iridium complex can still function as an efficient visible-light photocatalyst while assembled into a supramolecular structure.

3.6 Summary & Conclusions

Only a handful of luminescent metallosupramolecular compounds have been reported previously that show a reasonable affinity for neutral organic molecules.[22,32,41,49,52] Using a complex-as-ligand based approach, a novel iridium functionalised Pd_2L_4 system was designed, synthesised and fully characterised by NMR and ESI-MS. Although unstable below approximately 10 μM, the **151**·8OTf forms a stable system that shows an affinity for a range of neutral and anionic hydrophobic compounds in a 1:1 mixture of H_2O/CH_3CN. More importantly, unlike many metallosupramolecular self-assembled structures, the beneficial photoredox properties of the constituent iridium complexes remain almost completely unaffected by complexation to palladium. As such, this system shows great promise as a potential supramolecular photoredox catalyst and represents a jump forward in the current state of the field. However, initial attempts at achieving regio- or stereo-selective photoredox catalysis were unsuccessful and no significant difference was observed between the selectively of **151**·8OTf and the corresponding mononuclear complex **146**·OTf. This was assumed to be due to the relatively low binding constants recorded and thus, further work was carried out in an attempt to modify the existing system to improve the overall guest binding properties.

3.7 Experimental

3.7.1 General Information

Unless stated otherwise, all reagents and solvents were purchased from Alfa Aesar, VWR or Sigma Aldrich and used without further purification. Column chromatography was carried out using Geduran Si60 (40-63 µm) as the stationary phase and TLC was performed on precoated Kieselgel 60 plates (0.20 mm thick, $60F_{254}$. Merck, Germany) and observed under UV light at 254 nm or 365 nm. All reactions were carried out under air, unless stated otherwise. *rac*-$(Ir(ppy)_2Cl)_2$,[10] Δ/Λ-$(Ir(ppy)_2Cl)_2$,[10] and $Pd(CH_3CN)_4 \cdot 2OTf$[67] were prepared according to literature procedures.

For general NMR and MS conditions, refer to Section 2.9.3.

Many of the compounds synthesised and characterised in this chapter contain OTf counter anions. Due to the strong C-F splitting and low concentrations, the OTf signal is often not observed in the ^{13}C NMR. Where sufficiently intense peaks are observed the signal is reported as 122.1 (q, J = 320.6 Hz), otherwise, evidence for the OTf counter anion is given solely by ^{19}F NMR (Figure 3.25).

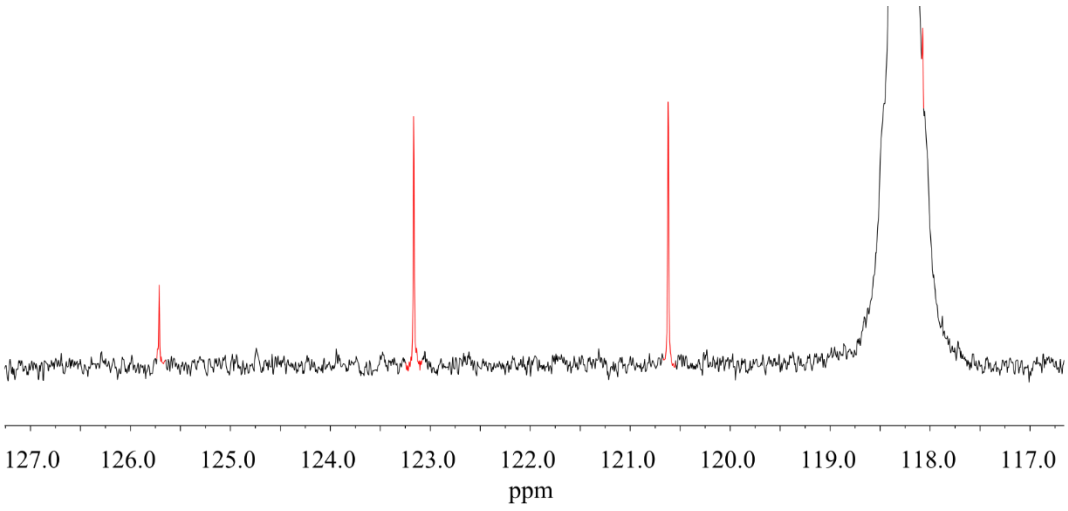

Figure 3.25: ^{13}C NMR (500MHz, CD_3CN, 300 K) of a saturated solution of KOTf showing C-F coupling.

All UV/Vis spectroscopy was carried out on either an Agilent Technologies, Cary 300 Series UV-Vis Spectrophotometer running Cary WinUV or a Perkin Elmer Lambda 45 UV-Vis

Spectrometer running Lambda 40. All emission spectroscopy was carried out on a Perkin Elmer LS 50 Luminescence Spectrometer running Lambda 40. The Frozen-glass emission experiments were carried out on a Perkin Elmer Lambda 55 Luminescence Spectrometer running FL Winlab. All emission lifetime measurements were carried out on an Edinburgh Analytical Instruments, TM300 Monochromator with a PicoQuant GmbH. 405 nm LASER. Circular dichroism was performed on a JASCO J-810 spectropolarimeter controlled using JASCO Spectra Manager software and data was collected over a wavelength range of 210-800 nm, at a scan speed of 100 nm/min, bandwidth of 1 nm and data pitch of 0.1 nm. Samples were measured at rt and at given concentrations using a fused silica cuvette with a 10 mm path length. Where required, cut-off filters (Andover Cooporation) were used. All data was analysed and plotted using Origin 2015 software. All measurements were made at room temperature (16-21 °C) at 100 μM in CH_3CN using a fused silica cuvette with a 10 mm path length, unless stated otherwise.

All electrochemistry was performed using an Autolab GPES 4.9. All of the samples were analysed in dry CH_3CN (500 μM for mononuclear complexes and 200 μM for cage compounds) using 50 mM tetraethylammonium hexafluorophosphate as the electrolyte. Measurements were performed using a platinum counter electrode, a glassy carbon working electrode and a Ag/Ag^+ quasi-reference electrode with ferrocene as an internal standard. All data was processed using Origin 2015.

3.7.1 Synthetic Procedures

149 - 2,2'-bi(4-ethynyl-1-methyl-imidazolyl)pyridine

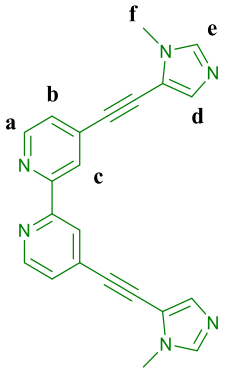

To 4,4'-dibromo-2,2'-pyridine (200.0 mg,), 5-ethynyl-1-methyl-(1H)-imidazole (202.8 mg, 3 eq., 194 μL), TBAF (602.9 mg, 3 eq.) and $PdCl_2(PPh_3)_2$ (26.8 mg, 6 mol%) in a dried schlenk flask was charged dry THF (15.0 mL). Following repeated cycles of vacuum degassing N_2 backfills, the solution was heated at reflux for 24 hours. The mixture was cooled and the solvent removed under reduced pressure. Water (30 mL) was charged and the product was extracted with CH_2Cl_2 (3 x 30 mL). The crude product was purified by silica column chromatography using 1% Et_3N, 1% methanol, 98% CH_2Cl_2. Residual TBA and Et_3N were removed by recrystallization from MeCN. The product was isolated as an off white powder (155.2 mg, yield = 67%). ^1H NMR (500 MHz, $CDCl_3$) δ 8.69 (dd, J = 5.0, 0.8 Hz, 2H, H_a), 8.51 (dd, J = 1.5, 0.8 Hz, 2H, H_c), 7.56 (s, 2H, H_e), 7.44 (d, J = 0.9 Hz, 2H, H_d), 7.40 (dd, J = 5.0, 1.6 Hz, 2H, H_b), 3.79 (s, 6H, H_f). ^{13}C NMR (126 MHz, $CDCl_3$) δ 155.79, 149.46, 139.18, 136.08, 132.00, 125.17, 122.74, 115.58, 94.52, 82.14, 32.43. *m/z* (HR-ESI): 365.15092 (predicted $[M+H]^+$ = 365.14850). mp = decomposes >250 °C.

146·OTf - [Ir(ppy)$_2$(emibipy)]OTf

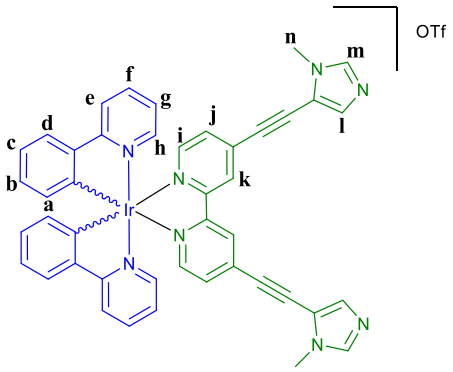

[(Ir(ppy)$_2$Cl)$_2$] (99.7 mg, 0.093 mmol) and **4** (67.7 mg, 0.186 mmol) were partially dissolved in ethylene glycol (20.0 mL). The solution was degassed under high-vacuum for 20 mins and backfilled with N_2 before being heated at 150 °C for 18 h. The solution was then cooled and diluted with H_2O (100 mL) before being washed with Et_2O (2 x 50 mL). KOTf (105.0 mg, 0.558 mmol) was charged and the resultant precipitate was filtered through celite. The orange solid was washed with copious amounts of H_2O and then washed off the celite with CH_2Cl_2. The solvent was removed under reduced pressure to yield the crude product. If necessary, purification could be achieved by silica column chromatography (gradient CH_2Cl_2 to 10% CH_3OH in CH_2Cl_2). The product was isolated as a bright orange/red solid (138.1 mg, yield = 73%). ^{1}H NMR (500 MHz, CD_3CN) δ 8.62 (d, *J* = 1.1 Hz, 2H, H_k), 8.07 (d, *J* = 8.0 Hz, 2H, H_e), 7.94 (d, *J* = 5.7 Hz, 2H, H_i), 7.90 – 7.84 (m, 2H, H_f), 7.81 (dd, *J* = 7.8, 1.0 Hz, 2H, H_d), 7.67 (ddd, *J* = 5.9, 1.4, 0.7 Hz, 2H, H_h), 7.64 (s, 2H, H_m), 7.53 (dd, *J* = 5.7, 1.6 Hz, 2H, H_j), 7.45 (d, *J* = 0.8 Hz, 2H, H_l), 7.09 – 7.03 (m, 2H, $H_{c,g}$), 6.93 (td, *J* = 7.5, 1.3 Hz, 2H, H_b), 6.27 (dd, *J* = 7.6, 0.9 Hz, 2H, H_a), 3.77 (s, *J* = 4.8 Hz, 6H, H_n). ^{13}C NMR (126 MHz, CD_3CN) δ 168.30, 156.63, 151.51, 150.87, 150.34, 145.01, 141.72, 139.62, 137.98, 134.61, 132.46, 131.39, 129.94, 126.76, 125.88, 124.53, 123.67, 120.90, 115.32, 93.92, 87.72, 32.82. ^{19}F NMR (471 MHz, CD_3CN) δ -79.31 (s). DOSY NMR (500 MHz, CD_3CN) –logD = 8.98 Hydrodynamic radius = 5.6 Å. *m/z* (HR-ESI): 865.23500 (predicted $[M]^+$ = 865.23739) 1015.19350 (predicted $[M+H]^{2+}$OTf = 1015.19724).

150·8OTf - $[Zn_2(Ir(ppy)_2emibipy)_4]8OTf$

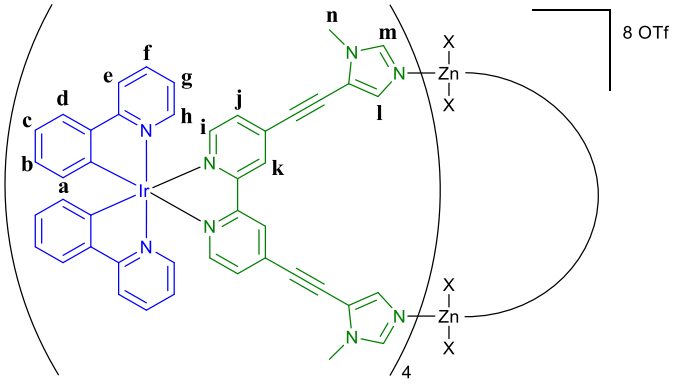

146·OTf (14.2 mg, 0.014 mmol) was dissolved in CH_3CN (5 mL). $Zn(OTf)_2$ (2.6 mg, 0.007 mmol) was charged and washed in with CH_3CN (1 mL). The solution was stirred at room temperature for 8 h and then concentrated under reduced pressure. The product was precipitated with Et_2O, filtered and washed with Et_2O to yield a bright orange solid (14.9 mg, 89%). ^{1}H NMR (500 MHz, CD_3CN) δ 8.75 (s, 24H, H_k), 8.07 (d, J = 8.6 Hz, 24H, H_e), 7.99 (s, 24H, H_m), 7.98 (d, J = 5.9 Hz, 24H, H_i), 7.90 – 7.82 (m, 24H, H_f), 7.81 (dd, J = 7.9, 0.9 Hz, 24H, H_d), 7.65 (d, J = 5.9 Hz, 24H, H_h), 7.59 – 7.53 (m, 48H, $H_{j,l}$), 7.10 – 6.99 (m, 48H, $H_{c,g}$), 6.97 – 6.88 (m, 24H, H_b), 6.26 (dd, J = 7.6, 1.2 Hz, 24H, H_a), 3.87 (s, 36H, H_n). ^{13}C NMR (126 MHz, CD_3CN) δ 168.25, 156.67, 151.69, 150.70, 150.35, 144.96, 142.23, 139.64, 135.88, 133.92, 132.42, 131.41, 130.09, 127.32, 125.88, 124.52, 123.72, 120.91, 116.83, 94.37, 85.36, 33.75. ^{19}F NMR (376 MHz, CD_3CN) δ -79.12. DOSY (400 MHz, CD_3CN) -log(m^2/s) = 9.27, hydrodynamic radius = 11.0 Å.

151·8OTf - [Pd$_2$(Ir(ppy)$_2$emibipy)$_4$]8OTf

General Procedure:

146·OTf (39.2 mg, 0.039 mmol) was dissolved in CH_3CN (10 mL) and Pd$(CH_3CN)_4$·2OTf (11.0 mg, 0.019 mmol) was charged as a solution in CH_3CN (0.2 mL). The mixture was stirred at room temperature for 16 hours. The solvent was removed under reduced pressure to give the product as a red solid (46.9 mg, yield = 100%).

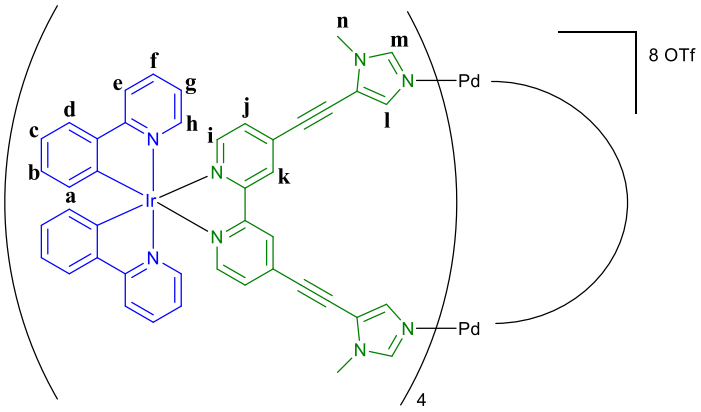

***rac*-[Pd$_2$(Ir(ppy)$_2$emibipy)$_4$]8OTf**

^{1}H NMR (500 MHz, CD_3CN)) δ 8.77 – 8.73 (m, 8H, H_k), 8.19 – 8.14 (m, 8H, H_m), 8.09 – 8.03 (m, 8H, H_e), 7.98 – 7.93 (m, 8H, H_i), 7.88 – 7.82 (m, 8H, H_f), 7.82 – 7.79 (m, 8H, H_d), 7.79 – 7.75 (m, 8H, H_l), 7.62 – 7.59 (m, 8H, H_h), 7.56 – 7.52 (m, 8H, H_j), 7.09 – 7.03 (m, 8H, H_c), 7.03 – 6.97 (m, 8H, H_g), 6.96 – 6.90 (m, 8H, H_b), 6.27 – 6.21 (m, 8H, H_a), 3.78 – 3.71 (m, 24H, H_n). *all peaks split by mixture of diastereomers so coupling constants not reported, see enantiopure. ^{13}C NMR (126 MHz, CD_3CN) δ 167.33, 155.52, 150.86, 149.54, 149.36, 143.97, 141.22, 138.70, 134.56, 132.46, 131.45, 130.49, 128.79, 126.76, 123.52, 122.83, 122.47, 120.00, 116.70, 93.98, 82.67, 33.51. ^{19}F NMR (471 MHz, CD_3CN) δ -78.96. DOSY NMR (500 MHz, CD_3CN) –logD = 9.28 Hydrodynamic radius = 11.3 Å.

Δ/Λ-[Pd$_2$(Ir(ppy)$_2$emibipy)$_4$]8OTf

^{1}H NMR (600 MHz, CD_3CN) δ 8.74 (d, J = 1.8 Hz, 8H, H_k), 8.17 (d, J = 1.3 Hz, 8H, H_m), 8.07 (d, J = 8.4 Hz, 8H, H_e), 7.96 (d, J = 5.9 Hz, 8H, H_i), 7.85 (td, J = 7.9, 1.5 Hz, 8H, H_f), 7.80 (dd, J = 7.9, 1.4 Hz, 8H, H_d), 7.76 (d, J = 1.3 Hz, 8H, H_l), 7.61 (d, J = 5.7 Hz, 8H, H_h), 7.54 (dd, J = 5.8, 1.6 Hz, 8H, H_j), 7.05 (td, J = 7.6, 1.2 Hz, 8H, H_c), 7.00 (ddd, J = 7.2, 5.8, 1.5 Hz, 8H, H_g), 6.92 (td, J = 7.4, 1.3 Hz, 8H, H_b), 6.24 (dd, J = 7.6, 1.2 Hz, 8H, H_a), 3.74 (s,

24H, H_n). ^{13}C NMR (126 MHz, CD_3CN) δ 168.26, 156.48, 151.77, 150.47, 150.28, 144.90, 142.12, 139.63, 135.52, 133.42, 132.38, 131.42, 129.71, 127.62, 125.89, 124.44, 123.76, 122.09 (q, *J* = 320.6 Hz), 120.93, 117.61, 94.91, 83.61, 34.42. ^{19}F NMR (471 MHz, CD_3CN) δ -79.01. DOSY NMR (500 MHz, CD_3CN) –logD = 9.29 Hydrodynamic radius = 11.5 Å.

3.7.3 Mass Spectrometry of Cage Compounds

151·8OTf - $[Pd_2(Ir(ppy)_2emibipy)_4]8OTf$

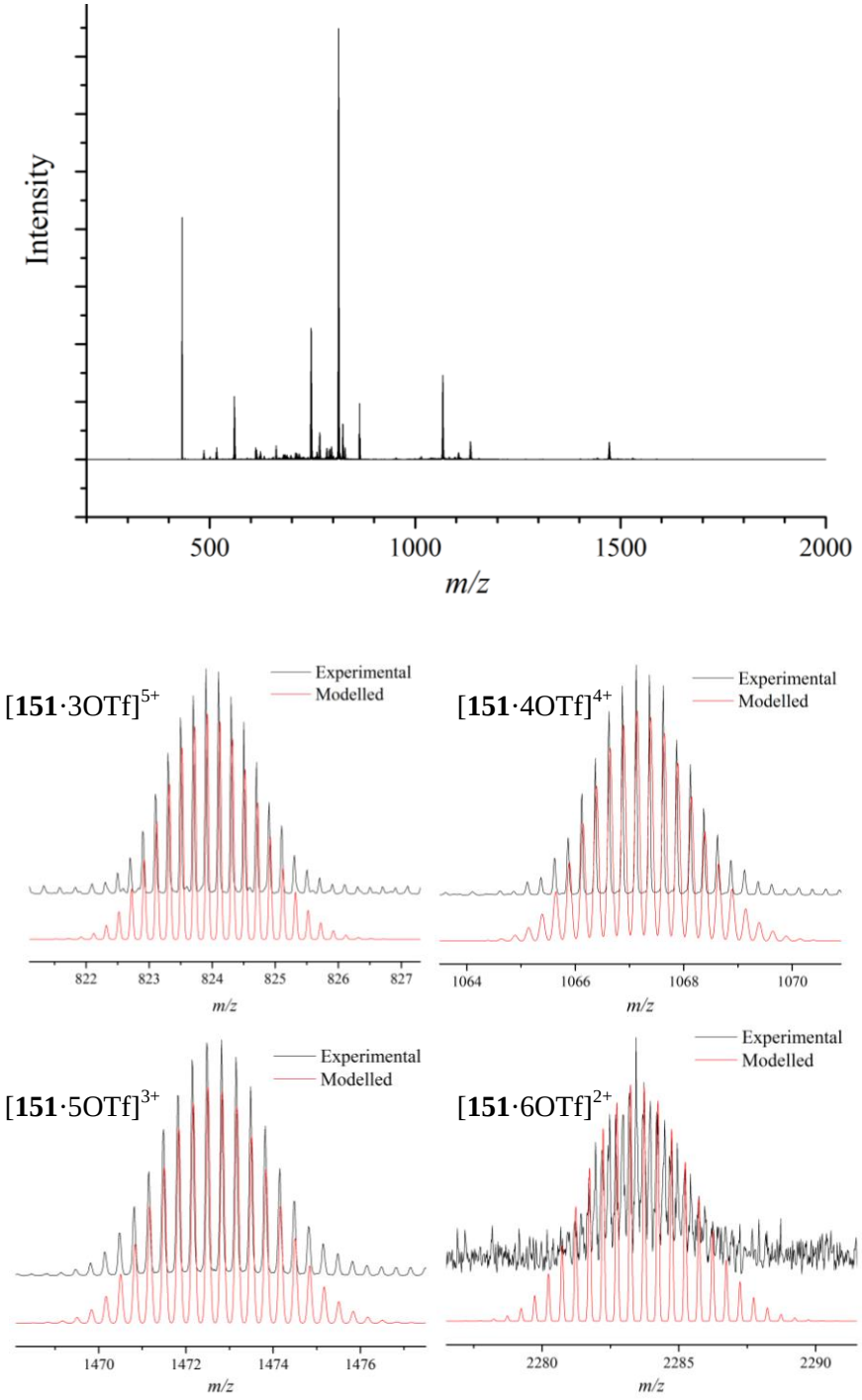

*Figure 3.26: Mass spectrum of **151**·8OTf. The peaks found by experiment (black) are shown in comparison with their modelled isotopic distributions (red).*

3.7.4 Stability of 151·8OTf

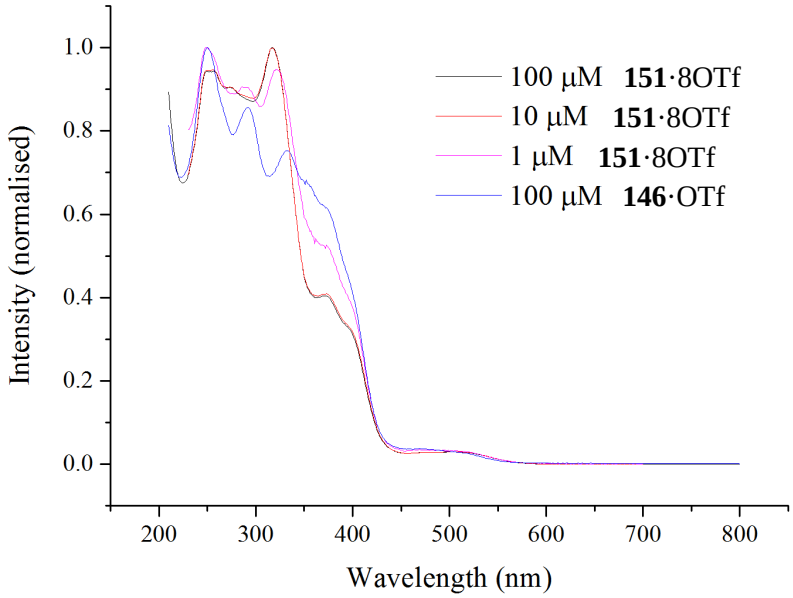

*Figure 3.27: Normalised absorption spectra for **151**·8OTf in CH_3CN at increasing dilutions. At concentrations < 1 μM, the cage has almost completely dissociated to give a spectrum that resembles the mononuclear complex.*

3.7.5 Absorption and Emission of 146·OTf and 151·8OTf

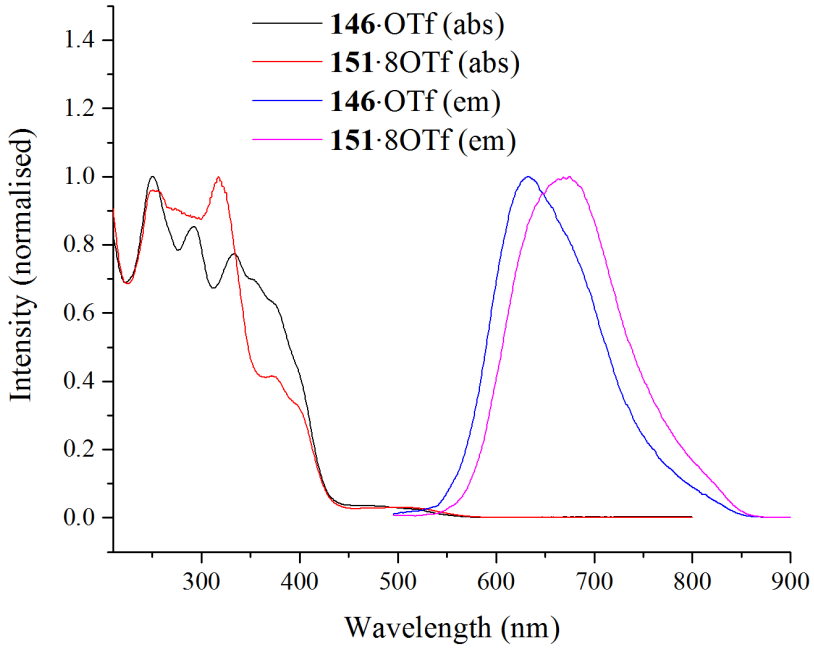

*Figure 3.28: Normalised plot of absorbance and emission (ex@377 nm) for **146**·OTf and **151**·8OTf in CH_3CN. Slight changes are observed in the absorption bands upon binding to palladium and the emission wavelength is red shifted.*

3.7.6 Quantum Yield Determination

Quantum yields were determined in CH_3CN using $Ru(bpy)_3Cl_2$ as a commercial standard. Absorption and emission data were obtained for each sample at the isobestic point with the standard and the relative emission intensities calculated. The quantum yield was recorded both in air and after degassing via argon purging.

*Table 3.4: Quantum yield values in CH_3CN for **146**·OTf and **151**·8OTf.*

Compound	Solvent	Atmosphere	Quantum Yield (%)
$Ru(bpy)_3Cl_2$	CH_3CN	air	1.8
		argon	9.5
146·OTf	CH_3CN	air	4.2
		argon	9.1
151·8OTf	CH_3CN	air	3.1
		argon	6.1

3.7.7 Circular Dichroism of Δ/Λ 146·OTf and 151·8OTf

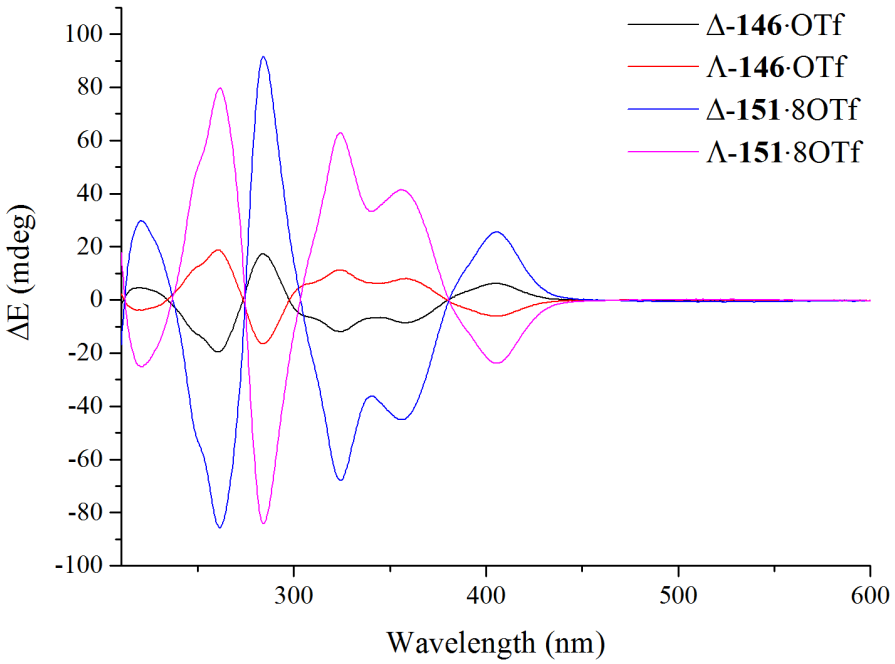

*Figure 3.29: Circular dichroism plot for isolated enantiopure **146**·OTf and **151**·8OTf in CH_3CN. Measurements taken at equal molarities and thus **151**·8OTf contains four times the concentration of photoactive iridium centres.*

3.7.8 Luminescent Lifetimes of 146·OTf and 151·8OTf

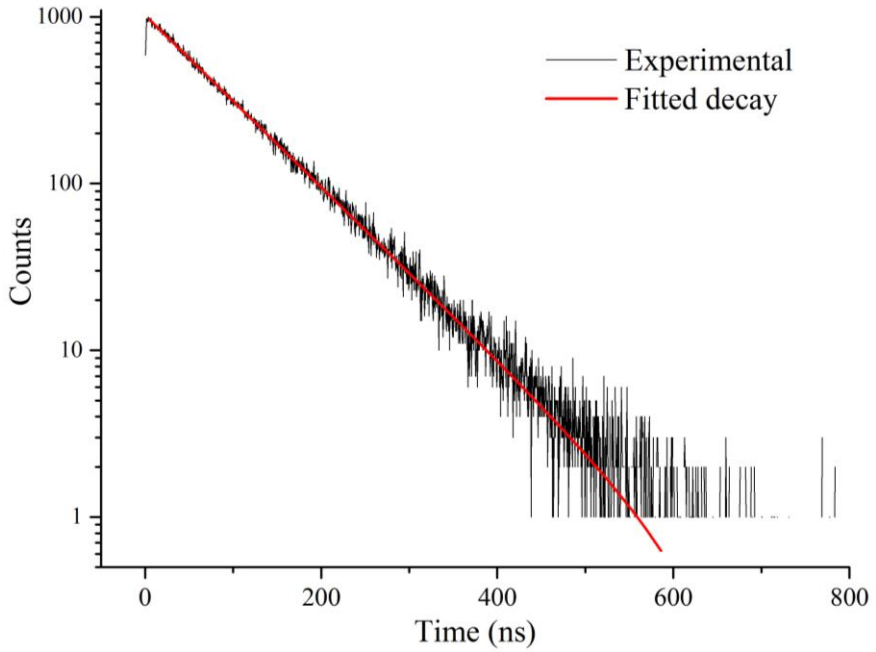

*Figure 3.30: Lifetime of **146**·OTf in acetonitrile showing experimental data (black) and fitted exponential decay function (red). Calculated lifetime = 84.44 ns.*

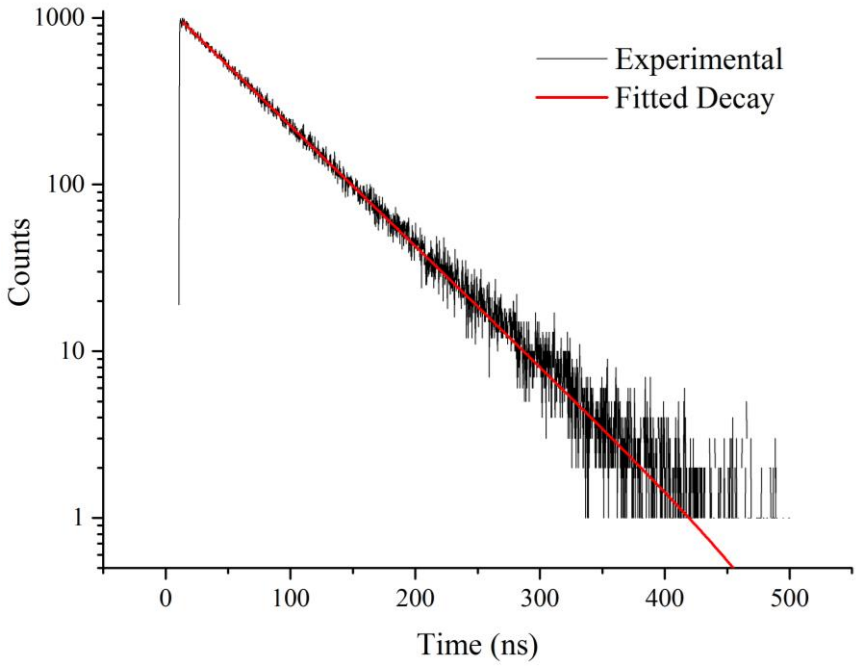

*Figure 3.31: Lifetime of **151**·8OTf in acetonitrile showing experimental data (black) and fitted exponential decay function (red). Calculated lifetime = 60.23 ns.*

3.7.9 Electrochemistry of 146·OTf

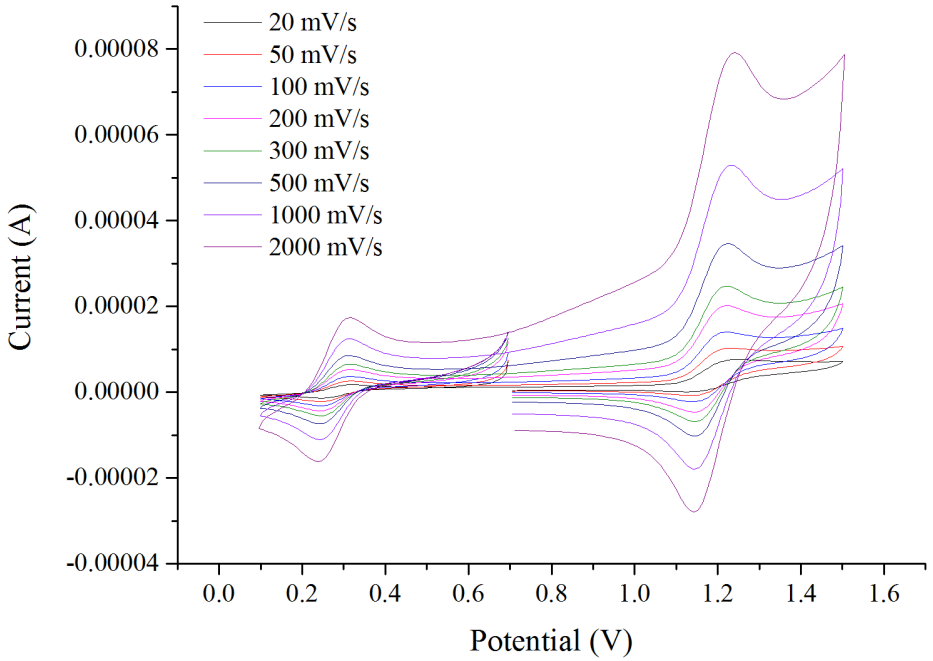

*Figure 3.32: Oxidation of **146**·OTf in CH_3CN versus Ag/Ag^+ with ferrocene as an internal standard.*

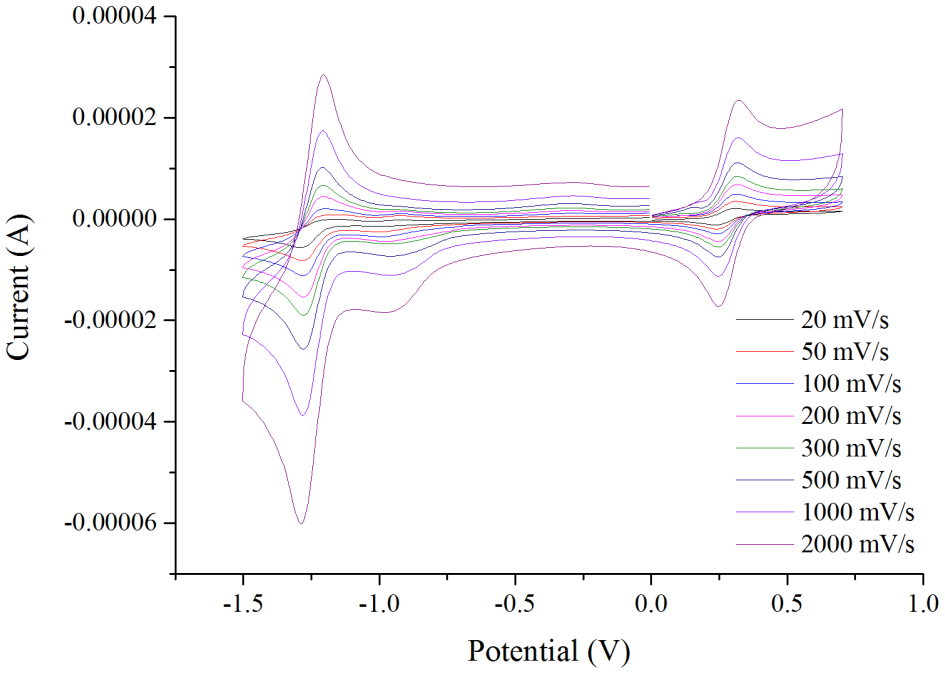

*Figure 3.33: Reduction of **146**·OTf in CH_3CN versus Ag/Ag^+ with ferrocene as an internal standard.*

3.7.10 Electrochemistry of 151·8OTf

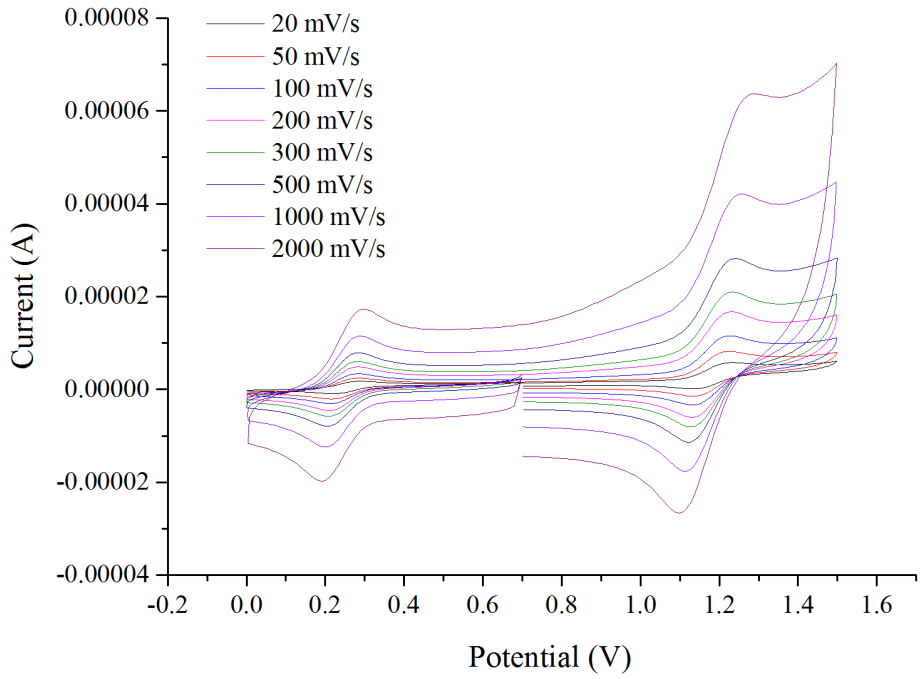

*Figure 3.34: Oxidation of **151**·8OTf in CH_3CN versus Ag/Ag^+ with ferrocene as an internal standard.*

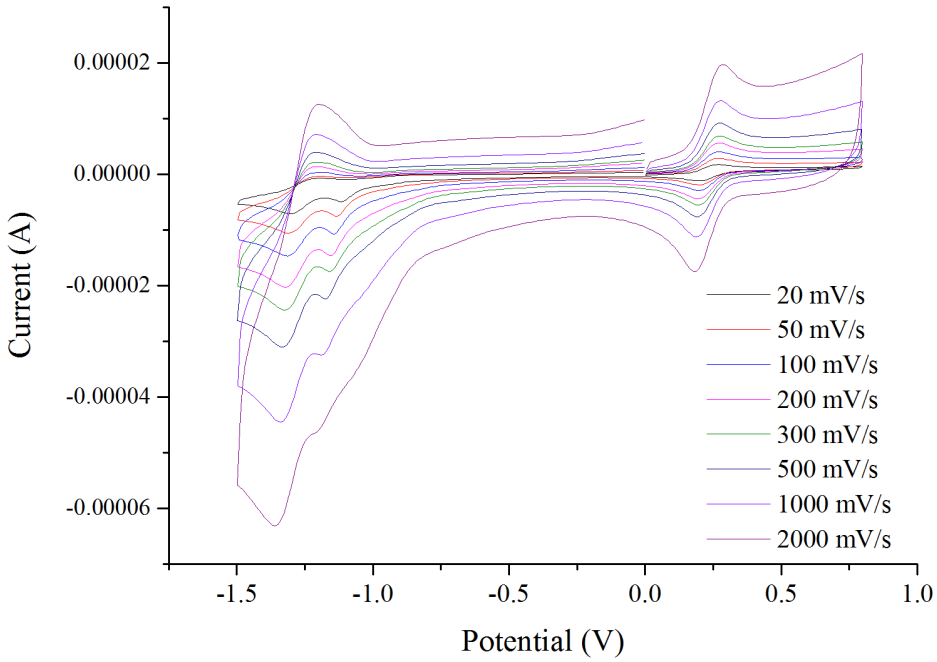

*Figure 3.35: Reduction of **151**·8OTf in CH_3CN versus Ag/Ag^+ with ferrocene as an internal standard.*

3.7.11 Crystal Structure of 146·OTf

All crystal data collection and analysis was carried out by Dr. Gary S. Nicol, The University of Edinburgh.

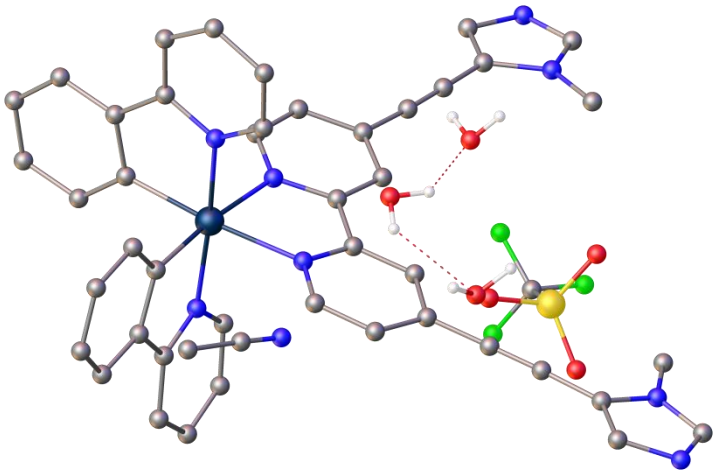

*Figure 3.36: The crystal structure of **146**·OTf.*

Single dark red block-shaped crystals of **146**·OTf were recrystallised from a 1:1 mixture of CH_3CN and H_2O by slow evaporation. A dark red block-shaped crystal with dimensions 0.14×0.12×0.05 was mounted on a MITIGEN holder in Paratone oil. Data were collected using a Bruker SMART APEXII diffractometer diffractometer equipped with an Oxford Cryosystems Cryostream 700+ low-temperature apparatus operating at T = 150.0 K.

Data were measured using ϕ and ω scans of n/a (d, scan_width)$^{\circ}$ per frame for n/a (d, scan_rate) s using MoK_α radiation (sealed tube, 50 kV, 30 mA). The total number of runs and images was based on the strategy calculation from the program Bruker APEX2. The actually achieved resolution was Θ = 26.404.

Cell parameters were retrieved using the **SAINT** (Bruker, V8.34A, 2013) software and refined using **SAINT** (Bruker, V8.34A, 2013) on 9220 reflections, 10 of the observed reflections. Data reduction was performed using the **SAINT** (Bruker, V8.34A, 2013) software which corrects for Lorentz polarisation. The final completeness is 100.00 out to 26.404 in Θ. The absorption coefficient (μ) of this material is 3.043 and the minimum and maximum transmissions are 0.7202 and 0.8855.[68]

The structure was solved in the space group C2/c (# 15) by Direct Methods using the **ShelXT**[69] structure solution program and refined by Least Squares using version of **ShelXL**.[70] All non-hydrogen atoms were refined anisotropically. Hydrogen atom positions were calculated geometrically and refined using the riding model. Water H atoms were identified from a difference Fourier map but then refined with fixed, or restrained, co-ordinates. In particular, H atoms bonded to O6 required a constraint on the co-ordinates. One H atom comes into close proximity with its symmetry-equivalent, though there is no other obvious residual peak corresponding to a missing H atom. Displacement ellipsoid restraints were used on the acetonitrile molecule. The largest residual peak is 3.3 electrons high located 0.81 A from Ir1. A semi-empirical absorption correction was applied.

$C_{47}H_{41}F_3IrN_9O_6S$, M_r = 1109.15, monoclinic, C2/c (No. 15), a = 33.9184(6) Å, b = 10.3853(2) Å, c = 28.2591(5) Å, β = 113.5090(10)°, α = γ = 90°, V = 9128.1(3) Å^3, T = 150.0 K, Z = 8, Z' = 1, μ(MoK$_\alpha$) = 3.043, 95017 reflections measured, 9354 unique (R_{int} = 0.0598) which were used in all calculations. The final wR_2 was 0.1027 (all data) and R_1 was 0.0381 (I > 2(I)).

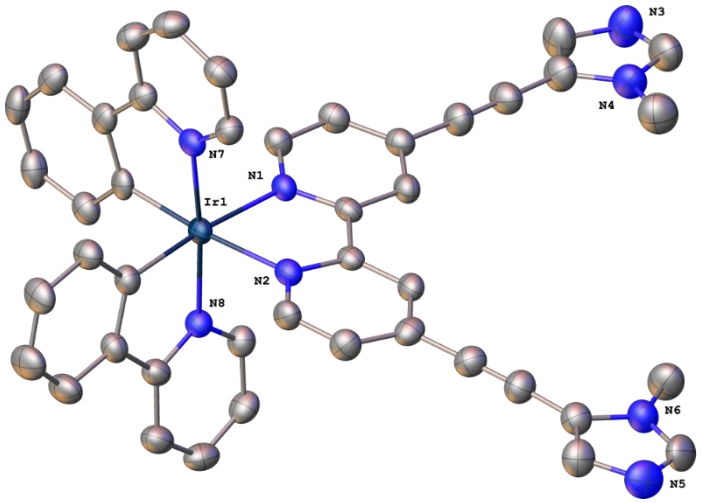

*Figure 3.37: The structure of **146**·OTf. Displacement ellipsoids are at the 50pc probability level. Solvent, counter anions and hydrogen atoms are omitted for clarity.*

3.7.12 Guest Binding Experiments

For each titration, a solution of host with a guest compound was titrated into a solution of host, maintaining a constant concentration of host compound throughout. For each observable peak shift of **151**·8OTf in the ^{1}H NMR spectra, the peak position was plotted against the concentration of guest. A global non-linear curve fitting function was then applied to the combined plots using the 1:1 binding model given by:[71]

$$y = y_0 + \Delta y\left(\frac{\left(1 + K_a(P + x)\right) - \sqrt{\left(1 + K_a(P + x)\right)^2 - 4K_aK_aPx}}{2K_aP}\right)$$

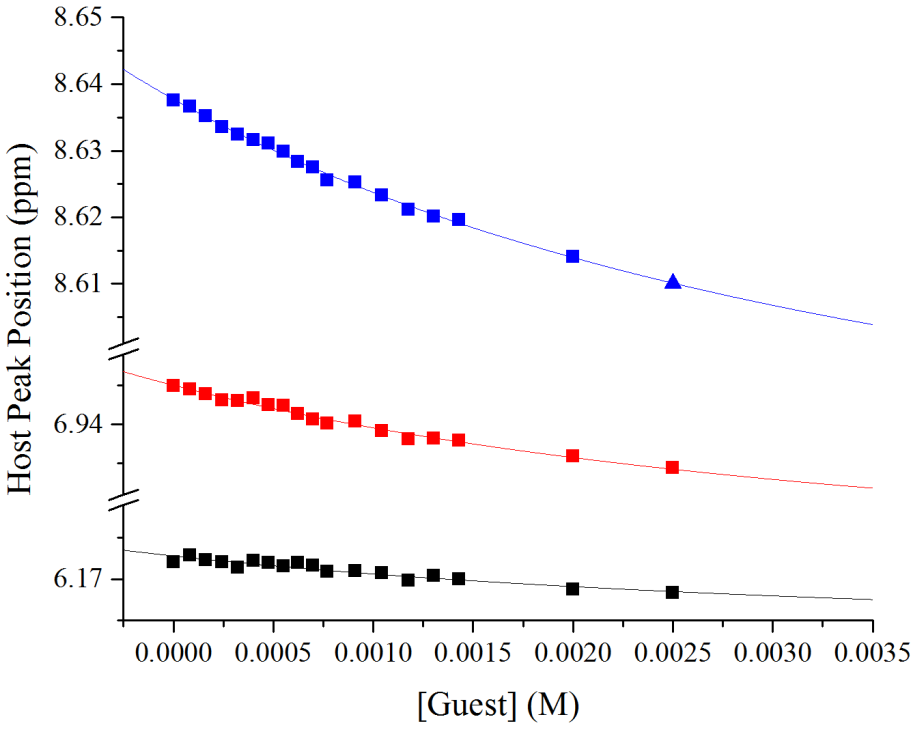

*Figure 3.38: Example data from titration of phenanthrene (**G**^{12}) with **151**·8OTf in a 1:1 mixture of D_2O/CD_3CN.*

For further discussion of ^{1}H NMR titration methods and approximation of associated experimental errors, please refer to Chapter 5.

3.7.13 Isomerisation of Stilbene and Azobenzene

Stilbene or azobenzene (0.5 mmol) were charged to a solution of **146**·OTf or **151**·8OTf (1 mL, 0.5 mM) in 1:1 D_2O/CD_3CN. The solution was irradiated with visible-light using a standard household 40 W fluorescent bulb at room temperature overnight. The reaction progress was monitored by ^1H NMR.

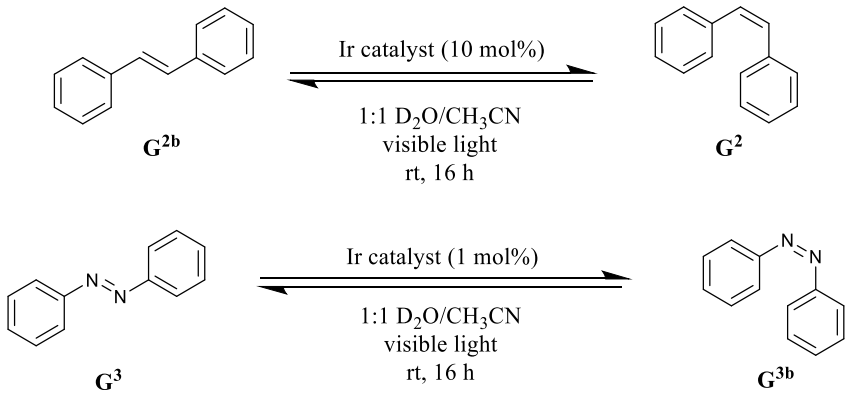

*Scheme 3.7: Visible-light photocatalytic isomerisation of stilbene and azobenzene using **146**·OTf and **151**·8OTf.*

3.7.14 Dimerisation of Acenaphthylene

Acenaphthylene (7.5 mg, 0.5 mmol) was charged to a solution of **146**·OTf or **151**·8OTf (1 mL, 0.5 mM) in 1:1 D_2O/CD_3CN. The solution was irradiated with visible-light using a standard household 40 W fluorescent bulb at room temperature overnight. The CD_3CN was removed under vacuum and the product extracted with CH_2Cl_2 and passed through a silica plug to remove the catalyst. The solvent was removed under vacuum and re-dissolved in $CDCl_3$ for NMR analysis.

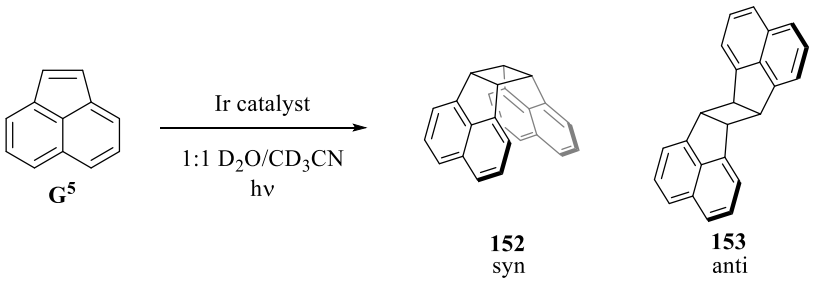

*Scheme 3.8: Visible-light photocatalytic dimerisation of acenaphthylene using **146**·OTf and **151**·8OTf and the relative ratios of the syn:anti dimer produced.*

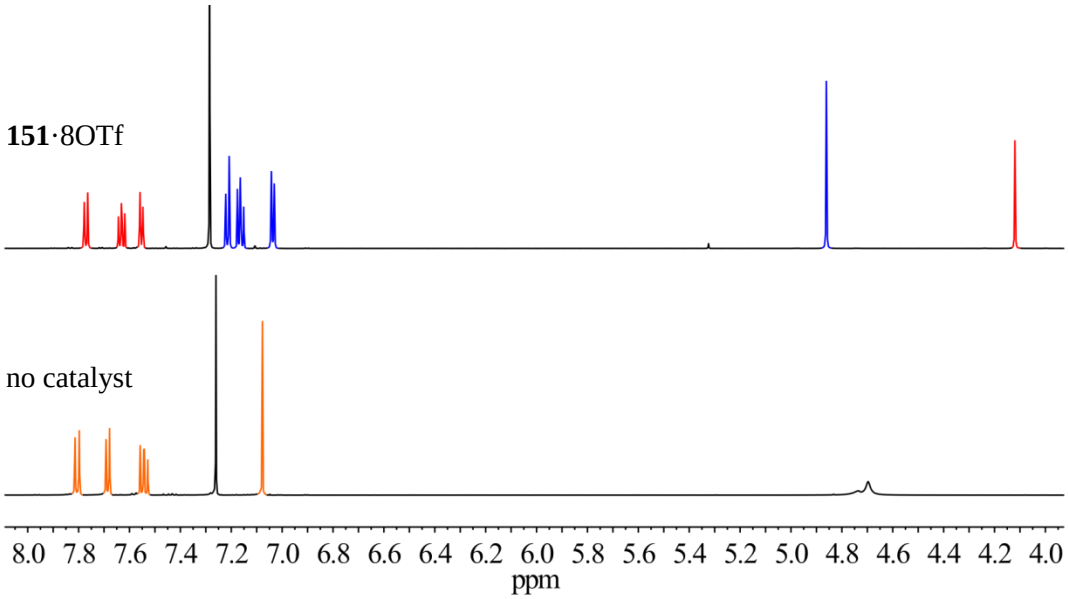

*Figure 3.39: ^1H NMR (500 MHz, $CDCl_3$, 300 K) of extracted product from the photodimerisation of acenaphthylene under visible light using no catalyst (bottom) or **151**·8OTf (top). The reaction produces both the syn (blue) and anti (red) confirmations whilst starting material (orange) remains unchanged without the presence of a photocatalyst.*

3.8 References

1 D. M. Schultz and T. P. Yoon, *Science*, 2014, **343**, 1239176.

2 T. P. Yoon, M. a Ischay and J. Du, *Nat. Chem.*, 2010, **2**, 527–532.

3 J. Xuan and W. Xiao, *Angew. Chem. Int. Ed.*, 2012, **51**, 6828–6838.

4 J. W. Tucker and C. R. J. Stephenson, *J. Org. Chem.*, 2012, **77**, 1617–1622.

5 D. Ravelli, D. Dondi, M. Fagnoni and A. Albini, *Chem. Soc. Rev.*, 2009, **38**, 1999–2011.

6 C. K. Prier, D. A. Rankic and D. W. C. MacMillan, *Chem. Rev.*, 2013.

7 J. M. R. Narayanam and C. R. J. Stephenson, *Chem. Soc. Rev.*, 2011, **40**, 102–113.

8 T. Koike and M. Akita, *Inorg. Chem. Front.*, 2014, **1**, 562–576.

9 M. Fagnoni, D. Dondi, D. Ravelli and A. Albini, *Chem. Rev.*, 2007, **107**, 2725–2756.

10 O. Chepelin, J. Ujma, X. Wu, A. M. Z. Slawin, M. B. Pitak, S. J. Coles, J. Michel, A. C. Jones, P. E. Barran and P. J. Lusby, *J. Am. Chem. Soc.*, 2012, **134**, 19334–19337.

11 M. Ferrer, D. Gómez-Bautista, A. Gutiérrez, J. R. Miranda, G. Orduña-Marco, L. A. Oro, J. J. Pérez-Torrente, O. Rossell, P. García-Orduña and F. J. Lahoz, *Inorg. Chem.*, 2014, **53**, 1699–1711.

12 S. Hiraoka, Y. Sakata and M. Shionoya, *J. Am. Chem. Soc.*, 2008, **130**, 10058–10059.

13 H. Li, Y. F. Han, Y. J. Lin, Z. W. Guo and G. X. Jin, *J. Am. Chem. Soc.*, 2014, **136**, 2982–2985.

14 A. Mayr and J. Guo, *Inorg. Chem.*, 1999, **38**, 921–928.

15 A. J. Metherell and M. D. Ward, *RSC Adv.*, 2016, **6**, 10750–10762.

16 A. J. Metherell and M. D. Ward, *Chem. Commun.*, 2014, **50**, 6330–2.

17 W. J. Ramsay, T. K. Ronson, J. K. Clegg and J. R. Nitschke, *Angew. Chemie - Int. Ed.*, 2013, **52**, 13439–13443.

18 Y. Sakata, S. Hiraoka and M. Shionoya, *Chem. - A Eur. J.*, 2010, **16**, 3318–3325.

19 M. Schmittel, V. Kalsani and J. W. Bats, *Inorg. Chem.*, 2005, **44**, 4115–4117.

20 M. Schmittel and K. Mahata, *Inorg. Chem.*, 2009, **48**, 822–824.

21 M. Schmittel and K. Mahata, *Chem. Commun.*, 2008, 2550–2552.

22 P. de Wolf, S. L. Heath and J. a. Thomas, *Chem. Commun.*, 2002, **44**, 2540–2541.

23 P. De Wolf, P. Waywell, M. Hanson, S. L. Heath, A. J. H. M. Meijer, S. J. Teat and J. A. Thomas, *Chem. - A Eur. J.*, 2006, **12**, 2188–2195.

24 R. V Slone, D. I. Yoon, R. M. Calhoun and J. T. Hupp, *J. Am. Chem. Soc.*, 1995, **117**, 11813–11814.

25 S. S. Sun and A. J. Lees, *Inorg. Chem.*, 2001, **40**, 3154–3160.

26 S. Sun, A. S. Silva, I. M. Brinn and A. J. Lees, *Inorg Chem*, 2000, **39**, 1344–1345.

27 Y. Liang, Y. Xie and J. Li, *J. Org. Chem.*, 2006, **71**, 379–381.

28 D. Tordera, M. Delgado, E. Ortí, H. J. Bolink, J. Frey, M. K. Nazeeruddin and E. Baranoff, *Chem. Mater.*, 2012, **24**, 1896–1903.

29 D. L. Davies, F. Lelj, M. P. Lowe, K. S. Ryder, K. Singh and S. Singh, *Dalton Trans.*, 2014, **43**, 4026–4039.

30 E. Orselli, G. S. Kottas, A. E. Konradsson, P. Coppo, R. Fro, L. De Cola, A. Van Dijken, M. Bu, H. Bo, P. Institut, N. Centech, W. Centre and B. U. V, *Inorg. Chem.*, 2007, **46**, 1441–1448.

31 Y. J. Yuan, Z. T. Yu, H. L. Gao, Z. G. Zou, C. Zheng and W. Huang, *Chem. - A Eur. J.*, 2013, **19**, 6340–6349.

32 P. D. Frischmann, V. Kunz and F. Würthner, *Angew. Chemie - Int. Ed.*, 2015, **54**, 7285–7289.

33 Z. Liu, W. He and Z. Guo, *Chem. Soc. Rev.*, 2013, **42**, 1568–1600.

34 M. C.-L. Yeung and V. W.-W. Yam, *Chem. Soc. Rev.*, 2015, **44**, 4192–4202.

35 Z. Hu, B. J. Deibert and J. Li, *Chem. Soc. Rev.*, 2014, **43**, 5815–5840.

36 O. S. Wenger, *Chem. Rev.*, 2013, **113**, 3686–3733.

37 X. Wang, O. S. Wolfbeis and R. J. Meier, *Chem. Soc. Rev.*, 2013, **42**, 7834–69.

38 K. K.-W. Lo, S. P.-Y. Li and K. Y. Zhang, *New J. Chem.*, 2011, **35**, 265–287.

39 D. L. Ma, V. P. Y. Ma, D. S. H. Chan, K. H. Leung, H. Z. He and C. H. Leung, *Coord. Chem. Rev.*, 2012, **256**, 3087–3113.

40 J. R. Lakowicz, *Principles of Fluorescence Spectroscopy*, 2010.

41 V. Vajpayee, H. Kim, A. Mishra, P. S. Mukherjee, P. J. Stang, M. H. Lee, H. K. Kim and K.-W. Chi, *Dalt. Trans.*, 2011, **40**, 3112–3115.

42 J. Yang, M. Bhadbhade, W. A. Donald, H. Iranmanesh, E. G. Moore, H. Yan and J. E. Beves, *Chem. Commun.*, 2015, **51**, 4465–4468.

43 K. Mahata, P. D. Frischmann and F. Würthner, *J. Am. Chem. Soc.*, 2013, **135**, 15656–15661.

44 A. B. Wragg, A. J. Metherell, W. Cullen and M. D. Ward, *Dalt. Trans.*, 2015, **44**, 17939–17949.

45 K. Li, L.-Y. Zhang, C. Yan, S.-C. Wei, M. Pan, L. Zhang and C.-Y. Su, *J. Am. Chem. Soc.*, 2014, **136**, 4456–4459.

46 P. D. Frischmann, V. Kunz, V. Stepanenko and F. Würthner, *Chem. - A Eur. J.*, 2015, **21**, 2766–2769.

47 E. Baranoff, E. Orselli, L. Allouche, D. Di Censo, R. Scopelliti, M. Grätzel and M. K. Nazeeruddin, *Chem. Commun.*, 2011, **47**, 2799–2801.

48 S. Lai, K. Cheung, M. Chi-wang and C. Che, *Angew. Chemie Int. Ed.*, 1998, **37**, 182–184.

49 S. J. Lee and W. Lin, *J. Am. Chem. Soc.*, 2002, **124**, 4554–4555.

50 B. Manimaran, P. Thanasekaran, T. Rajendran, R.-T. Liao, Y.-H. Liu, G.-H. Lee, S.-M. Peng, S. Rajagopal and K.-L. Lu, *Inorg. Chem.*, 2003, **42**, 4795–4797.

51 M. Sathiyendiran, R. T. Liao, P. Thanasekaran, T. T. Luo, N. S. Venkataramanan, G. H. Lee, S. M. Peng and K. L. Lu, *Inorg. Chem.*, 2006, **45**, 10052–10054.

52 M. Wang, V. Vajpayee, S. Shanmugaraju, Y. R. Zheng, Z. Zhao, H. Kim, P. S. Mukherjee, K. W. Chi and P. J. Stang, *Inorg. Chem.*, 2011, **50**, 1506–1512.

53 L. Zhang, Y.-H. Niu, A. K.-Y. Jen and W. Lin, *Chem. Commun.*, 2005, **2**, 1002–1004.

54 G. J. Zhao, B. H. Northrop, P. J. Stang and K. L. Han, *J. Phys. Chem. A*, 2010, **114**, 3418–3422.

55 V. V. Pavlishchuk and A. W. Addison, *Inorganica Chim. Acta*, 2000, **298**, 97–102.

56 L. Flamigni, A. Barbieri, C. Sabatini, B. Ventura and F. Barigelletti, *Top. Curr. Chem.*, 2007, **281**, 143–203.

57 D. C. Downing and G. F. Wright, *J. Am. Chem. Soc.*, 1946, **68**, 141.

58 H. M. D. Bandara and S. C. Burdette, *Chem. Soc. Rev.*, 2012, **41**, 1809–1825.

59 F. D. Lewis, A. M. Bedell, R. E. Dykstra, J. E. Elbert, I. R. Gould and S. Farid, *J. Am. Chem. Soc.*, 1990, **112**, 8055–8064.

60 K. Ohkubo, T. Nanjo and S. Fukuzumi, *Catal. Today*, 2006, **117**, 356–361.

61 N. Haga, H. Takayanagi and K. Tokumaru, *J. Org. Chem*, 1997, **3263**, 3734–3743.

62 M. Yoshizawa, Y. Takeyama, T. Kusukawa and M. Fujita, *Angew. Chemie Int. Ed.*, 2002, **41**, 1347–1349.

63 M. Yoshizawa, Y. Takeyama, T. Okano and M. Fujita, *J. Am. Chem. Soc.*, 2003, **125**, 3243–3247.

64 S. Karthikeyan and V. Ramamurthy, *Tetrahedron Lett.*, 2005, **46**, 4495–4498.

65 L. S. Kaanumalle and V. Ramamurthy, *Chem. Commun.*, 2007, 1062–1064.

66 L. S. Kaanumalle, R. Ramesh, V. S. N. M. Maddipatla, J. Nithyanandhan, N. Jayaraman and V. Ramamurthy, *J. Org. Chem.*, 2005, **70**, 5062–5069.

67 K. S. L. Chan, M. Wasa, X. Wang and J.-Q. Yu, *Angew. Chemie Int. Ed.*, 2011, **50**, 9081–9084.

68 SAINT-8.34A-2013 •Software for the Integration of CCD Detector System Bruker Analytical X-ray Systems, Bruker axs, Madison, WI (2013).

69 G. M. Sheldrick, *Acta Crystallogr. Sect. A Found. Crystallogr.*, 2015, **71**, 3–8.

70 G. M. Sheldrick, *Acta Crystallogr. Sect. A Found. Crystallogr.*, 2007, **64**, 112–122.

71 Y. R. Hristova, M. M. J. Smulders, J. K. Clegg, B. Breiner and J. R. Nitschke, *Chem. Sci.*, 2011, **2**, 638–641.

CHAPTER 4

Solvophobic Guest Binding in Photoactive Pd_2L_4 Cages

Contents

4.1 Synopsis

Although a complex-as-ligand approach has been shown to allow the synthesis of a photoactive metallosupramolecular assembly, the relatively low affinity for hydrophobic guest compounds prevented efficient regio-selective catalysis. Since the cage was coordinatively saturated, guest encapsulation was driven by the hydrophobic effect. The modular synthetic approach was utilised to synthesise a range of derivatives designed to improve the overall guest affinity. In order to improve the cage hydrophobicity, additional phenyl rings were added to close off the open portals. However, this had an adverse effect on the cage stability and lowered the binding strength of previously known guests. Merthods to improve the water solubility of the system were attempted and included nitrate ion metathesis, the introduction of PEG side chains and the addition of charged functional groups but without success. However, a “click” based methodology was developed for simple modification of the parent system and improves the previous modular construction still further with the aim of producing superior assemblies in the future.

4.2 Introduction

One of the potential barriers to stereo- and regio-selective catalysis within the internal cavity of **151**·8OTf was the relatively weak association of neutral guest molecules. As palladium was required to form a stable supramolecular structure (Figure 4.1), the resultant Pd_2L_4 system is coordinatively saturated and there are no specific metal-ligand interactions providing a driving force for guest encapsulation (See previously, Figure 3.3).[1–4] Since the host:guest interactions achieved through the hydrophobic effect are weak, bulk phase background reactions are likely to dominate when carrying out catalytic reactions. In addition, the instability of the system at high dilutions hinders detailed photophysical investigations of any photoredox reaction pathways. However, the modular synthesis of the cage structure allows for the relatively straight forward alteration of the cage properties through modification of the constituent parts. As such, a number of different methods were investigated to increase the system stability of **151**·8OTf and increase the affinity for neutral organic guests.

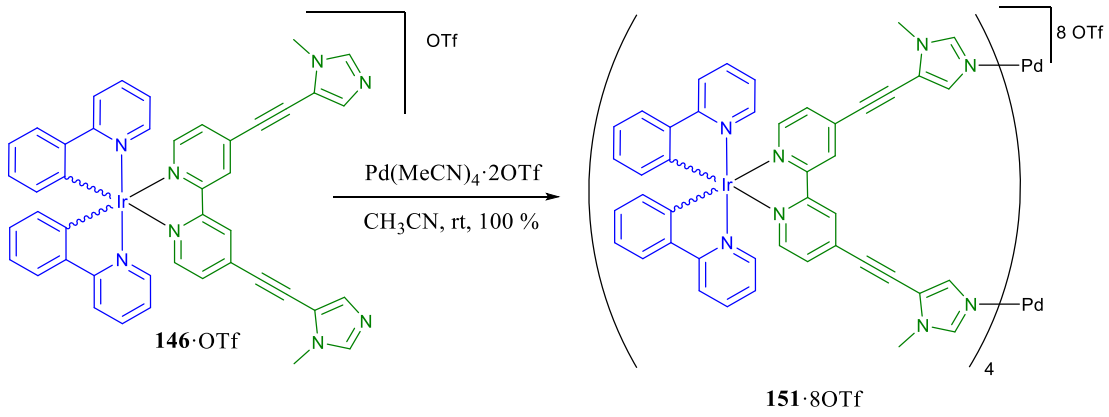

*Figure 4.1: The structure of the iridium functionalised Pd_2L_4 cage, **151**·8OTf, self-assembled from the mononuclear complex, **146**·OTf.*

4.3 Restricted Portal Size

4.3.1 Introduction

While **151**·8OTf contains an internal cavity, the portals in and out are very large and allow rapid exchange of small molecules with the surrounding bulk media. As a result, the internal cavity is only partially hydrophobic since many areas are open to the surrounding solvent. In order to increase the association of neutral organic molecules with the interior of the cage, a variety of extended structural analogues were prepared (Figure 4.2). Molecular modelling suggested that substitution of the phenylpyridine ligand with an additional bulky group could reduce the size of the cage portals and thus increase the hydrophobicity of the cage cavity (Figures 4.3). The restricted openings would also increase the energy barrier for guest association and dissociation potentially resulting in slow binding conditions.

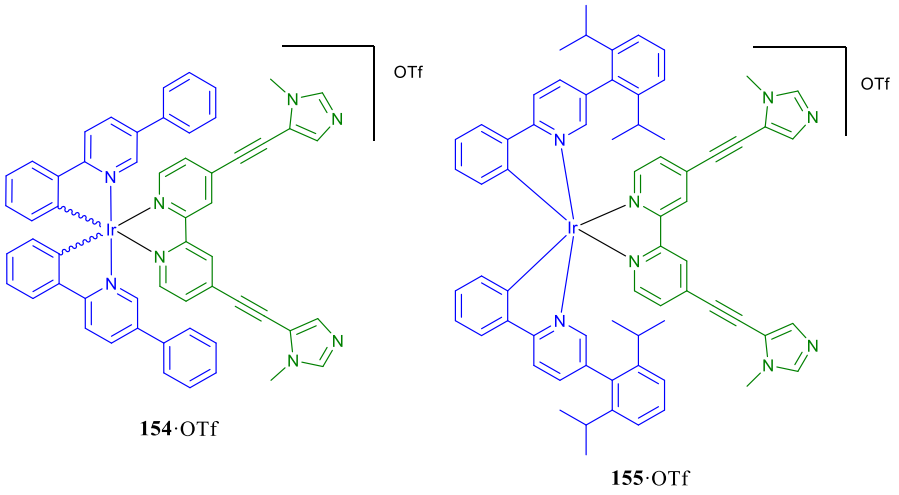

154·OTf **155**·OTf

Figure 4.2: Proposed structures of extended 2-phenylpyridine analogues.

Synthesis of **154**·OTf and **155**·OTf was carried out in an analogous manner to the parent **146**·OTf complex. Upon formation of the Pd_2L_4 assembly **156**·8OTf, a very complex ^{1}H NMR spectrum was observed rather than the slight "splitting" previously described for **151**·8OTf (Figure 4.4). ^{1}H DOSY confirmed that every signal belonged to a species of similar size and the synthesis of the homochiral variant confirmed that the "splitting" was still due to a complex distribution of the iridium chiral centres. Identical absorbance and emission data were also recorded for both the racemic and enantiopure **156**·8OTf. The additional complexity observed in the ^{1}H NMR spectra of *rac*-**156**·8OTf can be attributed to

the increased configurational communication between the iridium centres as a result of the overlapping phenyl rings.

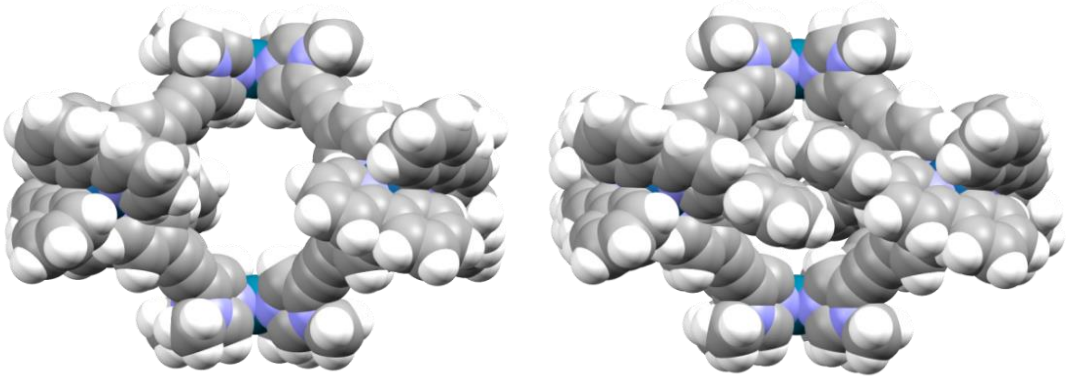

151 **156**

*Figure 4.3: Spartan models of **151** and **156** illustrating the reduction in portal size upon addition of extended phenyl groups.*

As seen for the formation of **151**·8OTf, significant peak shifts were observed for the imidazole and the internal hydrogen signals. A large down-field shift was also observed for the additional phenyl rings upon cage formation, consistent with strong π-π interactions. Similar observations were made for the diisopropyl variant, **157**·8OTf. However, due to the difficulties associated with preparing **157**·8OTf or the corresponding enantiopure analogues in significant quantities, this system was not investigated further.

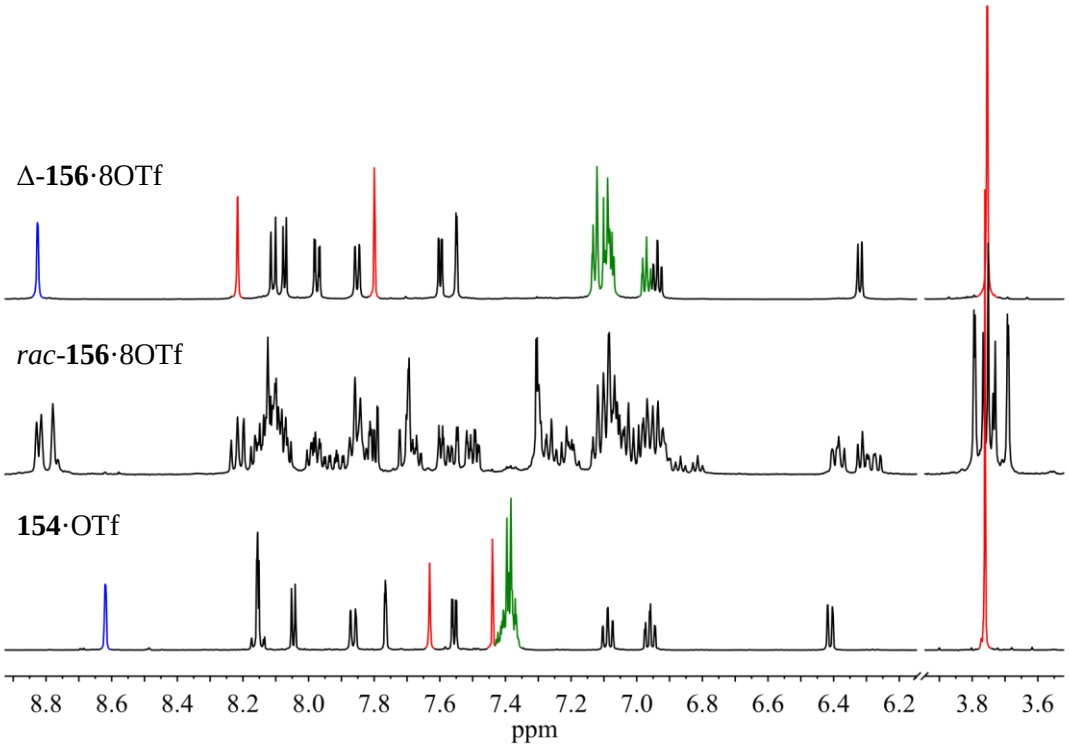

Figure 4.4: ^{1}H NMR (500 MHz, CD_3CN, 300 K) of ***154***·*OTf,* rac-***156***·*8OTf and Δ-****156****·8OTf. Significant shifts are observed for the methyl imidazole (red), the internal proton (blue) and the extended phenyl group (green) upon cage formation. Overlap between the additional phenyl groups, in combination with a distribution of iridium chiral centres, creates a complex peak pattern for* rac-***156***·*8OTf.*

4.3.2 Stability

As described in Chapter 3, the stability of **156**·8OTf was investigated both under dilute conditions and through scrambling experiments. Diluting the system below approximately 10 μM resulted in disassembly of the cage structure and set a lower concentration limit on both luminescence investigations and catalytic screening. As well as closing off the cage portals, the additional phenyl groups present in **156**·8OTf were shown to overlap in molecular modelling (Spartan) and interact by ^{1}H NMR spectroscopy. If the π-π interactions provided an additional force for holding the iridium complexes together, then an increase in the stability of the system would be expected.

In order to assess the kinetic stability of **156**·8OTf, a scrambling experiment was carried out whereby equal quantities of Δ- and Λ-**156**·8OTf were combined in CD_3CN at room temperature and the resultant rearrangement of the system to a statistical equilibrium was monitored by ^{1}H NMR in a method analogous to that outlined in Chapter 3 (Figure 4.5).

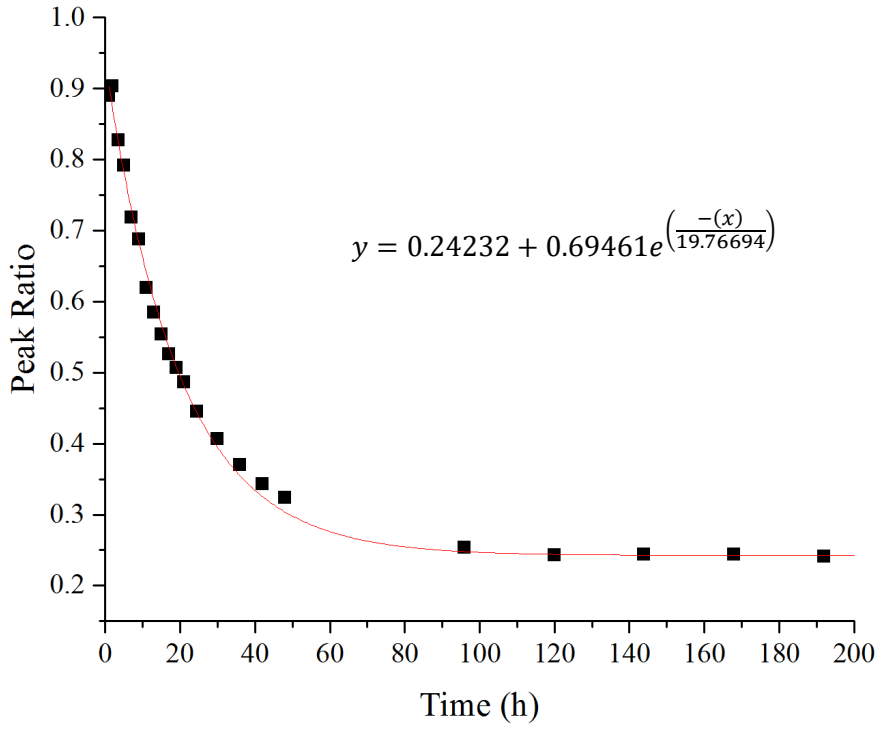

*Figure 4.5: Δ/Λ-**156**·8OTf scrambling experiment in CD_3CN at room temperature. The proportion of scrambling was measured by the ratio of the central triplet peak to the total peak area for the methyl imidazole proton signal. The fitted exponential decay (red) gives a half-life of 13.7 h.*

Fitting an exponential decay function to the relative ratio of enantiopure to mixed **156**·8OTf in solution showed a much more rapid rearrangement of the system compared with **151**·8OTf (Table 4.1). The half-life of **156**·8OTf (13.7 h) was an order of magnitude lower than **151**·8OTf (132 h). As such, the additional phenyl groups appear to significantly disrupt rather than stabilise the supramolecular structure.

Table 4.1: Stability of cage systems assessed by scrambling experiments.

Host	Ligand	Mean lifetime (h)	Half-life (h)
151·8OTf	2-phenylpyridine	189.8	131.6
156·8OTf	2,5-diphenylpyridine	19.8	13.7

All measurements made in CD_3CN at room temperature.

As described in Chapter 2, it was postulated that *rac*-**151**·8OTf exists as a statistical mixture of diastereomers. The same is also true of *rac*-**156**·8OTf but the increased steric bulk provided by the additional phenyl groups results in a much more complex spectrum due to increased interactions between the neighbouring iridium complexes. However, this steric clash is also likely to destabilise the formation of heterochiral variants since a mismatch would result in a direct steric clash between adjacent groups rather than a favourable overlap. In this sense, the homochiral variants would be expected to be far more stable than the heterochiral structures and thus, it was surprising that scrambling between Δ and Λ-**156**·8OTf even occurs. Although entropy could provide some of the driving force for rearrangement to an extended range of structures, it seems likely that any interaction between the adjacent iridium complexes is unfavourable and the palladium-imidazole interaction is weakened in all possible configurations.

4.3.3 Photophysical & Electrochemical Properties

Comparison of the photophysical and electrochemical properties of **154**·OTf and **156**·8OTf with the original 2-phenylpyridine system, **146**·OTf and **151**·8OTf, shows remarkable similarities (Table 4.2). Neither the emission wavelength nor the redox potentials show any major variation and thus both systems should behave in a similar manner with respect to photoredox catalysis.

Table 4.2: Comparison of luminescent properties and redox potentials for original 2-phenylpyridine systems and the corresponding 5-phenyl substituted variants.

Compound	Ligand	λ_{em} (nm)	$E_{1/2}$ M/M$^-$ (V)	$E_{1/2}$ M$^+$/M (V)
146·OTf	2-phenylpyridine	632	-1.52	0.89
151·8OTf	2-phenylpyridine	675	-1.51	0.94
154·OTf	2, 5-diphenylpyridine	634	-1.48	0.91
156·8OTf	2, 5-diphenylpyridine	682	-1.49	0.94

Measurements made in CH_3CN in air. Redox potentials measured in CH_3CN/TBA versus Ag/Ag^+ and reported versus Fc/Fc^+

The similarity between each of the systems can be explained by the location of the relevant HOMO and LUMO orbitals. For most cyclometallated iridium complexes, the HOMO is located on the metal centre and the LUMO is located on the charge-neutral ancillary ligand. Thus, any substitution of the 2-phenylpyridine only influences the redox potentials through alterations in the metal centred HOMO due to remote electron withdrawal or donation. Since the additional phenyl groups are only slightly electron donating, very little change is observed in both the redox potentials and the emission wavelength. In contrast, substitution or alteration of the ancillary ligand can result in large changes in the reduction potential or emission wavelength, as discussed previously in section 3.4.2.

4.3.4 Guest Binding

Restriction of the portal size was hypothesised to increase the barrier to guest exchange and create a more enclosed hydrophobic pocket that could bind neutral organic guests more strongly. The best guests previously found for **151**·8OTf were examined for **156**·8OTf to explore whether an increase in binding constant could be observed (Figure 4.6). Due to the need to use enantiopure **156**·8OTf to allow monitoring of the peak shifts in the required ^{1}H NMR titrations, only a restricted selection of guests were investigated.

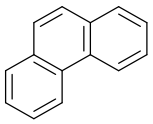

G^{12}

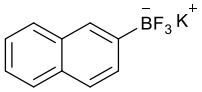

G^{30}

*Figure 4.6: **151**·8OTf guests investigated for enhanced binding in **156**·8OTf.*

Comparison of the measured binding constants reveals that the reduction in portal size actually reduced the affinity of **G^{12}** and **G^{30}** for the internal cavity of **156**·8OTf (Table 4.3). Although the barrier to guest exchange was expected to increase, both guests still showed fast exchange on an NMR timescale. The reduction in binding affinity may be explained by steric restraint of the cavity altering the guest orientation and reducing any preferential interactions such as π-π stacking.

*Table 4.3: Comparison of binding constants for guest compounds within **2**·8OTf and **5**·8OTf.*

#	Guest	Host	Ka (M^{-1})	Error
G^{12}	phenanthrene	**151**·8OTf	257	±33
		156·8OTf	62.8	±14
G^{30}	potassium trifluoronapthylborane	**151**·8OTf	429.2	±73
		156·8OTf	139.5	±24

Although further exploration of guest structures could result in species that show a stronger affinity for the cavity of **156**·8OTf than **151**·8OTf, restriction of the portal size did not show any potential for significantly increasing guest binding and thus, alternative strategies were explored for strengthening the host:guest affinity.

4.4 Designing Water Soluble Derivatives

4.4.1 Introduction

The hydrophobic effect has been used extensively as a general method for driving the encapsulation of neutral organic molecules within the cavities of metallosupramolecular architectures.[5–13] The driving force occurs since water forms an unstable network around hydrophobic compounds. The resultant reduction in the number of strong hydrogen bond interactions, normally present in the bulk phase, results in "high-energy water". Interactions between the host and guest reduces the amount of "high energy water" required to solvate both species and provides an enthalpic driving force for guest encapsulation – the so called "non-classical hydrophobic effect".[14]

The incorporation of palladium as a building block for the assembly of Pd_2L_4 assemblies gave greater structural stability. However, the use of a square planar metal centre removed the ability to bind organic guest molecules through metal-ligand interactions. As an alternative, the hydrophobic effect was used to drive the encapsulation of a range of neutral organic guests in a 50:50 mixture of water and acetonitrile (See Chapter 3). However, the need to incorporate acetonitrile for cage solubility dramatically reduced the strength of the hydrophobic effect and was thought to result in the relatively weak binding constants.[13] In order to increase the affinity of neutral compounds for the cage interior, a range of alternative cage systems were designed and synthesised in an effort to increase the cage solubility in exclusively water.

4.4.2 Nitrate Counter Anions

Many of the currently known water soluble metallosupramolecular systems make use of nitrate counter anions.[10,15] In particular, the Fujita group has made extensive use of nitrate anions for the formation of water soluble systems.[11,16,17] Previous work within the group has also shown how exchanging the associated counter anions for nitrate drastically increased the water solubility of cobalt based cages.[18]

Ion metathesis during the synthesis of the iridium complex, **146**·X, was attempted by the addition of saturated $KNO_{3(aq)}$ to precipitate the crude product from the ethylene glycol/H_2O mixture but the additional aqueous solubility prevented efficient precipitation from the polar mixture. A small quantity was recovered but the isolated compound was impure and the

added polarity afforded by the nitrate anion made conventional purification by column chromatography difficult.

Rather than isolate the nitrate salt directly, **146**·BF_4 (isolated by direct addition of KBF_4 to the ethylene glycol/H_2O mixture) was treated with an anion exchange resin to exchange the associated counter anion for Cl^- (Scheme 4.1). Subsequent treatment with $AgNO_3$ then provided the corresponding nitrate salt, albeit in low yields. ^1H and ^{19}F NMR spectroscopy with 1,2-difluorobenzene as an internal standard showed that removal of the BF_4 anions had been mostly successful, <1% still remained. However, given the small proportion remaining and low yields achieved, the complex was taken forward for further investigations.

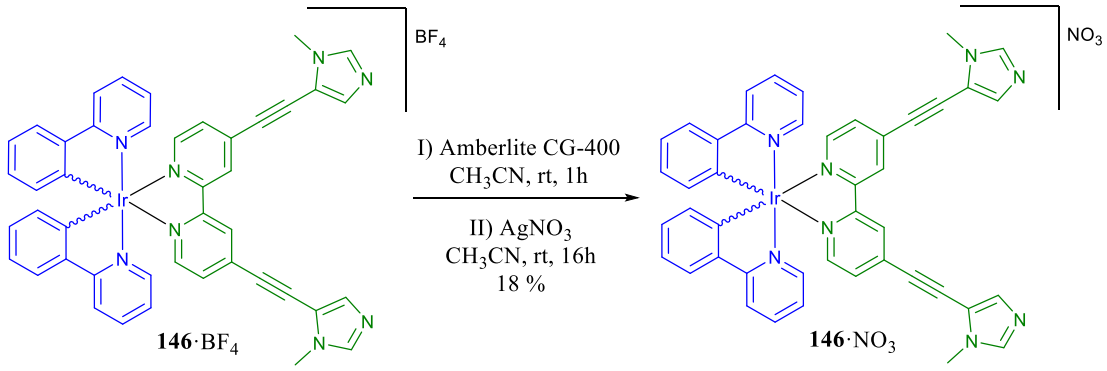

*Scheme 4.1: Anion exchange process of the synthesis of **146**·NO_3.*

Since **146**·NO_3 was not fully soluble in H_2O, the cage formation was carried out using $Pd(NO_3)_2$ in a 2:1 mixture of CD_3CN and H_2O. After stirring at room temperature for 3 days, a complex ^1H NMR spectrum with broad peaks was observed and ^1H DOSY confirmed an increase in the hydrodynamic radius from 6.8 Å to 11.1 Å. Additional heating at 70 ºC did not produce any visible change in the ^1H NMR spectrum but the ^1H DOSY showed a decrease in radius to 8.4 Å. No evidence for the formation of a Pd_2L_4 system could be obtained by mass spectrometry.

The lack of evidence of a distinct structure by ^1H NMR spectroscopy suggested difficulties in the self-assembly process and this was attributed to the increased coordinating ability of nitrate versus OTf. This was expected to be minimised in more polar solvents as demonstrated by the assembly of similar palladium based systems in H_2O or DMSO[4] but the insolubility of **146**·NO_3 prevented the process from being carried out in those alternative solvent systems. Interestingly, Fujita et al. reported that increasing the concentration of NO_3^-

in solution could actually favour the formation of large $Pd_{12}L_{24}$ supramolecular systems. They postulate that this was due to stabilisation of cationic intermediates in close proximity with each other. A similar process could be taking place during the formation of **151**·$8NO_3$ but the increased cationic charge due to the iridium complex, along with the coordinating ability of NO_3^-, stabilises the constituents parts to such a degree that the Pd_2L_4 system is no longer the thermodynamic minimum.

4.4.3 Polyethyleneglycol Solubilising Groups

Water solubility is often achieved by incorporating polar or charged functional groups into a compound structure. In order to allow the straightforward modification of the cage structure, a "click" based methodology was developed using the well-known copper-catalysed alkyne-azide cyclisation reaction to generate a range of phenyltriazole ligands (Figure 4.7).[19]

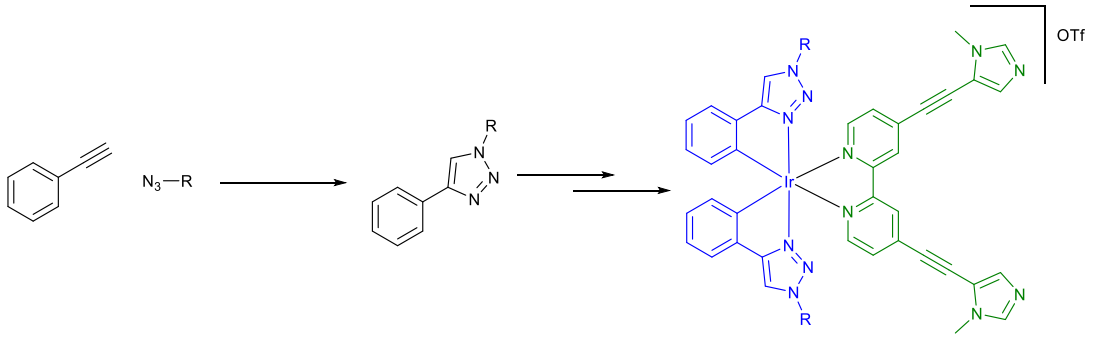

Figure 4.7: General reaction methodology for the click functionalisation of iridium complexes.

The initial synthetic target was the polyethyleneglycol (PEG) functionalised phenyltriazole system. PEG groups have been used extensively to aid water solubility in a range of systems[20–23] and have also been previously reported for aiding the solubility of metallosupramolecular cage compounds in water.[18] After preparation of the PEG-phenyltriazole ligand, the corresponding iridium complex was prepared in an analogous method to the 2-phenylpyridine parent system except that synthesis of the bridged chloride intermediate, **7**, did not proceed as expected. Precipitation of the product from 2-methoxyethanol did not occur even after cooling. ^{1}H NMR analysis of the isolated crude product showed a mixture of multiple species that could not be separated by silica column chromatography. However, ESI-MS of the isolated compound gave a single peak for the correct mono-nuclear $[Ir(C\text{^}N)_2]^+$ ion and the crude material was used without further

purification to afford the PEG functionalised complex, **159**·OTf (Figure 4.8). The difficulties observed in isolating the phenyltriazole based iridium bridged chloride dimer have previously been reported for similar iridium compounds and can attributed to the low stability of the bridged chloride structure and the formation of a range of different transient species in solution.[24]

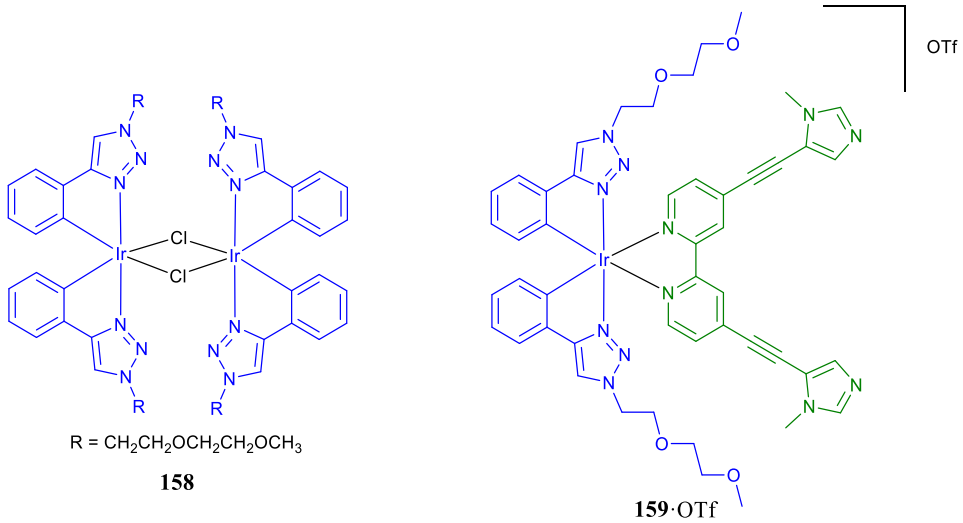

Figure 4.8: The structures of the PEG functionalised iridium complex, ***8****·OTf, and the required bridged chloride intermediate* ***7****.*

The solubility of **159**·OTf was found to be similar to **146**·OTf with a maximum water:acetonitrile ratio of 2:1 at ^{1}H NMR detectable concentrations. However, the corresponding cage compound was synthesised in order to confirm that the assembly did not gain additional water solubility from the combination of eight PEG groups surrounding the exterior of the cage structure (Figure 4.9). As expected, the cage formation with [Pd(CH_3CN)$_4$·2OTf] led to additional signals in the ^{1}H NMR spectrum and the distinctive 1:2:1 peak distribution for the methyl imidazole signals (Figure 4.10). ^{1}H DOSY confirmed that every signal belonged to a large species with a similar hydrodynamic radius to the parent system, 13.2 Å versus 11.2 Å respectively.

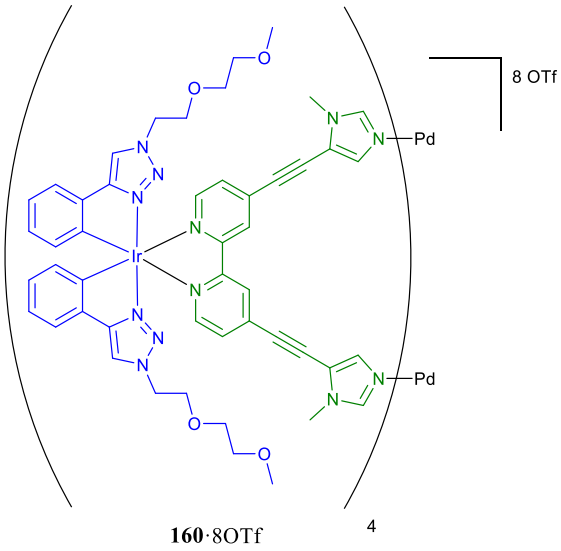

Figure 4.9: The structure of the [8]PEG functionalised cage, ***9****·8OTf.*

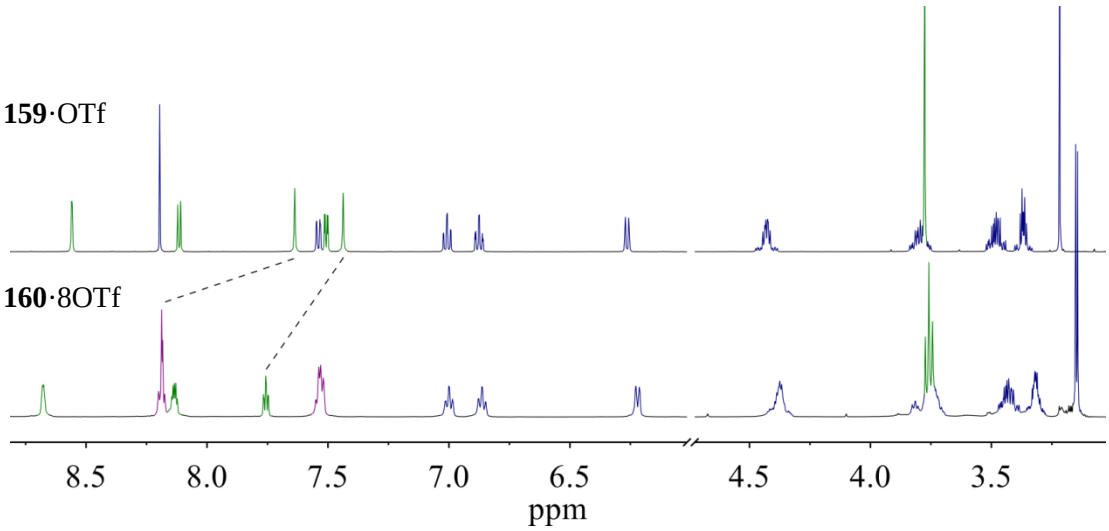

Figure 4.10: ^{1}H NMR (500 MHz, CD_3CN, 300 K) of ***159****·OTf and* ***160****·8OTf indicating the characteristic 1:2:1peak distribution observed upon cage formation. Overlapping peaks are coloured purple.*

Despite the successful formation of a PEG functionalised cage system, the resultant aqueous solubility **160**·8OTf was not significantly different from the maximum 2:1 D_2O/CD_3CN ratio observed for the parent system, **151**·8OTf.

Although PEG molecules are water soluble, the terminal methyl group significantly reduces the overall polarity of the molecule. Since the parent compound, **151**·OTf, is soluble in polar mixtures of water and organic solvents, due to the inherent cationic charge, it was thought

that the mild polarity of the short ethylene glycol chain was not enough to increase the water solubility of **160**·OTf. Rather than prepare the alcohol variant of the PEG azide to give the hydroxyPEG-phenyltriazole (**161**), the click reaction was repeated with the commercially available 4-ethynyl-benzenemethanol to give the hydroxybenzyltriazole PEG (**162**) containing both the original water solubilising PEG group and an additional free hydroxyl group (Figure 4.11).

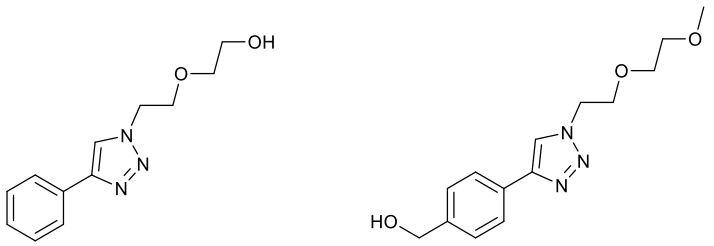

161 **162**

*Figure 4.11: The structures of OHPEG-phenyltriazole (**161**, not prepared) and hydroxybenzyltriazolePEG (**162**).*

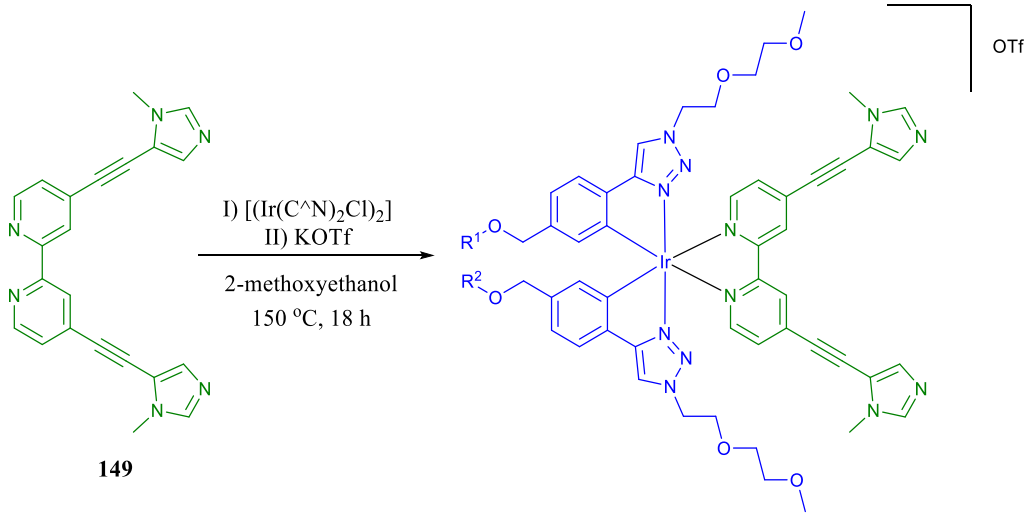

149

163·OTf $R^1 = R^2 = H$
164·OTf $R^1 = H$, $R^2 = CH_3OCH_2CH_2$
165·OTf $R^1 = R^2 = CH_3OCH_2CH_2$

*Scheme 2: Synthesis of the proposed hydroxybenzyl-PEG functionalised iridium complex (**163**·OTf) and isolation of mono- (**164**·OTf) and di- (**165**·OTf) methoxyethoxy adducts.*

Complexation of **162** with iridium to prepare the bridged chloride dimer gave the previously discussed complicated ^{1}H NMR spectrum and the isolated solid was used without further purification. However, the following complexation reaction with the ancillary ligand **149**

gave a mixture of products in the crude reaction mixture. Purification by silica column chromatography yielded the unexpected mono- and di-methoxyethoxy ether compounds (Scheme 4.2).

Given the difficulties in purifying or analysing the bridged chloride intermediate, it was initially uncertain whether the ether linkage was formed during the initial cyclometallation reaction or from residual 2-methoxyethanol during the complexation of **149**. However, ESI-MS of the crude bridged chloride in CH_3CN showed almost complete conversion to the mono- or di-ether coupled analogues after the cyclometallation step (Figure 4.12).

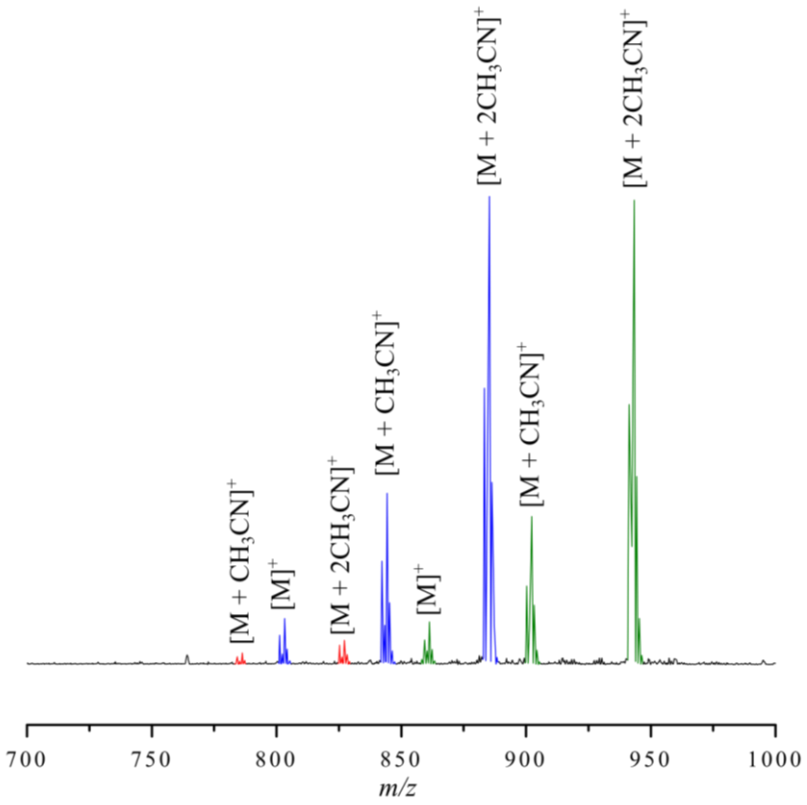

*Figure 4.12: ESI-MS of [(Ir(OHbenzylptPEG)$_2$Cl)$_2$]. Peaks a labelled as **163** (red), **164** (blue) and **165** (green). Each ion exists as the free, mono- and di-CH_3CN adduct where M = Ir(C^N)$_2$.*

Although the unexpected ether formation reduced the polarity of the intended hydroxyl group, the resultant compounds still contained additional PEG chains and could be assembled into Pd_2L_4 systems in an analogous manner to the parent 2-phenylpyridine system

(Figure 4.13). However, the solubility of the isolated complexes and the resultant cage were not found to vary significantly from the maximum 2:1 H_2O/CH_3CN ratio observed for previous systems.

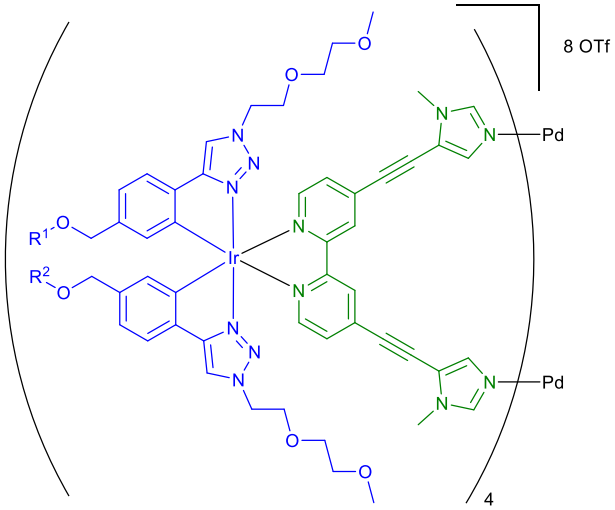

166·OTf $R^1 = R^2 = CH_3OCH_2CH_2$

*Figure 4.13: The structure of the PEG functionalised cage (**166**·8OTf) prepared from the di-methoxyethoxy adduct (**165**·OTf).*

4.4.4 Charged Solubilising Groups

Due to the lack of water solubility provided by PEG groups and the incompatibility of polar hydroxyl groups to the synthesis of iridium complexes, charged functional groups were explored as potential water solubilising groups. Since these groups could potentially interfere with the synthesis and isolation of the iridium complexes, protecting group chemistry was utilised such that the deprotection step could be carried out just before or after the self-assembly of the Pd_2L_4 cage systems (Figure 4.14).

Synthesis of the required ligands was carried out in an analogous manner to the previous "click" procedure from known literature azides. The corresponding iridium bridged chloride intermediates displayed similar properties to the previously isolated phenyltriazole complexes and were used without further purification. Both **167**·OTf and **169**·OTf were isolated in reasonable yields after purification by conventional silica column chromatography. As with the previous structural modifications, assembly of the corresponding Pd_2L_4 systems still occurred readily in solution.

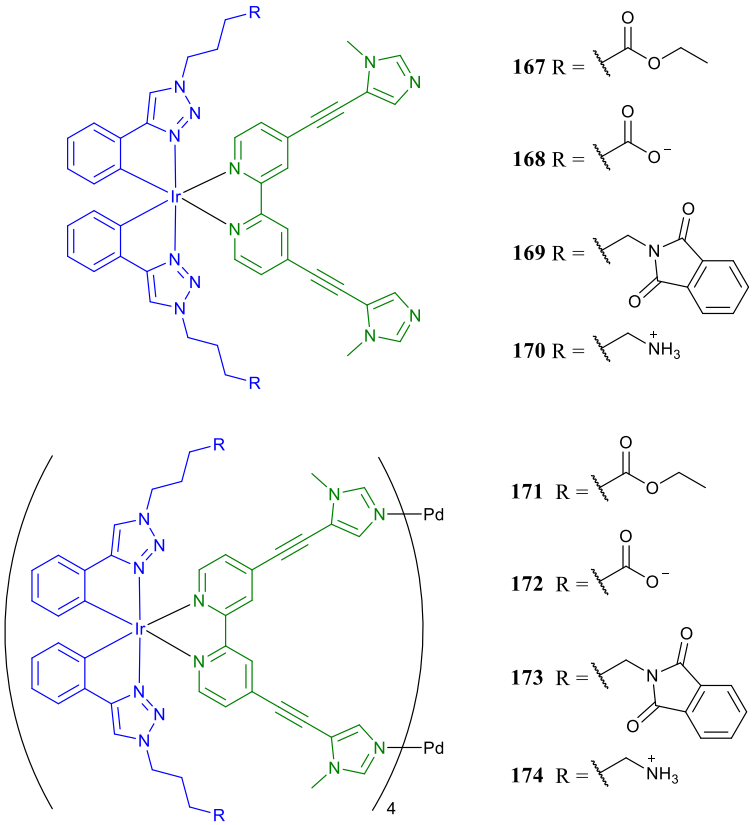

*Figure 4.14: The proposed structures of iridium complexes and corresponding Pd_2L_4 cages functionalised with anionic (**168**, **172**) and cationic (**170**, **174**) water solubilising groups along with the corresponding protecting groups.*

Saponification of **167**·OTf was carried out with OH^- in CH_3OH/CH_2Cl_2 to give the water soluble complex **168**·OTf.[25] However, ^{1}H NMR analysis showed a mixture of very similar species in solution. ^{1}H DOSY also confirmed the similarity of the mixed species but they could not be separated by any means, potentially due to the complicated zwitterionic nature of the cationic iridium centre with anionic solubilising groups. A similar deprotection process could not be carried out with **171**·8OTf since hydroxide rapidly reacted with the coordinated palladium to form insoluble $Pd(OH)_2$ and the free complex **167**·OTf or **168**·OTf.

Similarly, deprotection of **169**·OTf using N_2H_4 produced an impure mixture that could not be purified by column chromatography,[26,27] recrystallisation or acid/base extraction, however, the resultant compounds were soluble in H_2O.

Although the introduction of charged solubilising groups did result in water soluble iridium complexes, the resultant compounds could not be purified through any conventional techniques.

4.5 Summary & Conclusions

As described in Chapter 3, although **151**·8OTf showed an affinity for a range of neutral guests, the measured binding constants were relatively low. In an attempt to increase the binding constants, to reduce competition between bulk phase background reactions during catalysis, a range of sterically crowded and water soluble variants were explored.

The addition of phenyl groups to the peripheral cyclometallated ligands was expected to stabilise the cage system and increase guest binding. Despite the overlapping aromatic rings predicted by molecular modelling and the strong up-field shifts consistent with π-π interactions upon formation of **156**·8OTf, the stability of the system decreased by approximately 10 fold. The additional phenyl groups were also intended to reduce the portal size and increase the hydrophobicity of the internal cavity, however, for those guests studied the binding constants decreased. Alternative guests that show a preference for the more enclosed cavity may exist but no dramatic increase in the overall binding strength of guests was observed.

An alternative approach was then employed to increase the guest binding affinity by increasing the solubility of **151**·8OTf in H_2O and thus strengthen the hydrophobic effect. Incorporation of NO_3^- anions through anion metathesis led to an increase in water solubility but the cage formation could not be accomplished in the presence of NO_3^-, potentially due to increased stabilisation of the cationic species and competitive binding to Pd^{2+}.

Due to the modular synthesis developed for **151**·8OTf, derivatisation of the structure was relatively straight forward using "click" chemistry to functionalise phenyl-triazole ligands with water solubilising groups. The addition of PEG groups did not significantly alter the solubility of the iridium complexes or corresponding cage compounds and the more polar hydroxyl groups were incompatible with the synthetic conditions. The introduction of charged solubilising groups was successful in producing water soluble species but purification of the resultant mixtures could not be achieved.

Alteration of **151**·8OTf to increase guest binding by increasing the hydrophobicity of the internal cavity and enhancing the hydrophobic effect in H_2O was unsuccessful. However, a number of alternative systems were successfully prepared and characterised by the straight forward modification of **151**·8OTf using a combination of "click" chemistry and a modular

approach to synthesis. This demonstrates the success and flexibility of the complex-as-ligand approach for designing stable, photoactive metallosupramolecular assemblies.

4.6 Experimental

4.6.1 General Information

Unless stated otherwise, all reagents and solvents were purchased from Alfa Aesar, VWR or Sigma Aldrich and used without further purification. Column chromatography was carried out using Geduran Si60 (40-63 µm) as the stationary phase and TLC was performed on precoated Kieselgel 60 plates (0.20 mm thick, $60F_{254}$. Merck, Germany) and observed under UV light at 254 nm or 365 nm. All reactions were carried out under air, unless stated otherwise.

[*rac*-$(Ir(ppy)_2Cl)_2$],[28] *rac*-[$(Ir(Phppy)_2Cl)_2$],[29] 1-azido-2-(2-methoxyethoxy)ethane,[18] 4-azido-butanoic acid ethyl ester,[30] 4-phenyl-1H-1,2,3-triazole-1-butanoic acid ethyl ester,[30] azido butyl phthalimide,[31] $[Pd(CH_3CN)_4 \cdot 2OTf]$[32] were prepared according to literature procedures. The synthesis of compounds **146**·OTf and **151**·8OTf are described in full in Chapter 3.

For detailed information on the analytical methods, please refer to Sections 2.9.1 and 3.7.1.

4.6.2 Synthetic Procedures

2-phenyl-5-(2,6-diisopropylphenyl)pyridine

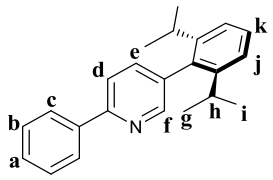

5-bromo-2-phenylpyridine (300.8 mg, 1.285 mmol), 2,6-diisopropylphenylboronic acid (397.2 mg, 1.927 mmol) and $Pd(PPh_3)_4$ (14.8 mg, 1 mol%) were dissolved in toluene (20 mL). K_2CO_3 (2M in H_2O, 10 mL) was charged and the mixture was degassed under N_2 and heated at reflux for 3 days. The crude mixture was cooled and HCl (2M in H_2O, 30 mL) charged. The product extracted with Et_2O, dried over $MgSO_4$ and the solvent was removed under vacuum. The crude product was purified by silica chromatography running 80% hexane, 20% CH_2Cl_2 to give a colourless solid (175.9 mg, 43 %). ^{1}H NMR (500 MHz, $CDCl_3$) δ 8.54 (dd, *J* = 2.2, 0.8 Hz, 1H, H_f), 8.11 – 8.08 (m, 2H, H_c), 7.83 (dd, *J* = 8.0, 0.8 Hz, 1H, H_d), 7.59 (dd, *J* = 8.0, 2.2 Hz, 1H, H_e), 7.54 – 7.49 (m, 2H, H_b), 7.46 – 7.42 (m, 1H, H_a), 7.40 (t, *J* = 7.8 Hz, 1H, H_k), 7.26 (d, J = 7.8 Hz, 2H, H_j), 2.64 (hept, *J* = 6.8 Hz, 2H, H_h),

1.14 – 1.09 (m, 12H, H_g, H_i). ^{13}C NMR (126 MHz, $CDCl_3$) δ 155.81, 150.15, 147.51, 139.14, 137.98, 135.56, 134.82, 129.18, 128.97, 128.76, 126.93, 122.94, 119.82, 30.56, 24.23. *m/z* (HR-ESI): 292.13321 (predicted $[M+H]^+$ = 292.13410) mp = 128-130 ºC.

Δ/Λ-[(Ir(Phppy)$_2$Cl)$_2$]

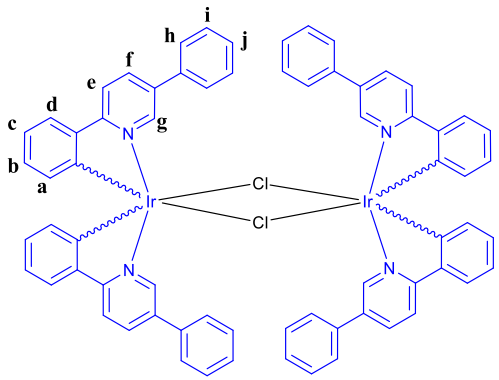

Δ/Λ-[(Ir(Phppy)$_2$Cl)$_2$] was prepared using an analogous procedure to that previously reported for Δ/Λ-[(Ir(ppy)$_2$Cl)$_2$].[28] *rac*-[(Ir(Phppy)$_2$Cl)$_2$] (125.9 mg, 0.091 mmol), L-Serine (28.8 mg, 0.274 mmol) and NaOMe (14.8 mg, 0.274 mmol) were dissolved in CH_3OH (50 mL) and stirred at 40 ºC for 16 h. The solvent was removed under vacuum and the crude products separated by silica column chromatography running 0.5% Et_3N, 1.0% CH_3OH in CH_2Cl_2. The faster running diastereomer Δ-[(Ir(Phppy)$_2$(L-Serine)] was isolated pure, dissolved in CH_3OH (25 mL) and $HCl_{(aq)}$ (35%, 0.5 mL) was charged. The mixture was stirred at room temperature for 1 h and the resultant precipitate filtered, washed with CH_3OH and dried under vacuum to yield Δ-[(Ir(Phppy)$_2$Cl)$_2$] as a bright yellow solid (31.6 mg, 25%). The remaining impure fractions were retained, converted to [(Ir(Phppy)$_2$Cl)$_2$] and the procedure repeated with D-Serine to afford Λ-[(Ir(Phppy)$_2$Cl)$_2$] as a bright yellow solid (22.9 mg, 18%). Δ/Λ-[(Ir(Phppy)$_2$Cl)$_2$] ^{1}H NMR (500 MHz, $CDCl_3$) δ 9.81 (d, *J* = 2.1 Hz, 4H, H_g), 7.53 (d, *J* = 8.5 Hz, 4H, H_e), 7.47 – 7.36 (m, 16H, H_d, H_i, H_j), 7.32 (dd, *J* = 8.5, 2.2 Hz, 4H, H_f), 7.15 – 7.11 (m, 8H, H_h), 6.79 – 6.73 (m, 4H, H_c), 6.58 – 6.53 (m, 4H, H_b), 5.91 (dd, *J* = 7.8, 0.8 Hz, 4H, H_a). ^{13}C NMR (126 MHz, $CDCl_3$) δ 167.00, 149.37, 145.81, 143.67, 135.75, 133.97, 133.06, 130.62, 129.36, 129.01, 128.50, 126.24, 123.64, 121.42, 117.70. *m/z* (HR-ESI): 1376.25094 (predicted $[M]^+$ = 1376.24930).

rac-[(Ir(^{i}Pr$_2$Phppy)$_2$Cl)$_2$]

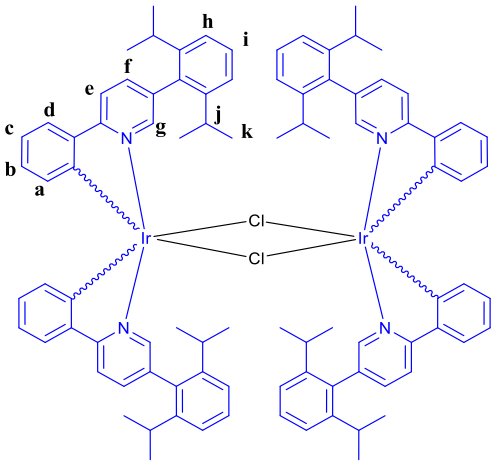

2-phenyl-5-(2,6-diisopropylphenyl)pyridine (175.9 mg, 0.558 mmol) and Na_3IrCl_6 (132.1 mg, 0.279 mmol) were partially dissolved in 2-methoxyethanol (30 mL). The mixture was stirred at room temperature until complete dissolution (5 h) and then heated at reflux under N_2 for 16 h. The solvent was removed under vacuum and the crude residue purified by silica chromatography running 50% CH_2Cl_2 and 50% hexane to give a bright yellow solid (111.8 mg, 47%). ^{1}H NMR (500 MHz, $CDCl_3$) δ 9.25 (s, 4H, H_g), 7.92 (d, J = 8.2 Hz, 4H, H_e), 7.64 (d, J = 8.2, 4H, H_f), 7.56 (dd, J = 7.8, 1.4 Hz, 4H, H_d), 7.41 (t, J = 7.8 Hz, 4H, H_i), 7.31 – 7.22 (m, 8H, H_h), 6.90 – 6.81 (m, 4H, H_c), 6.76 – 6.67 (m, 4H, H_b), 6.28 (d, J = 7.6 Hz, 4H, H_a), 2.89 – 2.71 (m, 8H, H_j), 1.28 – 1.09 (m, 48H, H_k). ^{13}C NMR (126 MHz, $CDCl_3$) δ 166.24, 150.73, 147.47, 144.35, 138.71, 135.11, 134.44, 132.29, 129.44, 129.18, 124.09, 123.13, 123.08, 121.92, 118.08, 30.98 (C_j), 30.87 (C_j), 24.73 (C_k), 24.57 (C_k), 24.17 (C_k), 24.05 (C_k). *isopropyl groups split into multiple environments due to restricted rotation. *m/z* (HR-ESI): 821.34760 (predicted [Ir(^{i}Pr$_2$Phppy)$_2$]$^{+}$ = 821.34414), 862.37550 (predicted [Ir(^{i}Pr$_2$Phppy)$_2$+CH_3CN]$^{+}$ = 862.37122), 862.37550 (predicted [Ir(^{i}Pr$_2$Phppy)$_2$+2CH_3CN]$^{+}$ = 862.37122).

154·OTf - [Ir(Phppy)$_2$(emibipy)]OTf

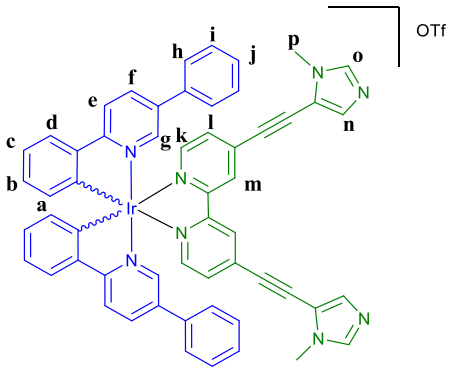

[(Ir(Phppy)$_2$Cl)$_2$] (27.4 mg, 0.020 mmol) and **149** (14.5 mg, 0.040 mmol) were partially dissolved in ethylene glycol (2.0 mL). The solution was degassed under high-vacuum for 20 mins and backfilled with N_2 before heating at 150 °C for 18 h. The solution was then cooled and diluted with H_2O (10 mL) before being washed with Et_2O (2 x 5 mL). KOTf (22.5 mg, 0.120 mmol) was charged and the resultant precipitate was filtered through celite. The orange solid was washed with copious amounts of H_2O and then washed off the celite with CH_2Cl_2. The solvent was removed under reduced pressure to yield the crude product. If necessary, purification could be achieved by silica column chromatography (gradient CH_2Cl_2 to 10% CH_3OH in CH_2Cl_2). The product was isolated as a bright orange/red solid (19.0 mg, yield = 64%). ^{1}H NMR (500 MHz, CD_3CN) δ 8.62 (d, *J* = 1.7 Hz, 2H, H_m), 8.19 – 8.12 (m, 2H, H_e, H_f), 8.05 (dd, *J* = 5.7, 0.5 Hz, 2H, H_k), 7.86 (dd, *J* = 7.9, 1.0 Hz, 2H, H_d), 7.77 (dd, *J* = 1.8, 1.0 Hz, 2H, H_g), 7.63 (s, 2H, H_o), 7.56 (dd, *J* = 5.7, 1.7 Hz, 2H, H_l), 7.44 (d, *J* = 0.9 Hz, 2H, H_n), 7.43 – 7.34 (m, 10H, H_h, H_i, H_j), 7.13 – 7.05 (m, 2H, H_c), 6.99 – 6.92 (m, 2H, H_b), 6.41 (dd, *J* = 7.6, 0.8 Hz, 2H, H_a), 3.79 – 3.72 (m, 6H, H_p). ^{13}C NMR (126 MHz, CD_3CN) δ 167.15, 156.81, 151.64, 150.78, 147.57, 144.67, 141.75, 138.05, 137.97, 137.33, 136.44, 134.63, 132.67, 131.49, 130.21, 130.00, 129.79, 127.70, 127.06, 126.05, 123.82, 120.98, 115.31, 93.93, 87.88, 32.81. ^{19}F NMR (471 MHz, CD_3CN) δ -79.30 (s). ^{1}H DOSY NMR (500 MHz, CD_3CN) –logD = 9.01, hydrodynamic radius = 6.0 Å. *m/z* (HR-ESI): 1017.30190 (predicted $[M]^+$ = 1017.29999).

155·OTf - [Ir(^{i}Pr$_2$Phppy)$_2$(emibipy)]OTf

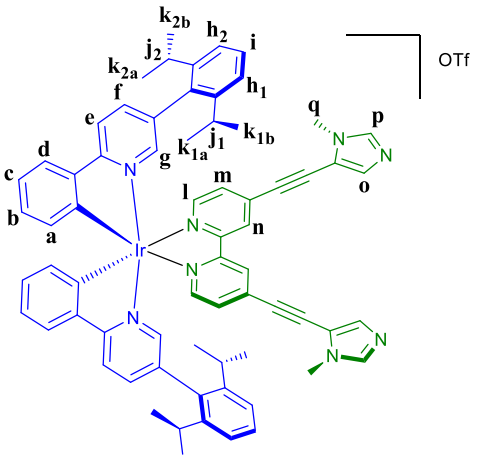

[(Ir(^{i}Pr$_2$Phppy)$_2$Cl)$_2$] (16.0 mg, 0.009 mmol) and **149** (6.8 mg, 0.019 mmol) were partially dissolved in ethylene glycol (2.0 mL). The solution was degassed under high-vacuum for 20 mins and backfilled with N_2 before heating at 150 °C for 18 h. The solution was then cooled and diluted with H_2O (10 mL) before being washed with Et_2O (2 x 5 mL). KOTf (10.5 mg, 0.056 mmol) was charged and the resultant precipitate was filtered through celite. The orange solid was washed with copious amounts of H_2O and then washed off the celite with CD_2Cl_2. The solvent was removed under reduced pressure to yield the crude product. If necessary, purification could be achieved by silica column chromatography (gradient CD_2Cl_2 to 10% CH_3OH in CD_2Cl_2). The product was isolated as a bright orange/red solid (15.4 mg, yield = 62%). ^{1}H NMR (601 MHz, CD_3CN) δ 8.47 (d, *J* = 1.5 Hz, 2H, H_n), 8.17 (d, *J* = 8.4 Hz, 2H, H_e), 7.90 (d, *J* = 7.1 Hz, 2H, H_d), 7.86 (d, *J* = 5.7 Hz, 2H, H_l), 7.74 (dd, *J* = 8.3, 1.9 Hz, 2H, H_f), 7.63 (s, 2H, H_p), 7.51 (d, *J* = 1.8 Hz, 2H, H_g), 7.43 (dd, *J* = 5.7, 1.6 Hz, 2H, H_m), 7.41 (s, 2H, H_o), 7.31 (t, *J* = 7.8 Hz, 2H, H_i), 7.21 (dd, *J* = 7.8, 0.9 Hz, 2H, H_{h2}), 7.12 (m, 4H, H_c, H_{h1}), 7.04 – 7.00 (m, 2H, H_b), 6.48 (d, *J* = 7.6 Hz, 2H, H_a), 3.72 (s, 6H, H_q), 2.68 (hept, *J* = 6.8 Hz, 2H, H_{j2}), 2.04 (hept, *J* = 7.1 Hz, 2H, H_{j1}), 1.18 (d, *J* = 6.8 Hz, 6H, H_{k2a}), 1.00 (d, *J* = 6.8 Hz, 6H, H_{k2b}), 0.90 (d, *J* = 6.9 Hz, 6H, H_{k1a}), 0.60 (d, *J* = 6.8 Hz, 6H, H_{k1b}). ^{13}C NMR (126 MHz, CD_3CN) δ 166.87, 156.35, 151.27, 150.54, 149.74, 148.01, 147.61, 144.86, 141.77, 140.95, 138.06, 137.04, 134.75, 134.33, 132.67, 131.46, 130.22, 130.00, 126.45, 126.17, 123.90, 123.89, 123.76, 120.60, 115.22, 93.67, 88.04, 32.77, 31.55, 31.28, 24.76, 24.08, 23.61, 23.52. ^{19}F NMR (471 MHz, CD_3CN) δ -79.31 (s). ^{1}H DOSY NMR (500 MHz, CD_3CN) –logD = 9.04, hydrodynamic radius = 6.5 Å. *m/z* (HR-ESI): 1185.48590 (predicted $[M]^+$ = 1185.48779) 1335.44640 (predicted $[M+H]^{2+}$OTf = 1335.44764).

156·8OTf - $[Pd_2(Ir(Phppy)_2emibipy)_4]8OTf$

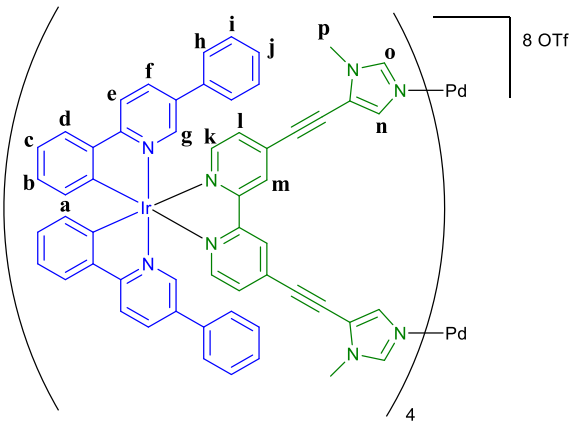

General Method

$[Ir(Phppy)_2emibipy]OTf$ (15.2 mg, 0.013 mmol) was dissolved in CH_3CN (5 mL). $[Pd(CH_3CN)_4·2OTf]$ (3.71 mg, 0.007 mmol) was charged as a solution in CH_3CN (267 µL). The solution was stirred at room temperature for 16 h. The solution was concentrated under vacuum. The product was precipitated with Et_2O, filtered, washed with Et_2O and dried under vacuum to yield a bright orange/red solid (10.5 mg, 59%).

rac-$[Pd_2(Ir(Phppy)_2emibipy)_4]8OTf$

^1H & ^{13}C NMR too complicated for detailed analysis due to complex mixture of diastereomers. ^{19}F NMR (471 MHz, CD_3CN) δ -79.30. ^1H DOSY NMR (500 MHz, CD_3CN) –logD = 9.31, hydrodynamic radius = 12.1 Å.

Δ/Λ-$[Pd_2(Ir(Phppy)_2emibipy)_4]8OTf$

^1H NMR (601 MHz, CD_3CN) δ 8.83 (d, J = 1.4 Hz, 8H, H_m), 8.22 (d, J = 0.6 Hz, 8H, H_o), 8.11 (d, J = 8.4 Hz, 8H, H_f), 8.07 (d, J = 5.8 Hz, 8H, H_k), 7.97 (dd, J = 8.6, 2.1 Hz, 8H, H_e), 7.85 (dd, J = 8.0, 0.8 Hz, 8H, H_d), 7.80 (d, J = 1.2 Hz, 8H, H_n), 7.60 (dd, J = 5.7, 1.6 Hz, 8H, H_l), 7.55 (d, J = 2.1 Hz, 8H, H_g), 7.15 – 7.06 (m, 40H, H_c, H_h, H_i), 6.99 – 6.95 (m, 8H, H_j), 6.95 – 6.92 (m, 8H, H_b), 6.32 (dd, J = 7.6, 0.7 Hz, 12H, H_a), 3.75 (s, 6H). ^{13}C NMR (126 MHz, CD_3CN) δ 167.14, 156.56, 152.07, 150.48, 147.22, 144.65, 142.27, 138.21, 137.32, 136.38, 135.74, 133.51, 132.57, 131.57, 129.93, 129.93, 129.37, 128.07, 127.69, 126.11, 123.97, 122.27 (q, J = 320.9 Hz), 121.04, 117.69, 94.99, 84.00, 34.52. ^{19}F NMR (471 MHz, CD_3CN) δ -78.94. ^1H DOSY NMR (500 MHz, CD_3CN) –logD = 9.31, hydrodynamic radius = 12.1 Å.

157·8OTf – *rac*-[Pd$_2$(Ir(^{i}Pr$_2$Phppy)$_2$emibipy)$_4$]8OTf

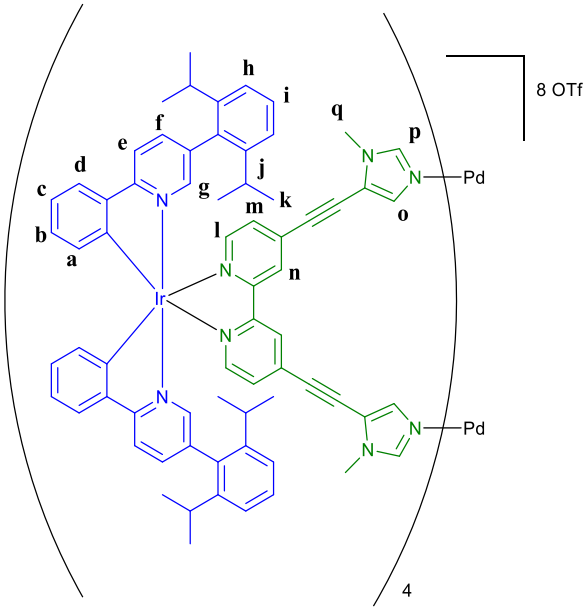

rac-[Ir(^{i}PrPhppy)$_2$emibipy]OTf (5.8 mg, 4.35 µmol) was dissolved in CD_3CN (0.5 mL). [Pd(CH_3CN)$_4$·2OTf] (1.24 mg, 2.18 µmol) was charged as a solution in CD_3CN (20 µL). The mixture was stirred at room temperature for 16 h to give a bright red solution (100% by NMR). ^{1}H & ^{13}C NMR too complicated for detailed analysis due to complex mixture of diastereomers. ^{19}F NMR (471 MHz, CD_3CN) δ -79.07. DOSY NMR (500 MHz, CD_3CN) – logD = 9.37, hydrodynamic radius = 13.9 Å.

146·BF_4 - [Ir(ppy)$_2$(emibipy)]BF_4

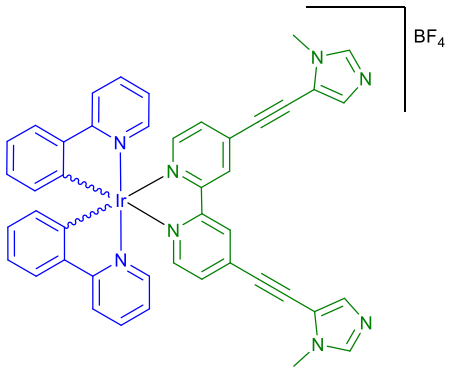

[(Ir(ppy)$_2$Cl)$_2$] (226.7 mg, 0.211 mmol) and **149** (154.0 mg, 0.423 mmol) were partially dissolved in ethylene glycol (40.0 mL). The solution was degassed under high-vacuum for 20 mins and backfilled with N_2 before heating at 150 °C for 18 h. The solution was then cooled and diluted with H_2O (150 mL) before being washed with Et_2O (2 x 100 mL). KBF_4 (133.1 mg, 1.055 mmol) was charged and the resultant precipitate was filtered through celite. The orange solid was washed with copious amounts of H_2O and then washed off the celite with CH_2Cl_2. The solvent was removed under reduced pressure to yield the crude product. The product was isolated as a bright orange/red solid (138.1 mg, yield = 73%). ^{1}H NMR (500 MHz, CD_3CN) δ 8.62 (d, *J* = 1.5 Hz, 2H, H_k), 8.07 (d, *J* = 8.1 Hz, 2H, H_e), 7.94 (d, *J* = 5.6 Hz, 2H, H_i), 7.90 – 7.83 (m, 2H, H_f), 7.81 (dd, *J* = 7.9, 1.3 Hz, 2H, H_d), 7.67 (d, *J* = 5.9 Hz, 2H, H_h), 7.64 (s, 2H, H_m), 7.52 (dd, *J* = 5.7, 1.6 Hz, 2H, H_j), 7.45 (d, *J* = 0.9 Hz, 2H, H_l), 7.08 – 7.03 (m, 4H, H_c, H_g), 6.97 – 6.90 (m, 2H, H_b), 6.27 (dd, *J* = 7.8, 1.0 Hz, 2H, H_a), 3.77 (s, 6H, H_n). ^{13}C NMR (126 MHz, CD_3CN) δ 285.28, 273.62, 268.48, 267.87, 267.33, 262.00, 258.70, 256.61, 254.96, 251.59, 249.45, 248.37, 246.92, 243.76, 242.87, 241.52, 240.65, 237.88, 232.32, 210.92, 204.71, 149.81. ^{19}F NMR (471 MHz, CD_3CN) δ -151.63 (^{10}B), -151.68 (^{11}B). *m/z* (HR-ESI): 865.23800 (predicted $[M]^+$ = 865.23739).

146·NO_3 - [Ir(ppy)$_2$(emibipy)]NO_3

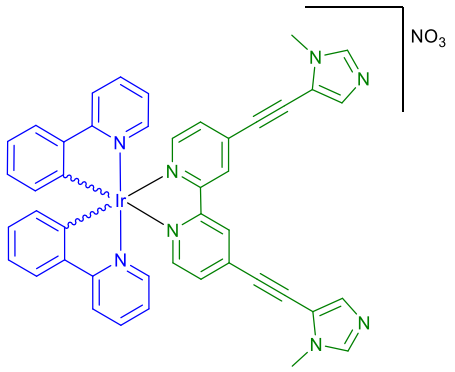

[Ir(ppy)$_2$(emibipy)]BF_4 (47.1 mg, 0.049 mmol) was dissolved in CH_3CN (3 mL). Amberlite CG-400 resin (100 mg) was charged and the mixture was gently agitated at room temperature for 1 h. The mixture was filtered, $AgNO_3$ (8.4 mg, 0.049 mmol) charged and the solution stirred at room temperature for 18 h in a darkened flask. The resultant mixture was filtered through celite and the solvent removed under vacuum to yield an orange/red solid (8.1 mg, 18%). ^{1}H NMR (500 MHz, 2:1 CD_3CN/D_2O) δ 8.63 (d, *J* = 1.7 Hz, 2H, H_k), 8.04 (d, *J* = 8.2 Hz, 2H, H_e), 7.91 (d, *J* = 5.7 Hz, 2H, H_i), 7.87 – 7.80 (m, 2H, H_f), 7.77 (dd, *J* = 8.0, 1.3 Hz, 2H, H_d), 7.73 (s, 2H, H_m), 7.61 (dd, *J* = 5.8, 1.5 Hz, 2H, H_h), 7.49 (dd, *J* = 5.7, 1.6 Hz, 2H, H_j), 7.42 (s, 2H, H_l), 7.06 – 6.97 (m, 4H, H_c, H_g), 6.91 – 6.85 (m, 2H, H_b), 6.22 (dd, *J* = 7.6, 1.2 Hz, 2H, H_a), 3.74 (s, 6H, H_n). ^{13}C NMR (126 MHz, 2:1 CD_3CN/D_2O) δ 168.14, 156.56, 151.49, 150.79, 150.19, 145.00, 141.86, 139.75, 136.97, 134.35, 132.42, 131.38, 129.98, 126.89, 125.90, 124.60, 123.74, 120.95, 115.67, 93.95, 86.91, 33.10. ^{1}H DOSY NMR (500 MHz, 2:1 CD_3CN/D_2O) –logD = 9.32, hydrodynamic radius = 6.8 Å. *m/z* (HR-ESI): 865.23520 (predicted $[M]^+$ = 865.23739).

2-PEG-phenyl triazole

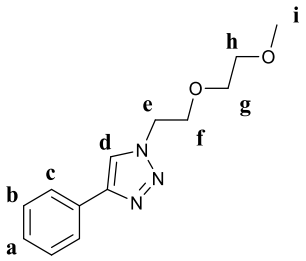

Phenylacetylene (306.42 mg, 3.000 mmol) and azido-2-PEG (435.45 mg, 3.000 mmol) were dissolved in a mixture of water (6 mL) and ^{t}BuOH (6 mL). Sodium ascorbate (10 mol%, 1M in H_2O) and Cu(II)SO_4.5H_2O (1 mol%, 300 mM in H_2O) were charged and immediate precipitation was observed. The mixture was stirred thoroughly at room temperature for 16 h. The mixture was diluted with H_2O (50 mL) and the product was extracted with CH_2Cl_2. The organic layer was dried over $MgSO_4$ and the solvent removed under vacuum to yield a yellow oil that slowly crystallised to form an off-white solid (512.1 mg, 69%). ^{1}H NMR (500 MHz, $CDCl_3$) δ 8.01 (s, 1H, H_d), 7.88 – 7.79 (m, 2H, H_c), 7.46 – 7.38 (m, 2H, H_b), 7.36 – 7.30 (m, 1H, H_a), 4.59 (t, *J* = 5.0 Hz, 2H, H_e), 3.89 (t, *J* = 5.0 Hz, 2H, H_f), 3.67 – 3.57 (m, 2H, H_g), 3.55 – 3.46 (m, 2H, H_h), 3.37 (s, 3H, H_i). ^{13}C NMR (126 MHz, $CDCl_3$) δ 130.88, 128.81, 128.02, 125.69, 121.10, 71.76, 70.56, 69.57, 59.04, 50.35. *m/z* (HR-ESI): 248.14028 (predicted $[M]^+$ = 248.13935), 270.12176 (predicted $[M+Na]^+$ = 270.12130), 517.25381 (predicted $[2M+Na]^+$ = 517.25391). mp (32-34 ºC).

158 – $[(Ir(ptPEG)_2)Cl)_2]$

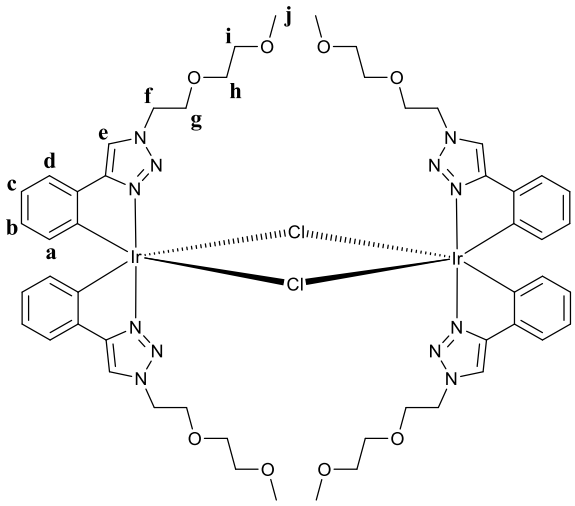

Phenyl triazole-2-PEG (423.4 mg, 1.712 mmol) and $Na_3IrCl_6.xH_2O$ (405.7 mg, 0.0856 mmol) were partially dissolved in 2-methoxyethanol (125 mL). The mixture was stirred at room temperature for 2 h until complete dissolution and then heated at reflux for 16 h. The solvent was removed under vacuum to yield a yellow oil. Purification by silica chromatography running 100% CH_2Cl_2 to 10% CH_3OH in CH_2Cl_2 still showed multiple species by ^1H NMR. DOSY confirms all signals belong to similar sized species. Used without further purification. *m/z* (HR-ESI): 685.25560 (predicted $[Ir(ptPEG)_2]^+$ = 685.21143).

159·OTf - [Ir(ptPEG)$_2$emibipy]OTf

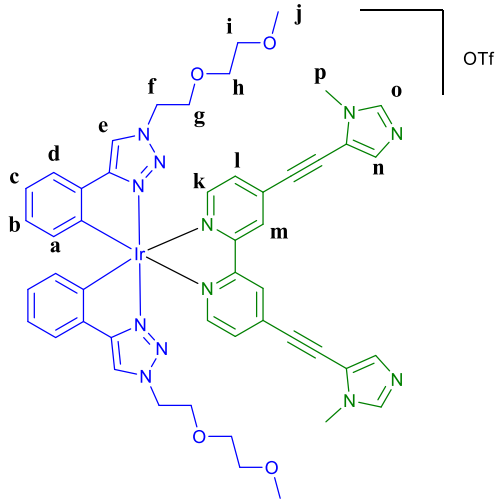

Crude $(Ir(ptPEG)_2Cl)_2$ (31.2 mg) and **149** (15.8 mg, 0.043 mmol) were partially dissolved in ethylene glycol (2.0 mL). The solution was degassed under high-vacuum for 20 mins and backfilled with N_2 before heating at 150 °C for 18 h. The solution was then cooled and diluted with H_2O (10 mL) before being washed with Et_2O (2 x 5 mL). KOTf (24.5 mg, 0.130 mmol) was charged and the resultant precipitate was filtered through celite. The orange solid was washed with copious amounts of H_2O and then washed off the celite with CH_2Cl_2. The solvent was removed under reduced pressure to yield the crude product. If necessary, purification could be achieved by silica column chromatography (gradient CH_2Cl_2 to 10% CH_3OH in CH_2Cl_2). The product was isolated as a bright orange/red solid (29.4 mg, yield = 57%). ^{1}H NMR (500 MHz, CD_3CN) δ 8.56 (d, *J* = 1.7 Hz, 2H, H_m), 8.20 (s, 2H, H_e), 8.12 (d, *J* = 5.7 Hz, 2H, H_k), 7.64 (s, 2H, H_o), 7.54 (dd, *J* = 7.6, 1.0 Hz, 2H, H_d), 7.51 (dd, *J* = 5.7, 1.6 Hz, 2H, H_l), 7.44 (s, 2H, H_n), 7.04 – 6.98 (m, 2H, H_c), 6.91 – 6.84 (m, 2H, H_b), 6.26 (dd, *J* = 7.5, 0.5 Hz, 2H, H_a), 4.50 – 4.35 (m, 4H, H_f), 3.85 – 3.73 (m, 4H, H_g), 3.78 (s, 6H, H_p), 3.55 – 3.43 (m, 4H, H_h), 3.41 – 3.30 (m, 4H, H_i), 3.22 (s, 6H, H_j). ^{13}C NMR (126 MHz, CD_3CN) δ 157.62, 157.42, 152.23, 146.68, 141.72, 137.86, 136.92, 134.34, 133.44, 129.31, 129.04, 125.86, 123.87, 123.32, 121.28, 93.95, 87.46, 72.44, 70.99, 69.31, 58.99, 52.93, 32.86. ^{19}F NMR (471 MHz, CD_3CN) δ -79.32 (s). ^{1}H DOSY NMR (500 MHz, CD_3CN) –logD = 9.02, hydrodynamic radius = 6.2 Å. *m/z* (HR-ESI): 1049.44710 (predicted $[M]^+$ = 1049.35507).

160·8OTf - $[Pd_2(Ir(ptPEG)_2emibipy)_4]8OTf$

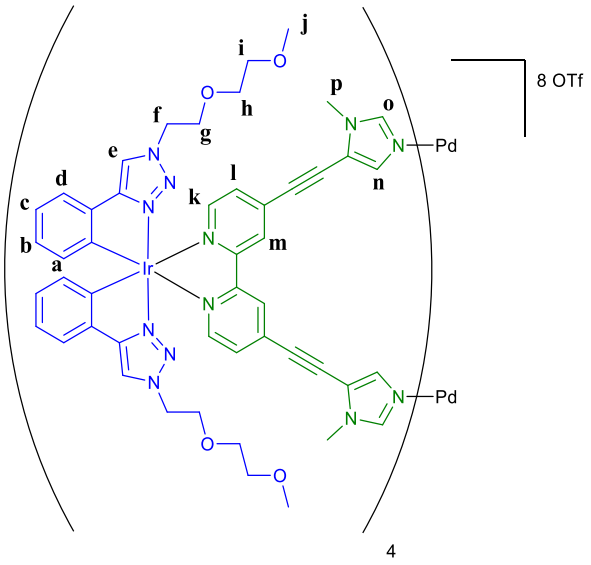

[Ir(ptPEG)$_2$emibipy]OTf (4.7 mg, 3.92 µmol) was dissolved in CD_3CN (0.5 mL). [Pd(CH_3CN)$_4$·2OTf] (1.12 mg, 1.97 µmol) was charged as a solution in CD_3CN (63 µL). The solution was left at room temperature for 5 h to give a bright red solution (100% by NMR). Product not isolated. ^{1}H NMR (500 MHz, CD_3CN) δ 8.71 – 8.65 (m, 8H, H_m), 8.23 – 8.17 (m, 16H, H_e, H_o), 8.17 – 8.08 (m, 8H, H_k), 7.79 – 7.72 (m, 8H, H_n), 7.59 – 7.47 (m, 16H, H_d, H_l), 7.03 – 6.97 (m, 8H, H_c), 6.90 – 6.83 (m, 8H, H_b), 6.25 – 6.20 (m, 8H, H_a), 4.46 – 4.31 (m, 16H, H_f), 3.86 – 3.68 (m, 40H, H_g, H_p), 3.49 – 3.37 (m, 16H, H_h), 3.37 – 3.26 (m, 16H, H_i), 3.17 – 3.12 (m, 24H, H_j). ^{13}C NMR (126 MHz, CD_3CN) δ 157.56, 157.20, 152.48, 146.20, 142.22, 136.77, 135.32, 133.31, 133.10, 129.31, 128.83, 126.70, 123.93, 123.30, 122.16 (q, *J* = 321.0 Hz), 121.26, 117.70, 94.95, 83.41, 72.34, 70.93, 69.24, 58.89, 52.83, 34.46. ^{19}F NMR (471 MHz, CD_3CN) δ -79.03. ^{1}H DOSY NMR (500 MHz, CD_3CN) –logD = 9.35, hydrodynamic radius = 13.2 Å.

162 - OH benzyl ptPEG

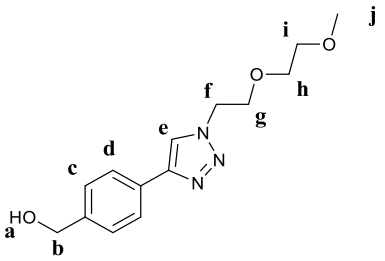

Ethynyl benzyl alcohol (461.8 mg, 3.494 mmol) and azido-2-PEG (507.2 mg, 3.494 mmol) were dissolved in a mixture of water (6 mL) and ^{t}BuOH (6 mL). Sodium ascorbate (10 mol%, 1M in H_2O) and Cu(II)SO_4.5H_2O (1 mol%, 300 mM in H_2O) were charged and immediate precipitation was observed. The mixture was stirred thoroughly at room temperature for 16 h. The mixture was diluted with H_2O (50 mL) and the product was extracted with CH_2Cl_2. The crude product was purified by silica chromatography running 100% CH_2Cl_2 to 10% CH_3OH in CH_2Cl_2 to give a colourless solid (592.3 mg, 61%). ^{1}H NMR (500 MHz, $CDCl_3$) δ 8.02 (s, 1H, H_e), 7.89 – 7.76 (m, 2H, H_d), 7.49 – 7.37 (m, 2H, H_c), 4.74 (d, *J* = 5.3 Hz, 2H, H_b), 4.61 (t, *J* = 5.0 Hz, 2H, H_f), 3.92 (t, *J* = 5.0 Hz, 2H, H_g), 3.66 – 3.62 (m, 2H, H_h), 3.56 – 3.53 (m, 2H, H_i), 3.38 (s, 3H, H_j), 2.17 (bt, *J* = 5.8 Hz, 1H, H_a). ^{13}C NMR (126 MHz, $CDCl_3$) δ 147.47, 140.83, 130.12, 127.43, 125.84, 121.03, 71.75, 70.53, 69.54, 65.02, 59.03, 50.32. *m/z* (HR-ESI): 278.15103 (predicted $[M+H]^+$ = 278.14922), 300.13270 (predicted $[M+Na]^+$ = 300.13240), 577.27589 (predicted $[2M+Na]^+$ = 577.27504). mp (65-67 ºC).

$[(Ir(OHbenzylptPEG)_2)Cl)_2]$

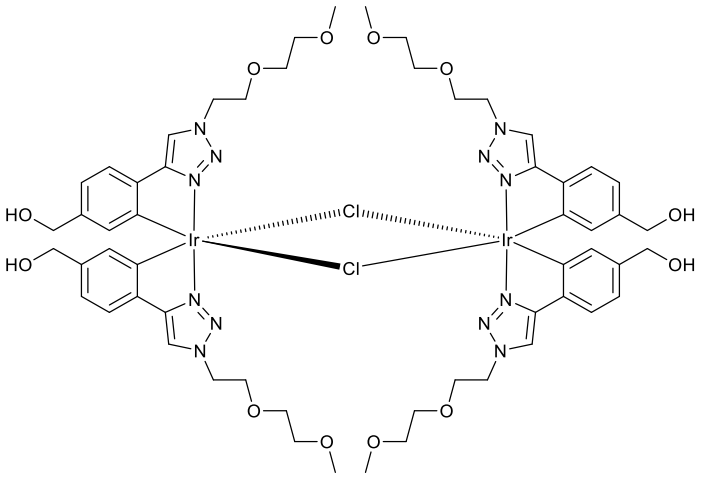

OHbenzylptPEG (204.3 mg, 0.737 mmol) and Na_3IrCl_6 (174.6 mg,0.368 mmol) were partially dissolved in 2-methoxyethanol (100 mL). The mixture was stirred at room temperature until complete dissolution was observed (1 h) and then heated at reflux under N_2 for 16 h. The solvent was removed under vacuum and H_2O (100 mL) charged. The crude product was extracted into CH_2Cl_2 and the solvent was removed under vacuum. Product used without further purification. *m/z* (HR-ESI): See section 3.6.2.

Crude $(Ir(OHbenzylptPEG)_2Cl)_2$ (92.0 mg) and **149** (42.9 mg, 0.118 mmol) were partially dissolved in ethylene glycol (10.0 mL). The mixture was degassed under high-vacuum for 20 mins and backfilled with N_2 before heating at 150 °C for 18 h. The solution was then cooled and diluted with H_2O (50 mL) before being washed with Et_2O (2 x 25 mL). KOTf (66.6 mg, 0.354 mmol) was charged but no precipitate was observed. The solvent was removed under reduced pressure and the crude product purified by silica chromatography running 100% CH_2Cl_2 to 10% CH_3OH in CH_2Cl_2. Two different products were isolated:

164·OTf - [Ir(monoPEG-ptPEG)$_2$(emibipy)]OTf

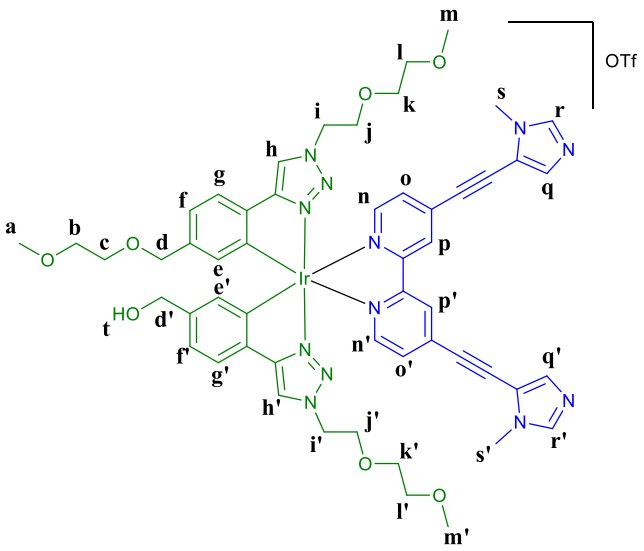

164·OTf. Yield = 17.1 mg, 11%. ^{1}H NMR (500 MHz, CD_3CN) δ 8.54 – 8.45 (m, 2H, H_p, $H_{p'}$), 8.24 – 8.17 (m, 2H, H_h, $H_{h'}$), 8.13 – 8.05 (m, 2H, H_n, $H_{n'}$), 7.79 – 7.65 (m, 2H, H_r, $H_{r'}$), 7.55 – 7.39 (m, 6H, H_f, $H_{f'}$, H_o, $H_{o'}$, H_q, $H_{q'}$), 7.03 – 6.94 (m, 2H, H_g, $H_{g'}$), 6.23 – 6.17 (m, 2H, H_e, $H_{e'}$), 4.51 – 4.40 (m, 4H, H_i, $H_{i'}$), 4.38 (s, 2H, $H_{d\ or}$ $H_{d'}$), 4.30 (s, 2H, $H_{d\ or}$ $H_{d'}$), 3.84 – 3.73 (m, 10H, H_j, $H_{j'}$, H_s, $H_{s'}$), 3.52 – 3.42 (m, 8H, H_b, H_c, H_k, $H_{k'}$), 3.38 – 3.32 (m, 4H, H_l, $H_{l'}$), 3.27 (s, 3H, H_a), 3.21 – 3.19 (m, 6H, H_m, $H_{m'}$). ^{13}C NMR (126 MHz, CD_3CN) δ 157.37, 157.33, 152.11, 146.60, 141.68, 139.58, 137.83, 136.12, 134.30, 132.60, 128.98, 125.80, 123.53, 123.16, 122.10 (q, *J* = 320.8 Hz), 121.23, 115.33, 93.90, 87.46, 73.76, 72.53, 72.37, 70.91, 70.30, 69.32, 58.92, 58.90, 52.88, 32.80. Unable to distinguish all 13C peaks due to partial desymmetrisation. ^{19}F NMR (471 MHz, CD_3CN) δ -79.31. *m/z* (HR-ESI): 1167.41400 (predicted $[M]^+$ = 1167.41754).

165·OTf - [Ir(diPEG-ptPEG)$_2$(emibipy)]OTf

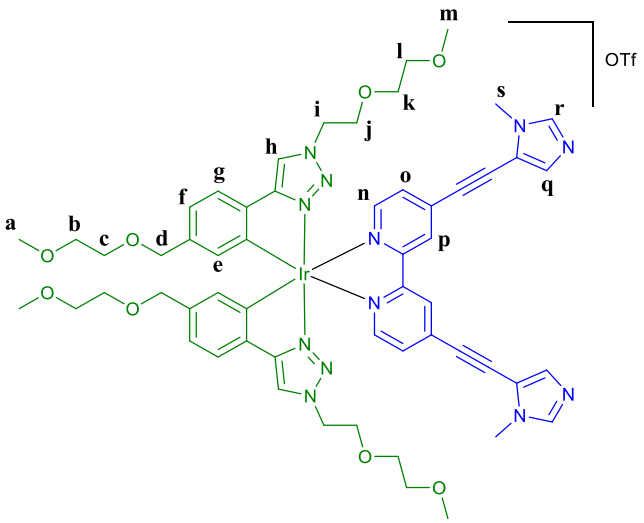

165·OTf. Yield = 11.5mg, 7%. ^{1}H NMR (500 MHz, CD_3CN) δ 8.55 (d, *J* = 1.5 Hz, 2H, H_p), 8.21 (s, 2H, H_h), 8.11 – 8.04 (m, 2H, H_n), 7.63 (s, 2H, H_r), 7.52 (d, *J* = 7.7 Hz, 2H, H_o), 7.50 – 7.46 (m, 2H, H_f), 7.43 (d, *J* = 0.9 Hz, 2H, H_q), 6.99 (dd, *J* = 7.8, 1.6 Hz, 2H, H_g), 6.20 (d, *J* = 1.5 Hz, 2H, H_e), 4.51 – 4.37 (m, 4H, H_i), 4.30 (s, 4H, H_d), 3.83 – 3.73 (m, 4H, H_j), 3.77 (s, 6H, H_s), 3.53 – 3.41 (m, 12H, H_b, H_c, H_k), 3.39 – 3.31 (m, 4H, H_l), 3.27 (s, 6H, H_a), 3.21 (s, 6H, H_m). ^{13}C NMR (126 MHz, CD_3CN) δ 157.37 , 157.33 , 152.11 , 146.60 , 141.68 , 139.58 , 137.83 , 136.12 , 134.30 , 132.60 , 128.98 , 125.80 , 123.53 , 123.16 , 121.23 , 115.33 , 93.90 , 87.46 , 73.76 , 72.53 , 72.37 , 70.91 , 70.30 , 69.32 , 58.92 , 58.90 , 52.88 , 32.80 . ^{19}F NMR (471 MHz, CD_3CN) δ -79.31. ^{1}H DOSY NMR (500 MHz, CD_3CN) –logD = 9.08, hydrodynamic radius = 7.1 Å. *m/z* (HR-ESI): 1225.45660 (predicted $[M]^+$ = 1225.45940).

166·8OTf - [Pd$_2$(Ir(PEGptPEG)$_2$emibipy)$_4$]OTf

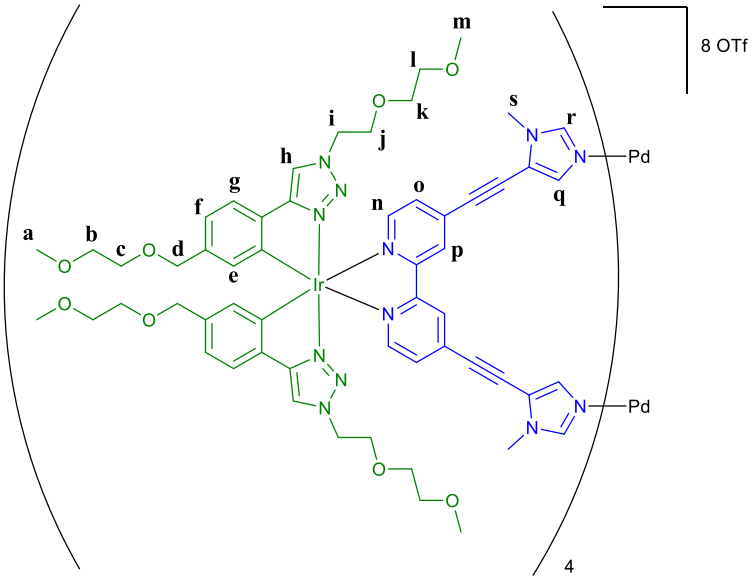

[Ir(PEGptPEG)$_2$emibipy]OTf (5.7 mg, 3.78 µmol) was dissolved in CD_3CN (0.5 mL). [Pd$(CH_3CN)_4$·2OTf] (1.08 mg, 1.90 µmol) was charged as a solution in CD_3CN. The solution was left at room temperature for 16 h to give a bright red solution (100% by NMR). Product not isolated. ^{1}H NMR (500 MHz, CD_3CN) δ 8.69 (m, 8H, H_p), 8.25 – 8.13 (m, 16H, H_h, H_r), 8.15 – 8.04 (m, 8H, H_n), 7.77 (m, 8H, H_q), 7.58 – 7.46 (m, 16H, H_f, H_o), 7.03 – 6.95 (m, 8H, H_g), 6.15 (m, 8H, H_e), 4.48 – 4.32 (m, 16H, H_i), 4.28 (s, 16H, H_d), 3.75 (m, 24H, H_s), 3.83 – 3.66 (m, 16H, H_j), 3.54 – 3.36 (m, 48H, H_b, H_c, H_k), 3.34 – 3.26 (m, 16H, H_l), 3.25 (m, 24H, H_m), 3.14 (m, H_a). ^{13}C NMR (126 MHz, CD_3CN) δ 157.37, 157.33, 152.11, 146.60, 141.68, 139.58, 137.83, 136.12, 134.30, 132.60, 128.98, 125.80, 123.53, 123.16, 122.10 (q, *J* = 320.7 Hz), 121.23, 115.33, 93.90, 87.46, 73.76, 72.53, 72.37, 70.91, 70.30, 69.32, 58.92, 58.90, 52.88, 32.80. *HSQC confirmed peak at 58.94 represents two overlapping carbon environments. ^{19}F NMR (471 MHz, CD_3CN) δ -79.08. ^{1}H DOSY NMR (500 MHz, CD_3CN) –logD = 9.41, hydrodynamic radius = 15.2 Å.

$[(Ir(pt\text{-}ester)_2Cl)_2]$

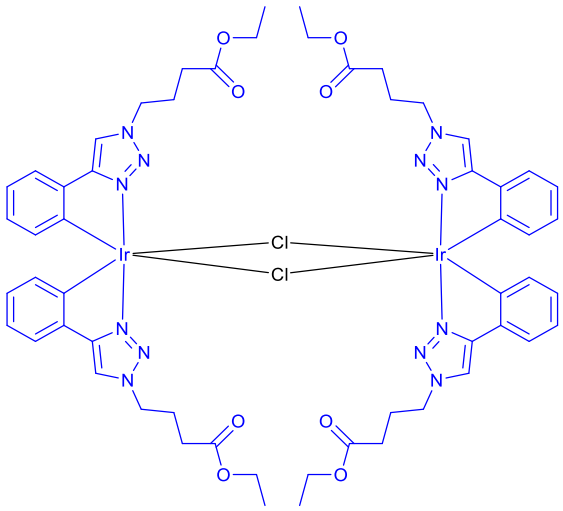

Ethylbutylate phenyl triazole (228.5 mg, 0.881 mmol) and Na_3IrCl_6 (208.8 mg, 0.441 mmol) were partially dissolved in 2-methoxyethanol (100 mL). The mixture was stirred at room temperature until complete dissolution was observed (1 h) and then heated at reflux under N_2 for 16 h. The solvent was removed under vacuum and H_2O (100 mL) charged. The crude product was extracted into $CHCl_3$, dried over $MgSO_4$ and the solvent was removed under vacuum. A solid was isolated re-dissolving the crude product in CH_3CN followed by precipitation with Et_2O. The solid was filtered, washed with Et_2O and dried under vacuum to give a beige solid (260.0 mg, 79%). Used without further purification. *m/z* (HR-ESI): 709.20640 (predicted $[ML_2]^+$ = 709.21090), 750.23390 (predicted $[ML_2(CH_3CN)]^+$ = 750.23745), 791.26020 (predicted $[ML_2(CH_2CN)_2]^+$ = 791.26400).

167·OTf - [Ir(pt-ester)$_2$(emibipy)]OTf

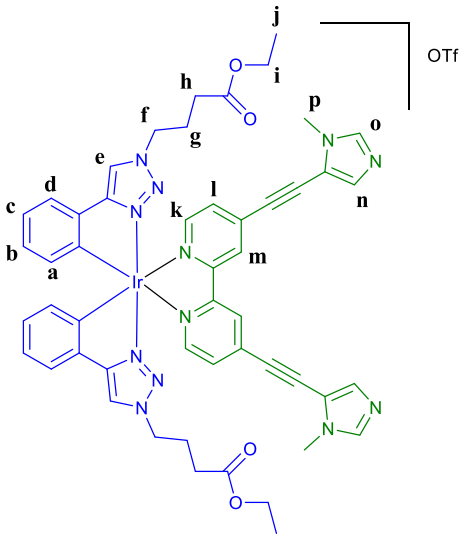

Crude (Ir(pt-ester)$_2$Cl)$_2$ (30.9 mg) and **149** (15.1 mg, 0.041 mmol) were partially dissolved in ethylene glycol (5.0 mL). The solution was degassed under high-vacuum for 20 mins and backfilled with N_2 before heating at 150 °C for 16 h. The solution was then cooled and diluted with H_2O (50 mL) before being washed with Et_2O (2 x 25 mL). KOTf (23.4 mg, 0.124 mmol) was charged and the resultant precipitate filtered onto celite, washed with water and dried under vacuum. The product was washed off the celite with CH_2Cl_2 and the solvent removed under vacuum. The crude product was purified by silica chromatography running 100% CH_2Cl_2 to 10% CH_3OH in CH_2Cl_2 to give the product as a bright orange solid (15.3 mg, 30%). ^{1}H NMR (500 MHz, CD_3CN) δ 8.55 (d, *J* = 1.6 Hz, 2H, H_m), 8.13 (s, 2H, H_e), 8.10 (d, *J* = 5.8 Hz, 2H, H_k), 7.64 (s, 2H, H_o), 7.53 (dd, J = 7.6, 0.9 Hz, 2H, H_d), 7.50 (dd, *J* = 5.7, 1.6 Hz, 2H, H_l), 7.44 (s, 2H, H_n), 7.06 – 6.97 (m, 2H, H_c), 6.92 – 6.83 (m, 2H, H_b), 6.27 (d, *J* = 7.3 Hz, 2H, H_a), 4.34 (t, *J* = 6.9 Hz, 4H, H_f), 4.00 (q, *J* = 7.1 Hz, 4H, H_i), 3.78 (s, 6H, H_p), 2.21 (t, *J* = 6.9 Hz, 4H, H_h), 2.08 (m, 4H, H_g), 1.16 (t, *J* = 7.1 Hz, 6H, H_j). ^{13}C NMR (126 MHz, CD_3CN) δ 172.93, 157.67, 157.39, 152.16, 146.66, 141.68, 137.80, 136.82, 134.24, 133.45, 129.28, 128.92, 125.75, 123.79, 123.35, 120.83, 93.91, 87.34, 61.24, 51.95, 32.81, 31.12, 25.73, 14.51. ^{19}F NMR (376 MHz, CD_3CN) δ -79.33. ^{1}H DOSY NMR (500 MHz, CD_3CN) –logD = 9.06, hydrodynamic radius = 6.8 Å. *m/z* (HR-ESI): 1073.35140 (predicted $[M]^+$ = 1073.35454).

168·OTf - [Ir(pt-acid)$_2$(emibipy)]OTf

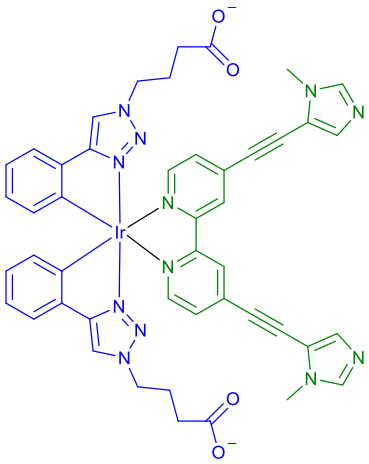

[Ir(pt-ester)$_2$(emibipy)]OTf (3.7 mg, 3.03 µmol) was dissolved in a mixture of CH_3OH (0.2 mL) and CH_2Cl_2 (1.8 mL). NaOH (2M in CH_3OH, 9.08 µmol) was charged and stirred at room temperature for 72 h. The solvent removed under vacuum and the residue re-dissolved in D_2O for analysis. Compound not isolated pure.

171·8OTf - [Pd$_2$(Ir(pt-ester)$_2$(emibipy))$_4$]8OTf

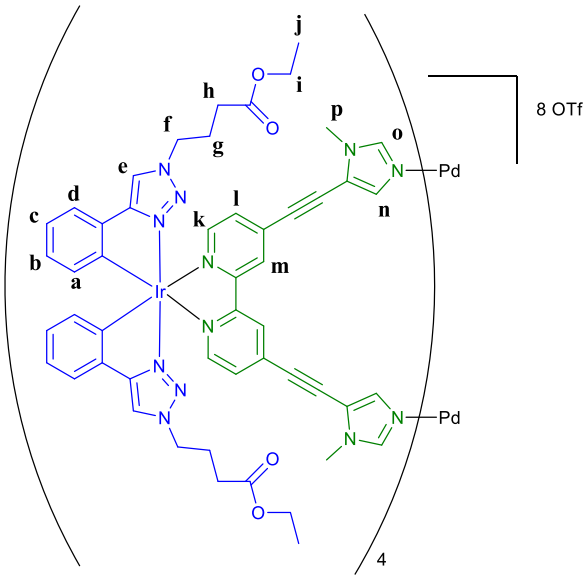

[Ir(pt-ester)$_2$emibipy]OTf (2.6 mg, 2.13 µmol) was dissolved in CD_3CN (0.5 mL). [Pd$(CH_3CN)_4$·2OTf] (0.61 mg, 1.07 µmol) was charged as a solution in CD_3CN. The mixture was left at room temperature for 16 h to give a bright red solution (100% by NMR). Product not isolated. ^{1}H NMR (500 MHz, CD_3CN) δ 8.73 – 8.56 (m, 8H, H_m), 8.21 – 8.14 (m,

8H, H_o), 8.14 – 8.05 (m, 16H, H_e, H_k), 7.78 – 7.70 (m, 8H, H_n), 7.57 – 7.49 (m, 16H, H_d, H_l), 7.03 – 6.96 (m, 8H, H_c), 6.90 – 6.81 (m, 8H, H_b), 6.26 – 6.16 (m, 8H, H_a), 4.33 – 4.23 (m, 16H, H_f), 3.96 – 3.87 (m, 16H, H_i), 3.79 – 3.70 (m, 24H, H_p), 2.20 – 2.14 (m, 16H, H_h), 2.05 – 1.98 (m, 16H, H_g), 1.10 – 1.02 (m, 24H, H_j). ^{13}C NMR (126 MHz, CD_3CN) δ 172.88, 157.69, 157.23, 152.50, 146.20, 142.23, 136.71, 135.33, 133.37, 133.04, 129.35, 128.77, 126.65, 123.92, 123.39, 120.92, 117.71, 94.98, 83.35, 61.18, 51.90, 34.47, 31.09, 25.69, 14.50. ^{19}F NMR (471 MHz, CD_3CN) δ -79.04. ^{1}H DOSY NMR (500 MHz, CD_3CN) –logD = 9.36, hydrodynamic radius = 13.6 Å.

Butyl phthalimide phenyl triazole

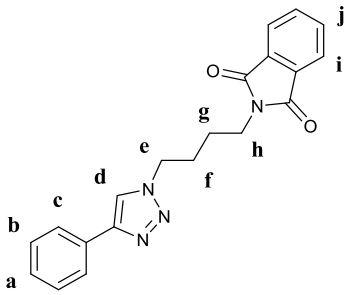

Phenylacetylene (218.8 mg, 2.142 mmol) and azido butylphthalimide (523.3 mg, 2.142 mmol) were dissolved in a mixture of water (6 mL) and ^{t}BuOH (6 mL). Sodium ascorbate (10 mol%, 1M in H_2O) and Cu(II)SO_4.5H_2O (1 mol%, 300 mM in H_2O) were charged and immediate precipitation was observed. The mixture was stirred thoroughly at 60 ºC for 6 h. The mixture was diluted with H_2O (50 mL) and the product was extracted with CH_2Cl_2. The organic layer was dried over $MgSO_4$ and the solvent removed under vacuum to yield a yellow oil. The product was purified by silica chromatography in CH_2Cl_2 to give a colourless solid (242.6 mg, 33%). ^{1}H NMR (500 MHz, $CDCl_3$) δ 7.87 – 7.79 (m, 4H, H_c, H_i), 7.78 (s, 1H, H_d), 7.74 – 7.68 (m, 2H, H_j), 7.45 – 7.38 (m, 2H, H_b), 7.35 – 7.28 (m, 1H, H_a), 4.46 (t, *J* = 7.2 Hz, 2H, H_e), 3.75 (t, *J* = 6.9 Hz, 2H, H_h), 2.10 – 1.93 (m, 2H, H_f), 1.84 – 1.71 (m, 2H, H_g). ^{13}C NMR (126 MHz, $CDCl_3$) δ 168.51, 147.96, 134.20, 132.12, 130.77, 128.94, 128.22, 125.85, 123.45, 119.73, 49.69, 37.00, 27.68, 25.70. mp (116-130 ºC). *m/z* (HR-ESI): 347.15200 (predicted $[M+H]^+$ = 347.15025), 369.13350 (predicted $[M+Na]^+$ = 369.13220).

[(Ir(pt-phthN)$_2$Cl)$_2$]

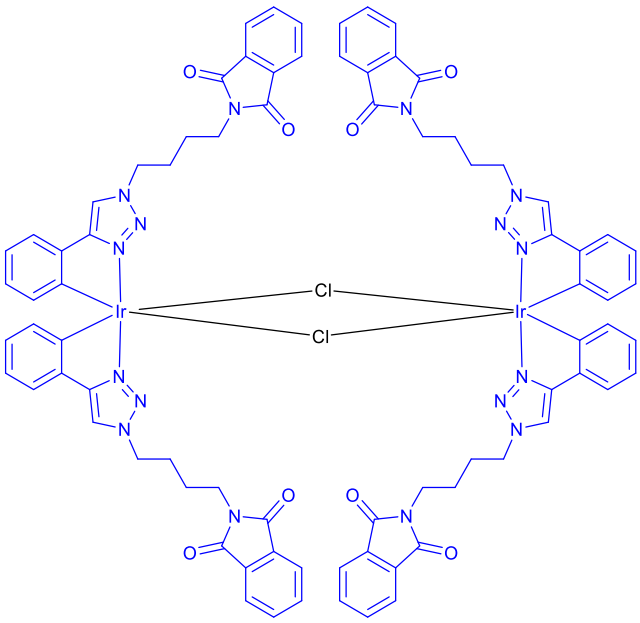

Butylphthalimide phenyl triazole (153.2 mg, 0.442 mmol) and Na_3IrCl_6 (104.5 mg, 0.221 mmol) were partially dissolved in 2-methoxyethanol (10 mL). The mixture was stirred at room temperature until complete dissolution was observed (1 h) and then heated at reflux under N_2 for 16 h. EtOH (20 mL) was charged and the resultant solid filtered. The crude product was suspended in H_2O, extracted into $CHCl_3$, dried over $MgSO_4$ and the solvent was removed under vacuum to give a beige/green semi-solid (107.7 mg, 53%). Used without further purification. *m/z* (HR-ESI): 883.23460 (predicted $[Ir(C\text{^}N)_2]^+$ = 883.23270), 924.26110 (predicted $[Ir(C\text{^}N)_2(CH_3CN)]^+$ = 924.25924), 965.28730 (predicted $[Ir(C\text{^}N)_2(CH_3CN)_2]^+$ = 965.28579).

169·OTf - [Ir(pt-phthN)$_2$(emibipy)]OTf

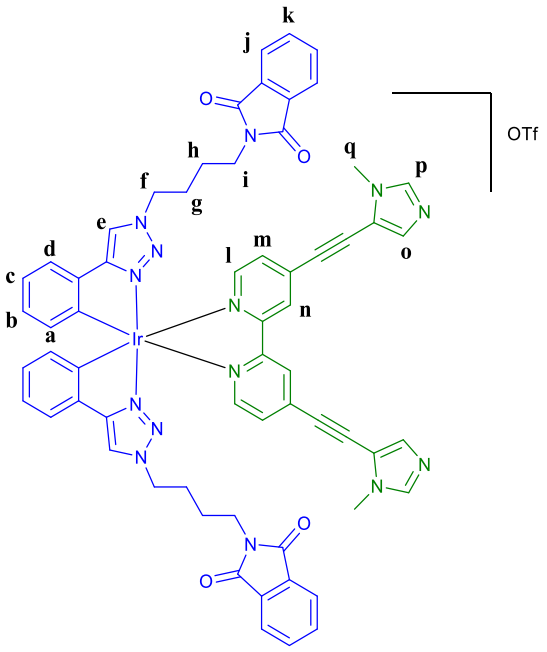

Crude (Ir(pt-phthN)$_2$Cl)$_2$ (50.2 mg) and **149** (19.9 mg, 0.055 mmol) were partially dissolved in ethylene glycol (8.0 mL). The solution was degassed under high-vacuum for 20 mins and backfilled with N_2 before heating at 150 °C for 16 h. The solution was then cooled and diluted with H_2O (50 mL) before being washed with Et_2O (2 x 25 mL). KOTf (30.9 mg, 0.164 mmol) was charged and the resultant precipitate filtered onto celite, washed with water and dried under vacuum. The product was washed off the celite with CH_2Cl_2 and the solvent removed under vacuum. The crude product was purified by silica chromatography running 100% CH_2Cl_2 to 10% CH_3OH in CH_2Cl_2 to give the product as a bright orange solid (58.1 mg, 76%). ^{1}H NMR (500 MHz, CD_3CN) δ 8.50 (dd, *J* = 1.7, 0.7 Hz, 2H, H_n), 8.11 (s, 2H, H_e), 8.07 (dd, *J* = 5.7, 0.7 Hz, 2H, H_l), 7.81 – 7.74 (m, 4H, H_j), 7.74 – 7.68 (m, 4H, H_k), 7.64 (s, 2H, H_p), 7.52 – 7.49 (m, 2H, H_d), 7.43 (dd, *J* = 5.7, 1.6 Hz, 2H, H_m), 7.41 (s, 2H, H_o), 7.01 – 6.94 (m, 2H, H_c), 6.89 – 6.83 (m, 2H, H_b), 6.24 (d, *J* = 7.2 Hz, 2H, H_a), 4.33 (t, *J* = 6.7 Hz, 4H, H_f), 3.73 (s, 6H, H_q), 3.57 – 3.34 (m, 4H, H_i), 1.91 – 1.77 (m, 4H, H_g), 1.63 – 1.46 (m, 4H, H_h). ^{13}C NMR (126 MHz, CD_3CN) δ 169.21, 157.64, 157.35, 152.13, 146.66, 141.63, 137.81, 136.81, 135.07, 134.15, 133.43, 133.10, 129.31, 128.89, 125.77, 123.77, 123.75, 123.32, 120.82, 115.35, 93.95, 87.32, 52.34, 37.59, 32.79, 27.60, 26.01. ^{19}F NMR (471 MHz, CD_3CN) δ -79.31. ^{1}H DOSY NMR (500 MHz, CD_3CN) –logD = 9.07, hydrodynamic radius = 7.0 Å. *m/z* (HR-ESI): 1247.37480 (predicted $[M]^+$ = 1247.37634).

170·OTf - [Ir(pt-NH_2)$_2$(emibipy)]

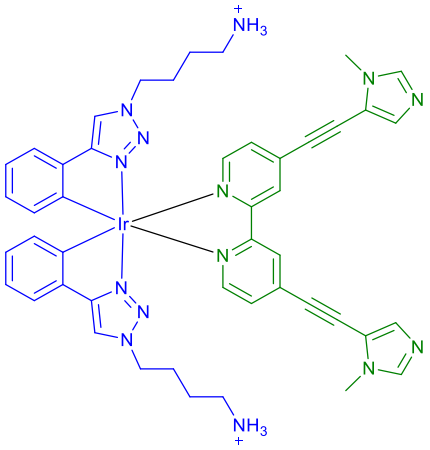

[Ir(pt-phthN)$_2$(emibipy)]OTf (12.1 mg, 8.66 µmol) was dissolved in ethanol (25 mL). Hydrazine hydrate 80% (50 µL) was charged and refluxed under N_2 for 72 h. The solution was cooled, acidified with 1M $HCl_{(aq)}$ and refluxed for 1 h. The solution was cooled and salicylaldehyde (300 µL) was charged and the resultant mixture stirred under N_2 at room temperature for 1 h. The precipitate was extracted with Et_2O and the aqueous layer basified to pH 9-10 with a combination of $NaCO_{3\ (aq)}$ (sat) and $NaOH_{(aq)}$ (2.5 M). The resultant precipitate was filtered, washed with ethanol and re-dissolved in CD_3OH for analysis. Compound not isolated pure.

173·8OTf - $[Pd_2(Ir(pt\text{-}phthN)_2(emibipy))_4]8OTf$

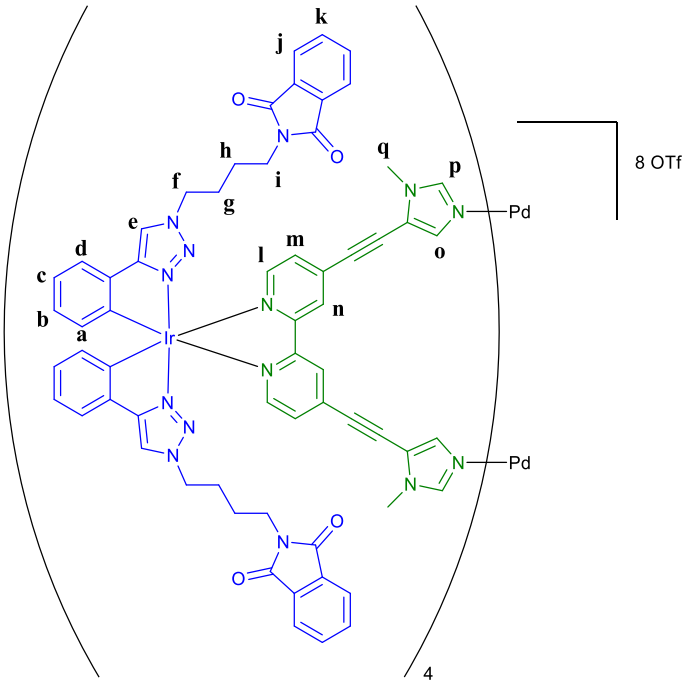

[Ir(pt-phthN)$_2$emibipy]OTf (3.1 mg, 2.22 µmol) was dissolved in CD_3CN (0.5 mL). [Pd(CH_3CN)$_4$·2OTf] (0.63 mg, 1.11 µmol) was charged as a solution in CD_3CN. The mixture was left at room temperature for 16 h to give a bright red solution (100% by NMR). Product not isolated. ^{1}H NMR (500 MHz, CD_3CN) δ 8.60 – 8.57 (m, 8H, H_n), 8.25 – 8.19 (m, 8H, H_p), 8.13 – 8.08 (m, 8H, H_l), 8.07 (s, 8H, H_e), 7.82 – 7.76 (m, 8H, H_o), 7.67 – 7.61 (m, 16H, H_j), 7.61 – 7.56 (m, 16H, H_k), 7.51 – 7.43 (m, 16H, H_d, H_m), 7.01 – 6.94 (m, 8H, H_c), 6.87 – 6.81 (m, 8H, H_b), 6.21 – 6.16 (m, 8H, H_a), 4.28 – 4.20 (m, 16H, H_f), 3.76 – 3.68 (m, 24H, H_q), 3.37 – 3.31 (m, 16H, H_i), 1.78 – 1.69 (m, 16H, H_g), 1.45 – 1.37 (m, 16H, H_h). ^{13}C NMR too complex/weak for full analysis. ^{19}F NMR (471 MHz, CD_3CN) δ -79.05. ^{1}H DOSY NMR (500 MHz, CD_3CN) –logD = 9.35, hydrodynamic radius = 13.2 Å.

4.6.3 Mass Spectrometry of Cage Compounds

156·8OTf - $[Pd_2(Ir(Phppy)_2emibipy)_4]8OTf$

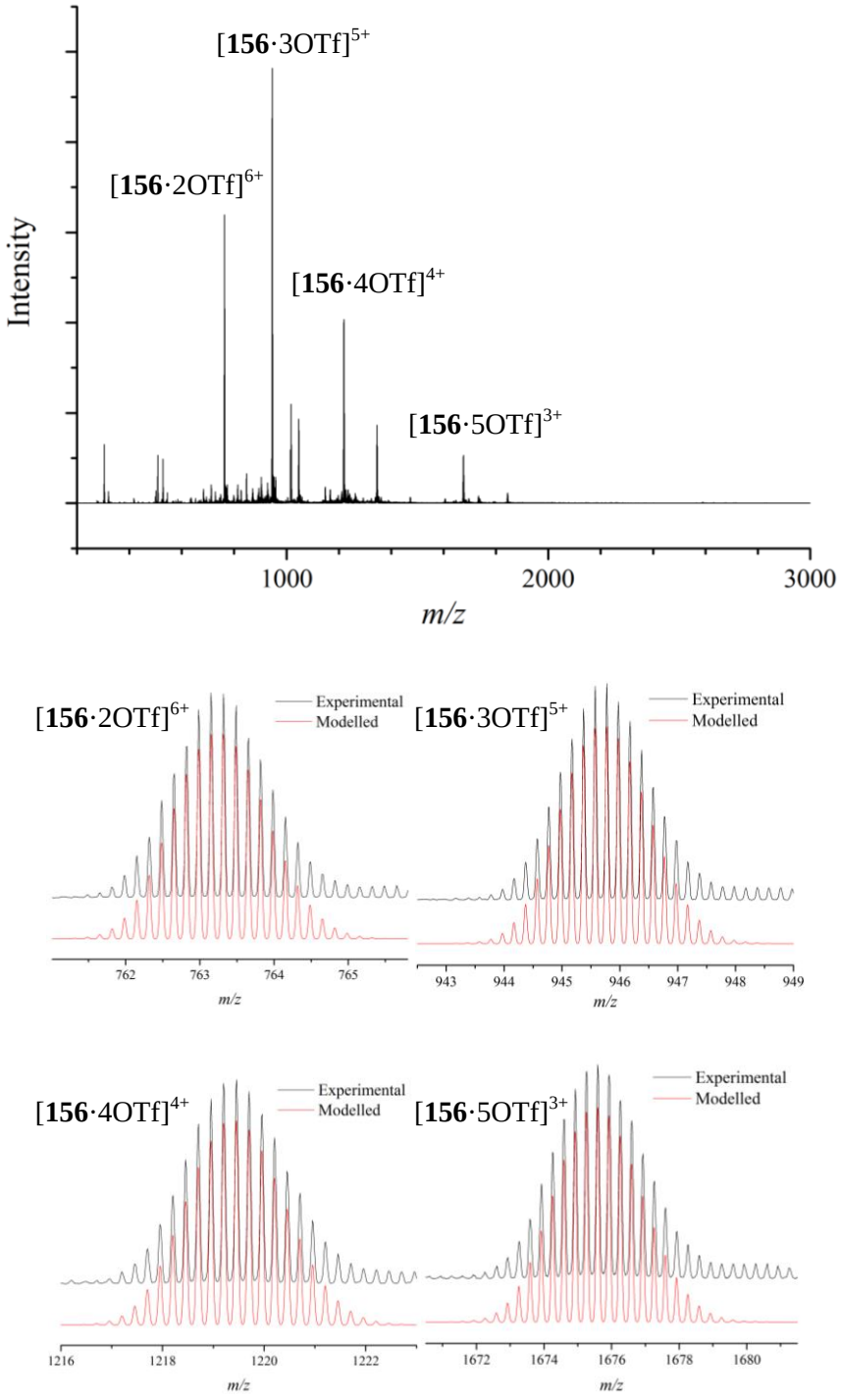

*Figure 4.15: ESI-MS of **156**·8OTf. The peaks found by experiment (black) are shown in comparison with their modelled isotopic distributions (red).*

157·8OTf - $[Pd_2(Ir(^iPr_2Phppy)_2emibipy)_4]8OTf$

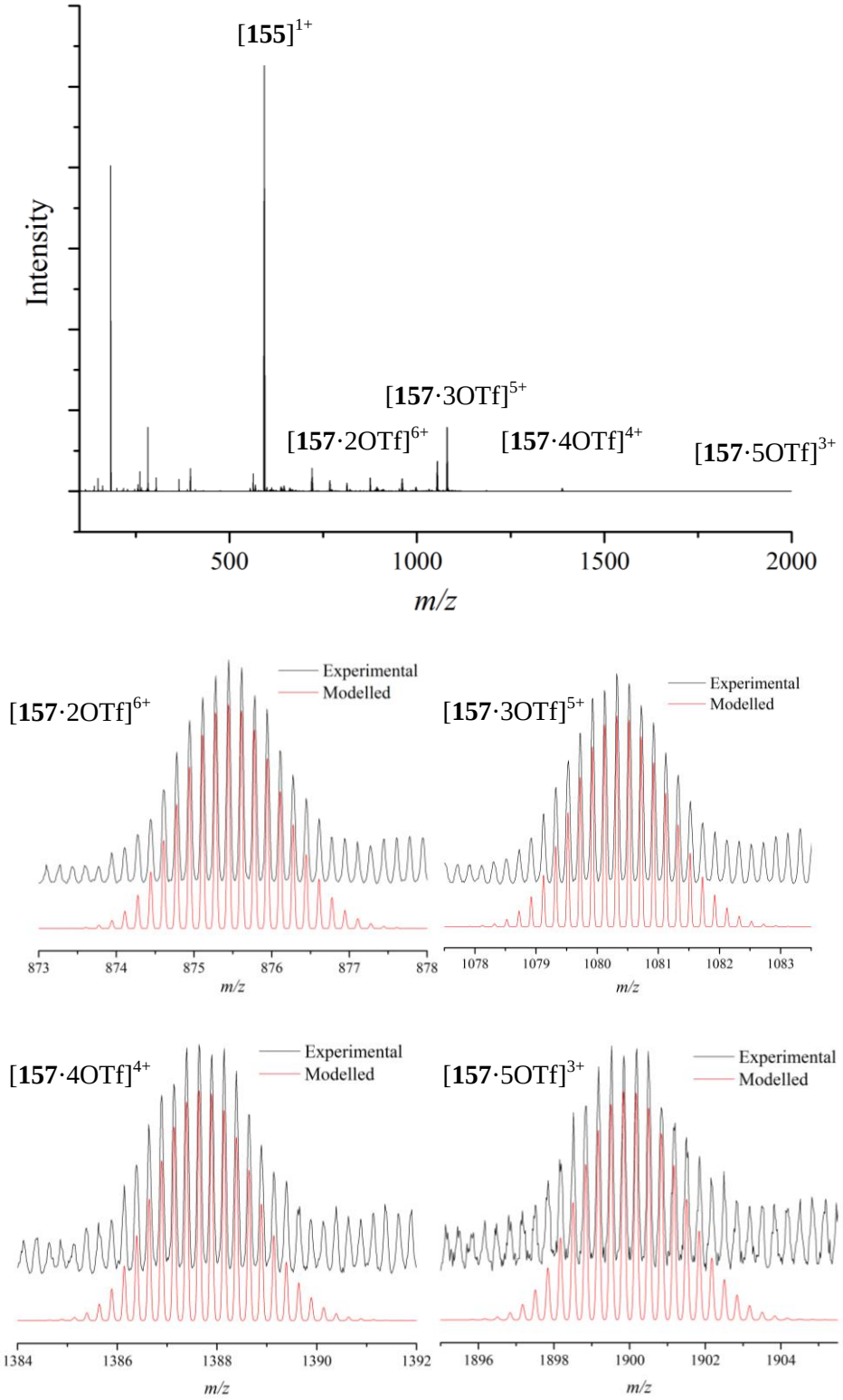

*Figure 4.16: ESI-MS of **157**·8OTf. The peaks found by experiment (black) are shown in comparison with their modelled isotopic distributions (red).*

160·8OTf - $[Pd_2(Ir(ptPEG)_2emi)_4]OTf$

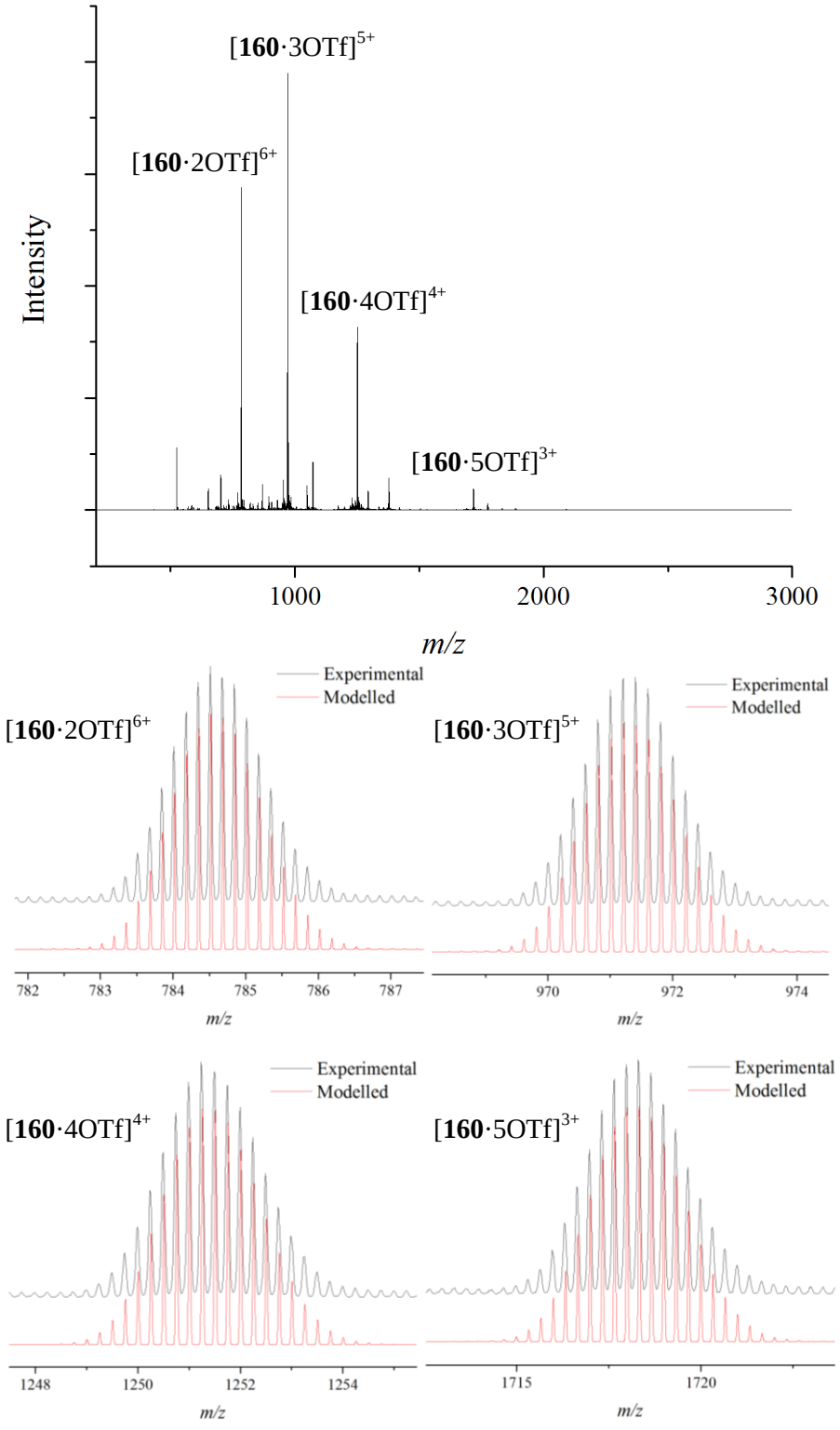

*Figure 4.17: ESI-MS of **160**·8OTf. The peaks found by experiment (black) are shown in comparison with their modelled isotopic distributions (red).*

166·8OTf - $[Pd_2(Ir(PEGptPEG)_2emi)_4]OTf$

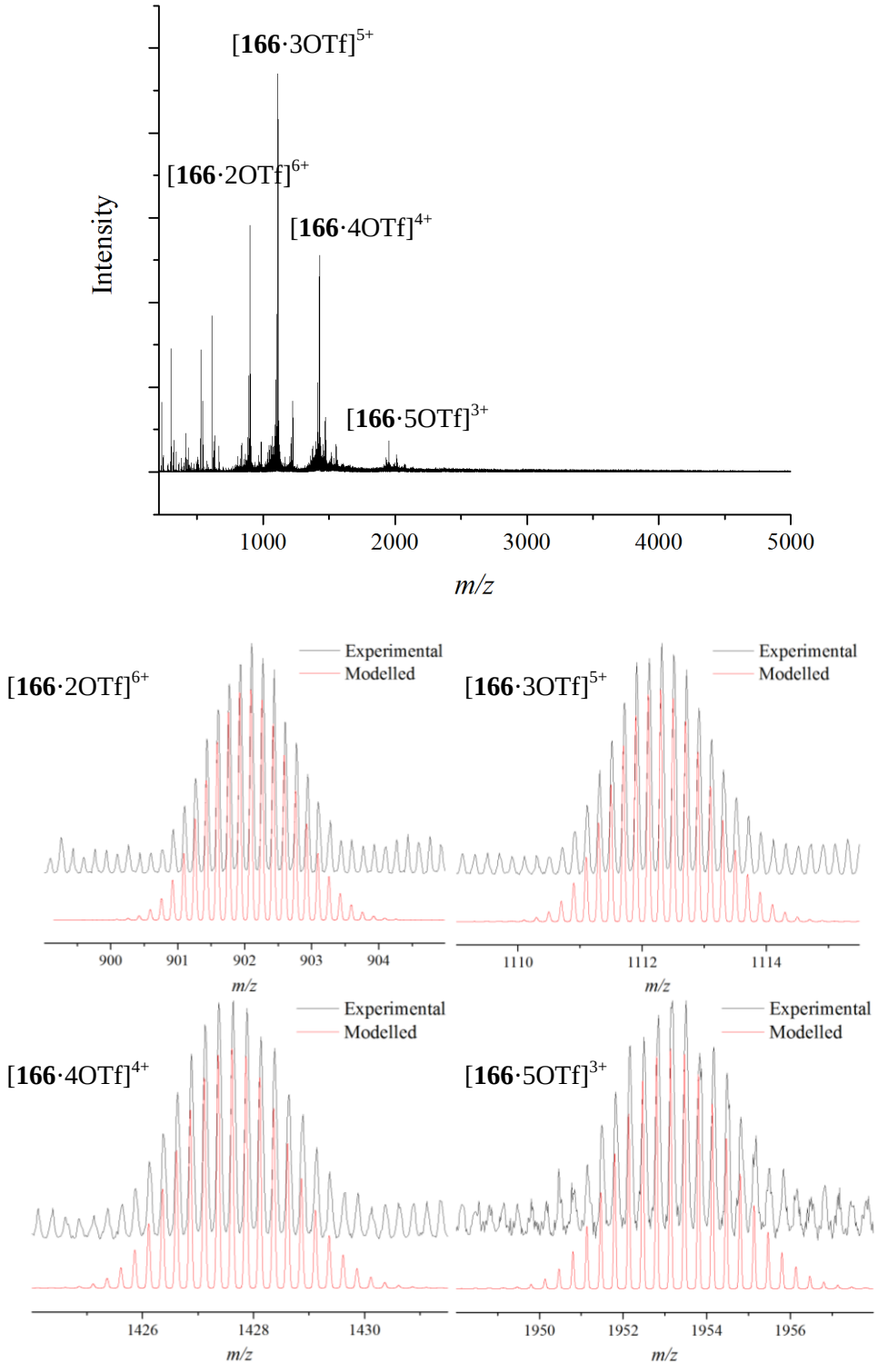

*Figure 4.18: ESI-MS of **166**·8OTf. The peaks found by experiment (black) are shown in comparison with their modelled isotopic distributions (red).*

171·8OTf - $[Pd_2(Ir(pt\text{-}ester)_2emi)_4]OTf$

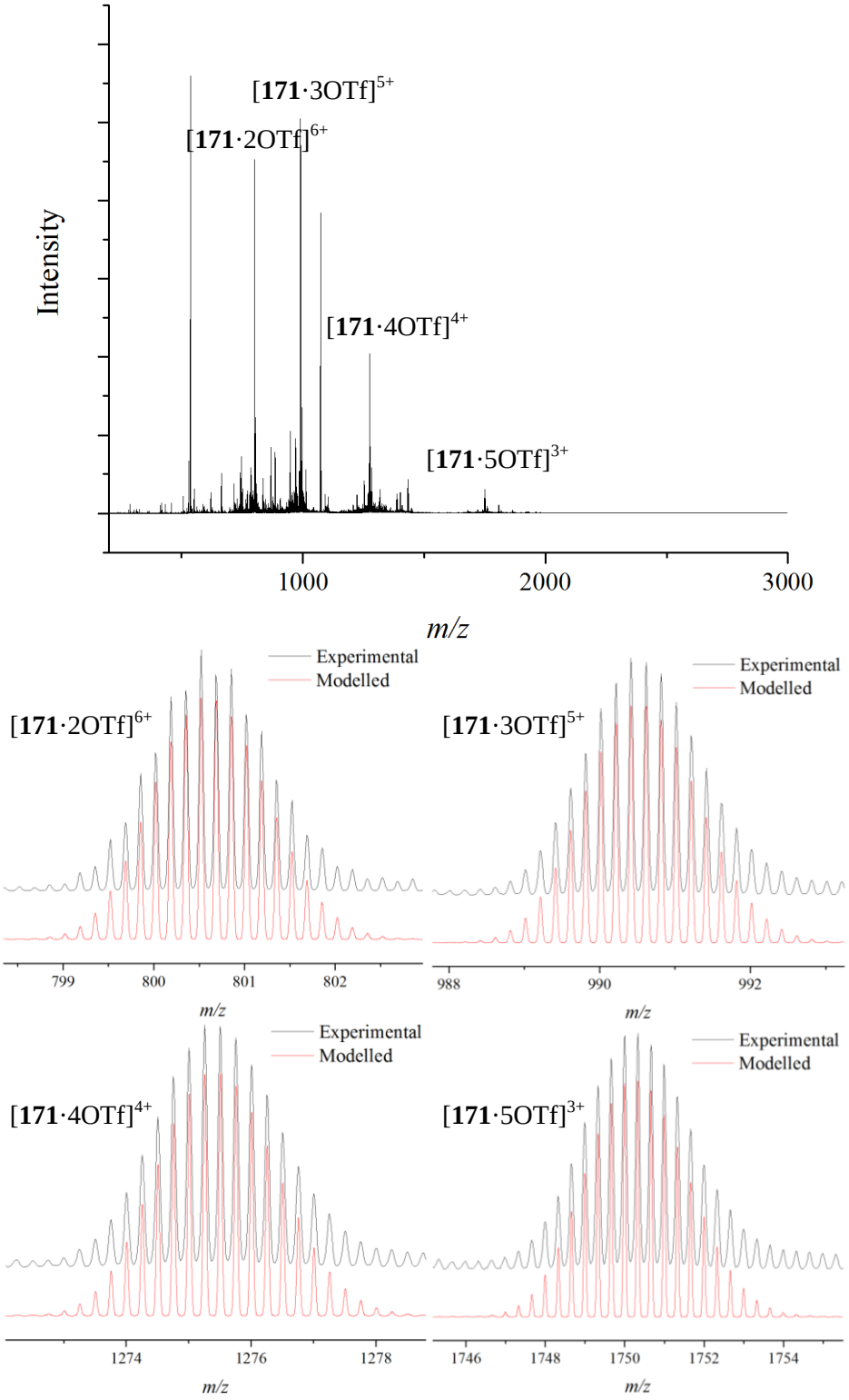

*Figure 4.19: ESI-MS of **171**·8OTf. The peaks found by experiment (black) are shown in comparison with their modelled isotopic distributions (red).*

173·8OTf - $[Pd_2(Ir(pt\text{-}phthN)_2emibipy)_4]OTf$

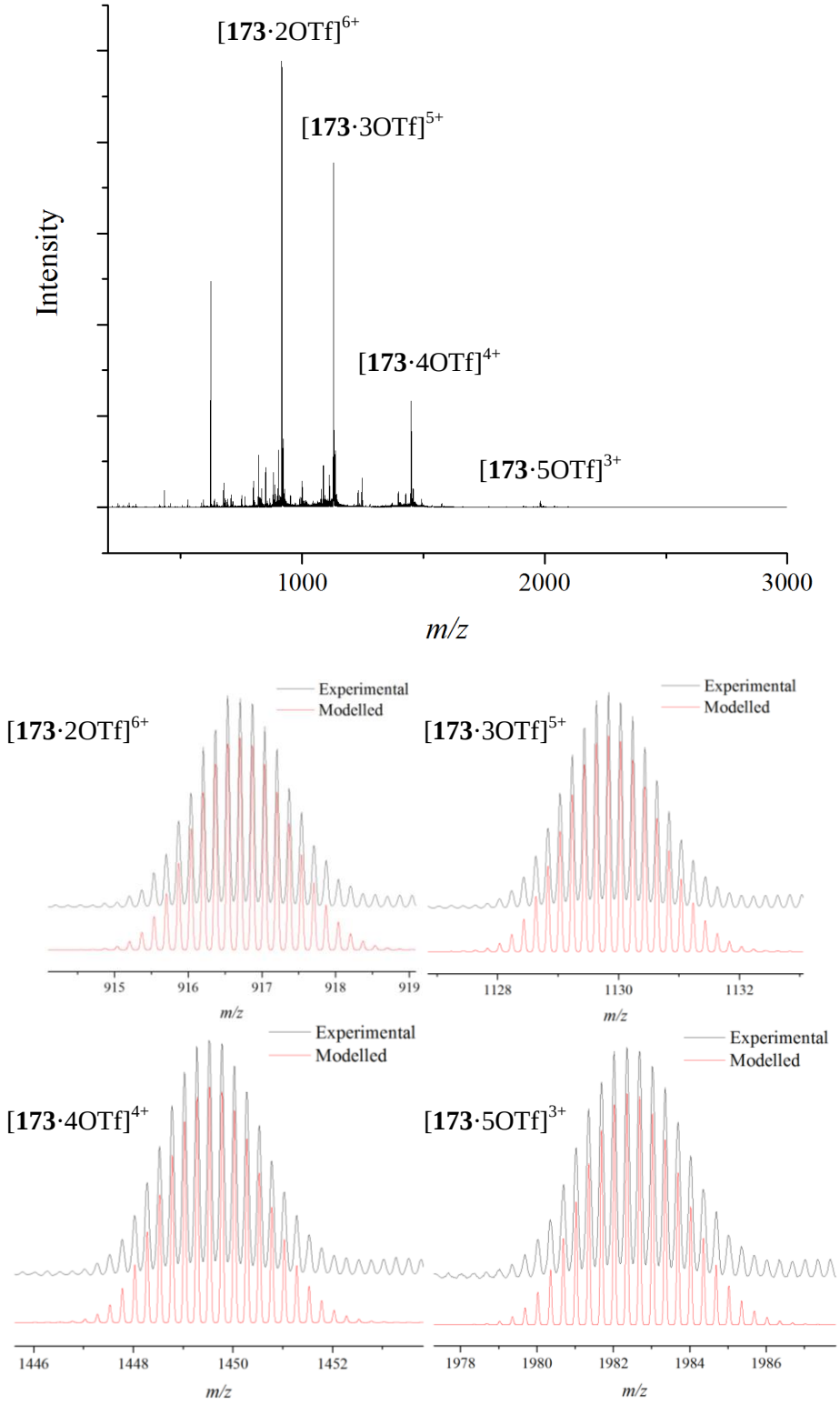

*Figure 4.20: ESI-MS of **173**·8OTf. The peaks found by experiment (black) are shown in comparison with their modelled isotopic distributions (red).*

4.6.4 Stability of 156·8OTf

The stability of **156**·8OTf was assessed using an analogous method to that outlined for **151**·8OTf in Chapter 3.

4.6.5 Guest Binding

All guest binding experiments were carried out following the procedures outlined in Chapter 3.

4.6.5 Photophysics of 156·8OTf

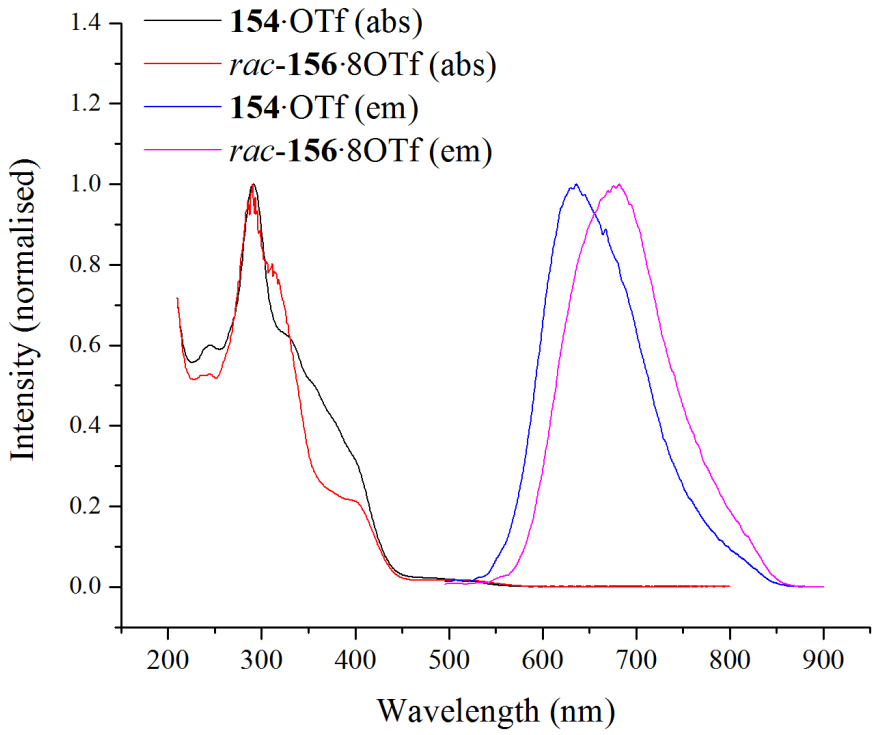

*Figure 4.21: Absorbance and emission (CH_3CN, 300 K) of **154**·OTf and **156**·8OTf.*

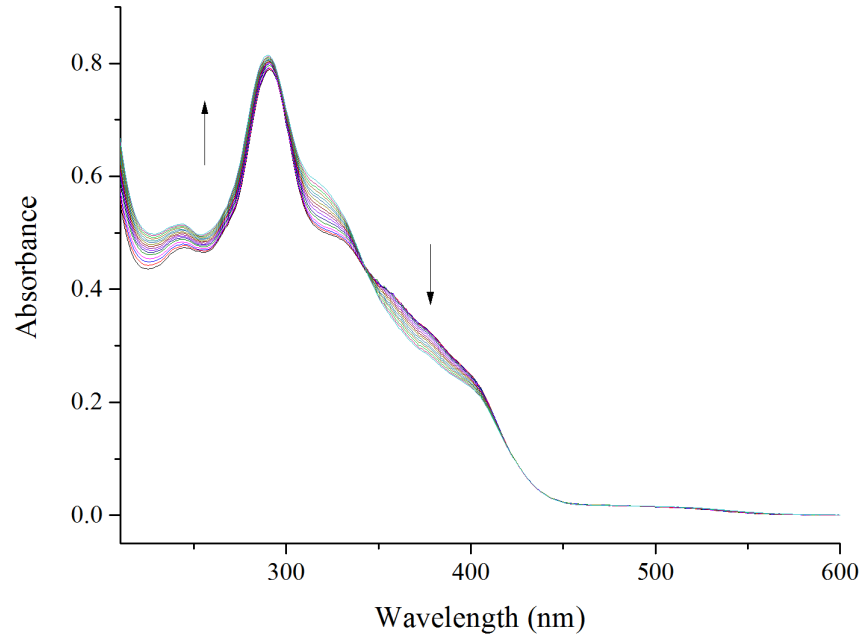

*Figure 4.22: The addition of Pd^{2+} to **154**·OTf monitored by absorbance (CH_3CN, 300 K). A similar decrease in the ^{1}MLCT bands and increase in the LC bands was observed compared with the original **151**·8OTf system.*

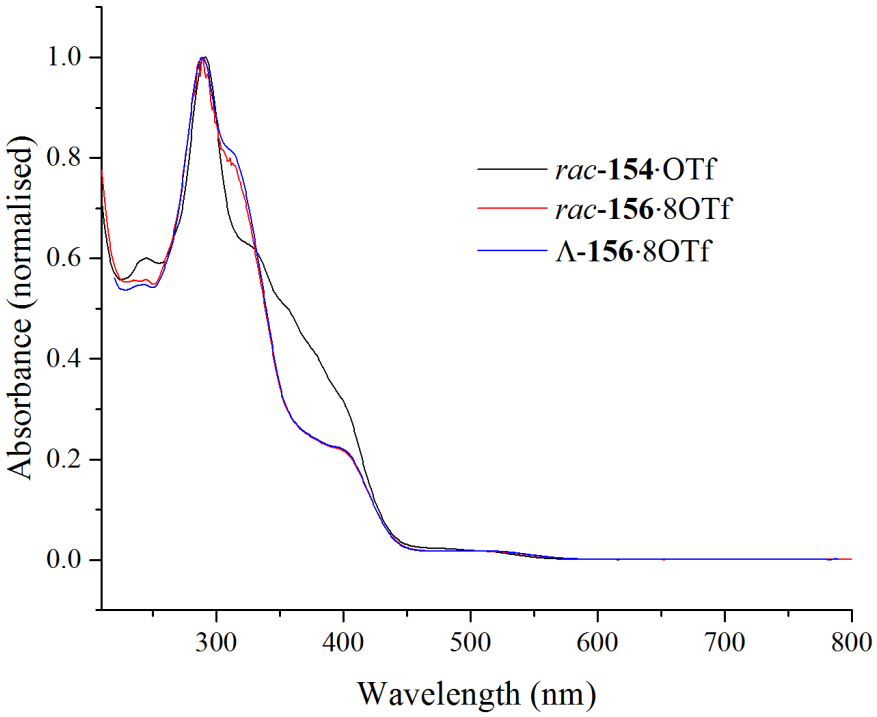

*Figure 4.23: Absorbance and emission (CH_3CN, 300 K) of racemic and enantiopure **156**·8OTf.*

4.6.6 Electrochemistry of 154·OTf and 156·8OTf

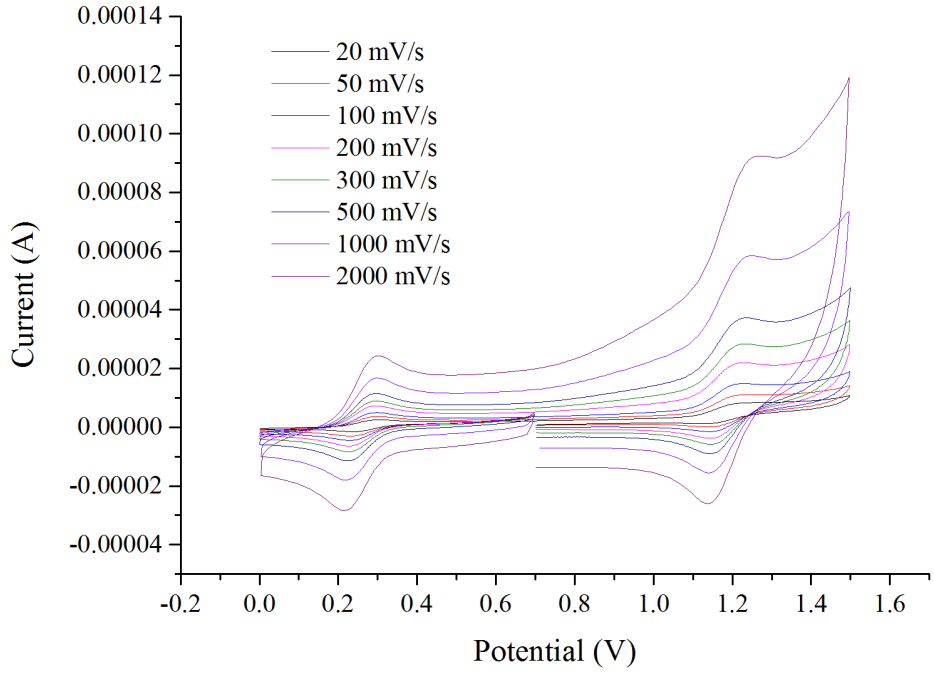

*Figure 4.24: Oxidation of **154**·OTf in CH_3CN versus Ag/Ag^+ with ferrocene as an internal standard.*

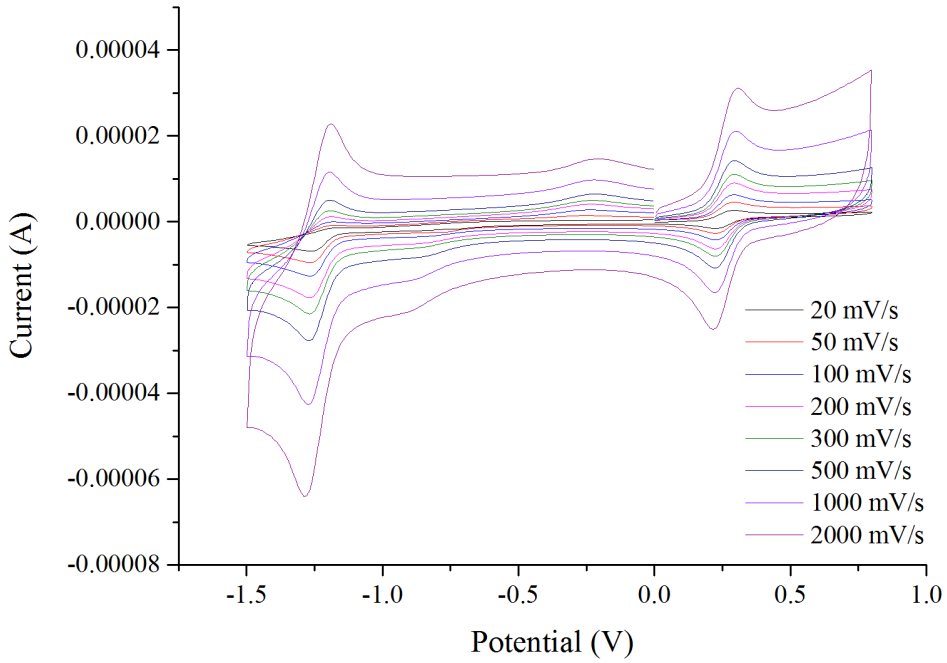

*Figure 4.25: Reduction of **154**·OTf in CH_3CN versus Ag/Ag^+ with ferrocene as an internal standard.*

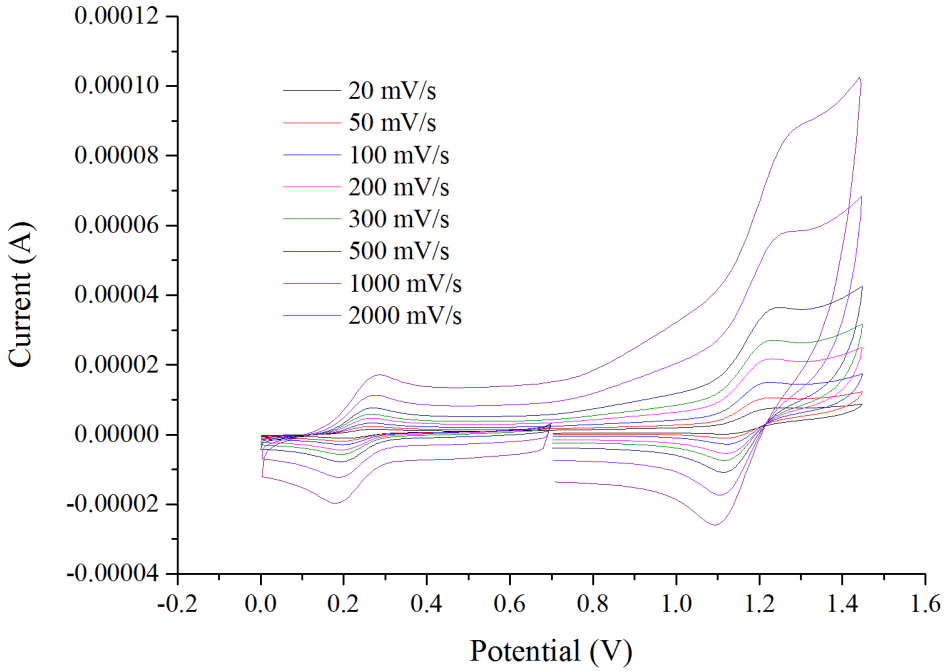

*Figure 4.26: Oxidation of **156**·OTf in CH_3CN versus Ag/Ag^+ with ferrocene as an internal standard.*

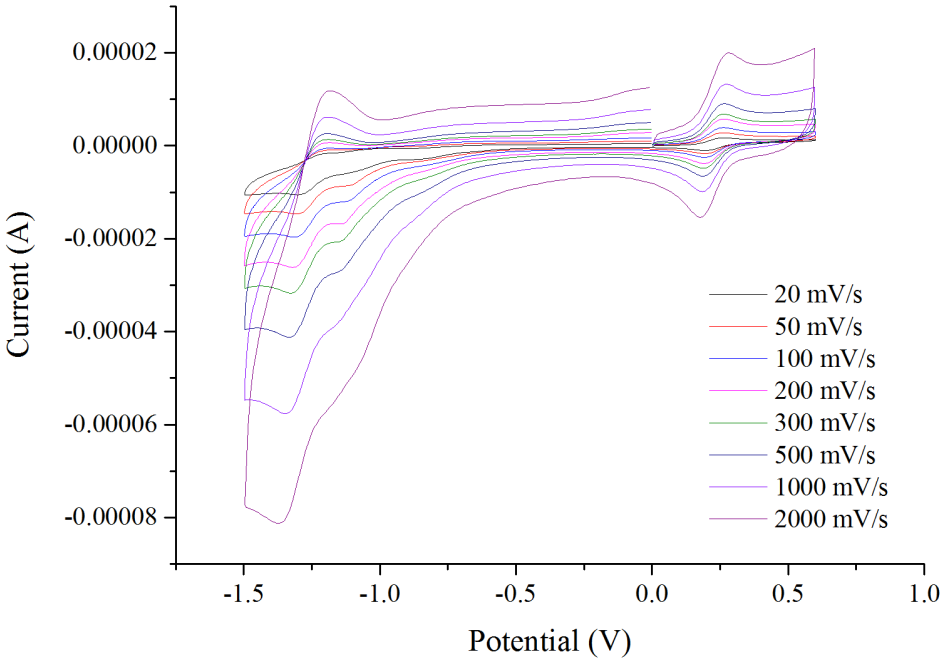

*Figure 4.27: Reduction of **156**·OTf in CH_3CN versus Ag/Ag^+ with ferrocene as an internal standard.*

4.6 References

1 G. H. Clever, S. Tashiro and M. Shionoya, *Angew. Chemie - Int. Ed.*, 2009, **48**, 7010–7012.

2 J. E. M. Lewis, E. L. Gavey, S. a. Cameron and J. D. Crowley, *Chem. Sci.*, 2012, **3**, 778.

3 Z. Li, N. Kishi, K. Hasegawa, M. Akita and M. Yoshizawa, *Chem. Commun.*, 2011, **47**, 8605–8607.

4 P. Liao, B. W. Langloss, A. M. Johnson, E. R. Knudsen, F. S. Tham, R. R. Julian and R. J. Hooley, *Chem. Commun.*, 2010, **46**, 4932.

5 J. L. Brumaghim, M. Michels and K. N. Raymond, *European J. Org. Chem.*, 2004, **2004**, 4552–4559.

6 P. Mal, B. Breiner, K. Rissanen and J. R. Nitschke, *Science*, 2009, **324**, 1697–1699.

7 W. Cullen, K. a. Thomas, C. a. Hunter and M. D. Ward, *Chem. Sci.*, 2015, **6**, 4025.

8 W. Cullen, S. Turega, C. A. Hunter and M. D. Ward, *Chem. Sci.*, 2015, **6**, 625–631.

9 M. Yoshizawa, M. Tamura and M. Fujita, *Science*, 2006, **312**, 251–254.

10 N. Kishi, Z. Li, Y. Sei, M. Akita, K. Yoza, J. S. Siegel and M. Yoshizawa, *Chem. - A Eur. J.*, 2013, **19**, 6313–6320.

11 K. Ono, J. K. Klosterman, M. Yoshizawa, K. Sekiguchi, T. Tahara and M. Fujita, *J. Am. Chem. Soc.*, 2009, **131**, 12526–12527.

12 T. Murase, S. Horiuchi and M. Fujita, *J. Am. Chem. Soc.*, 2010, **132**, 2866–2867.

13 M. Whitehead, S. Turega, A. Stephenson, C. a. Hunter and M. D. Ward, *Chem. Sci.*, 2013, **4**, 2744.

14 F. Biedermann, W. M. Nau and H.-J. Schneider, *Angew. Chemie Int. Ed.*, 2014, **53**, 11158–11171.

15 M. Yoshizawa, T. Kusukawa, M. Fujita, S. Sakamoto and K. Yamaguchi, *J. Am. Chem. Soc.*, 2001, **123**, 10454–10459.

16 M. Fujita, M. Tominaga, A. Hori and B. Therrien, *Acc. Chem. Res.*, 2005, **38**, 369–378.

17 M. Fujita, S.-Y. Yu, T. Kusukawa, H. Funaki, K. Ogura and K. Yamaguchi, *Angew. Chemie Int. Ed.*, 1998, **37**, 2082–2085.

18 P. R. Symmers, M. J. Burke, D. P. August, P. I. T. Thomson, G. S. Nichol, M. R. Warren, C. J. Campbell and P. J. Lusby, *Chem. Sci.*, 2015, **6**, 756–760.

19 V. V. Rostovtsev, L. G. Green, V. V. Fokin and K. B. Sharpless, *Angew. Chemie - Int. Ed.*, 2002, **41**, 2596–2599.

20 H. Yang, L. Li, L. Wan, Z. Zhou and S. Yang, *Inorg. Chem. Commun.*, 2010, **13**, 1387–1390.

21 H. Nie, W. Guo, Y. Yuan, Z. Dou, Z. Shi, Z. Liu, H. Wang and Y. Liu, *Nano Res.*, 2010, **3**, 103–109.

22 I. Kalinina, K. Worsley, C. Lugo, S. Mandal, E. Bekyarova and R. C. Haddon, *Chem. Mater.*, 2011, **23**, 1246–1253.

23 O. Hayashida, Y. Nakamura and T. Sato, *Advances in Chemical Engineering and Science*, 2014, **4**, 409-416.

24 B. Beyer, C. Ulbricht, D. Escudero, C. Friebe, A. Winter, L. González and U. S. Schubert, *Organometallics*, 2009, **28**, 5478–5488.

25 V. Theodorou, K. Skobridis, A. G. Tzakos and V. Ragoussis, *Tetrahedron Lett.*, 2007, **48**, 8230–8233.

26 L. S. Hafner and R. Evans, *J. Am. Chem. Soc.*, 1957, **79**, 3783-3786.

27 A. F. Childs, L. J. Goldsworthy, G. F. Harding, F. E. King, A. W. Nineham, W. L. Norris, S. G. P. Plant, B. Selton and A. L. L. Tompsett, *J. Chem. Soc.*, 1948, 2174-2177.

28 O. Chepelin, J. Ujma, X. Wu, A. M. Z. Slawin, M. B. Pitak, S. J. Coles, J. Michel, A. C. Jones, P. E. Barran and P. J. Lusby, *J. Am. Chem. Soc.*, 2012, **134**, 19334–19337.

29 S. Metz and S. Bernhard, *Chem. Commun.*, 2010, **46**, 7551–7553.

30 G. Colombano, C. Travelli, U. Galli, A. Caldarelli, M. G. Chini, P. L. Canonico, G. Sorba, G. Bifulco, G. C. Tron and A. a. Genazzani, *J. Med. Chem.*, 2010, **53**, 616–623.

31 S. Varghese, D. Gupta, T. Baran, A. Jiemjit, S. D. Gore, R. a. Casero and P. M. Woster, *J. Med. Chem.*, 2005, **48**, 6350–6365.

32 K. S. L. Chan, M. Wasa, X. Wang and J.-Q. Yu, *Angew. Chemie Int. Ed.*, 2011, **50**, 9081–9084.

CHAPTER 5

Enhanced Guest Binding in Organic Solvents

Contents

5.1 Synopsis

Previous attempts at increasing the affinity of a Pd_2L_4 cage for organic guests in polar solvents were unsuccessful. As an alternative, the potential of guest binding in organic solvents was investigated. A control compound, a simple Pd_2L_4 system developed previously by Hooley and co-workers, was studied as a receptor for hydrogen bond acceptor guests. The self-assembly process allows the generation of hydrogen bond donor pockets, not normally observed in solution, due to complexation of Pd^{II} to the pyridines. Quinones were identified as ideal guests and naphthoquinone was used as a standard for exploring the effects of switching counter anions and solvent on the host:guest affinity. Reducing the polarity of the solvent from CH_3OH to CH_2Cl_2 and switching the counter anion from OTf to the non-coordinating BArF resulted in over a 10^4 fold increase in the binding constant. Additionally, extending the guest aromatic π surface gave pentacenedione with a binding constant of 7.98 x 10^8 M^{-1}, one of the highest reported for metallosupramolecular systems. Alternative compounds, including ketones, aldehydes, amides and nitro groups, were also shown to interact with the cage cavity. The ability to significantly alter the affinity of organic guests within metallosupramolecular cages by simply altering the associated counter ion or solvent offers a wide range of possibilities including the enhancement of many potential applications.

5.2 Introduction

Almost all of the fundamental applications of supramolecular container compounds rely on binding guest compounds within the interior cavity and as such, the strength of the interactions between the container and guest are very important to the field.[1] Previous work in the field has focused on purely determining whether there is an interaction between the host and guest, either by direct detection using x-ray crystallography and mass spectrometry or by monitoring changes upon guest encapsulation using techniques such as ultraviolet-visible spectroscopy and NMR.[2–10] However, more recently, a more concerted effort has been made to quantify these interactions through the use of titration techniques[11–19] with the aim of better understanding the binding process and ultimately predicting suitable host:guest partners computationally.[20]

Many supramolecular species have been found to encapsulate guest compounds in a range of different conditions. The most widely utilized technique for the encapsulation of neutral guest compounds in metallosupramolecular containers is the hydrophobic effect whereby apolar compounds are driven inside the hydrophobic cage cavity in H_2O or other highly polar solvents. This provides a widely applicable and general method for binding organic substrates without specific host:guest interactions but there are limitations. Due to the specific hydrogen bond lattice required to generate the hydrophobic effect, the strength of binding drops off dramatically in solvents other than water which can severely limit the breadth of container design.[12,16] Synthesis of water soluble metallosupramolecular containers can be challenging, as although they often carry a high charge, many designs incorporate large hydrophobic ligands as structural elements (see chapter 3 and 4). In addition, any increase in the overall charge by altering the number or type of coordinated metals can also reduce the hydrophobicity of the internal cavity.

In order to allow binding in apolar solvents, specific interactions such as hydrogen bonding and metal-ligand complexation are required. However, the associated counter ions usually accompanying metallosupramolecular species have been found to act as guests in their own right, with binding constants reported of up to 10^6 M^{-1}.[6,13,21,22] Competition between the counter ion guests can therefore result in significantly weaker binding to neutral guest compounds, particularly for highly charged systems. In addition, due to ion pairing between the cage and counter ions, the effective concentration of ions around the cage system is much

higher than the bulk medium, further increasing the binding strength of ions relative to neutral guests.

To avoid these issues and maximize host guest interactions we hypothesized that subtle changes to the associated counter ions and the solvent could alter the guest binding constants for a range of suitable guests. By incorporating large, non-coordinating counter anions, ion-pairing with the cage is reduced and enhanced binding of neutral guest compounds is observed. Similar approaches have already been applied to a range of cationic hydrogen bond donor catalysts.[23–25]

5.3 The Model System

5.3.1 Introduction

Hooley and co-workers previously reported a Pd_2L_4 capsule based on bis-pyridine ligands prepared as its NO_3^- salt.[26] The system is relatively simple; requiring only a two-step synthesis from commercial compounds and can be prepared on a multi-gram scale. The system's simplicity also aids analysis of host:guest interactions and the high degree of symmetry reduces the total number of NMR signals. The well-defined hydrogen bond donor sights within the cavity also provide a simplified binding model for prediction of appropriate guest compounds.

The authors originally reported weak binding constants for a number of linear organic compounds in DMSO that were chosen based on their ability to interact with the Pd^{II} ions. However, based on our hypothesis, the conditions chosen (NO_3^- counter anions in DMSO) would heavily compete with any favourable binding interactions and prevent any measurable guest association with hydrogen bond acceptor guests. In order to confirm this, **1**·OTf was prepared (Figure 5.1) and a range of suitable guests were screened by comparing the ^1H NMR spectrum in CH_3CN before and after the addition of the guest.

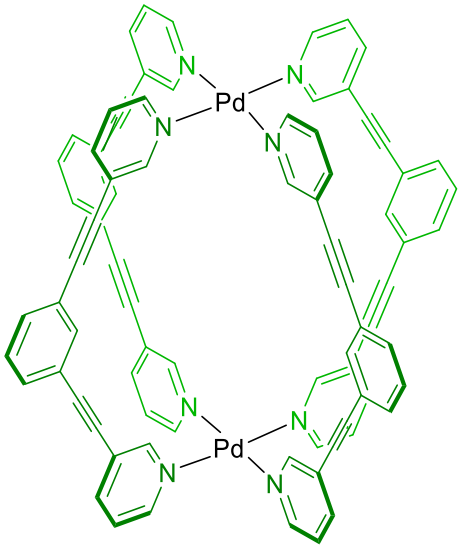

175·4X

X = OTf, BF_4, PF_6, SbF_6 or BArF

Figure 5.1: The structure of the Pd_2L_4 metallosupramolecular cage chosen as a model system for studying host:guest interactions.

Naphthoquinone was found to produce significant shifts in the ^{1}H NMR spectrum of **175**·4OTf (Figure 5.2). As expected, the cage peaks most affected by the presence of a guest are the internal protons, both on the pyridine ring and the central benzene ring. Further evidence towards the binding mode was provided by the deshielding of the pyridyl protons due to hydrogen bonding with the carbonyl groups and shielding of the central benzene rings due to CH-π interactions

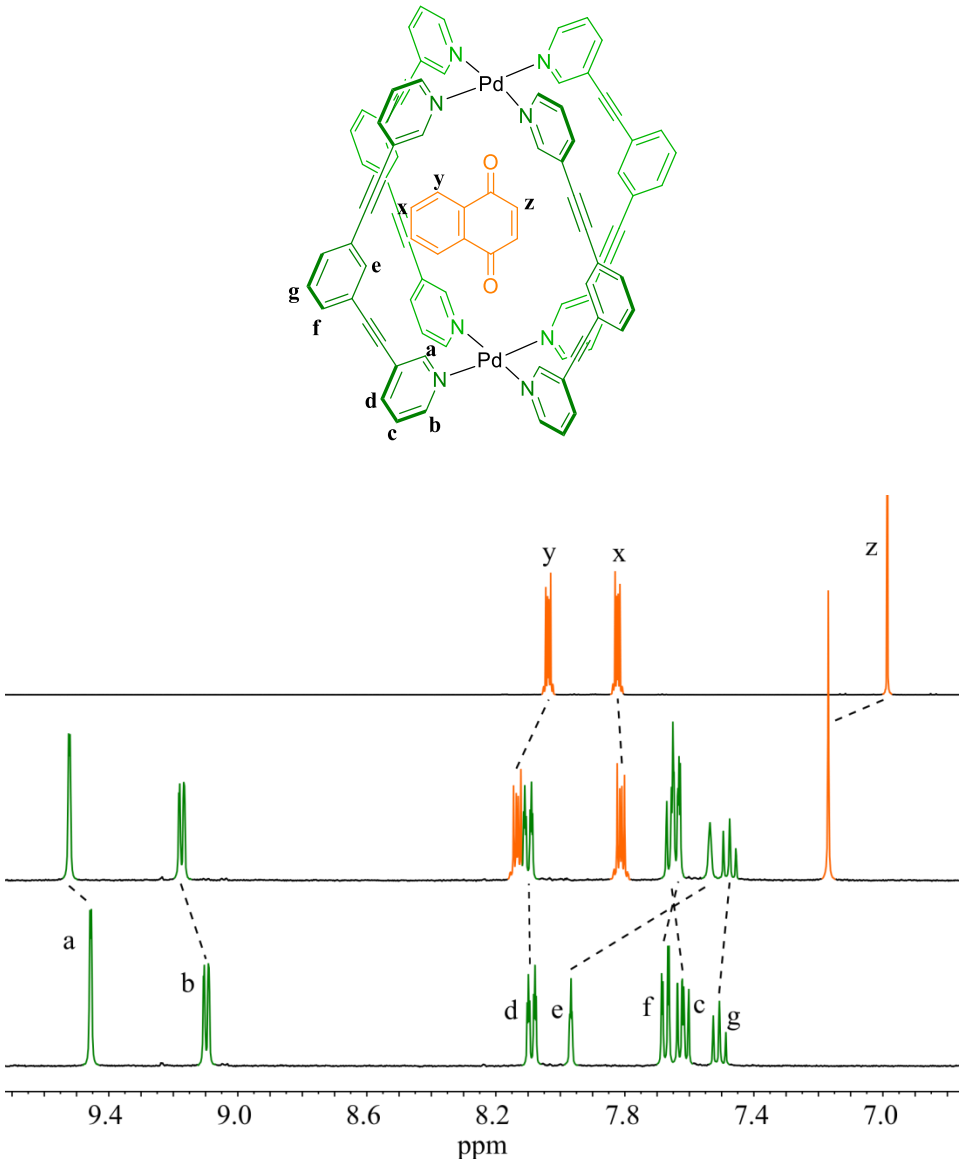

*Figure 5.2: An example ^{1}H NMR (500 MHz, CD_3CN, 300 K) spectrum of **1**·4OTf (green), naphthoquinone (orange) and combined.*

5.3.2 System Stability

Before selecting the system for further studies, the stability of the cage under dilute conditions was assessed due to the need to perform dilution experiments with slow binding guests (Figure 5.3). The system was found to be stable in solution at room temperature for the duration of the project (> 6 months) at concentrations above 50 μM. At concentrations less than 50 μM the cage equilibrium shifts towards free ligand until at concentrations below 5 μM, the intact cage is no longer observed. Only the cage or free ligand are observed throughout this concentration range and no partial structures were identified suggesting significant cooperativity towards cage assembly. Care was therefore taken to maintain concentrations ≥ 50 μM at all times during the following guest binding experiments.

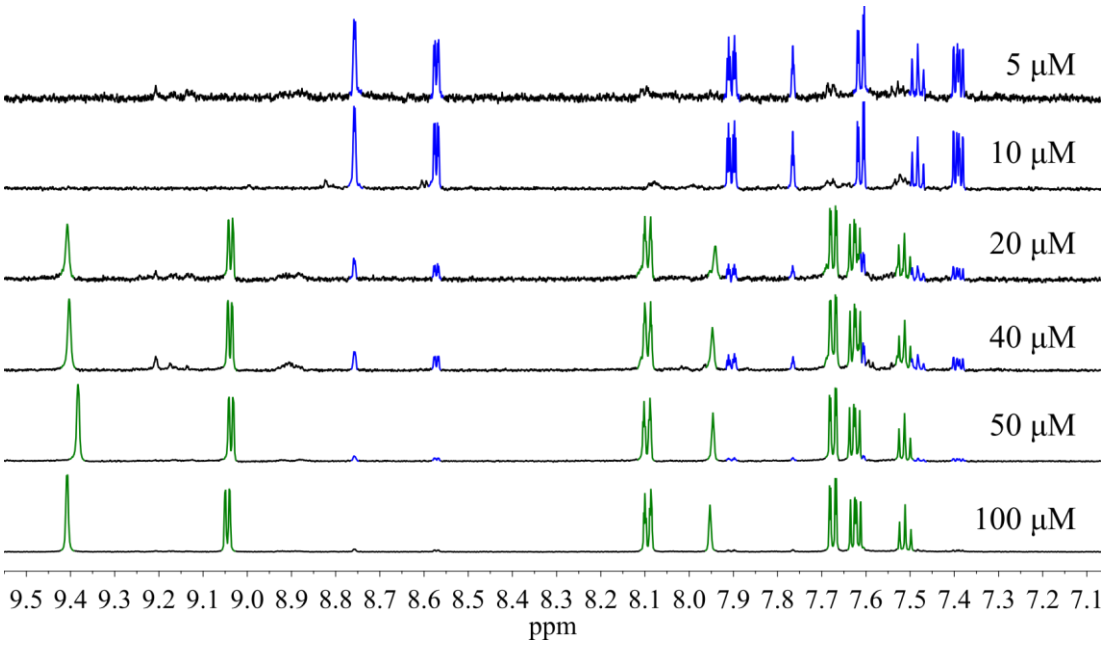

*Figure 5.3: ^{1}H NMR (600 MHz, CD_3CN, 300 K) stability experiment showing degradation of **175**·4OTf (green)* under dilute conditions to form predominantly free ligand (blue).

5.3.3 Binding Experiments

In order to quantify the binding constants and investigate the host:guest system, titration experiments were carried out by ^{1}H NMR spectroscopy. For binding constants $<10^{5}\ M^{-1}$, ^{1}H NMR titrations were carried out with increasing concentrations of guest while keeping the host concentration constant. The host peak positions were then plotted against guest concentration and a fitting function based on a 1:1 binding model was applied.

For those guests with binding constants $>10^5$ M^{-1} approximately, slow binding on the ^1H NMR timescale was observed at room temperature that prevented the use of standard NMR titrations. The low stability of the cage compounds also prevented measurements based on dilution experiments. As such, binding constants were measured through a series of competition experiments using anthraquinone as a universal standard. Anthraquinone itself was measured versus benzoquinone for which the binding constant was known through conventional ^1H NMR titrations.

5.4 Enhanced Guest Binding

5.4.1 Solvent Properties

Solvents have always played a major part in all aspects of chemistry and their properties can heavily influence the outcome of a reaction.[27] Even in very concentrated samples, the solvent molecules often outnumber the compound of interest by a thousand to one and indeed, so called neat reactions performed without an added solvent still utilise one of the reactants to solvate each individual molecule. It is therefore no surprise that the chosen solvent often plays an essential role in the reaction pathway and that the wrong choice of solvent can lead to unwanted side reactions or prevent a reaction from proceeding at all.

For metallosupramolecular compounds, the central cavity is often occupied by solvent molecules and/or associated counter ions, demonstrated by the rapid degradation of crystals upon solvent loss. For host:guest interactions governed by hydrogen bonding, it would be expected that polar, hydrogen bond acceptor solvents would be more likely to compete for the hydrogen bond donor sites. Thus, apolar solvents that show no preference for the hydrogen bond donor sites could lead to stronger association constants for neutral guests in **175**·4OTf.

In order to investigate this hypothesis, the binding strength of naphthoquinone within **175**·4OTf was measured using ^{1}H NMR titrations in a number of different solvents ranging from the most polar, CD_3OD, to the least polar, CD_2Cl_2 (Table 5.1). For each experiment, the peak shifts for **175**·4OTf were plotted relative to the guest concentration and fitted globally against a 1:1 binding model. The associated experimental errors were found to be ±25 % (see section 5.7.8).

*Table 5.1: Association constants (K_a) for naphthoquinone and **175**·4OTf in a range of different organic solvents.*

Solvent	Host	K_a (M^{-1})	ΔG ($kJmol^{-1}$)	Solvent Dielectric Constant[28]	Solvent HBA (β)[29]
CD_3OD	**175**·4OTf	2.58 x 10^1	-8.1	33.0	5.8
CD_3CN	**175**·4OTf	2.07 x 10^2	-13.3	36.6	4.7
d_8-THF	**175**·4OTf	2.91 x 10^2	-14.2	7.5	5.3
CD_2Cl_2	**175**·4OTf	1.84 x 10^3	-18.8	8.9	1.1
CD_3NO_2	**175**·4OTf	1.99 x 10^3	-18.9	37.3	3.7

As expected, the K_a was found to increase by almost a factor of 10^2 simply by altering the polarity and hydrogen bond acceptor ability of the solvent. However, CD_3NO_2 was found to be very similar to CD_2Cl_2 despite having vastly different hydrogen bond acceptor (HBA) properties. CD_2Cl_2 is a very weak HBA and as such, a difference in the binding constant would be expected if association was based solely on the solvent properties. However, the binding strength of the associated counter anions will also increase in apolar solvents and thus the similar binding constants measured for naphthoquinone in CD_3NO_2 and CD_2Cl_2 suggest that the low HBA ability means that the solvent molecules no longer compete effectively for the binding site and so the guest binding strength is limited solely by the associated counter anion.

5.4.2 Counter Ion Properties

In order to assess the counter anion dependence of guest binding, a range of different analogues of the cage were prepared containing alternative anions using either a different starting palladium salt or ion metathesis. Samples were prepared with the original OTf^- as well as BF_4^-, PF_6^-, SbF_6^-, Ph_4B^- and $BArF^-$. Each of the compounds was fully characterised by NMR and mass spectrometry.

All of the systems were stable in solution above 50 μM with the exception of **175**·$4Ph_4B$, which completely degraded within hours. The ^{1}H NMR spectrum of the solution in CD_3CN showed the rapid formation of biphenyl along with the corresponding disassembly of the cage to give free ligand. This coupling process has been previously reported using both an electrochemical method and the addition of an oxidant such as cerium ammonium nitrate. Oxidation of the Ph_4B could lead to the formation of Pd^0 and explain the resultant degradation of the cage structure.

^{1}H NMR studies of the different counter ion species revealed similar proton shifts to that associated with the binding of guests within the cage cavity (Figure 5.4). In particular, the internal ortho-pyridyl proton, shows a distinctive downfield shift, analogous to that observed upon the introduction of a hydrogen bonding guest. Only for very large, bulky ions, such as $BArF^-$, can an “empty” cavity be observed where the resultant peak shift is determined solely by the solvent.[13]

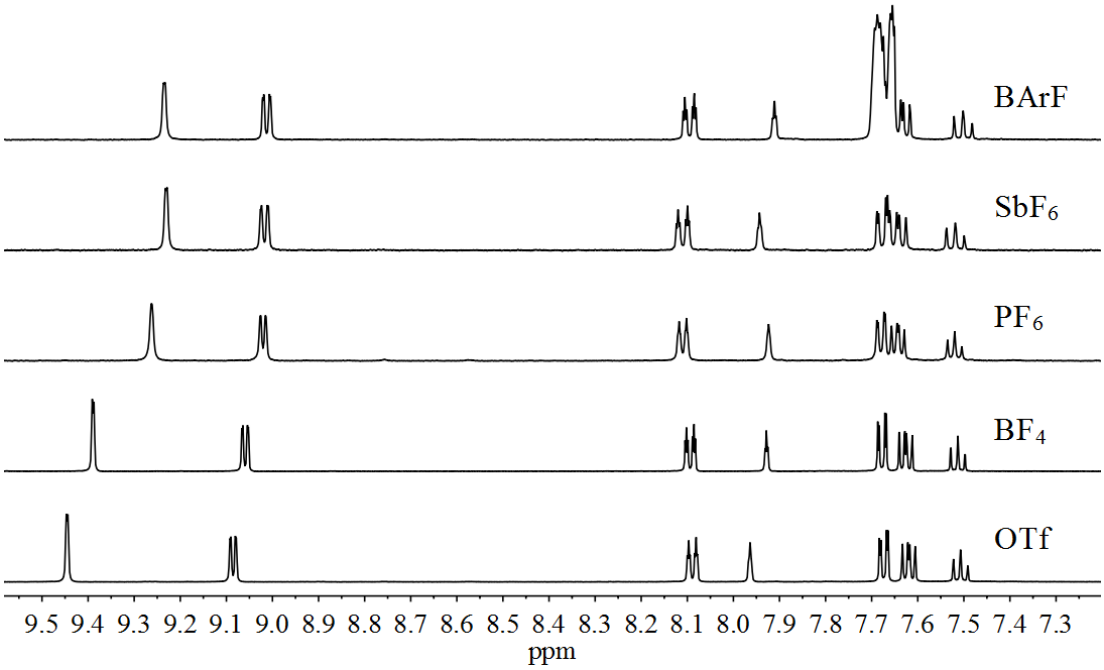

*Figure 5.4: Stack of ^{1}H NMR spectra for **175**·4X with different counter ions in CD_3CN. The shift in the internal ortho-pyridyl hydrogen (9.2-9.5 ppm) follows a similar trend to that observed for guest binding.*

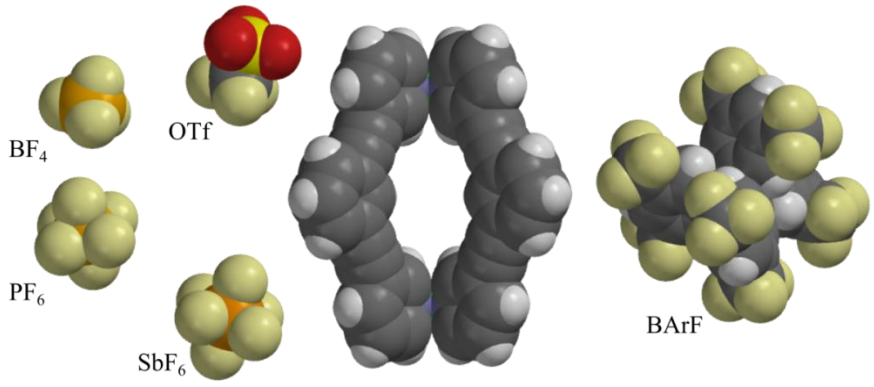

*Figure 5.5: A space-filling model of **175**$^{4+}$ along with individual models of the counter ions. OTf^-, BF_4^-, PF_6^-, SbF_6^- and $BArF^-$ are shown to highlight the relative sizes of the species involved. The large size of $BArF^-$ procludes encapsulation within the cavity.*

For those counter ions that are able to fit within the cavity, the expected trend is observed where the internal ortho-pyridyl peaks become more deshielded with an increase in the coordinating ability of the counter anion. OTf^- results in the largest shift due to specific hydrogen bonding interactions within the cavity of **175**·4OTf. The remaining perfluorinated

anions follow a trend in binding strength given by BF_4^- > PF_6^- > SbF_6^- which matches the calculated trend in polarity (Figure 5.6).

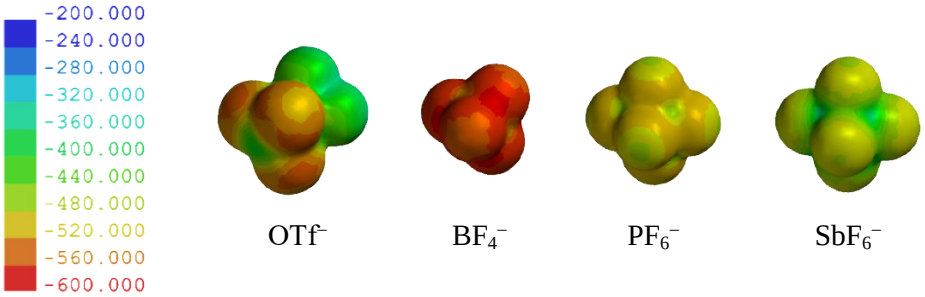

Figure 5.6: Calculated ionisation potential surfaces for OTf^-, BF_4^-, PF_6^- and SbF_6^-. Scale shown in kJ mol^{-1}.

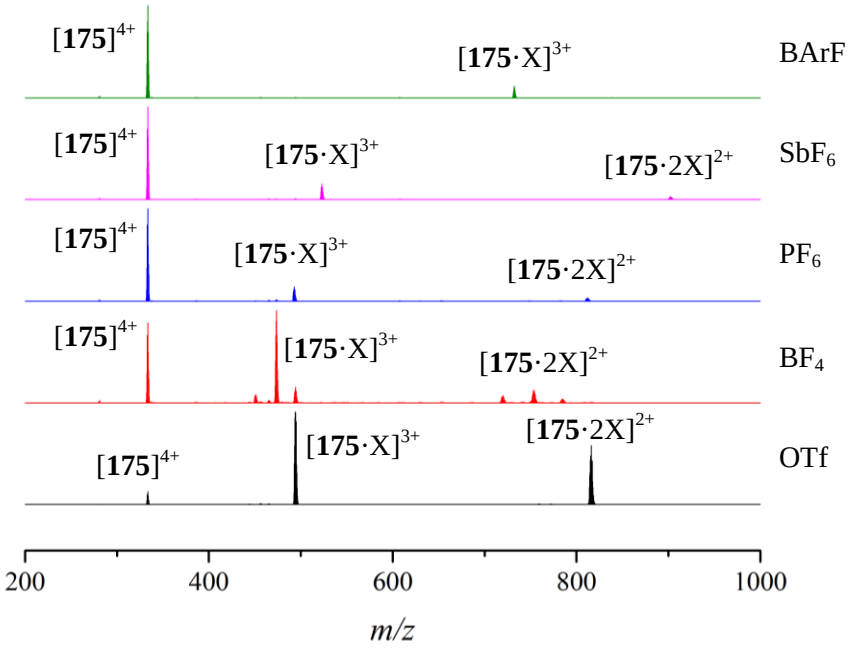

*Figure 5.7: ESI-MS of **175**·4X comparing the charge state distribution with different counter ions. **175**·4OTf shows a more wide-spread distribution of charge states indicating that the OTf^- counter ions are more tightly bound in the gas phase than the other, less coordinating anions.*

Mass spectrometry for each of **175**·4X also showed a trend towards more loosely bound ions (Figure 5.7). For **175**·4OTf, a wide spread of charge states was observed but for **175**·4BArF under identical spray conditions, the $[\mathbf{175}]^{4+}$ ion was observed with a much higher intensity

relative to the lower charge states, indicating easier removal of the associated counter ions in the gas phase.

For each of the different counter ions, the binding constant of naphthoquinone in CD_3NO_2 was measured using ^1H NMR titrations (Table 5.2). CD_3NO_2 was chosen as the test solvent since many of the **175**·4X salts had very low solubility in CD_2Cl_2, and the resultant strong guest binding conditions aided the experiment. The observed trend showed an increase of over ten fold in the binding strength from the most, OTf^-, to the least interacting, $BArF^-$. Since the BArF counter anions are too sterically crowded to enter the cage cavity, the binding constant of naphthoquinone reported in **175**·4BArF can represent the affinity of the guest versus bound solvent molecules.

*Table 5.2: Association constants (K_a) for naphthoquinone and **175**·X in CD_3NO_2.*

Solvent	Counter anion	K_a (M^{-1})	Δ G (kJmol^{-1})
CD_3NO_2	OTf^-	1.99×10^3	-18.9
CD_3NO_2	BF_4^-	6.52×10^3	-21.9
CD_3NO_2	PF_6^-	1.30×10^4	-23.6
CD_3NO_2	SbF_6^-	2.22×10^4	-24.9
CD_3NO_2	$BArF^-$	4.99×10^4	-27.0

5.4.3 Combined Binding Effects

In order to assess the ability to combine both the solvent and counter ion effects, the association constant of naphthoquinone in **175**·4BarF was measured in a range of solvents and compared with the previous data for **175**·4OTf (Table 5.3). Combining both a non-polar, non-coordinating solvent and a large, non-coordinating counter ion lead to a maximum binding constant of 3.49×10^5 M^{-1} for **175**·4BArF in CD_2Cl_2. This represents a total increase of over 10^4 in the binding strength of naphthoquinone by simply altering the solvent and associated counter ions. Note that the binding constant for **175**·4BArF in CD_2Cl_2 was measured using the competition experiments described in section 5.6.7 due to resultant slow binding on an ^1H NMR timescale brought about by the increase in binding strength.

*Table 5.3: Comparison of observed binding constants for naphthoquinone within **175**·4OTf and **175**·4BArF.*

Solvent	Counter Ion	K_a (M^{-1})	ΔG ($kJmol^{-1}$)	Difference in ΔG ($kJmol^{-1}$)
CD_3OD	OTf^-	$2.58 \pm 0.27 \times 10^1$	-8.1	7.5
	$BArF^-$	$5.26 \pm 0.18 \times 10^2$	-15.6	
CD_3CN	OTf^-	$2.07 \pm 0.03 \times 10^2$	-13.3	5.2
	$BArF^-$	$1.65 \pm 0.01 \times 10^3$	-18.5	
CD_3NO_2	OTf^-	$1.99 \pm 0.03 \times 10^3$	-18.9	8.1
	$BArF^-$	$4.99 \pm 0.94 \times 10^4$	-27.0	
CD_2Cl_2	OTf^-	$1.84 \pm 0.26 \times 10^3$	-18.8	13.0
	$BArF^-$	$3.49 \pm 0.47 \times 10^5$	-31.8	

In general, altering the solvent was more effective in increasing the affinity for naphthoquinone then altering the associated counter anion. This was unexpected, since moving to a less polar solvent would not only increase the affinity of the neutral guest for the cage cavity but also increase the ion-pairing effect of the counter anion, thereby cancelling out any benefit. However, the ion-pairing effect can be observed by comparing the differences in the binding properties of **175**·4OTf with **175**·4BArF in different solvents. Since **175**·4BArF can be considered a vacant cavity only occupied by solvent molecules, the difference in binding between **175**·4OTf and **175**·4BArF represents the binding strength of OTf^- within the cavity. As the solvent decreases in polarity to the non-polar CD_2Cl_2, a large increase in the binding affinity of OTf^- was observed due to the increased ion-pairing. Interestingly, the smallest change in ΔG is observed for CH_3CN rather than the most polar solvent, CD_3OD. Since the association constant of naphthoquinone was lowest in CD_3OD, this suggests that the low affinity for OTf^- in CD_3CN is due to preferential solvation of the anion. This matches the observation that **175**·4OTf is far more soluble in CD_3CN than any other solvent. This highlights the complex and subtle interplay of forces that govern the strength of guest binding in metallosupramolecular container compounds. However, particularly for systems in non-polar solvents, the use of large, non-coordinating anions can lead to significant enhancements in the affinity for neutral guests.

5.5 Structural Dependency

Although naphthoquinone was used as a model guest compound, **175**·4X also showed the propensity to bind a number of different quinone based compounds and alternative functional groups. For the stronger binding species, with a K_a above approximately 10^5, slow binding behaviour was observed relative to the ^{1}H NMR timescale. The instability of the cage systems at low concentrations prevented the use of dilution experiments. As such, the association constants for these guests were measured using a combination of competition experiments. The K_a of anthraquinone was first measured using benzoquinone as a standard. Anthraquinone was then used as a standard for all other strong binding species.

5.5.1 Quinone-based compounds

For quinone-based compounds, an increase in binding constant was observed upon increasing the π-π interactions around the quinone group by the addition of aromatic rings (Figure 5.8). The association constant increased by approximately 10^2 fold for each of the first two ring additions (Table 5.4). The addition of extra aromatic rings increased the binding strength still further but by smaller increments since protrusion from the cavity through the cage portals limits the effect of additional substitution away from the binding motif.

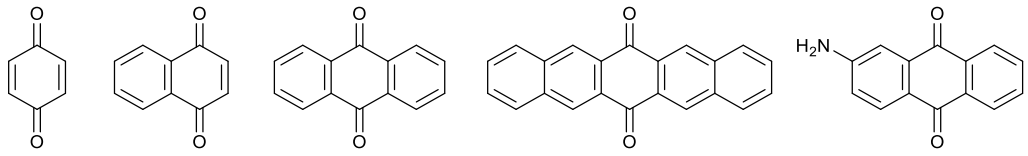

*Figure 5.8: The structures of increasing sterically crowded quinones investigated for host:guest properties within **175**·4BArF.*

Table 5.4: Calculated binding constants for a range of quinone guests.

Guest	Name	Host	K_a (M^{-1})	Δ G ($kJmol^{-1}$)
G^{29}	benzoquinone	**175**·BArF	7.24 x 10^3	-22.2
G^{28}	naphthoquinone	**175**·BArF	3.49 x 10^5	-31.8
G^{31}	anthraquinone	**175**·BArF	4.89 x 10^7	-44.2
G^{32}	pentacenedione	**175**·BArF	7.98 x 10^8	-51.1

Pentacenedione was found to bind with a K_a = 7.98 x 10^8 under the previously deduced ideal conditions of **175**·4BArF in CD_2Cl_2. This is one of the highest binding constants reported for any metallosupramolecular species to date. The high binding strength allowed the growth of X-ray quality crystals of $\mathbf{G^{32}}\subset\mathbf{175}$·4BArF from a solution of **175**·4OTf with 2 equivalents of pentacenedione in CH_3CN by vapour diffusion with $^{i}Pr_2O$ (Figure 5.9).

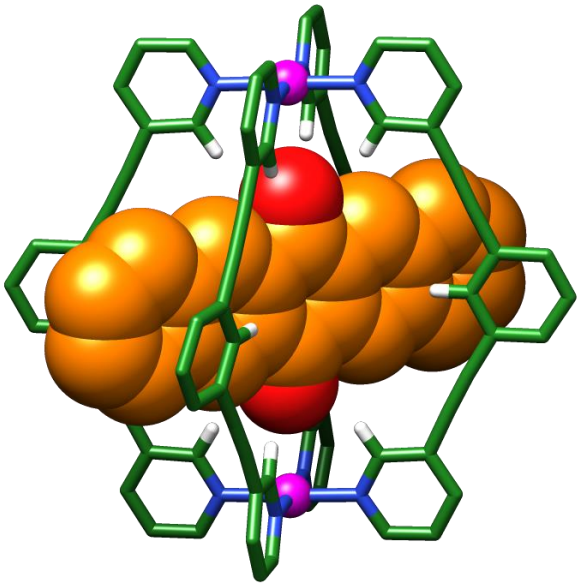

*Figure 5.9: Crystal structure of **175**·BArF containing bound **G**^{32}. Atoms are coloured hydrogen (white), carbon (green), nitrogen (blue), oxygen (red) and iridium (pink). External hydrogens, solvent molecules and counter anions are omitted for clarity.*

Each of the carbonyl groups is located in one of the tetradentate hydrogen bonding pockets created by the ortho-pyridyl hydrogens. The average H···O hydrogen bond distance is 2.55 Å and the average bond angles are 155.6° and 122.9° for C-H···O and H···O=C respectively. The crystal structure also shows a bend in the pyridyl ligands towards the pentacenedione which suggests a series of π-π or CH-π interactions that may contribute to the higher binding constants observed in solution (Figure 5.10). Although the observed ligand curvature was not present in the crystal structure originally reported by Hooley et al.,[26] the differences could arise solely from crystal packing effects.

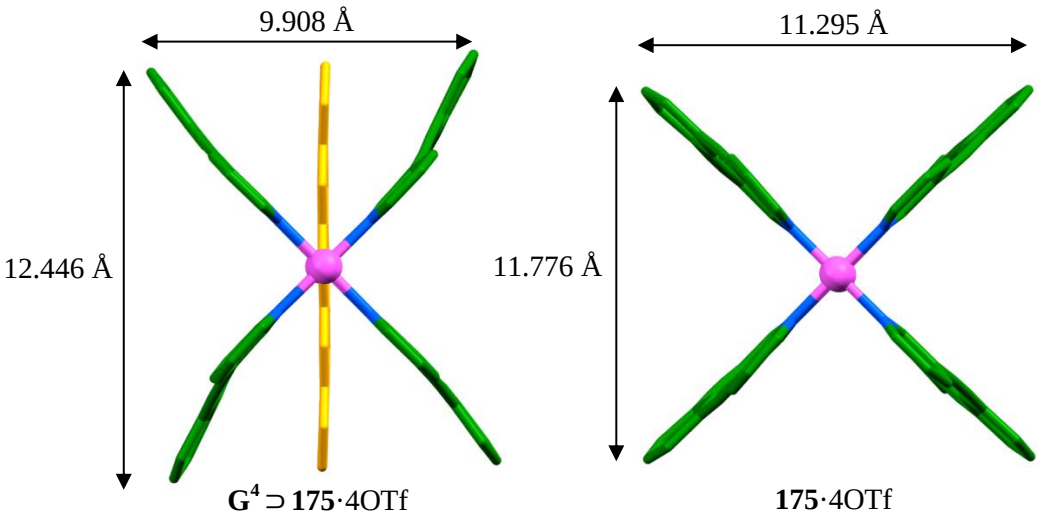

*Figure 5.10: Comparison of ligand geometry between **175**·4OTf with and without bound **G**[32].*

Mass spectrometry from a 50 µM solution of **175**·4BArF in CH_3CN with 2 equivalents of **G**[31] or **G**[32] also gave rise to peaks associated with each of the host:guest complex. This evidence for association in the gas phase, a phenomenon not observed for any of the weaker binding guests, also highlights the strength of the host:guest interactions. Dissociation of the host:guest complex was achieved though collision induced dissociation to form increasing levels of the empty cage followed by complete disassembly of the cage structure at higher energies.

Whilst the addition of slow binding symmetrical quinones reduces the cage symmetry from D_{4h} to D_{2h}, the inclusion of asymmetric quinones leads to almost complete desymmetrisation of the cage proton peaks. Addition of 1 equivalent of 2-aminoanthroquinone (**G**[33]) alters the system from a D_{4h} to a C_s point group and gives rise to a more complex ^{1}H NMR spectrum. ^{1}H DOSY NMR confirmed that all of the peaks belong to a single species. The splitting patterns are most easily observed for the hydrogen atoms within the internal cavity as these peaks are most affected by the inclusion of guest compounds. Figure 5.11 shows a comparison between the ^{1}H NMR spectrum of **G**[31] and **G**[33], both bound within **175**·4BArF. The ortho-pyridyl peak at ~9.6 ppm shows a distinct four-fold splitting due to the C_s symmetry i.e. separate environments are observed for top, bottom, front and back. However, the peak corresponding to the internal benzene peak at ~6.1 ppm is only split into two separate signals since they lie along the central plane and thus have no top/bottom. Interestingly, encapsulation within **175**·BArF also highlighted the presence of **G**[31] as an impurity present in the commercial sample of **G**[33]. A binding constant could not be obtained

for **G**^{33} due to insufficient quality data and the complexity of the ^{1}H NMR spectra but competition experiments showed that the binding strength was greater than that of **G**^{31} (>4.89 x 10^{7} M^{-1}).

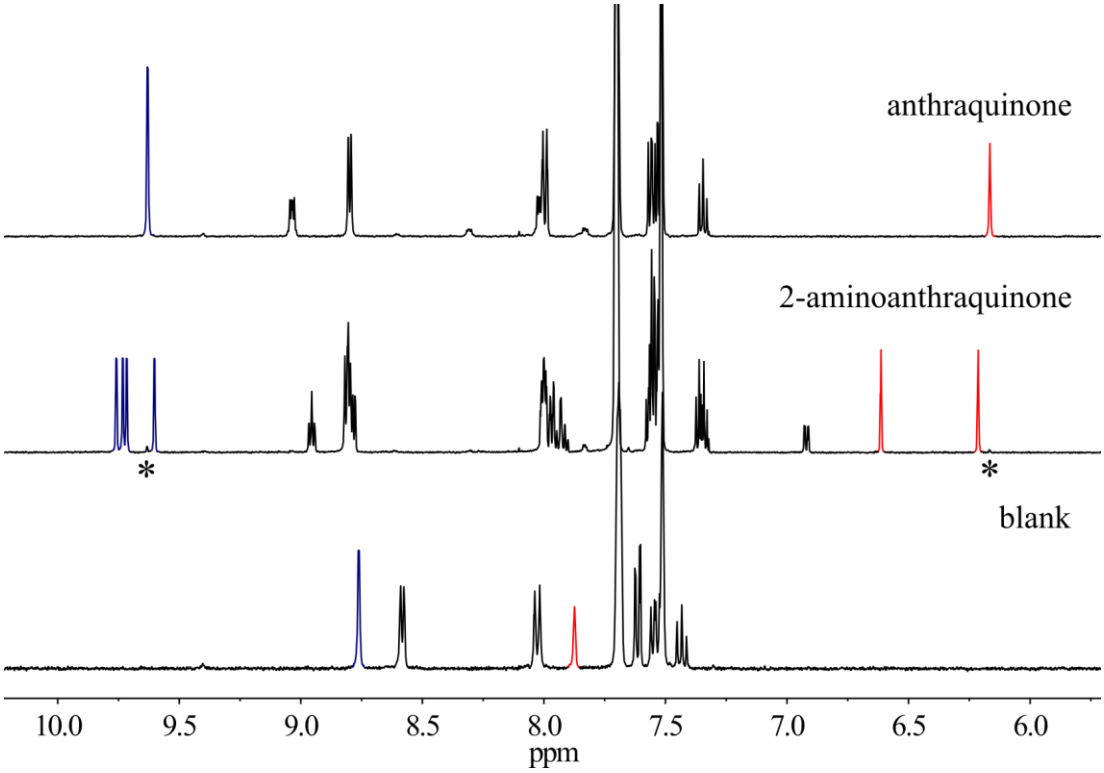

Figure 5.11: Comparison of ^{1}H NMR (500 MHz, CD_2Cl_2, 300 K) for ***G***^{31} *and* ***G***^{33} *bound within* ***175***·*4BArF. Four-fold splitting (blue) and two-fold splitting (red) are shown due to desymmetrisation from a D_{4h} to a C_s point group.* ***G***^{31} *was found to be present as a minor impurity in the commercial sample of* ***G***^{35} *(*).*

5.5.2 Alternative binding groups

As demonstrated above, quinones possess the ideal geometry and polarity to fit within the cavity of **175**·4X, however, other functional groups can also bind within the cavity due to similar hydrogen bond acceptor functional groups. Aldehydes, ketones, amides and nitro groups have all been shown to bind within the cage cavity (Figure 5.12 and Table 5.5).

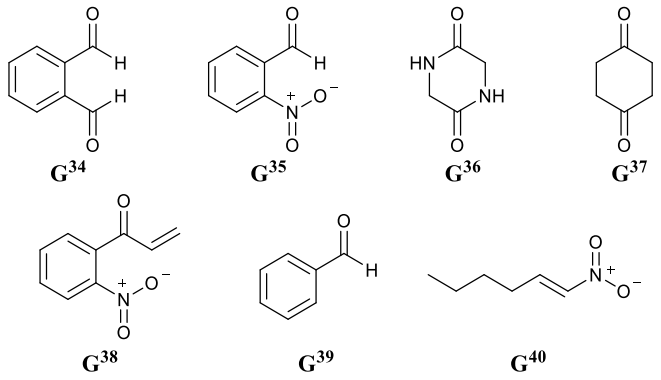

*Figure 5.12: The structures of compounds containing different hydrogen bond acceptor groups investigated for host:guest properties within **175**·4BArF.*

G^{34} and **G**^{35} were found to have very similar binding constants for **175**·4BArF in CD_2Cl_2. This suggests that the binding contribution of aldehydes within the hydrogen bond donor site is similar to that observed for nitro groups, an observation supported by the similar β_s reported in literature (5.8 and 5.3 for acetone and nitromethane respectively).[30] The binding constant for glycine anhydride in **175**·4BArF in CD_2Cl_2 could not be determined due to the binding lying within the transition from fast to slow exchange on the ^{1}H NMR timescale. A binding constant of 9.72 x 10^3 M^{-1} was determined in CD_3CN, a value higher than that recorded for naphthoquinone under the same conditions and therefore, based on the results obtained previously, much higher than the predicted binding constant of benzoquinone in CD_3CN. This highlights the propensity of amide groups to function as strong hydrogen bond acceptors as also shown by Hunter et al. with a covalent macrocyclic system.[31,32] The macrocyclic system was also shown to bind **G**^{37} in a similar manner to **G**^{29} but in comparison, **G**^{29} shows no measurable association with **175**·4BArF.

*Table 5.5: Measured binding constants within **175**·4BArF for a range of compounds containing different hydrogen bond acceptor groups.*

Guest	Name	Host	K_a (M^{-1})	Δ G ($kJmol^{-1}$)
G[34]	phthaldialdehyde	**175**·4BArF	4.73 x 10^2	-15.4
G[35]	2-nitrobenzaldehyde	**175**·4BArF	3.58 x 10^2	-14.7
G[36]	glycine anhydride[a]	**175**·4BArF	9.72 x 10^3	-22.9
G[37]	1,4-cyclohexadione	**175**·4BArF	N/D[b]	N/D[b]

a) determined in CD_3CN due to pseudo fast/slow exchange in CD_2Cl_2 b) association constant too weak to measure.

This dramatic reduction in binding compared with benzoquinone can be explained by the change in compound geometry. While benzoquinone, as well as all of the other ditopic guests discussed, maintain a planar geometry, 1,4-cyclohexadione exhibits a chair conformation due to the saturated carbon ring. Firstly, this shortens the oxygen to oxygen distance from 5.32 Å to 5.21 Å which increases the C-H···O hydrogen bond distance and reduces the strength of the interaction. Additionally, in order to align within the cavity such that both carbonyl groups can interact fully with the hydrogen bond donor sites, the angle must be either offset or alternatively, the interactions may only occur between two of the four hydrogen bond donors in each binding pocket. Either of these outcomes will significantly reduce the hydrogen bonding strength and give rise to the weak host:guest interaction observed. While the covalent macrocycle described by Hunter et al. may maintain a degree of flexibility that can accommodate small changes in the guest geometry,[31,32] the rigid framework provided by the metal-ligand coordination of **175**·4BArF, required for rational design and rapid synthesis, is highly sensitive to the exact position of binding groups.

5.6 Summary & Conclusions

The strength of host:guest interactions plays an integral role in governing the various potential applications of metallosupramolecular assemblies. Although many systems have been shown to bind both charged and neutral guests, many of these rely on the hydrophobic effect. Guest binding in apolar solvents has been comparatively less common as the strong coulombic attraction between the metallosupramolecular assembly and the associated counter ions results in strong competition for the internal cavity.

Quinones were found to bind strongly within the interior of **175**·4OTf in organic solvents, driven by the multiple hydrogen bonding pockets created by complexation of palladium to the pyridyl ligands. Further studies with a variety of counter anions (OTf^-, BF_4^-, PF_6^-, SbF_6^- and $BArF^-$) and solvents showed that the binding strength could be increased by a factor 25 by simple alteration of the conditions towards large non-coordinating anions and apolar solvents. In addition, combining the optimised conditions (**175**·4BArF in CH_2Cl_2) with a strong binding guest, pentacenedione (**G**^{32}), gave a measured association constant of 7.98 x 10^8 M^{-1}, one of the highest reported for metallosupramolecular systems.

Although quinones possess an ideal geometry for binding within **175**·4X, a range of other functional groups were also found to interact with the cage cavity including ketones, aldehydes, amides and nitro groups. The strong hydrogen bonding pockets present within **175**·4X could potentially be utilised to alter the reactivity of bound guests and potential catalytic processes are discussed later in Chapter 6.

It is hoped that this approach to enhancing guest binding can be applied to a large range of other metallosupramolecular systems and charged hosts and potentially aid progress in a number of research areas. This simple method for altering guest binding also allows the straight forward tuning of reaction conditions when both very weak and/or very strong binding needs to be avoided.

5.7 Experimental

5.7.1 General Information

Unless stated otherwise, all reagents and solvents were purchased from Alfa Aesar, VWR or Sigma Aldrich and used without further purification. Column chromatography was carried out using Geduran Si60 (40-63 µm) as the stationary phase and TLC was performed on precoated Kieselgel 60 plates (0.20 mm thick, $60F_{254}$. Merck, Germany) and observed under UV light at 254 nm or 365 nm. All reactions were carried out under air, unless stated otherwise. 1,3-Bis(3-ethynylpyridyl)benzene,[26] pentacenedione (**G^{4}**),[33] α-ethenyl-2-nitro-benzenemethanol,[34] 1-(2-nitrophenyl)-2-propen-1-one (**G^{10}**)[35] and $Pd(CH_3CN)_4 \cdot 2OTf$[36] were prepared according to literature procedures. 1-Nitrohexane was a kind gift from Patrick Fuchs (Zeitler Group, Universität Leipzig).

Molecular modelling of the counter anions was carried out using Spartan '10 V1.1.0 using an LACVP split basis set. A 6-31G* basis set was used for atoms H-Ar and a LANL2DZ effective core basis set was used for heavier atoms. Molecular modelling of the guests was carried out using a standard 6-31G* basis set.

For details regarding the NMR, MS, Ultraviolet-visible light spectroscopy and emission spectroscopy apparatus, please refer to Sections 2.9.1 and 3.7.1.

5.7.2 Synthetic Procedures

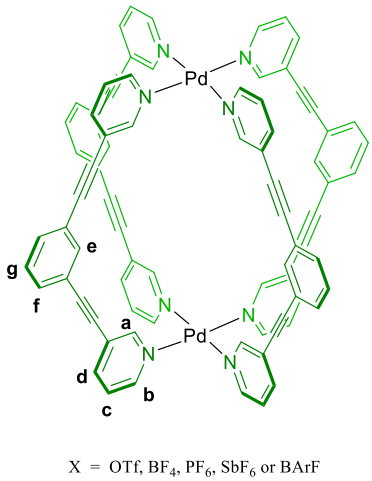

*Figure 13: Structure of **175**.4X showing NMR assignments.*

175.4OTf and **175**.4BF_4 were prepared using a modified literature procedure.[26]

Synthesis of 175·4X

A solution of Pd(CH_3CN)$_4$·2X (0.179 mmol) in CH_3CN (0.5 mL) was charged slowly to a solution of 1,3-bis(3-ethynylpyridyl)benzene (0.179 mmol) in CH_3CN (5 mL) whilst stirring. The solution was stirred overnight at room temperature. A solid was isolated by concentration of the solution under vacuum followed by precipitation with Et_2O. The solid was filtered, washed with Et_2O and dried under vacuum to yield the product as a white or off white powder.

175·4OTf Yield = 58.2 mg, 84%

175·4BF_4 Yield = 65.6 mg, 87%

Anion-metathesis

For most counter anions, the reduced solubility of the resultant cage in polar solvents allowed removal of any residual OTf by washing with MeOH (Method A) but an aqueous extraction was required for BArF (Method B).

Method A:

A solution of KPF_6 or $NaSbF_6$ (100 eq) in CH_3CN (1 mL) was charged to a solution of **175**.4OTf in CH_3CN (1 mL). After thoroughly mixing, the solution was concentrated and the product precipitated with MeOH (5 mL). The solid was filtered, washed with MeOH and dried under vacuum.

175.4PF_6 Yield = 4.1 mg, 38%

175.4SbF_6 Yield = 11.8 mg, 77%

Method B:

175.4OTf (52.0 mg, 0.027 mmol) and NaBArF (95.5 mg, 4 eq.) were dissolved in CH_3CN (5 mL) and MeOH (5 mL). After thoroughly mixing, the solution was diluted with water (3 mL). The resultant solid was filtered, washed with water and dried under vacuum. The solid was re-dissolved in DCM (10 mL) and NaBArF (95.5 mg, 4 eq.) and water were charged. The organic phase extracted and the solvent was removed under vacuum. The residue was re-dissolved in CH_3CN (1 mL) and MeOH (1 mL). The product was precipitated with water, filtered, washed with 1:1 MeOH/water and dried under vacuum to yield a white or off-white solid.

175.4BArF Yield = 94.1 mg, 73%

5.7.3 Characterisation

175·4OTf

^{1}H NMR (500 MHz, CD_3CN) δ 9.47 – 9.42 (m, 8H, H_a), 9.12 – 9.05 (m, 8H, H_b), 8.12 – 8.06 (m, 8H, H_d), 7.96 (t, *J* = 1.7 Hz, 4H, H_e), 7.70 – 7.65 (m, 8H, H_c), 7.65 – 7.59 (m, 8H, H_f), 7.51 (t, *J* = 7.7 Hz, 4H, H_g). ^{13}C NMR (126 MHz, CD_3CN) δ 153.98, 151.05, 143.86, 135.09, 134.25, 130.72, 128.33, 124.70, 123.17, 94.94, 85.30. *^{13}C OTf peak not observed due to strong coupling and low concentration. ^{19}F NMR (471 MHz, CD_3CN) δ -78.47. ^{1}H DOSY NMR (500 MHz, CD_3CN) –logD = 9.13 hydrodynamic radius = 8.0 Å.

175·4BF_4

^{1}H NMR (500 MHz, CD_3CN) δ 9.40 – 9.38 (m, 8H, H_a), 9.08 – 9.04 (m, 8H, H_b), 8.12 – 8.07 (m, 8H, H_d), 7.93 (td, *J* = 1.7, 0.6 Hz, 4H, H_e), 7.70 – 7.66 (m, 8H, H_c), 7.66 – 7.60 (m, 8H, H_f), 7.51 (td, *J* = 8.1, 0.7 Hz, 4H, H_g). ^{13}C NMR (126 MHz, CD_3CN) δ 153.96, 150.99, 143.87, 135.13, 134.21, 130.76, 128.36, 124.68, 123.16, 94.93, 85.39. ^{19}F NMR (471 MHz, CD_3CN) δ -150.93 (^{10}B), -150.99 (^{11}B). ^{1}H DOSY NMR (500 MHz, CD_3CN) –logD = 9.14 hydrodynamic radius = 8.1 Å.

175·4PF_6

^{1}H NMR (500 MHz, CD_3CN) δ 9.29 – 9.23 (m, 8H, H_a), 9.05 – 8.99 (m, 8H, H_b), 8.14 – 8.08 (m, 8H, H_d), 7.92 (t, *J* = 1.7 Hz, 4H, H_e), 7.70 – 7.67 (m, 8H, H_c), 7.67 – 7.62 (m, 8H, H_f), 7.52 (t, *J* = 7.8 Hz, 4H, H_g). ^{13}C NMR (126 MHz, CD_3CN) δ 153.83, 151.01, 144.00, 135.15, 134.21, 130.82, 128.51, 124.71, 123.12, 94.99, 85.28. ^{19}F NMR (471 MHz, CD_3CN) δ -72.79 (d, *J* = 706.6 Hz). ^{1}H DOSY NMR (500 MHz, CD_3CN) –logD = 9.15 hydrodynamic radius = 8.4 Å.

175·4SbF_6

^{1}H NMR (400 MHz, CD_3CN) δ 9.25 – 9.21 (m, 8H, H_a), 9.04 – 8.99 (m, 8H, H_b), 8.14 – 8.08 (m, 8H, H_d), 7.94 (t, *J* = 1.3 Hz, 8H, H_e), 7.70 – 7.66 (m, 8H, H_c), 7.66 – 7.62 (m, 8H, H_f), 7.52 (t, *J* = 7.7 Hz, 4H, H_g). ^{13}C NMR (126 MHz, CD_3CN) δ 153.80, 150.98, 144.03, 135.36, 134.14, 130.80, 128.54, 124.77, 123.11, 95.06, 85.23. ^{1}H DOSY NMR (500 MHz, CD_3CN) –logD = 9.15 hydrodynamic radius = 8.3 Å.

175·4BArF

^{1}H NMR (400 MHz, CD_3CN) δ 9.26 – 9.21 (m, 8H, H_a), 9.04 – 8.99 (m, 8H, H_b), 8.12 – 8.07 (m, 8H, H_d), 7.91 (t, *J* = 1.3 Hz, 4H, H_e), 7.72 – 7.65 (m, 56H, H_c, H_{BArF}), 7.65 – 7.61 (m, 8H, H_f), 7.55 – 7.46 (m, 4H, H_g). ^{13}C NMR (126 MHz, CD_3CN) δ 163.23 – 161.77 (m), 153.86, 151.00, 144.02, 135.89 – 135.38 (m), 135.23, 134.14, 130.83, 129.89 (q, *J* = 32.0 Hz), 128.52, 125.43 (q, *J* = 271.1 Hz), 124.70, 123.09, 118.74 – 118.57 (m), 95.01, 85.22. ^{19}F NMR (376 MHz, CD_3CN) δ -63.26. ^{1}H DOSY NMR (500 MHz, CD_3CN) –logD = 9.18 hydrodynamic radius = 9.0 Å.

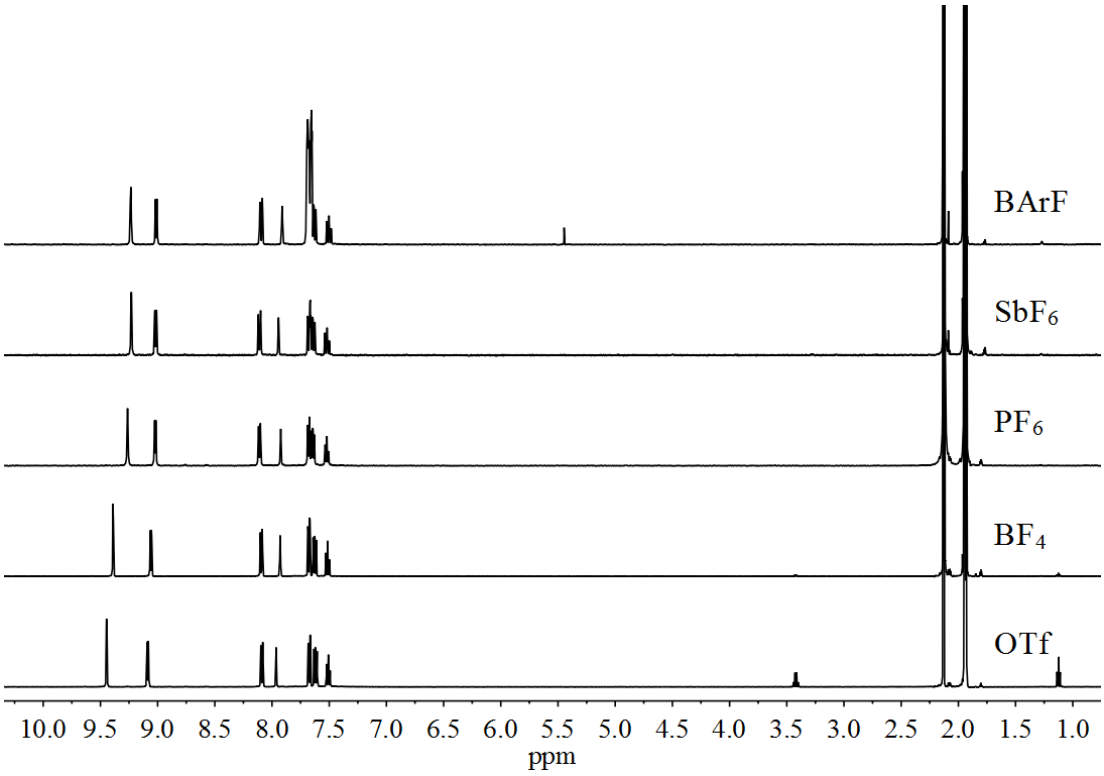

*Figure 5.14: ^{1}H NMR (500 MHz, CD_3CN, 300 K) of **175**$^{4+}$ with different counter anions.*

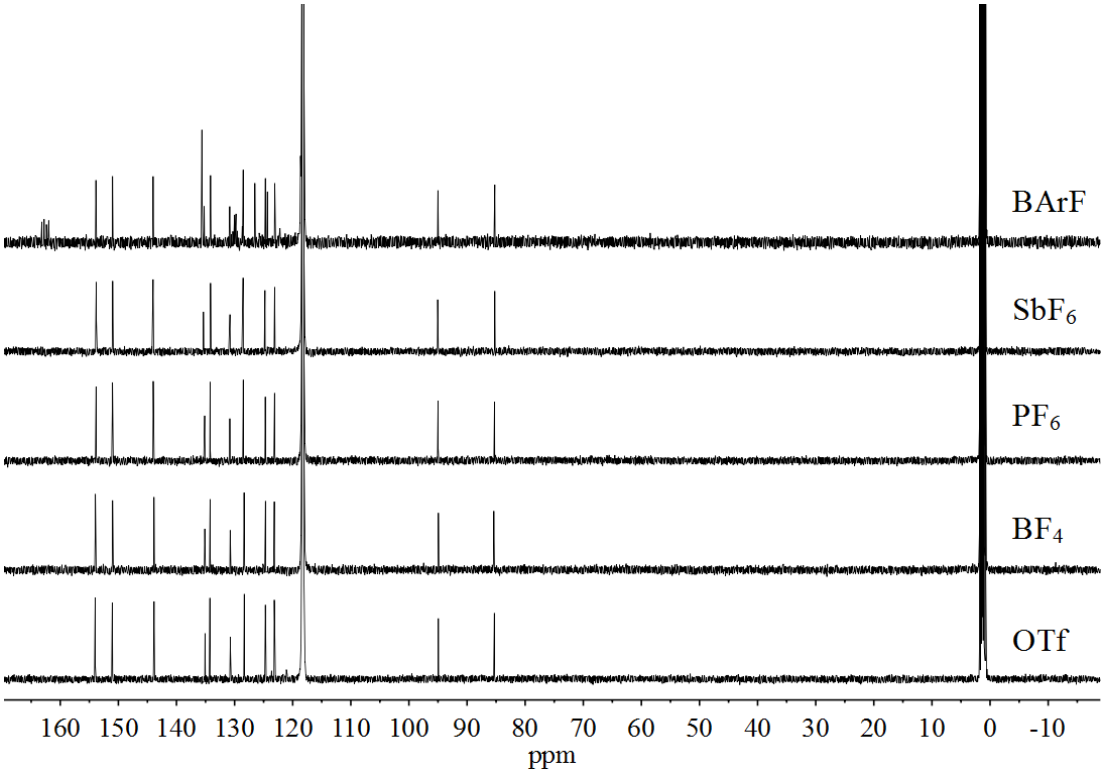

Figure 5.15: ^{13}C NMR (126 MHz, CD_3CN, 300 K) *of **175**$^{4+}$ with different counter anions.*

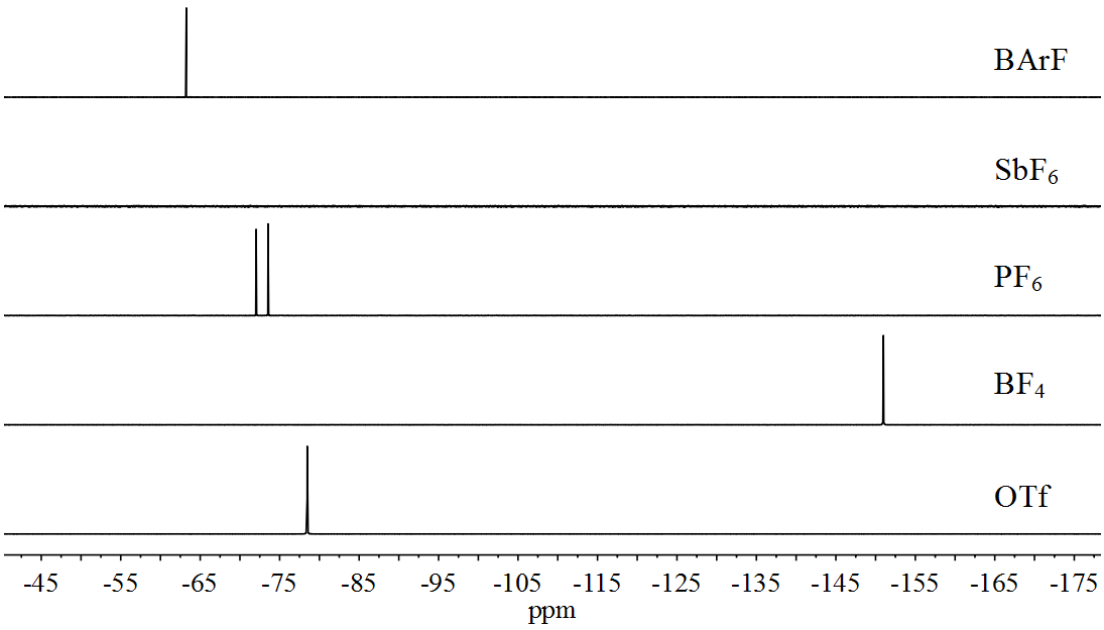

Figure 5.16: ^{19}F NMR (471 MHz, CD_3CN, 300 K) *of* ***175***$^{4+}$ *with different counter anions.*

5.7.4 Mass Spectrometry of Cage Compounds

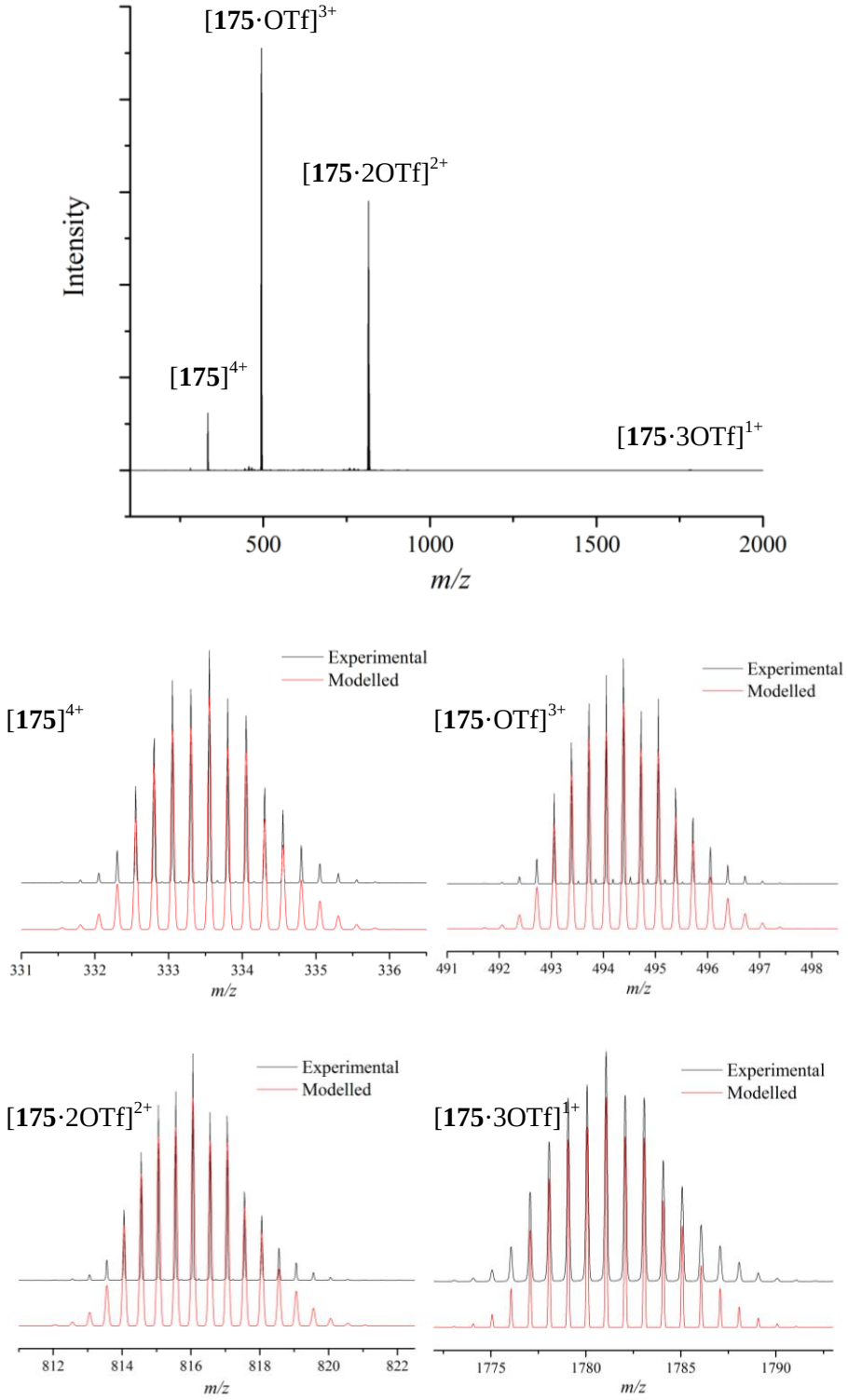

*Figure 5.17: ESI-MS of **175**·4OTf. The peaks found by experiment (black) are shown in comparison with their modelled isotopic distributions (red).*

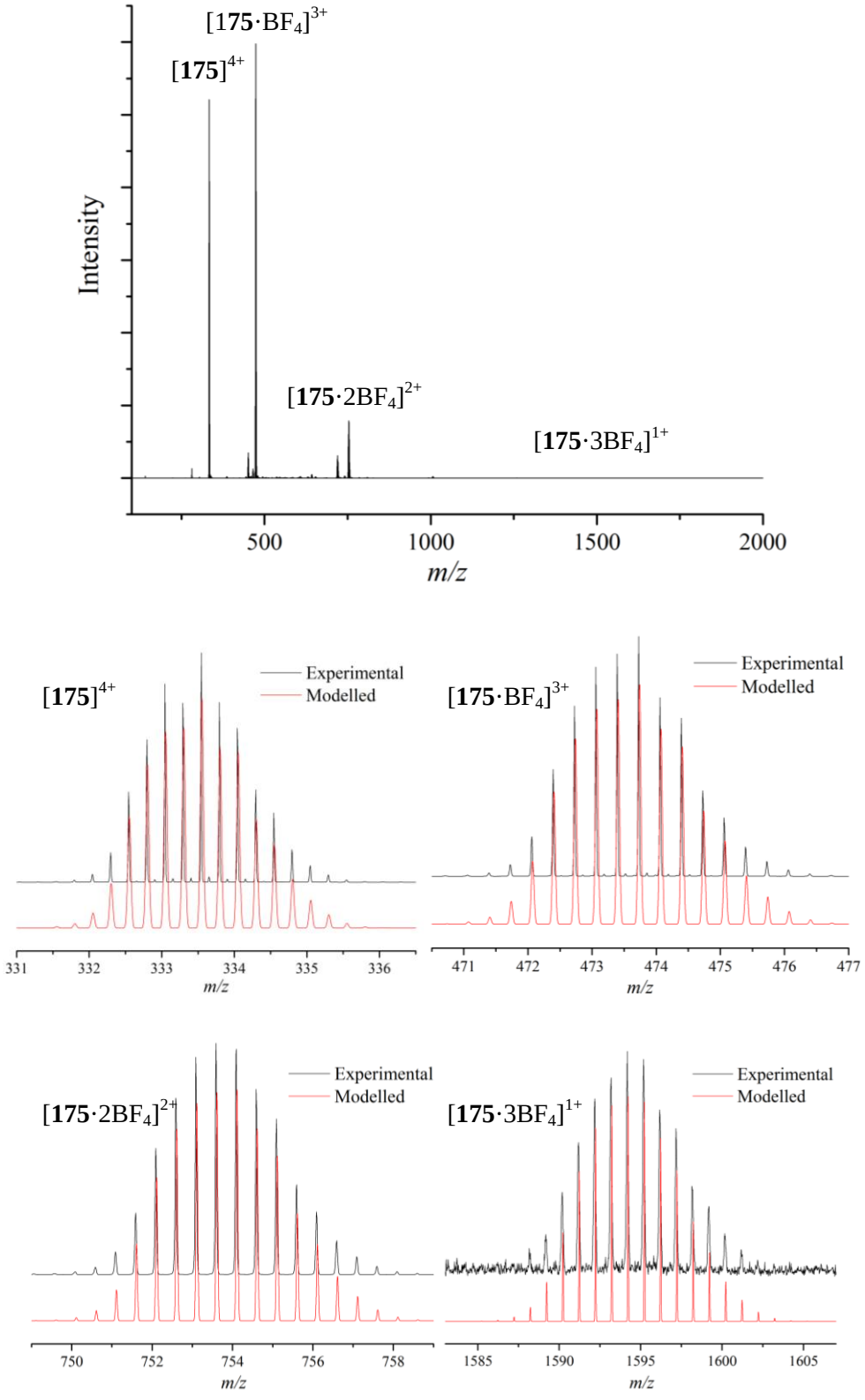

*Figure 5.18: ESI-MS of **175**·4BF₄. The peaks found by experiment (black) are shown in comparison with their modelled isotopic distributions (red).*

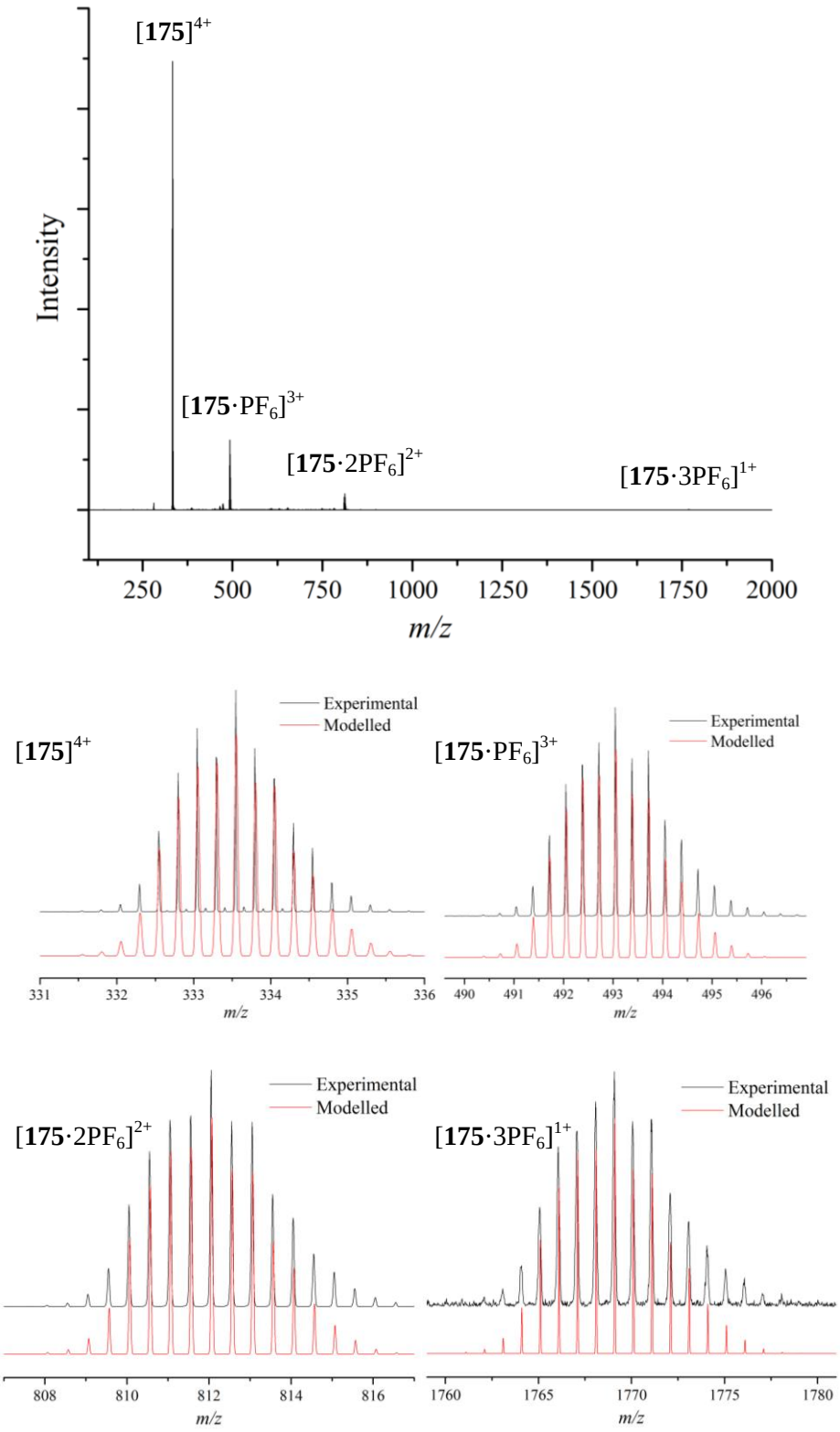

*Figure 5.19: ESI-MS of **175**·4PF$_6$. The peaks found by experiment (black) are shown in comparison with their modelled isotopic distributions (red).*

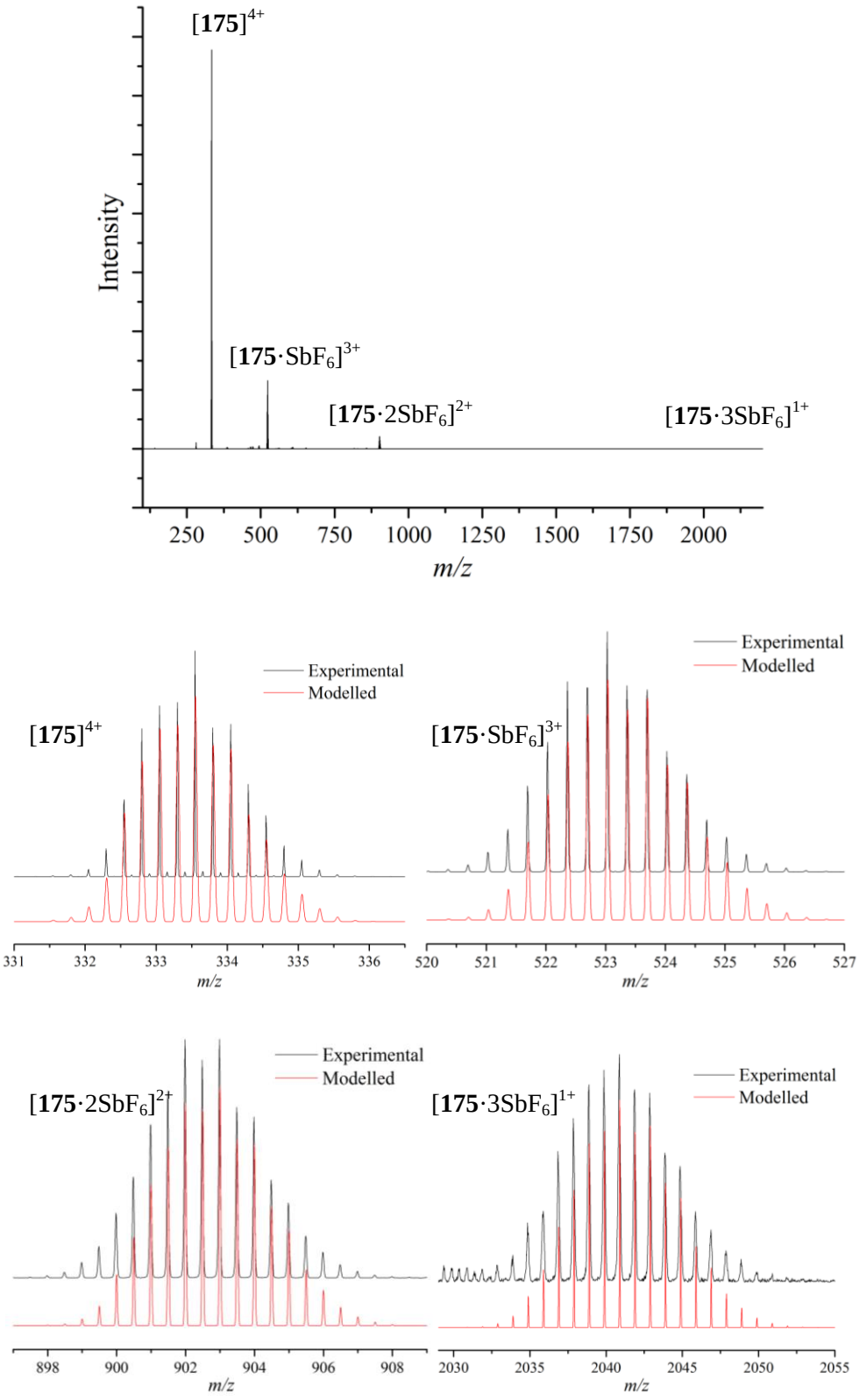

*Figure 5.20: ESI-MS of **175**·4SbF$_6$. The peaks found by experiment (black) are shown in comparison with their modelled isotopic distributions (red).*

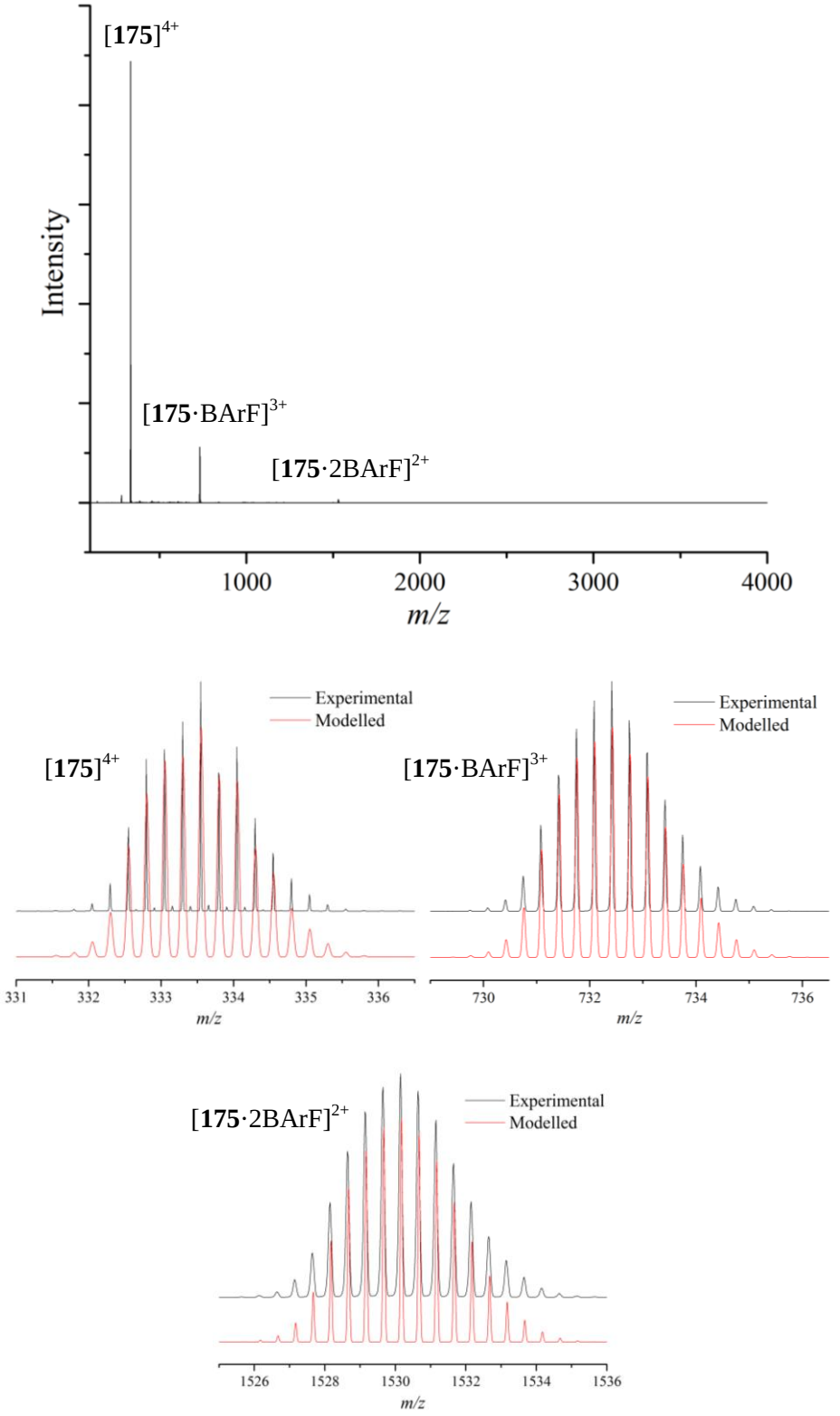

*Figure 5.21: ESI-MS of **175**·4BArF. The peaks found by experiment (black) are shown in comparison with their modelled isotopic distributions (red).*

5.7.5 Stability of 175·4Ph$_4$B

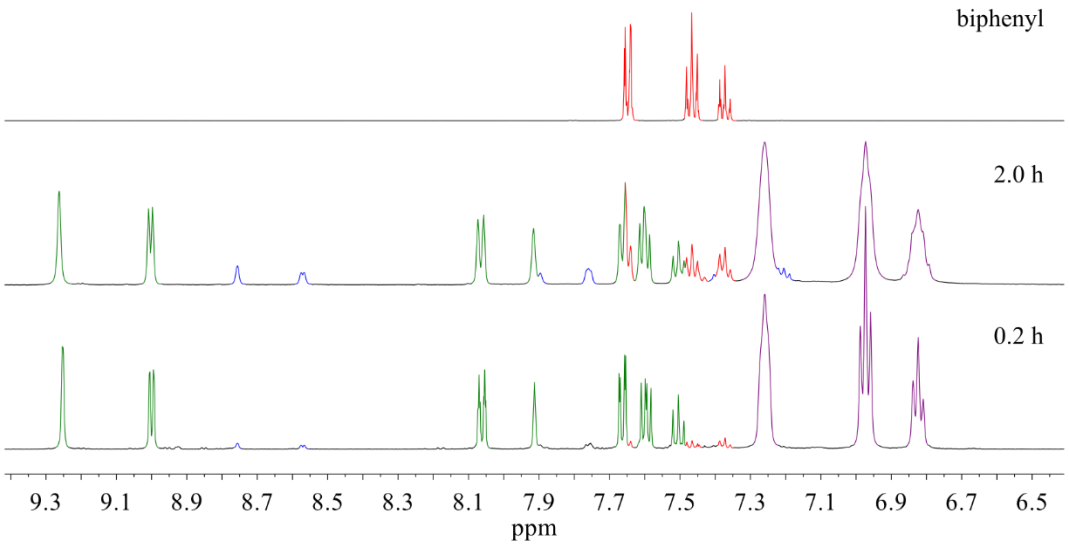

*Figure 5.22: Degradation of **175**·4X (green), where X = Ph$_4$B (purple) monitored by ^{1}H NMR (500 MHz, CD$_3$CN, 300 K). The disassembly of the cage structure is observed to give the free ligand (blue) and the cross-coupled biphenyl byproduct (red).*

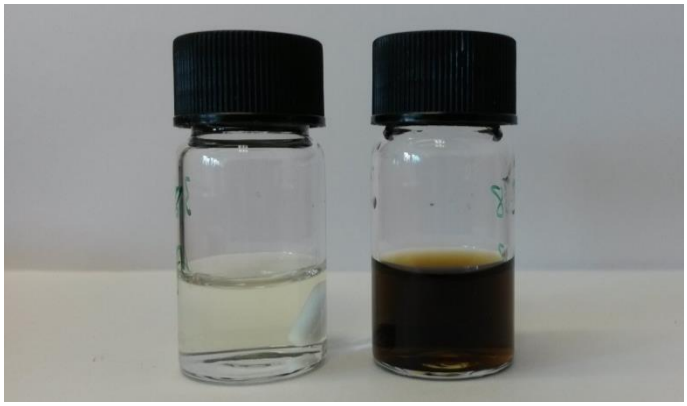

Figure 5.23: Comparison of NaBArF (left) and NaPh$_4$B (right) upon the addition of Pd^{2+}. Immediate precipitation of a black insoluble solid is observed for NaPh$_4$B.

5.7.6 ^{1}H NMR Titrations

For each titration, a solution of **175**·4X with a guest compound was titrated into a solution of **175**·4X, maintaining a constant concentration of **175**·4X throughout. For each observable peak shift of **175**·4X in the ^{1}H NMR spectra, the peak position was plotted against the concentration of guest. A global non-linear curve fitting function was then applied to the combined plots using the 1:1 binding model given by:[13]

$$y = y_0 + \Delta y\left(\frac{\left(1 + K_a(P + x)\right) - \sqrt{\left(1 + K_a(P + x)\right)^2 - 4K_aK_aPx}}{2K_aP}\right)$$

$$y = y_0 + \Delta y * z$$

$$y_0 = peak\ position\ with\ no\ guest$$

$$\Delta y = peak\ position\ with\ 100\%\ bound$$

$$x = concentration\ of\ guest$$

$$z = \frac{-b \pm \sqrt{(b)^2 - 4ac}}{2a}$$

$$where\ a = K_a * P, b = 1 + K_a(P + x)\ and\ c = K_a$$

$$P = concentration\ of\ host$$

Origin Function:

y=y0+DY*((1+Ka*(P+x))-sqrt(((1+Ka*(P+x))^2)-4*Ka*Ka*P*x))/(2*Ka*P)

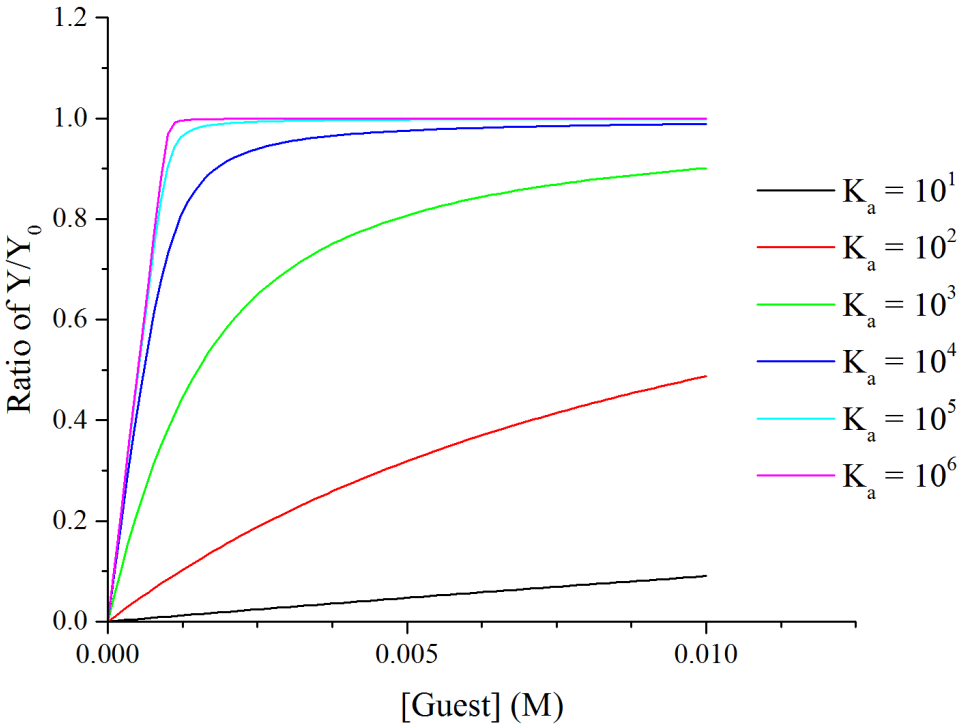

Figure 5.24: Modelled fitting functions for a range of binding constants with a host concentration of 1 mM. Note that at $K_a > 10^6$, the error in the calculated value becomes too large and the sample must either be diluted or measurements carried out with a competitor.

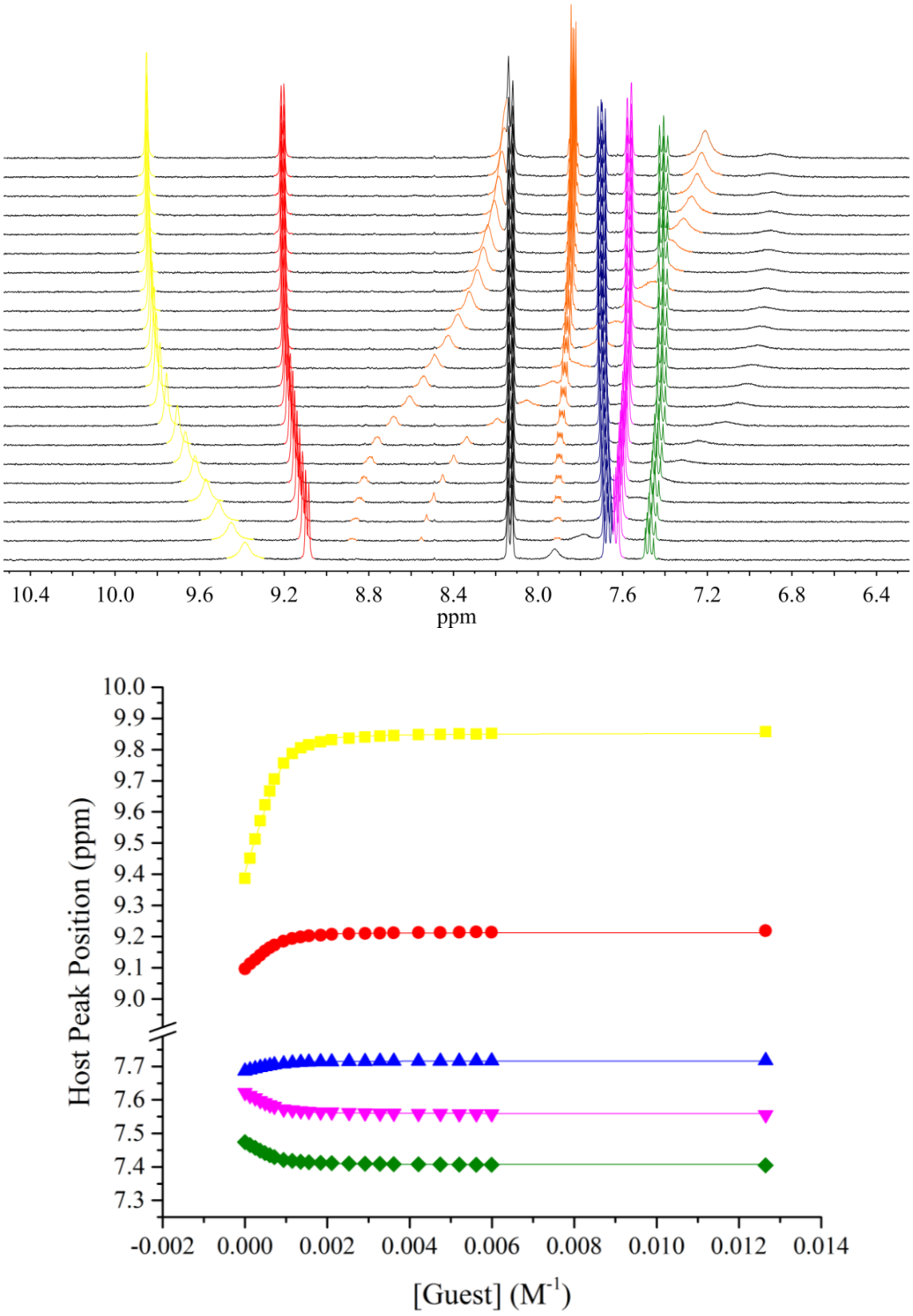

*Figure 5.25: An example of the fitting function applied to peak shifts for **175**·4SbF$_6$ upon titration of naphthoquinone in CD_3NO_2.The guest peaks are highlighted in orange and uncoloured peaks were not reported due to either no visible change or difficulties in obtaining accurate peak positions.*

5.7.7 Competition Experiments

For each titration, a solution of **175**·4X with a guest compound and a competitor was titrated into a solution of **175**·4X and the competitor, maintaining a constant concentration of **175**·4X and competitor whilst varying the concentration of the guest. The concentration of the host:guest complex, measured by peak integration, was plotted against the concentration of guest. A global non-linear curve fitting function was then applied to the combined plots using the 1:1 binding model given by:[13]

$$y = \frac{\big(B(x+P)+(R-P)\big) - \sqrt{\big(B(x+P)+(R-P)\big)^2 - 4(B-1)BxP}}{2(B-1)}$$

$$y = concentration\ of\ host/guest\ complex$$

$$x = total\ concentration\ of\ guest$$

$$P = concentration\ of\ host$$

$$R = total\ concentration\ of\ competitor$$

$$B = ratio\ of\ binding\ constants = \frac{K_{guest}}{K_{competitor}}$$

Origin Function:

y=((B*(x+P)+(R-P))-sqrt(((B*(x+P)+(R-P))^2)-4*(B-1)*(B*x*P)))/(2*(B-1))

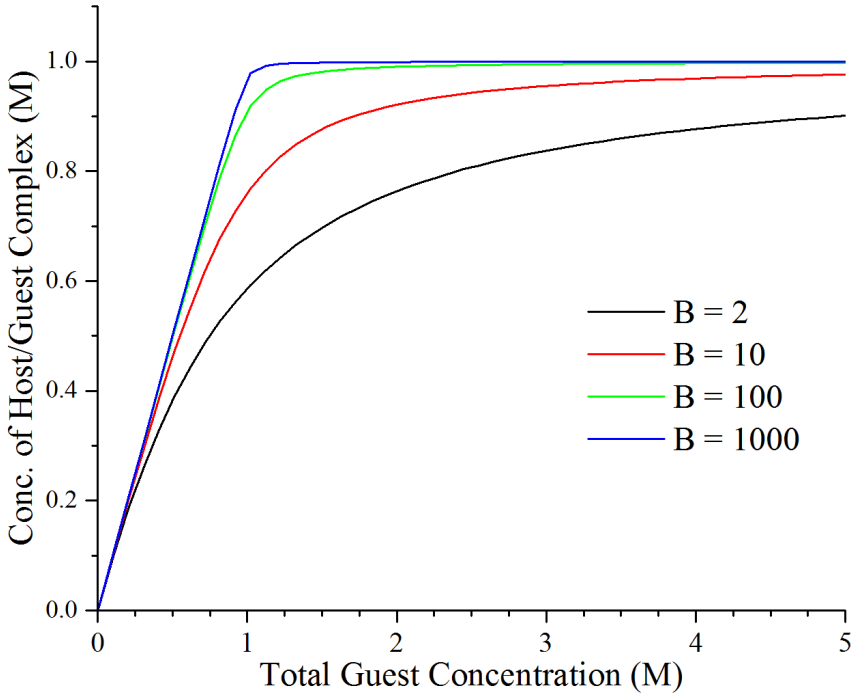

Figure 5.26: Modelled Fitting curves for competition experiments with host and competitor concentrations set at 1 mM. For B > 1000, more reliable results may be obtained by using a stronger competitor or increasing the concentration of the competitor. Note due to the peak integration required, either the guest or competitor must be in slow exchange on the ^{1}H NMR timescale.

5.7.8 Error Determination

A single example from each of the standard titrations and the competition titrations was repeated three times to assess the reliability and accuracy of the calculated binding constants. As only three data points were collected due to practical considerations, complex data analysis is not possible but the total range across the three titres was used to estimate the percentage experimental error associated with each technique.

*Table 5.6: Calculated binding constants for naphthoquinone in **175**·4SbF$_6$ over three separate titrations.*

Titration	K_a (M^{-1})	Standard Error	Range	% Experimental Error
1	22178	± 1713	-	-
2	38463	± 6664	-	-
3	35487	± 5530	-	-
Average	32043	± 4340	16285	± 25 %

*Table 5.7: Calculated binding constants for anthraquinone in **175**·4BArF over three separate competition experiments using benzoquinone as a competitor.*

Titration	K_a (M^{-1})	Standard Error	Range	% Experimental Error
1	3.99×10^7	$\pm 0.27 \times 10^7$	-	-
2	4.93×10^7	$\pm 0.36 \times 10^7$	-	-
3	5.75×10^7	$\pm 0.51 \times 10^7$	-	-
Average	4.89×10^7	$\pm 0.38 \times 10^7$	1.76×10^7	± 18 %

Although the errors associated with this experimental technique are large, the results are used to compare values on a logarithmic scale. In this case, ± 25 % error remains relatively small but never the less, the associated error should be taken into account when comparing compounds with similar binding constants.

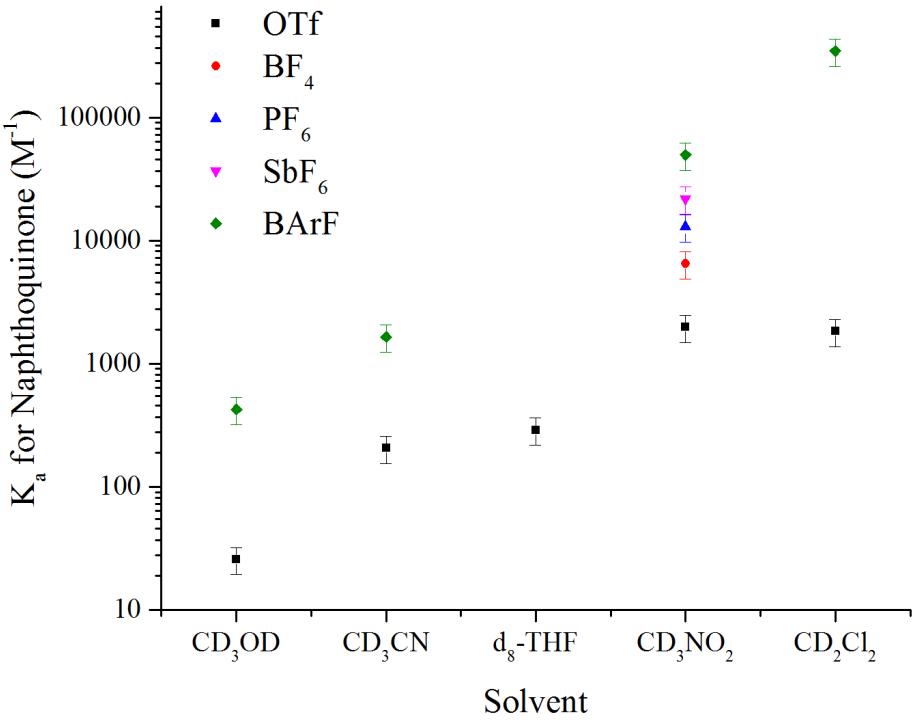

*Figure 5.27: A graphical representation of the binding constants calculated for naphthoquinone within **175**·4X. Error bars are shown for the estimated ± 25%.*

5.7.9 Mass Spectrometry of Host:Guest Complexes

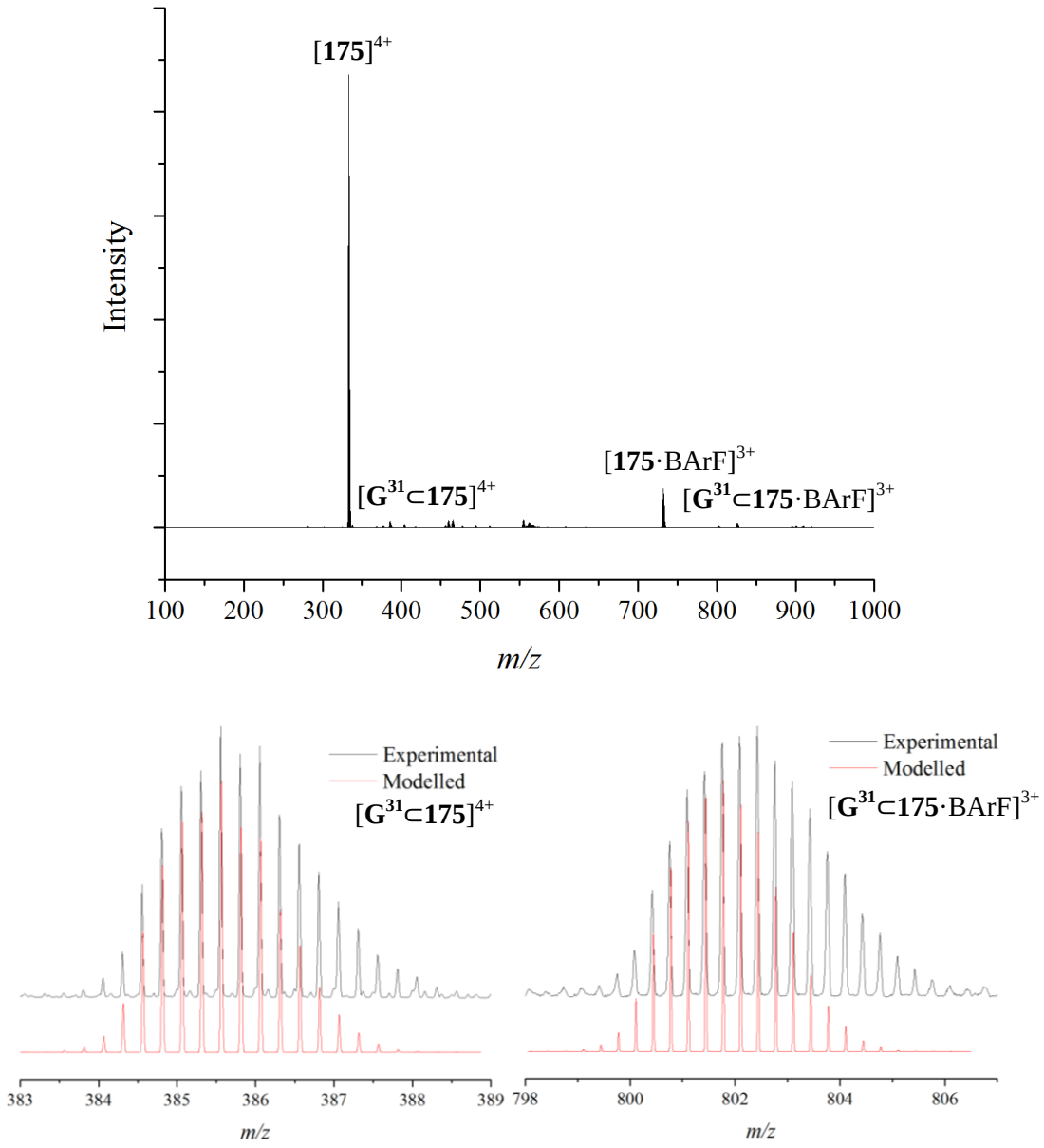

*Figure 5.28: ESI-MS of **175**·4BArF in CH_3CN with 2 equivalents of **G^{31}**. The host:guest peaks found by experiment (black) are shown in comparison with their modelled isotopic distributions (red).*

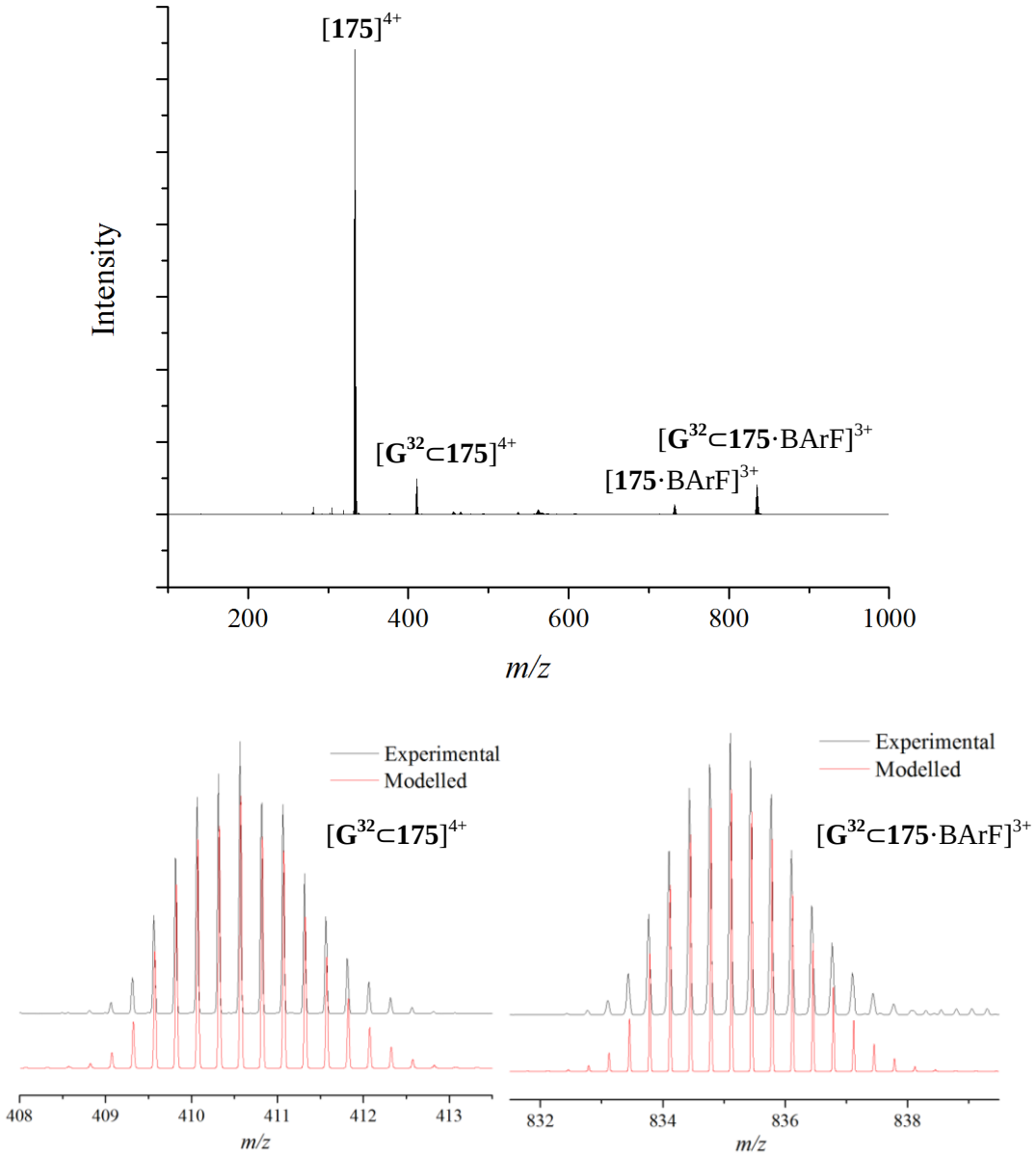

*Figure 5.29: ESI-MS of **175**·4BArF in CH_3CN with 2 equivalents of **G^{32}**. The host:guest peaks found by experiment (black) are shown in comparison with their modelled isotopic distributions (red).*

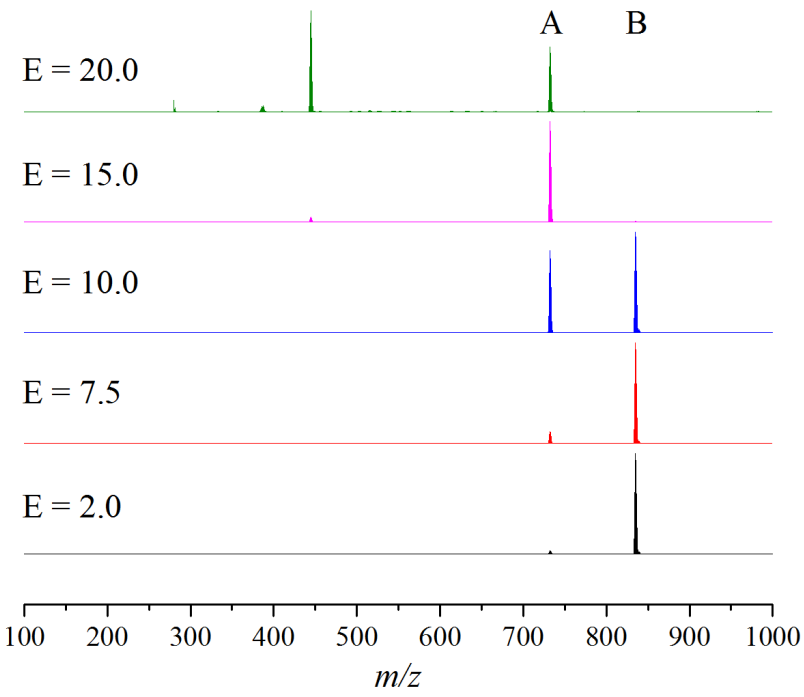

Figure 30: Normalised stack plot of MSMS of $[\mathbf{G}^{32}\subset\mathbf{175}\cdot BArF]^{3+}$ *isolated from ESI-MS of* $\mathbf{175}\cdot 4BArF$ *in* CH_3CN *with 2 equivalents of* $\mathbf{G}^{32}$*. Increasing collisional energy (E) results in the gradual dissociation of* $\mathbf{G}^{32}$ *followed by complete breakdown of the cage structure.*

5.8 References

1 Y. Z. Voloshin, I. Belaya and R. Krämer, *The Encapsulation Phenomenon*, 2016.

2 M. D. Johnstone, E. K. Schwarze, J. Ahrens, D. Schwarzer, J. J. Holstein, B. Dittrich, F. M. Pfeffer and G. H. Clever, *Chem. - A Eur. J.*, 2016, **22**, 10791-10795.

3 G. H. Clever, S. Tashiro and M. Shionoya, *Angew. Chemie - Int. Ed.*, 2009, **48**, 7010–7012.

4 J. K. Clegg, F. Li, K. a Jolliffe, G. V Meehan and L. F. Lindoy, *Chem. Commun. (Camb).*, 2011, **47**, 6042–6044.

5 A. Jiménez, R. A. Bilbeisi, T. K. Ronson, S. Zarra, C. Woodhead and J. R. Nitschke, *Angew. Chemie Int. Ed.*, 2014, **53**, 4556–4560.

6 J. E. M. Lewis and J. D. Crowley, *Supramol. Chem.*, 2014, **26**, 173–181.

7 T. Y. Kim, N. T. Lucas and J. D. Crowley, *Supramol. Chem.*, 2015, **27**, 734–745.

8 P. Mal, B. Breiner, K. Rissanen and J. R. Nitschke, *Science*, 2009, **324**, 1697–1699.

9 M. Yoshizawa, M. Tamura and M. Fujita, *Science*, 2006, **312**, 251–254.

10 Y. Kohyama, T. Murase and M. Fujita, *Chem. Commun.*, 2012, **48**, 7811–7813.

11 M. Han, R. Michel, B. He, Y. S. Chen, D. Stalke, M. John and G. H. Clever, *Angew. Chemie - Int. Ed.*, 2013, **52**, 1319–1323.

12 M. Whitehead, S. Turega, A. Stephenson, C. a. Hunter and M. D. Ward, *Chem. Sci.*, 2013, **4**, 2744.

13 Y. R. Hristova, M. M. J. Smulders, J. K. Clegg, B. Breiner and J. R. Nitschke, *Chem. Sci.*, 2011, **2**, 638–641.

14 I. Sánchez-Molina, B. Grimm, R. M. Krick Calderon, C. G. Claessens, D. M. Guldi and T. Torres, *J. Am. Chem. Soc.*, 2013, **135**, 10503–10511.

15 S. Turega, M. Whitehead, B. R. Hall, A. J. H. M. Meijer, C. A. Hunter and M. D. Ward, *Inorg. Chem.*, 2013, **52**, 1122–1132.

16 J. L. Bolliger, T. K. Ronson, M. Ogawa and J. R. Nitschke, *J. Am. Chem. Soc.*, 2014, **136**, 14545–14553.

17 J. Wang, C. He, P. Wu, J. Wang and C. Duan, *J. Am. Chem. Soc.*, 2011, **133**, 12402–12405.

18 Y. Jiao, J. Zhang, L. Zhang, Z. Lin, C. He and C. Duan, *Chem. Commun.*, 2012, 6022–6024.

19 C. He, J. Wang, P. Wu, L. Jia, Y. Bai, Z. Zhang and C. Duan, *Chem. Commun.*, 2012, 11880–11882.

20 W. Cullen, S. Turega, C. a. Hunter and M. D. Ward, *Chem. Sci.*, 2015, **6**, 2790–2794.

21 H. T. Chifotides, I. D. Giles and K. R. Dunbar, *J. Am. Chem. Soc.*, 2013.

22 F. Fochi, P. Jacopozzi, E. Wegelius, K. Rissanen, P. Cozzini, E. Marastoni, E. Fisicaro, P. Manini, R. Fokkens and E. Dalcanale, *J. Am. Chem. Soc.*, 2001, **123**, 7539–7552.

23 A. K. Turek, D. J. Hardee, A. M. Ullman, D. G. Nocera and E. N. Jacobsen, *Angew. Chemie - Int. Ed.*, 2015, 539–544.

24 S. Shirakawa, S. Liu, S. Kaneko, Y. Kumatabara, A. Fukuda, Y. Omagari and K. Maruoka, *Angew. Chem. Int. Ed. Engl.*, 2015, 1–5.

25 K. G. Lewis, S. K. Ghosh, N. Bhuvanesh and J. a. Gladysz, *ACS Cent. Sci.*, 2015, **1**, 50–56.

26 P. Liao, B. W. Langloss, A. M. Johnson, E. R. Knudsen, F. S. Tham, R. R. Julian and R. J. Hooley, *Chem. Commun.*, 2010, **46**, 4932.

27 C. Reichardt, *Solvents and Solvent Effects in Organic Chemistry*, 2003.

28 D. R. Lide and W. M. Haynes, *CRC Handbook of Chemistry and Physics - 90th Edition*, 2010.

29 C. A. Hunter, *Angew. Chemie - Int. Ed.*, 2004, **43**, 5310–5324.

30 J. L. Cook, C. A. Hunter, C. M. R. Low, A. Perez-velasco and J. G. Vinter, *Angew. Chemie Int. Ed.*, 2007, **46**, 3706-3709.

31 C. Allott, H. Adams, P. L. Bernad Jr., C. A. Hunter, C. Rotger and J. A. Thomas, *Chem. Commun.*, 1998, 2449–2450.

32 H. Adams, F. J. Carver, C. A. Hunter and N. J. Osborne, *Chem. Commun.*, 1996, 2529–2530.

33 V. U. Pandit, S. S. Arbuj, U. P. Mulik and B. B. Kale, *Environ. Sci. Technol.*, 2014, **48**, 4178–83.

34 J. J. Mason and J. Bergman, *Org Biomol Chem*, 2007, **5**, 2486–2490.

35 J. Barluenga, H. Fanlo, S. López and J. Flórez, *Angew. Chem. Int. Ed.*, 2007, **46**, 4136–40.

36 K. S. L. Chan, M. Wasa, X. Wang and J.-Q. Yu, *Angew. Chemie Int. Ed.*, 2011, **50**, 9081–9084.

CHAPTER 6

Hydrogen Bond Donor Metallosupramolecular Catalysis

Contents

6.1 Synopsis

The emergent hydrogen bond donor properties of a Pd_2L_4 system were investigated for catalytic activity in a range of organic transformations. The optical and electrochemical properties of a range of guest compounds were found to be highly dependent on encapsulation within the cage cavity. Initial reaction screening did not result in any observable rate enhancements, and Diels-Alder reactions were drastically inhibited due to the steric restraints within the enclosed cavity. However, using an alternative method, the oxidation potential of the mild oxidant, *p*-chloranil, was significantly increased upon binding within **175**·4X such that the oxidation of cinnamyl alcohol occurred through completely different reaction pathways to give both oligomerisation and Friedel-Crafts products.

6.2 Introduction

Molecular encapsulation within a cage species, self-assembled or not, can drastically alter the properties of the bound guest. In order to achieve catalysis, these properties must be carefully controlled to allow the stabilisation of transition states or reactive intermediates whilst showing a lower affinity for the resultant products. Within the field of metallosupramolecular catalysis, reaction rate enhancement is often achieved through preorganisation of the substrates and a subsequent increase in the effective molarity.[1–6] However, this method, particularly when applied to bi-molecular reactions, often leads to efficient product inhibition since the final geometry is, by definition, a more appropriate guest for the cage cavity. Alternatively, Raymond and co-workers showed how a similar preorganisation of a unimolecular reaction, termed "constrictive binding", can lead to efficient catalysis. In this case, the cationic intermediate is highly stabilised by the anionic cage cavity and subsequent formation of a neutral product reduces product inhibition and allows efficient catalytic turn-over.[7–15]

In terms of more conventional organocatalysis, hydrogen bond donors have shown great promise as non-covalent activating agents for previously unreactive functional groups.[16–19] Catalysis is achieved by stabilisation of reactive intermediates and/or increasing the susceptibility to nucleophilic attack as a result of electronic manipulation of the target substrate. Since activation is achieved through non-covalent interactions at a specific binding site, the introduction of additional chiral groups can lead to enantioselective catalysis (Scheme 6.1).[16–19]

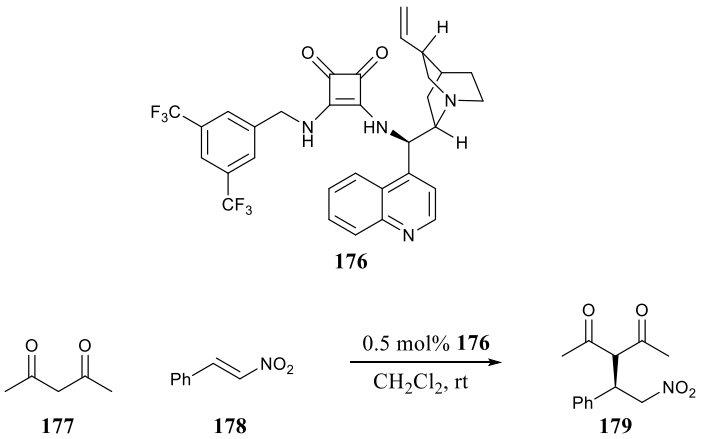

Scheme 6.1: An example of an enantioselective conjugate addition catalysed by a chiral squaramide hydrogen bond donor catalyst.[20]

Similar to many hydrogen bond donor organocatalysts, the Pd_2L_4 cage system developed by Hooley and co-workers and discussed extensively in Chapter 5, shows a strong affinity for 1,4-quinone type guests in organic solvents (Figure 6.1). Other functional groups including aldehydes, ketones, amides and nitro groups also showed preferential binding within the cage cavity through hydrogen bonding to the ortho-pyridyl positions. Due to the similarities with known organocatalysts, **175**·4X was investigated as potentially novel hydrogen bond catalyst whereby the beneficial properties are emergent from self-assembly of non-active components.

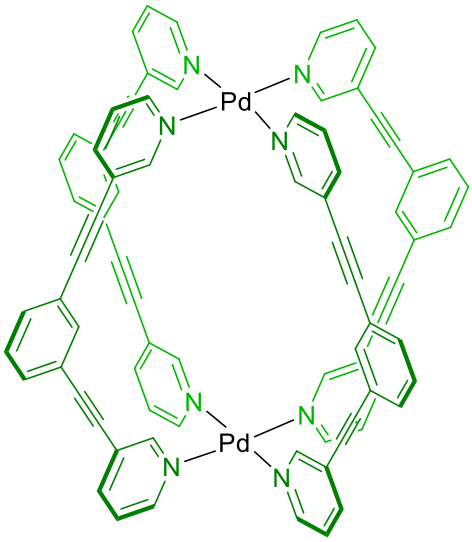

175·4X

X = OTf, BF_4, PF_6, SbF_6 or BArF

Figure 6.1: The structure of the Pd_2L_4 metallosupramolecular cage chosen utilised as a hydrogen bond donor catalyst.

6.3 Modulation of Guest Properties

The modulation of guest properties can be viewed as a potential forerunner to achieving supramolecular catalysis. A range of neutral organic guests were previously explored and discussed in detail in Chapter 5. Extended quinone compounds showed slow binding on an NMR timescale and binding constants of up to 7.98 x 10^8 M^{-1}. Quinones and their derivatives are well know to have interesting redox and photophysical properties. Substituted anthraquinones are often brightly coloured and fluoresce strongly under UV light (Figure 6.2)[21,22] while halogenated quinones are used as common oxidising, dehydrogenation and rearomatising agents e.g. *p*-chloranil and 2,3-dichloro-5,6-dicyano-1,4-benzoquinone (DDQ).[23–27]

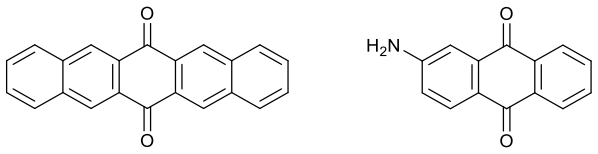

G32 **G33**

*Figure 6.2: Guest compounds that show modulation of optical properties when encapsulated within **175**·4X.*

6.3.1 Optical Properties

Strong binding of 2-aminoanthraquinone within **175**·4BArF leads to the desymmetrisation of the cage from a D_{4h} to a C_s point group and splitting of the ^{1}H NMR signals (see Chapter 5). Like many substituted anthraquinone compounds, 2-aminoanthraquinone is both highly coloured and emissive (emission λ_{max} = 540 nm) (Figure 6.3). Hydrogen bonding within the cavity results in a strong red shift in both the visible absorption band and the emission wavelength.

The significant red-shift observed for both the absorption and emission, 70 and 34 nm respectively, is potentially due to stabilisation of the LUMO by hydrogen bond formation within the cage cavity. Both computer modelling and literature suggest that the LUMO of 2-aminoanthraquinone is heavily situated on the oxygen atoms whilst the HOMO is located preferentially on the amino functionalised aromatic ring (Figure 6.4).[28] Stabilisation of the LUMO relative to the HOMO due to a reduction in electron density associated with the

oxygen atoms within the cage cavity will therefore lead to a smaller HOMO-LUMO gap and consequently lower energy absorption and emission.

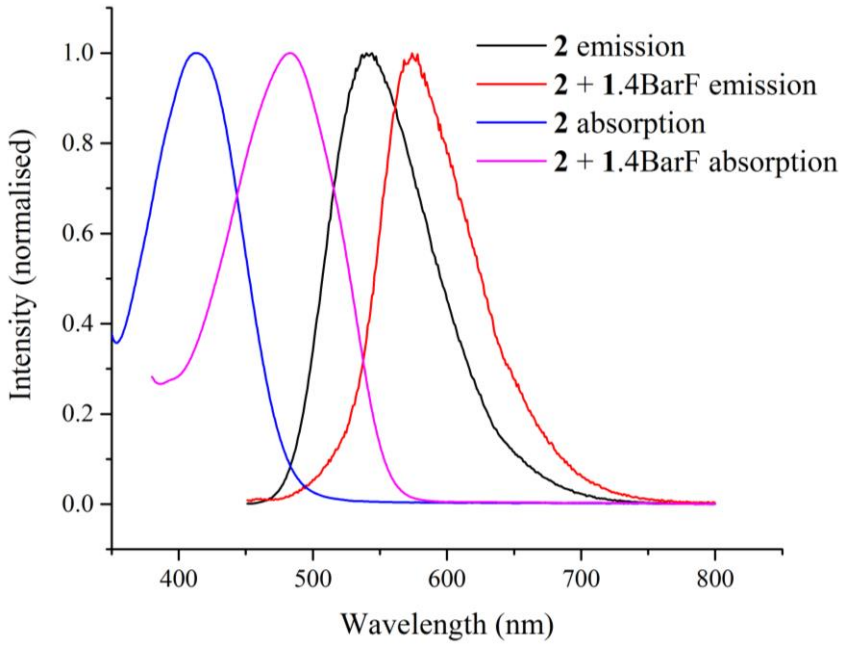

*Figure 6.3: Comparison of absorption and emission maxima for 2-aminoanthraquinone both in solution (CH_3CN) and after the addition of 1 eq. of **175**·4BArF.*

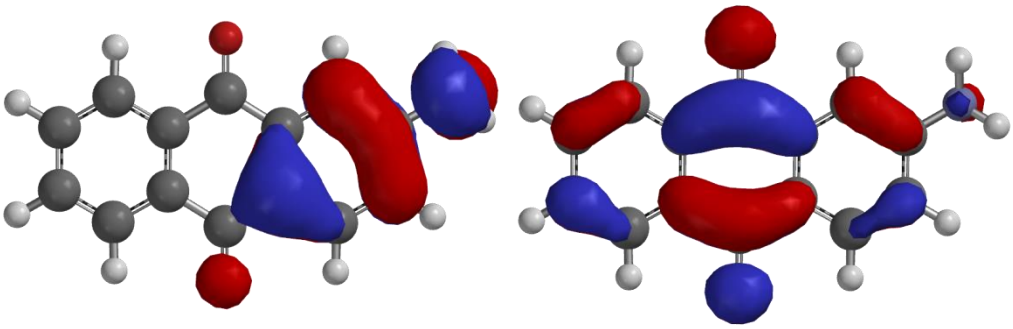

Figure 6.4: Computer modelling (DFT, B3LYP, 6-31G) of the HOMO and LUMO of 2-aminoanthraquinone.*

Pentacenedione shows strong emission in the solid state or thin film but only very weak emission in the solution phase. Encapsulation within **175**·4X results in strong emission enhancement with a 16 fold increase in emission intensity at the isosbestic point (Figures 6.5

and 6.6). The emission of encapsulated **G**^{32} also adopts well-structured bands and a small stokes-shift consistent with π-π transitions common to many polyaromatic systems. This drastic alteration in the photophysical properties of **G**^{32} is likely due to the cage preventing the formation of weakly emissive excimers. Although the solution behaviour of **G**^{32} has not been extensively reported,[29] strong emission is observed in the solid state (i.e. high concentrations) compared with the relatively weak emission from dilute solutions.[30] For comparison, the excimer formation of pyrene is a well-studied and documented phenomenon routinely used for studying short or long range interactions in both supramolecular and biological chemistry.[31–33]

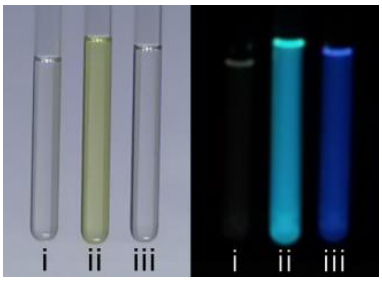

*Figure 6.5: Comparison of solution colour (100 μM, CH_2Cl_2) for i) **G**^{32} ii) **G**^{32}⊂**175**·4BArF and iii) **175**·4BArF under ambient lighting (left) and irradiation with 365 nm UV-light.*

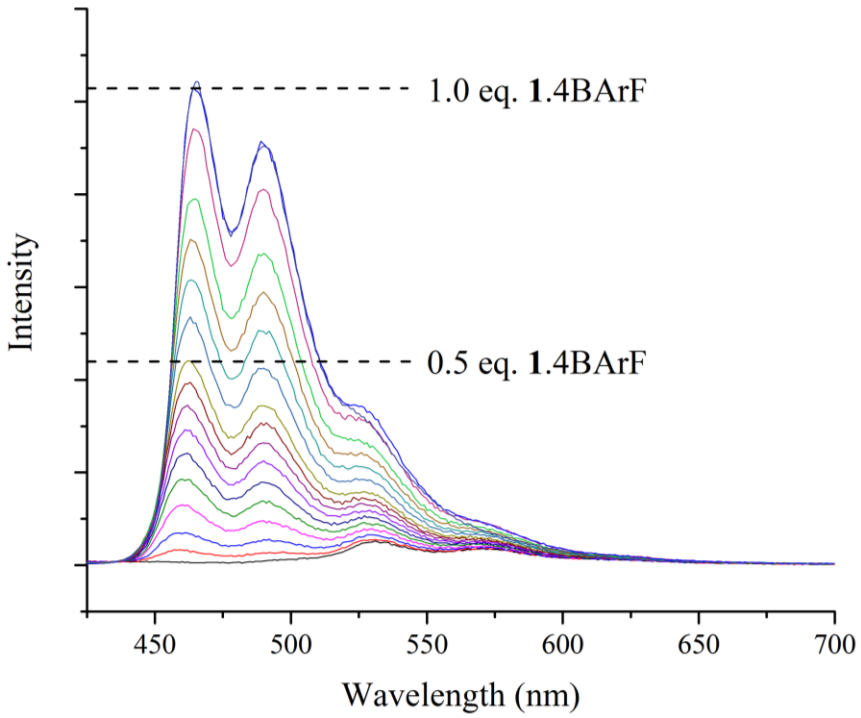

*Figure 6.6: Titration of **175**·4BArF into a solution of **G**^{32}.*

The unusual "turn-on" fluorescence of pentacenedione can also be utilised to probe the formation of **175**·4X. Since only the combined complex $\mathbf{G^{32}}\subset\mathbf{175}$·4X emits light at 450-500 nm, the presence of intact cage can be deduced by the addition of $\mathbf{G^{32}}$ and monitoring the emission under UV-light. The very high binding affinity of $\mathbf{G}^{32}$ for **175**·4X also aids in the nearly quantitative formation of $\mathbf{G^{32}}\subset\mathbf{175}$·4X at equimolar concentrations.

Vitamin K_1 (Figure 6.7), a common biomolecule used in the blood clotting pathway, is also based on a quinone backbone and was found to bind within the cage cavity of **175**·4BArF with a K_a = 2.66 x 10^3 in CD_2Cl_2. However, the lack of strong visible-light absorption outwith the spectral region of **175**·4BArF prevented any applications as a vitamin K_1 sensor.

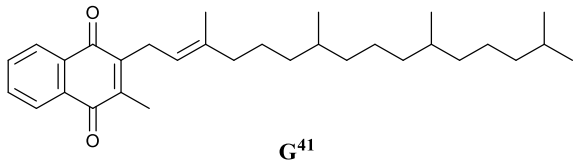

$\mathbf{G^{41}}$

Figure 6.7: The structure of Vitamin K_1.

6.3.2 Electrochemistry

While the optical properties of luminescent guests are highly sensitive to the cage environment, the hydrogen bonding environment within **175**·4X may also alter the redox potentials of encapsulated molecules. The redox chemistry of quinones has been widely studied for over a century and many simple quinones display fully reversible one and two electron reduction processes to form the semiquinone and dianion respectively. In aqueous media, the dianion is readily protonated to form the corresponding hydroquinone. The electrochemical reversibility of quinones makes them ideal candidates for a range of different redox processes and derivatives, such as ubiquinone, are widely used in biological systems as electron carriers.[34–36]

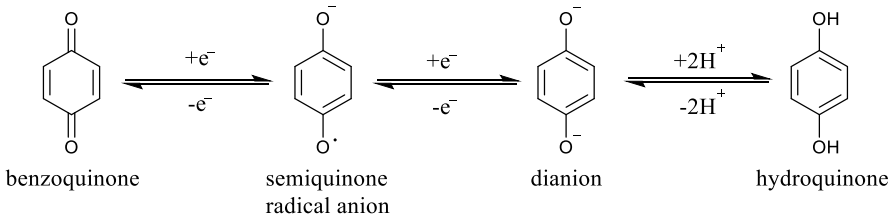

Scheme 6.2: Reduction process of benzoquinone.

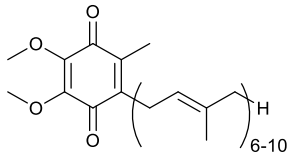

180

*Figure 6.8: The structure of ubiquinone, **180**, used in biological systems as an electron transporter.*

Previous literature has shown how the reduction potentials of quinones change in the presence of hydrogen bond donors and Brønsted acids. In general, a shift towards more positive potentials is observed upon addition of hydrogen bond donors due to stabilisation of the reduced semiquinone and dianion. A gradual change is observed due to the rapid association/dissociation of the interacting species. In contrast, protonation or deprotonation of the reduced compounds is often much slower and is therefore often responsible for irreversible processes at standard scan rates.

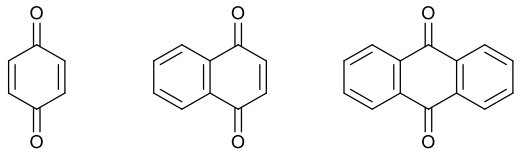

G^{29} **G**^{28} **G**^{31}

Figure 6.9: A range of 1,4-quinone guests explored for changes in redox potentials.

A similar process was expected for electrochemical measurements of **G**^{28},**G**^{29} and **G**^{31} but no protonation should occur due to the aprotic solvent and dry conditions. As expected, addition of **175**·4OTf to **G**^{28},**G**^{29} and **G**^{31} resulted in a general trend towards more positive reduction potentials indicating the propensity of **175**·4X to activate quinones towards reductive reaction pathways (Figure 6.10). Significant changes were also observed in the redox potentials of pentacenedione (**G**^{32}) upon the addition of **175**·4X but the low solubility made quantification difficult. Due to the complexity of the cyclic voltammetry measurements, the peak potentials were confirmed using differential pulse voltammetry (Figure 6.11).

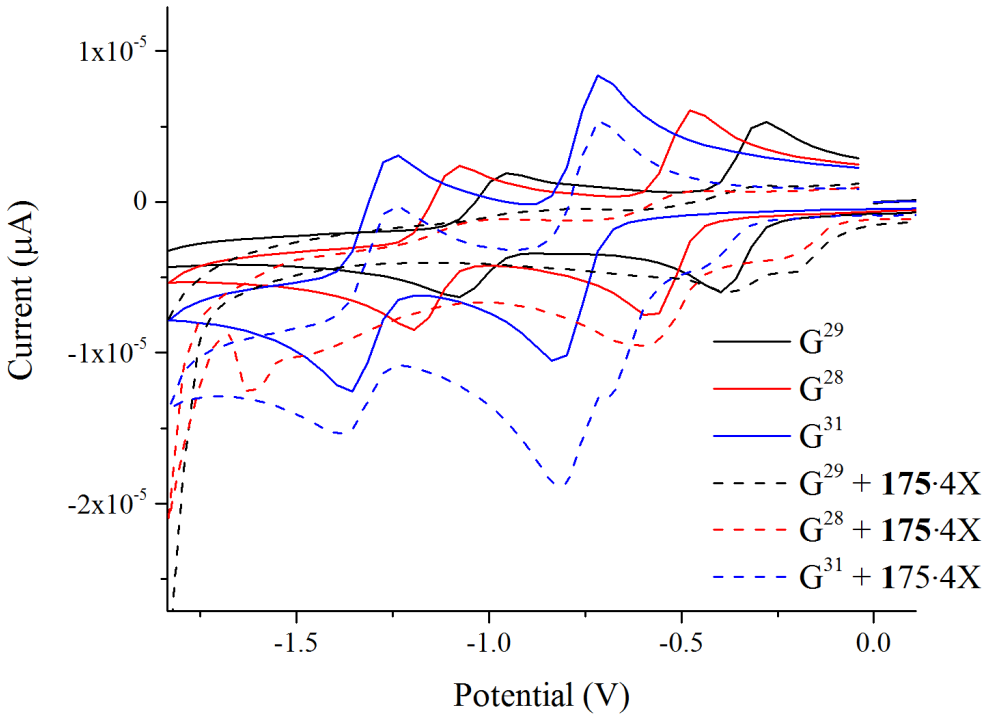

*Figure 6.10: Cyclic voltammetry (0.5 mM in CH_3CN, 0.1 M TBA·PF_6, 200 mV/s) of quinone guests with and without a stoichiometric loading of **175**·4OTf.*

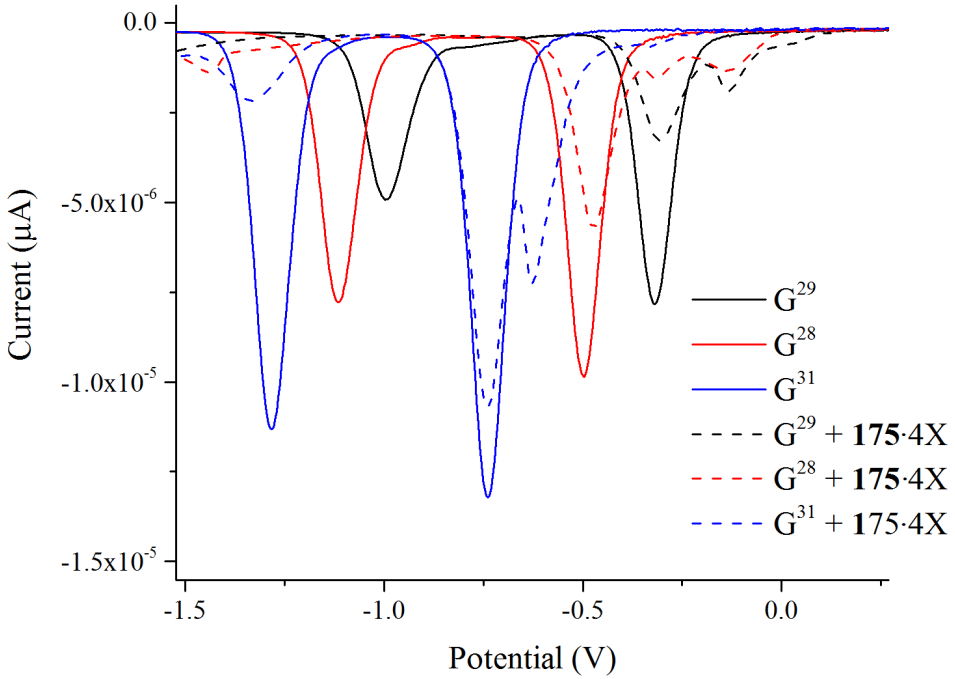

*Figure 6.11: Differential pulse voltammetry (0.5 mM in CH_3CN, 0.1 M TBA·PF_6) of quinone guests with and without a stoichiometric loading of **175**·4OTf.*

Table 6.1: Redox potentials of ***G*****[28]*****,G*****[29]** *and* ***G*****[31]** *in solution and encapsulated in* ***175****·4X.*

Compound	$E_{1/2}$	$E_{1/2}$ (with 1 eq. 175·4X)
G[29]	-0.998, -0.318	-0.306, -0.133
G[28]	-1.113, -0.495	-0.475, -0.318, -0.133
G[31]	-1.282, -0.739	-0.739, -0.627, -0.335

All measurements made in CD_3CN at room temperature.

In agreement with literature measurements with strong hydrogen bond donors, the second reduction peak disappeared for both **G[29]** and **G[28]** with 1 equivalent of **175**·4OTf and the first reduction peak became irreversible. However, the original reduction peaks for **G[31]** remained similar with 1 equivalent of **175**·4OTf but new peaks were observed at more positive potentials. As such, **G[28]** shows the most dramatic change upon addition of **175**·4OTf despite having the lowest association constant.

This can be attributed to the host:guest dynamics and the rate of association/dissociation of the encapsulated quinones. For **G[28]**, the kinetic barrier is low and rapid guest exchange means that at slow scan rates, the signals are affected by the strong association of the reduced compounds with the cage internal cavity. When the scan rate is increased, additional reversible peaks become visible (Figure 6.12). In contrast, the stronger binder, **G[31]**, displays a consistent peak pattern upon increasing the scan rate, consistent with the higher kinetic barrier confirmed by slow binding on a ^{1}H NMR timescale (Figure 6.13).

It should be noted that although the quinone compounds display very strong binding constants in previous ^{1}H NMR experiments, which would suggest almost complete encapsulation with 1 equivalent of **175**·4OTf, the high concentration of PF_6^- anions present during the electrochemical measurements would drastically reduce the percentage of quinone bound as a result of competitive binding.

Although the electrochemistry of the host:guest complexes is clearly very complicated, the overall effect of binding to **175**·4OTf is to shift the reduction potentials to a more positive position. Thus, the addition of **175**·4OTf will make reduction of quinone compounds much easier and should make the encapsulated compounds more susceptible to nucleophilic attack.

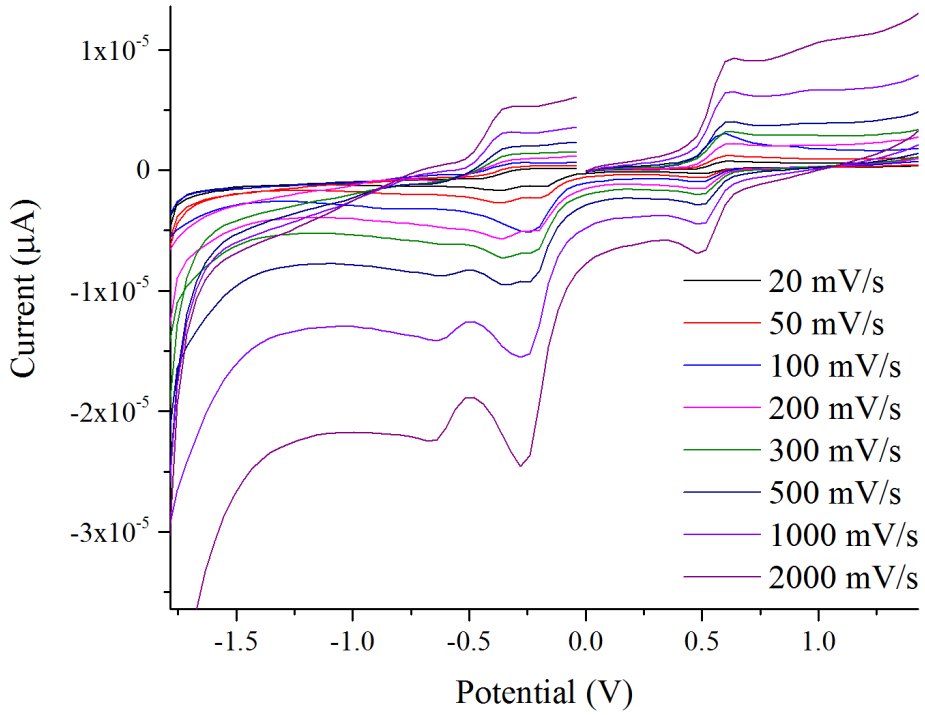

Figure 6.12: Cyclic voltammetry (0.5 mM in CH_3CN, 0.1 M TBA·PF_6) of a 1:1 mixture of ***G***^{28} *and* ***175***·*4OTf with variable scan rates.*

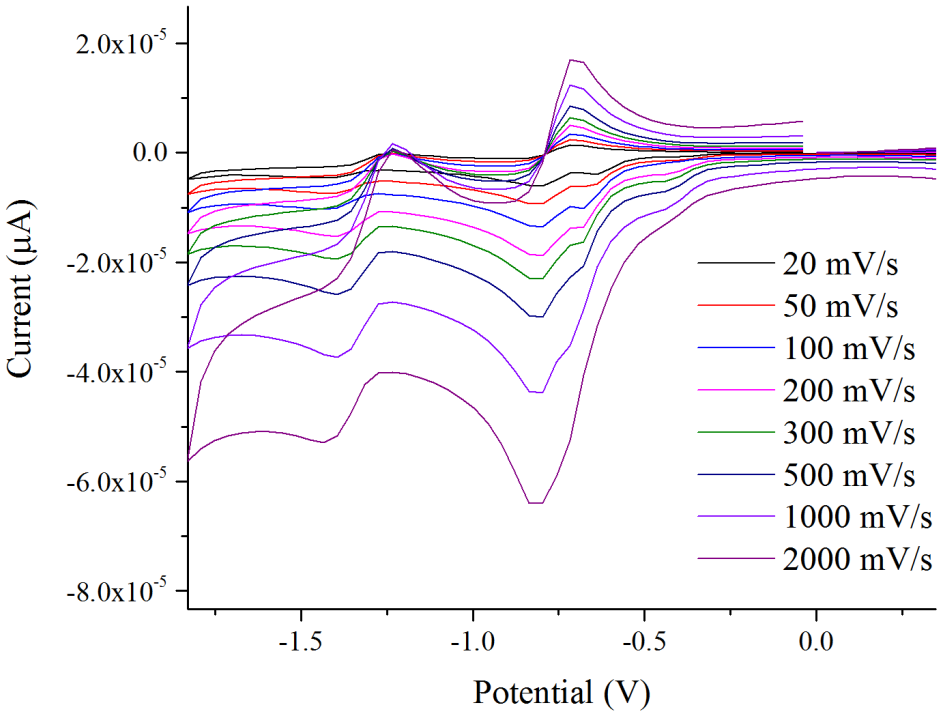

Figure 6.13: Cyclic voltammetry (0.5 mM in CH_3CN, 0.1 M TBA·PF_6) of a 1:1 mixture of ***G***^{5} *and* ***1***·*4OTf with variable scan rates.*

6.4 Stabilisation of Reactive Species

6.4.1 Diels-Alder

Fujita and co-workers pioneered the use of metallosupramolecular container compounds as molecular flasks for a range of 2+2 and 2+4 cycloadditions. The stoichiometric rate enhancement observed for a range of Diels-Alder reactions is ascribed to the dramatic increase in effective concentration brought about by co-encapsulation of two compatible substrates within a single cavity. However, strong product inhibition prevented any catalytic turn over.

Solution phase Diels-Alder reactions have been studied extensively due to their widely applicable use in organic synthesis and the production of important medicinal and industrial compounds. Lewis acid catalysis has been developed as an efficient method for improving both the reaction rate and selectivity of Diels-Alder reactions.[37–44] In a similar manner, hydrogen bond donor catalysts have also shown great utility in promoting and controlling the outcome of Diels-Alder reactions.[45–49] Thus, the hydrogen bonding environment of **175**·4OTf was considered as a catalyst for promoting the Diels-Alder reaction between naphthoquinone and selected dienes.

Reaction of naphthoquinone with cyclopentadiene readily forms the Diels-Alder adduct at room temperature in CD_3CN (Scheme 6.3). However, repeating the reaction in the presence of **175**·4OTf led to a reduction in the reaction rate rather than the intended increase. Interestingly, the initial reaction rate was only slightly affected but as the reaction proceeded, the effect became more pronounced until approximately one equivalent of naphthoquinone remained, at which point the reaction had all but ceased (Figure 6.14). Initially, with only a catalytic quantity of cage present, the reaction proceeded as normal for the 95% of naphthoquinone free in solution. As naphthoquinone was used up, the proportion of encapsulated naphthoquinone increased until the reaction rate slowed to the point at which the dimerisation of cyclopentadiene occurred at a competitive rate and prevented the reaction from going to completion.

This behaviour was attributed to efficient protection of naphthoquinone from the bulk media by **175**·4OTf, presumably by steric confinement, despite the potential activation of the substrate through hydrogen bonding. In order for a Diels-Alder process to proceed, there must be efficient overlap of the dienophile and diene. If the steric constraints within the cage

cavity prevent the formation of this intermediate, any reaction will be prevented. A similar process was described by Nitschke and co-workers for the protection of white phosphorus in aqueous media.[50]

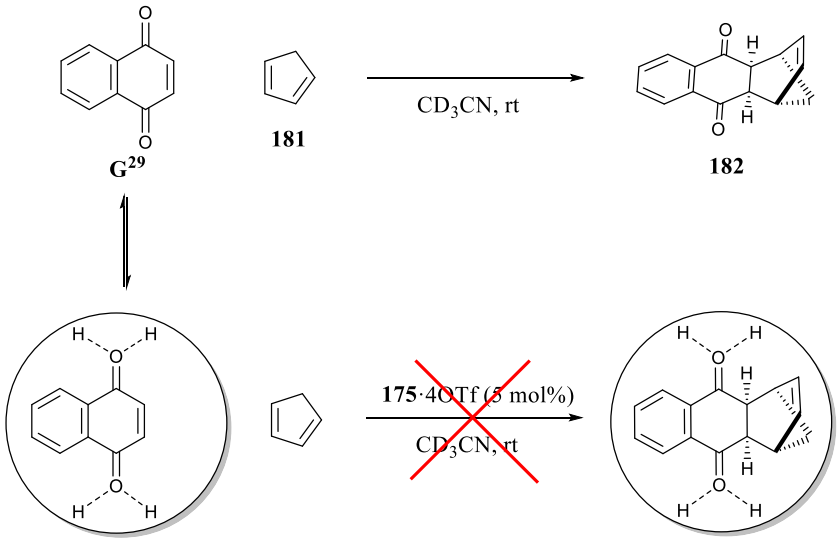

*Scheme 6.3: The investigated Diels-Alder reaction between naphthoquinone (**G**[29]) and cyclopentadiene (**181**).*

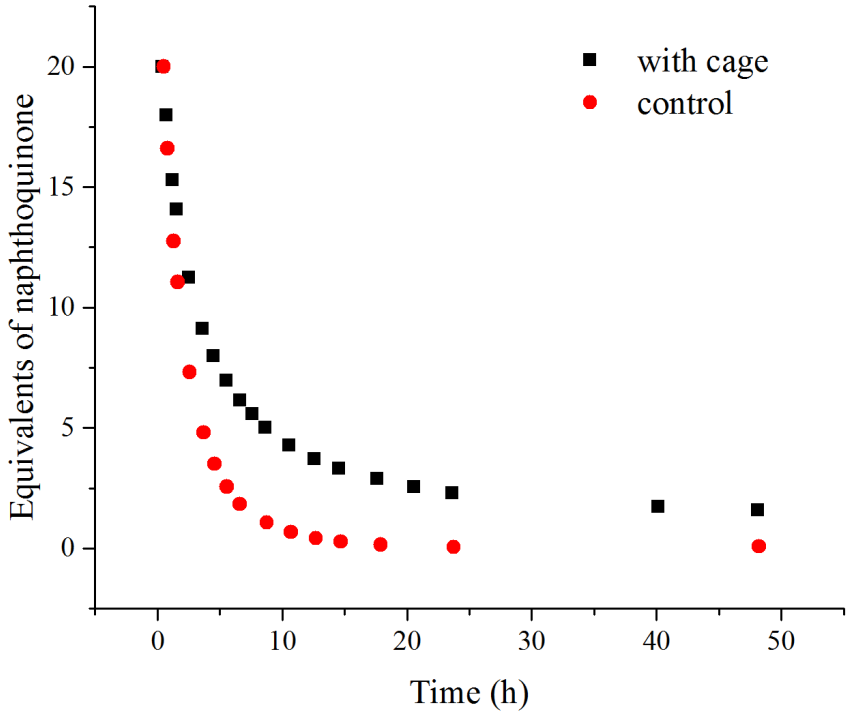

Figure 6.14: Reaction rate for the reaction between naphthoquinone and cyclopentadiene.

6.5 Supramolecular Catalysis

175·4X was screened for catalytic activity in a number of different chemical reactions, all based around activation of quinone substrates through hydrogen bonding within the internal cavity.

6.5.1 Nucleophilic Substitution

Nucleophilic substitution of naphthoquinone and related halogenated analogues is well known process for the synthesis of highly coloured dye compounds. Hydrogen bond donation to the carbonyl groups was predicted to enhance the electron withdrawing effect and make the alkene more susceptible to nucleophilic attack. The resultant enolate type intermediate would also be stabilised by the positive hydrogen bonding pockets (Scheme 6.4). The reaction of naphthoquinone or 2,3-dichloronaphthoquinone with a range of primary amines proceeded readily in CH_2Cl_2 to produce highly coloured products. However, GC analysis of the reaction mixtures showed no noticeable difference in the reaction rate upon the addition of **175**·4BArF. As with the Diels-Alder reaction described above, the absence of any acceleration in the reaction rate could be explained by sterics.

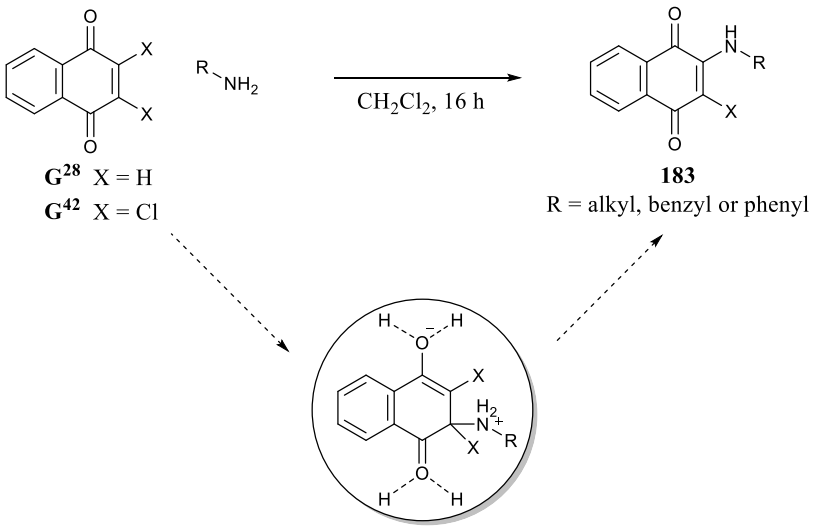

Scheme 6.4: Nucleophilic substitution of naphthoquinone analogues with amines.

6.5.2 Nitroaldol

In a similar manner to the nucleophilic substitution, encapsulation within the hydrogen bonding environment of **175**·4BArF was expected to activate α,β-unsaturated carbonyl

compounds in a range of nitroaldol reactions. Reactions were attempted with both naphthoquinone and **G**[38] in nitromethane (Scheme 6.5). **G**[38] was intended to extend the reaction site further out of the cage interior to help reduce any steric constraints preventing reactions taking place. In all cases, no obvious signs of the intended reaction were observed, even when nitromethane was used as the solvent, and the addition of non-nucleophilic bases led to either partial or complete degradation of **175**·4BArF (Table 6.2).

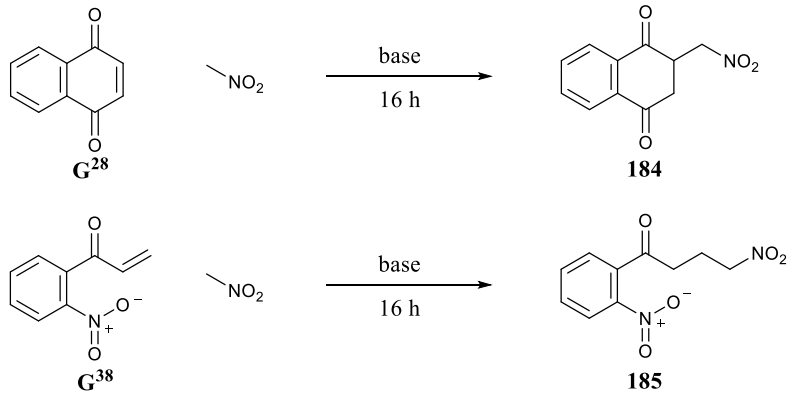

Scheme 6.5: Nitroaldol reaction between known guests and nitromethane.

Table 6.2: Nitroaldol reactions with nitromethane.

Compoud	Base	Solvent	Observation
G[29]	none	neat	No reaction
G[29]	2,6-lutidine	neat	Yellow to dark brown, partial cage dissociation
G[29]	DBU	neat	Yellow to dark brown, complete cage dissociation
G[38]	none	neat	No reaction
G[38]	2,6-lutidine	neat	Yellow to dark brown, partial cage dissociation
G[38]	DBU	neat	Yellow to dark brown, complete cage dissociation

Current literature utilises hydrogen bond donors (HBD) as catalysts for activation of nitroalkenes.[20,51–53] Hydrogen bonds formed between the catalyst and the nitro group further increase the electron withdrawing effect of the nitro group and make the alkene more susceptible to nucleophilic attack. Standard reagents such as nitrostyrene were thought to be too sterically encumbered to undergo reaction within the cage cavity; however, the flexible alkyl chain of nitrohexene was thought to allow encapsulation. Small ^{1}H NMR shifts consistent with weak guest encapsulation were observed upon the addition of 1-nitrohexene to **175**.4OTf in CH_3CN.

Nitroethane was chosen as a potential nucleophile due to the small size and unreactivity towards the cage (Scheme 6.6). The use of Et_3N as a base gave the largest change in both the crude ^1H NMR and GC traces. However, the crude reaction mixture was incredibly complex suggesting a large range of reaction and degradation pathways and no single species could be isolated or identified (Table 6.3).

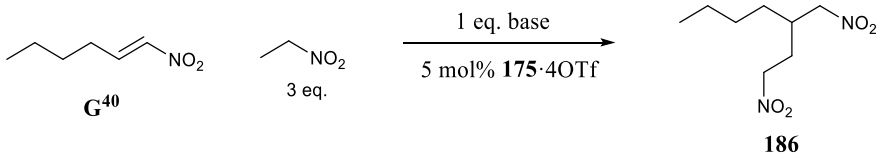

Scheme 6.6: Nitroaldol reaction between 1-nitrohexene and nitroethane.

Table 6.3: Conditions used for nitroaldol reactions between 1-nitrohexene and nitroethane.

Compound	Base	Observation
G^{40}	none	No reaction
G^{40}	DBU	Small peaks in NMR, complete cage dissociation
G^{40}	Na_2CO_3	No reaction
G^{40}	Et_3N	New peaks in NMR, partial cage dissociation

6.5.3 2-Hydroxynaphthoquinone (Lawsone)

Lawsone was examined as a potential substrate for a number of reactions; however, the addition of a base, such as DBU, Et_3N or Na_2CO_3, to Lawsone in the presence of **175**·4BArF resulted in complete degradation of the assembled structure. Slight shifts were also observed for the ^1H NMR spectrum of Lawsone. A possible explanation for the NMR shifts and rapid cage degradation is the deprotonation of Lawsone to form a bidentate ligand which rapidly displaces the pyridine ligands of the cage to form complex **188** (Scheme 6.7).

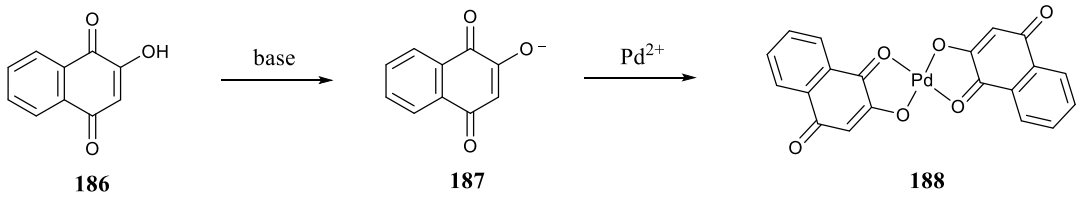

Scheme 6.7: Proposed base-induced ligand complexation of Lawsone to palladium.

6.5.4 Baeyer-Villiger Oxidation

The Baeyer-Villiger oxidation was deemed an appropriate reaction for **175**·4BArF catalysis as the hydrogen bonding environment could increase the susceptibility of the carbonyl to nucleophilic attack from the peroxy acid whilst the resultant rearrangement would produce a more weakly bound ester, preventing strong product inhibition. Sodium perborate was chosen as a mild peroxide source to avoid the need for strong oxidants that could degrade **175**·4BArF. Benzoic, acetic and trifluoroacetic acid were used as additives to generate the required peroxy acid *in situ* (Scheme 6.8). However, no reaction was observed by TLC for any of the reaction conditions tested.

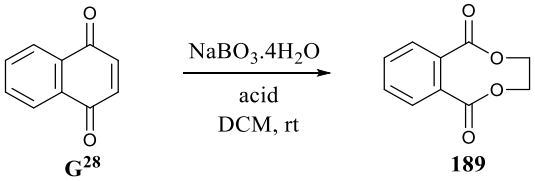

G[28] **189**

Scheme 6.8: The proposed Baeyer-Villiger oxidation reaction of naphthoquinone.

6.5.5 Imine Formation

Hydrogen bond donation could also potentially stabilise the initial intermediate formed from nucleophilic attack of a primary amine on an aldehyde in a method analogous to the more general acid catalysed formation of imines. Initial NMR studies showed a weak interaction between benzaldehyde and the cage internal cavity indicating the propensity of the system to hydrogen bond to substrates containing only a single aldehyde group.

Upon addition of n-butyl amine, no reaction was observed by TLC, with or without the presence of **175**·4OTf (Scheme 6.9). The addition of molecular sieves or Mg_2SO_4 to aid the removal of water did not improve the result. It should be noted that previous studies with palladium based cages have shown they are absorbed irreversibly onto the surface of the molecular sieves.

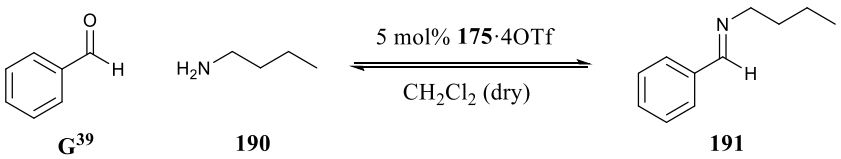

G[39] **190** **191**

Scheme 6.9: Imine formation between benzaldehyde and n-butyl amine.

In all of the attempted reactions described above, encapsulation of substrates within the cage cavity either directly hinders the reaction rate or produces no detectable rate enhancement despite the likely hydrogen bond activation. As such, steric confinement within the cavity appears to prevent any reactivity. In order avoid this, encapsulation of the catalyst, rather than the substrate, was explored.

6.6 Catalyst Activation

6.6.1 Enhanced Oxidation with *p*-Chloranil

Hydrogen bond donors have been shown to decrease the reduction potential of quinones through stabilisation of the hydroquinone form.[54–5657] As shown previously, electrochemical analysis of benzoquinone in the presence of **175**·4OTf altered the first reduction potential from -0.318 V to -0.133 V (vs Ag/AgCl). Another quinone, *p*-chloranil, is commonly used as an oxidant in organic synthesis but many processes are slow due to the relatively mild reduction potential (0.010 V vs SCE).[58] Switching to the to more highly oxidising derivative DDQ, is also unfavourable due to the high cost and potential release of highly toxic cyanide. Encapsulation of *p*-chloranil within the hydrogen bonding cavity of **175**·4BArF could therefore increase the reduction potential and thus increase the rate of oxidation.

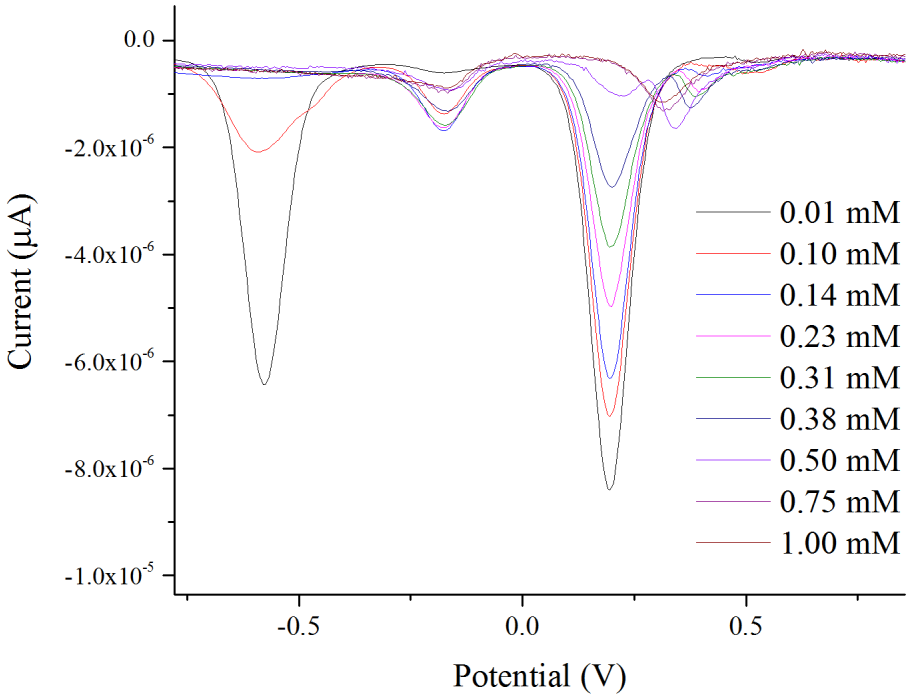

Figure 6.15: Differential Pulse Voltammetry of p*-chloranil with increasing concentrations of* ***175****·4OTf.*

Initial electrochemical studies showed a similar trend to that observed for **G**[28],**G**[29] and **G**[31]. Addition of **175**·4OTf to a solution of *p*-chloranil resulted in the appearance of new peaks at more positive potentials (Figure 6.15). With excess **175**·4OTf, and therefore near complete encapsulation of all of the *p*-chloranil, the resultant first and second reduction peaks are

situated at significantly more oxidising potentials, 0.315 V and -0.176 V vs Ag^+/AgCl respectively. This increase in the reduction potential of *p*-chloranil by 120 mV suggests that encapsulation within **175**·4X could significantly increase the compound's oxidising ability and synthetic utility.

6.6.2 Oligomerisation of Cinnamyl Alcohol

In order to assess the benefits of encapsulating *p*-chloranil within **175**·4X, the oxidation of cinnamyl alcohol to cinnamyl aldehyde was chosen as a model reaction (Scheme 6.10). Initial experiments, monitored by GC, showed a small rate enhancement (1.5x) in the rate of consumption of **192** upon addition **175**·4OTf in CH_3CN at reflux. Using a combination of **175**·4BArF in CH_2Cl_2 at room temperature to maximise binding gave a rate of enhancement of approximately 10 fold (Figure 6.16). Control experiments with pentacenedione as competitive binder proceeded at the background rate indicating that the internal cavity of the cage was essential for the rate enhancement rather than just the presence of the cage, free ligand or palladium ions.

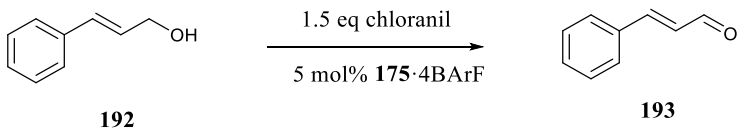

192 **193**

Scheme 6.10: Oxidation of cinnamyl alcohol to cinnamyl aldehyde.

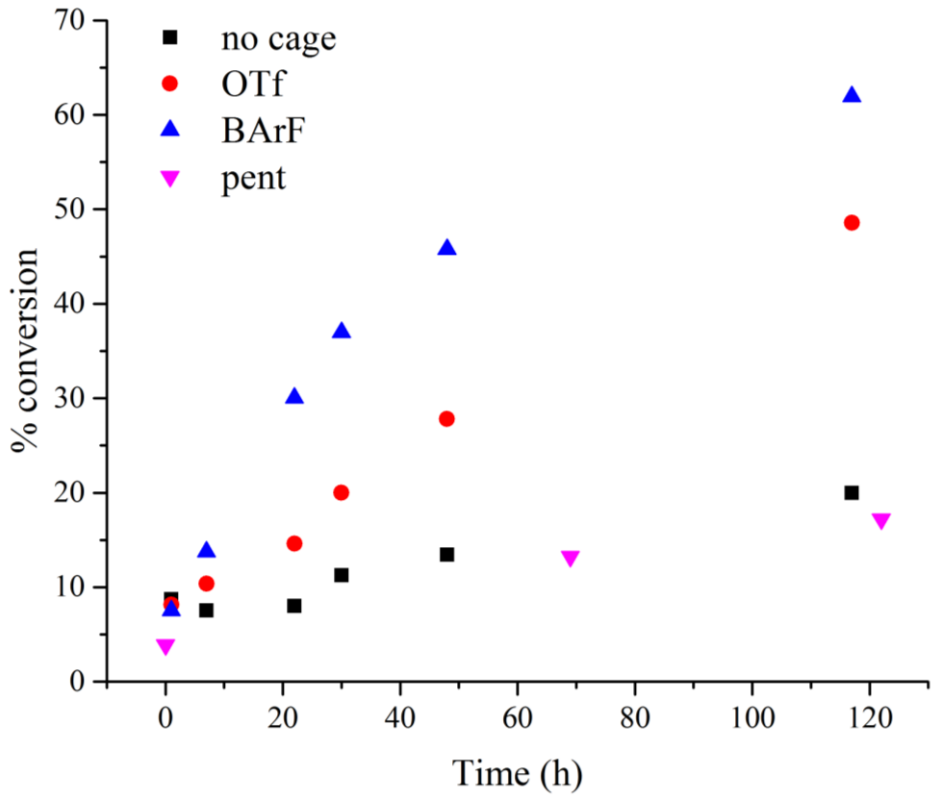

Figure 6.16: Percentage conversion of cinnamyl alcohol as measured by GC peak integration.

However, the initial rate studies described above were carried out using GC to directly compare the product and reactant peak integrals. In order to confirm these observations, the same reactions were then repeated with a standard to quantify the conversion correctly and check that no by-products were produced.

Using pentadecane as an internal standard, the control reactions were shown to very slowly oxidise the cinnamyl alcohol as expected. However, the cage-catalysed reaction was shown to produce another product not visible by GC and the apparent increase in oxidation rate measured previously was due solely to a reduction in the reactant peak. The unobserved product was presumably removed by the silica plug required prior to running a GC sample.

^{1}H NMR studies of the reaction process showed the rapid consumption of cinnamyl alcohol resulting in the loss of the alkene signals and formation of a broadened series of aromatic signals consistent with polymerisation (Figure 6.17). No precipitation was visible in the samples studied.

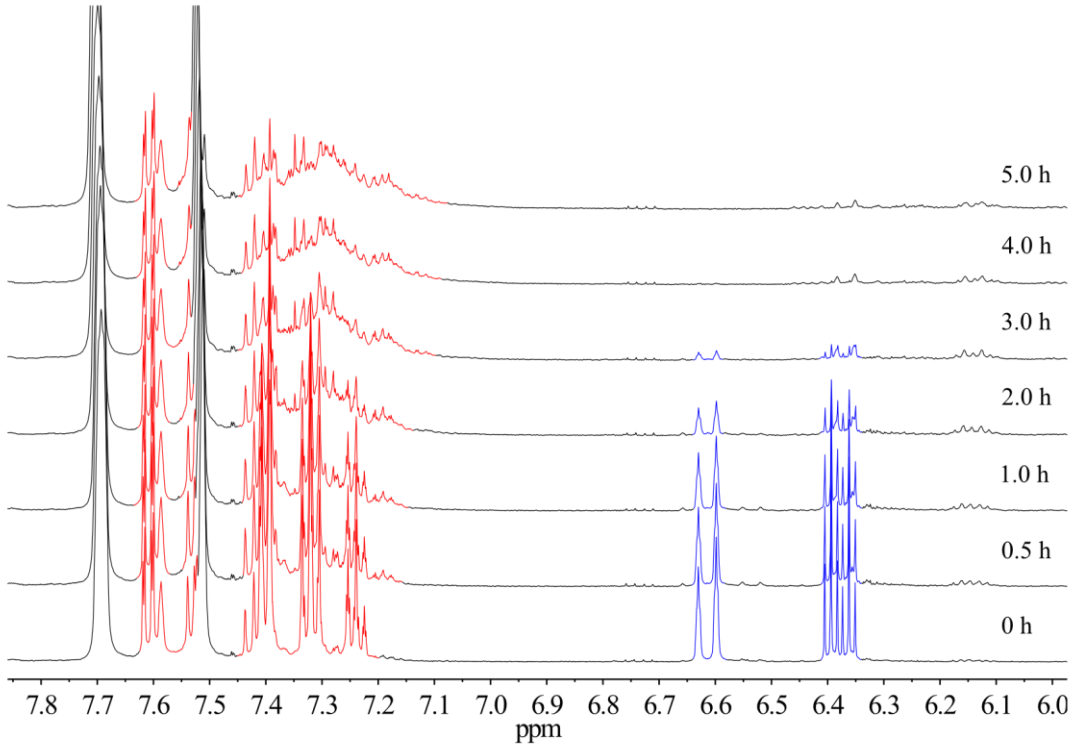

*Figure 6.17: Partial ^{1}H NMR (500 MHz, CH_2Cl_2, 300 K) of cinnamyl alcohol oligomerisation in the presence of p-chloranil/**175**·4BArF showing the rapid disappearance of the alkene peaks (blue) and corresponding broadening of the aromatic peaks (red).*

Phenolic derivatives of cinnamyl alcohol are well known to undergo dehydrogenative polymerisation to form lignins.[59–61] This complex biological process normally involves the use of peroxidase enzymes and/or hydrogen peroxide. Despite the lack of a phenolic moiety in the cinnamyl alcohol studied, a similar mechanism for the polymerisation of cinnamyl alcohol in the presence of chloranil/**175**·BArF was proposed based on the formation of an oxidised radical cation intermediate. As with lignins, the linkages are always formed between the β position and a variety of nucleophilic sites. Due to the lack of a phenolic site, the reaction is assumed to progress via coupling to the alcohol or alkene groups. However, further studies are required to elucidate the exact nature of this process and confirm the identity of the products formed but given the complexity of lignin type polymers and the extensive research to date, this may require an in-depth and time intensive investigation.

Interestingly, the same process can be replicated with alternative quinone oxidants (Figure 6.18). Reaction monitoring by GC showed that the trend in reagent conversion matched the trend in the first reduction potential (Table 6.4). Although the reduction potentials of 2,6-

dichlorobenzoquinone and 2,5-dichlorobenzoquinone are identical in solution, 2,5-dichlorobenzoquinone gave a greater product yield. This was explained by the difference in the reduction potentials in the presence of **175**·4OTf, presumably due to a difference in the relative association constants arising from a different molecular shape. However, it should be noted that the electrochemical conditions could not be matched to exact conditions used for the reaction due to the need to use BArF counter anions to enable maximum guest occupancy.

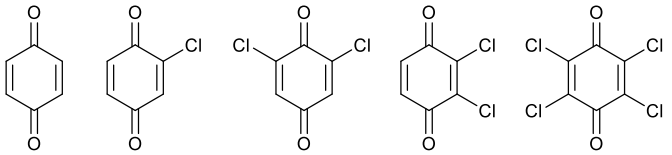

Figure 6.18: Alternative quinones used as oxidants for the polymerisation of cinnamyl alcohol.

*Table 6.4: Redox potentials of **G**[29] along with **G**[43]- **G**[46] both in solution and encapsulated within **175**·4X.*

Compound	Name	$E_{1/2}$ (V)[a]	$E_{1/2}$ (1 eq 1·4OTf) (V)[a]	Conversion (%)[b]
G[29]	benzoquinone	-0.318	-0.133	6.2
G[43]	2-chlorobenzoquinone	-0.142	0.039	11.7
G[44]	2,6-dichlorobenzoquinone	-0.001	0.180	20.3
G[45]	2,5-dichlorobenzoquinone	-0.001	0.190	26.7
G[46]	*p*-chloranil	0.195	0.315	99.7

a) all measurements made in TBA·PF_6 0.1 M in CH_3CN versus Ag^+/AgCl b) total conversion after 24 h by GC using pentadecane as an internal standard

6.6.3 Friedel-Crafts Type Reactions

Initial attempts to quantify the oxidative polymerisation of cinnamyl alcohol were made using mesitylene as the GC standard but this resulted in the complete alteration of the reaction pathway. Control experiments still showed that both the *p*-chloranil and the cage cavity were required for the reaction to occur but in this case, mesitylene was consumed during the reaction process and multiple new peaks were identified by GC. The two main products were isolated by column chromatography and analysed by ^{1}H NMR spectroscopy. The signals show the formation of coupled products between the cinnamyl aldehyde and the

mesitylene (Scheme 6.11). Both the mono- (major product) and di- (minor product) coupled species were identified. The isolated products indicated a Friedel-Crafts type coupling between mesitylene and cinnamyl alcohol with the alcohol functioning as a leaving group. The up-field position of the methylene bridge indicated that the oxygen is not present in the structure and the characteristic alkene coupling is still observed.

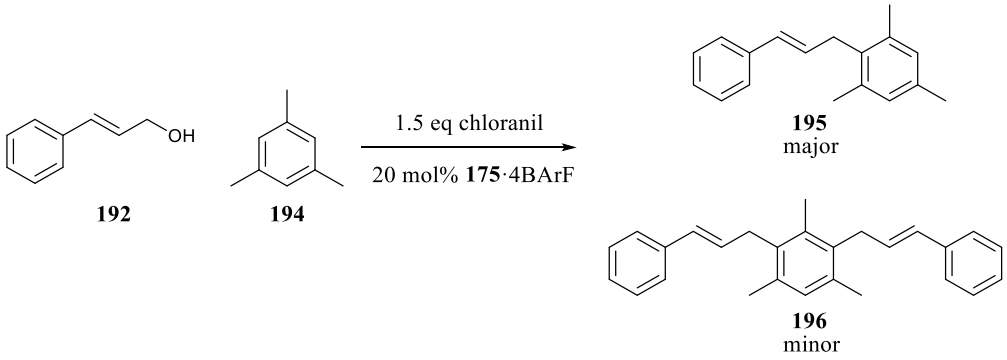

Scheme 6.11: Proposed reaction between cinnamyl alcohol and mesitylene in the presence of both chloranil and the cage catalyst.

No reaction was observed when cinnamyl alcohol was replaced with a range of different alcohols, including the saturated derivative 3-phenylpropan-1-ol (**197c**) (Scheme 6.12). This confirmed that the reaction did not take place via nucleophilic attack of the directly oxidised mesitylene. Therefore, both the previously described oligomerisation and this Friedel-Crafts process proceed through the initial oxidation of cinnamyl alcohol. As such, the electron-rich mesitylene acts as a trapping agent and prevents the cinnamyl alcohol reacting with itself.

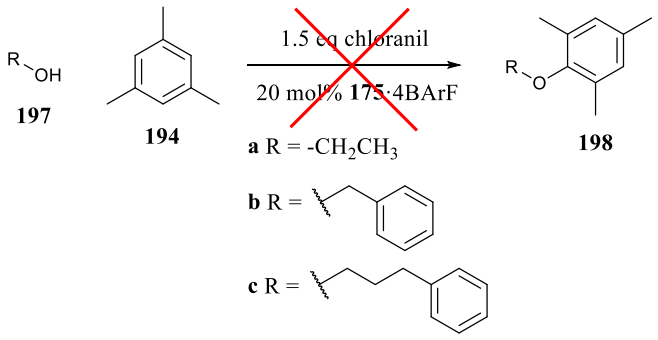

Scheme 6.12: Reactivity of mesitylene towards alternative O-nucleophiles.

Based on this hypothesis, the reaction was repeated with both electron-poor and electron-rich aromatics. As expected, replacing mesitylene with benzene did not give any observable Friedel-Crafts products and the cinnamyl alcohol polymerised according to the process

previously described when mesitylene was absent. Presumably, the cinnamyl alcohol functions as a better reaction partner than the electron poor benzene.

Surprisingly though, when the process was repeated with the electron rich anisole, the cage catalyst was completely degraded and again, no Friedel-Crafts products were observed. This result can be explained by direct oxidation of the electron rich anisole by the activated *p*-chloranil. This prevents oxidation of the cinnamyl alcohol and results in additional, as of yet, unknown reaction pathways.

6.7 Summary & Conclusions

Encapsulation within the multiple hydrogen bond donor cavity of **175**·4X was shown to modulate the properties of a number of guest compounds. The absorption and emission of coloured quinone derivatives were significantly red-shifted upon binding. Furthermore, pentacenedione exhibited a 16 fold enhancement in emission intensity and a significant blue shift in the presence of **175**·4X, attributed to isolation of individual pentacendione molecules from the bulk phase and removal of the excimer formation pathway.

The reduction potentials of quinones were all shown to be highly dependent on the presence of **175**·4X and significant shifts to more positive potentials were observed. As a result of these observations, **1**·4X was screened as a potential hydrogen bond donor catalyst in a range of organic transformations but with no obvious rate increase detected. Indeed, **175**·4X was found to efficiently protect naphthoquinone from undergoing a Diels-Alder reaction with cyclopentadiene despite the hydrogen bond activation, presumably due to steric constraints preventing the necessary molecular overlap. In an alternative method, the oxidation power of *p*-chloranil was increased upon encapsulation in **175**·4X, such that the oxidation of cinnamyl alcohol proceeded via a completely different reaction pathway resulting in oligomerisation. This pathway could be further altered by the addition of mesitylene to give the Friedel-Crafts adduct. As such, a self-assembled system, with emergent properties not present in the constituent parts, was able to drastically alter reaction pathways through hydrogen bond activation of a quinone based oxidant.

6.8 Experimental

6.8.1 General Information

Unless stated otherwise, all reagents and solvents were purchased from Alfa Aesar, VWR or Sigma Aldrich and used without further purification. Column chromatography was carried out using Geduran Si60 (40-63 µm) as the stationary phase and TLC was performed on precoated Kieselgel 60 plates (0.20 mm thick, $60F_{254}$. Merck, Germany) and observed under UV light at 254 nm or 365 nm. All reactions were carried out under air, unless stated otherwise. 1,3-Bis(3-ethynylpyridyl)benzene,[62] pentacenedione (**G^{4}**),[63] α-ethenyl-2-nitro-benzenemethanol,[64] 1-(2-nitrophenyl)-2-propen-1-one (**G^{10}**)[65] and $Pd(CH_3CN)_4 \cdot 2OTf$[66] were prepared according to literature procedures. 1-Nitrohexane was a kind gift from Patrick Fuchs (Zeitler Group, Universität Leipzig).

For details regarding the NMR, MS, Ultraviolet-visible light spectroscopy and emission spectroscopy apparatus, please refer to Sections 2.9.1 and 3.7.1.

6.8.2 Absorption of 2-aminoanthraquinone

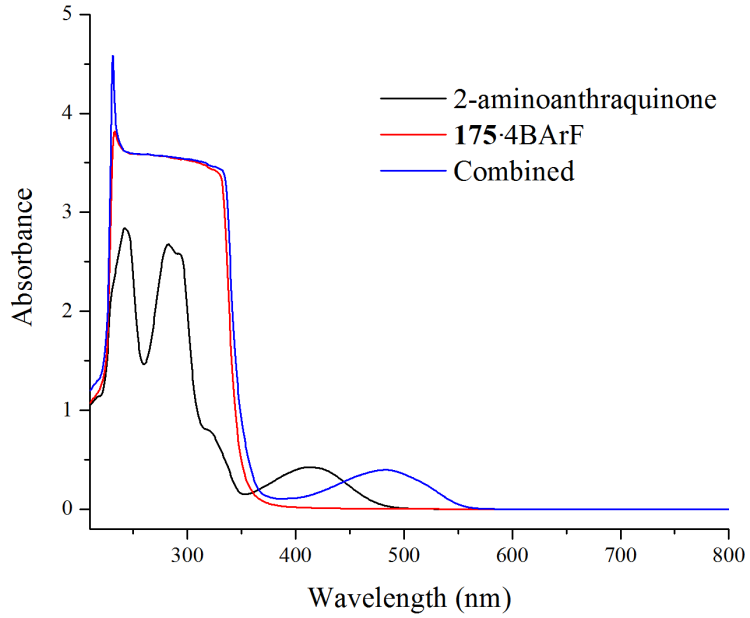

*Figure 6.19: Absorption of 2-aminoanthraquinone (CH_2Cl_2, 100 µM, 300 K) with and without the presence of **175**·4BArF.*

6.8.3 Emission of 2-aminoanthraquinone

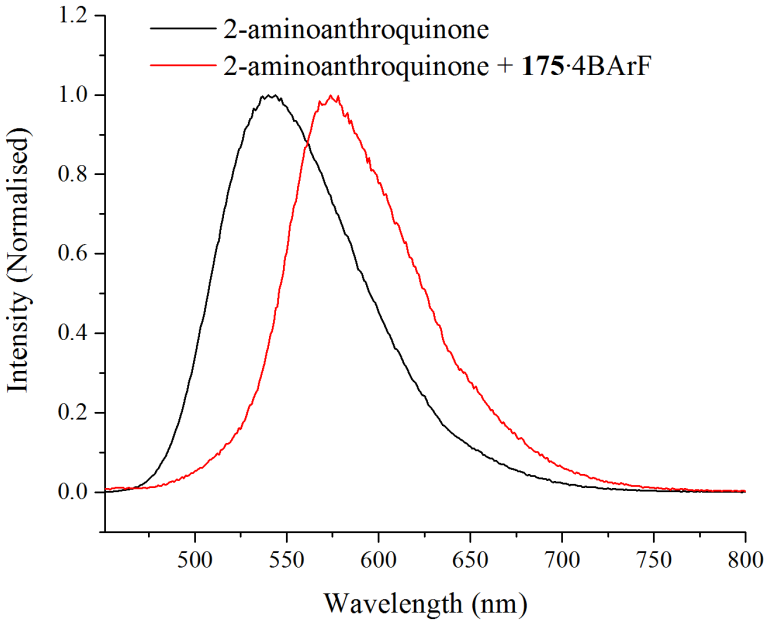

*Figure 6.20: Normalised emission (CH_2Cl_2, 100 µM, 300 K) of 2 -aminoanthraquinone with and without the presence of **175**·4BArF.*

6.8.4 Absorption & Emission of Pentacenedione Host:Guest Complex

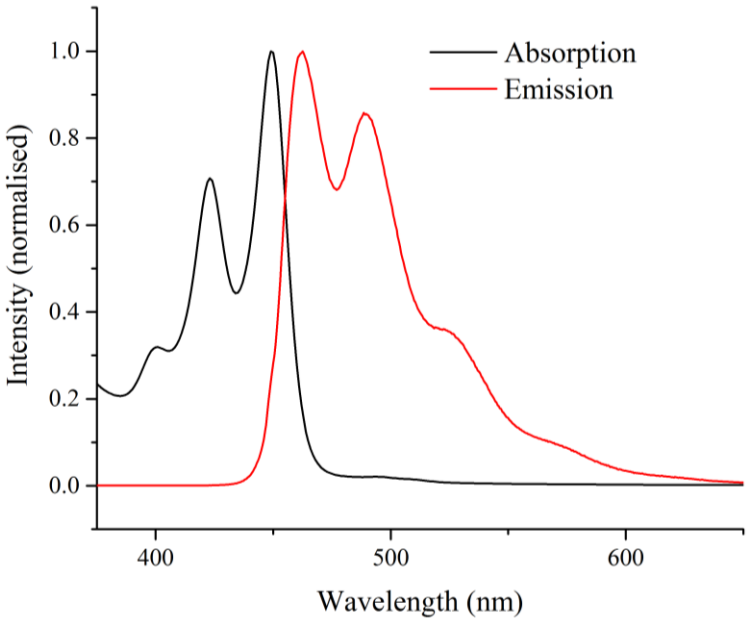

*Figure 6.21: Normalised absorption and emission (CH_2Cl_2, 100 µM, 300 K) of a 1:1 mixture of pentacenedione and **175**·4BArF.*

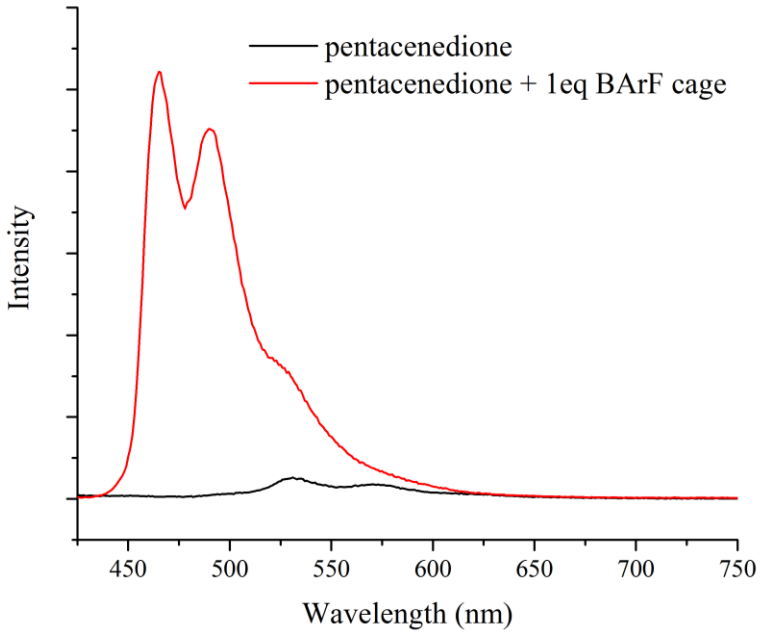

*Figure 6.22: Emission spectra (CH_2Cl_2, 100 µM, 300 K) of pentacenedione with and without the presence of 1 equivalent of **175**·4BArF.*

*Table 6.5: Comparison of pentacendione emission free and encapsulated within **175**·4BArF.*

Compound	Excitation	λmax	Area	Relative Quantum Yield
G^{32}	412 nm	531	1.924 x 10^7	1
G^{32} + **175**·4BArF	412 nm	465	2.995 x 10^8	15.6

6.8.5 Vitamin K_1 Sensing

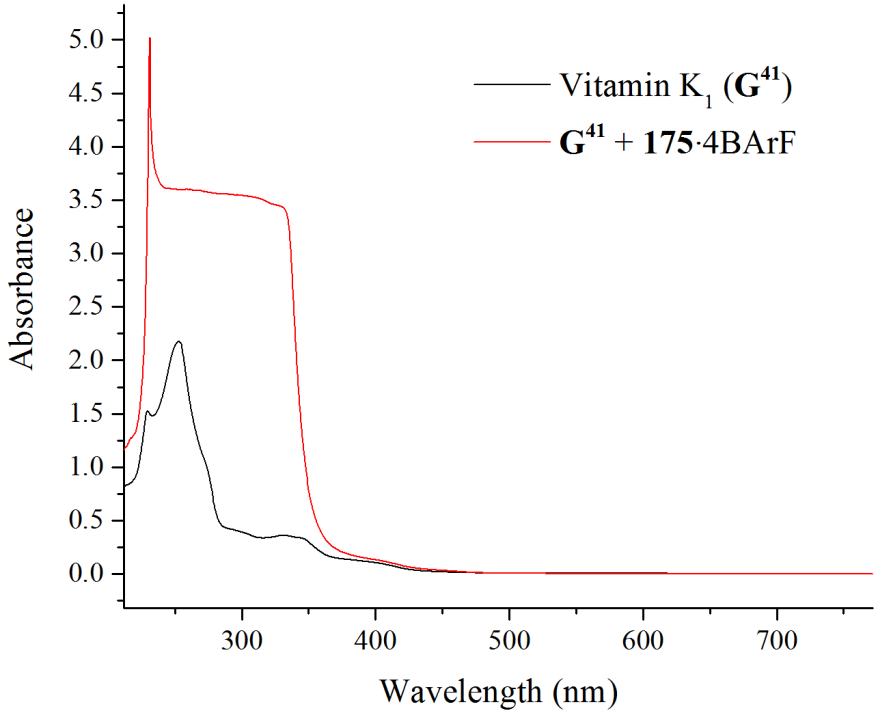

*Figure 6.23: Ultraviolet-visible light spectroscopy (CH_2Cl_2, 100 μM, 300 K) of vitamin K_1 with and without the presence of 1 equivalent of **175**·4BArF.*

6.8.6 Electrochemistry of 1,4-quinones

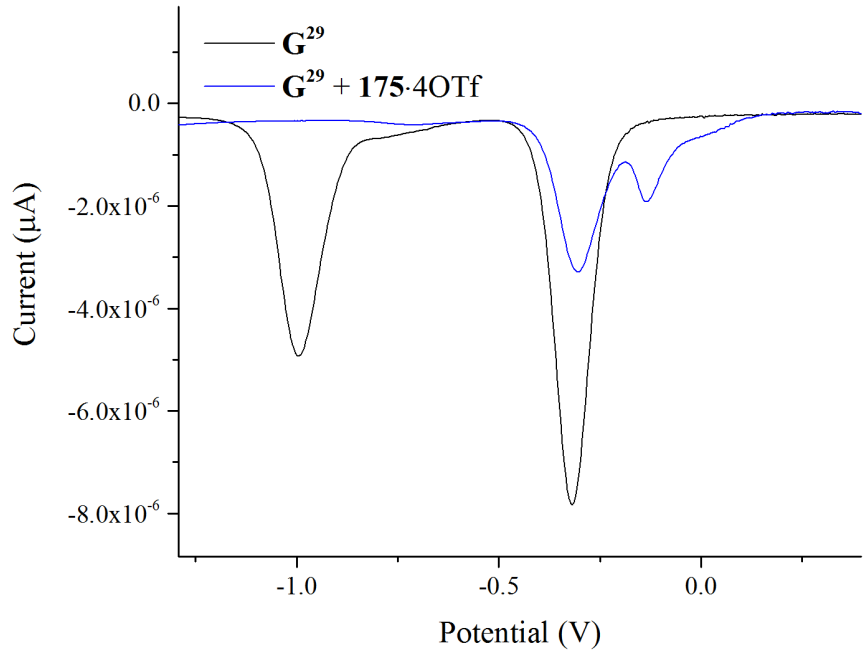

Figure 6.24: Differential Pulse Voltammetry of ***G*** ^{29} *before (black) and after the addition of* ***175***·*4OTf (blue).*

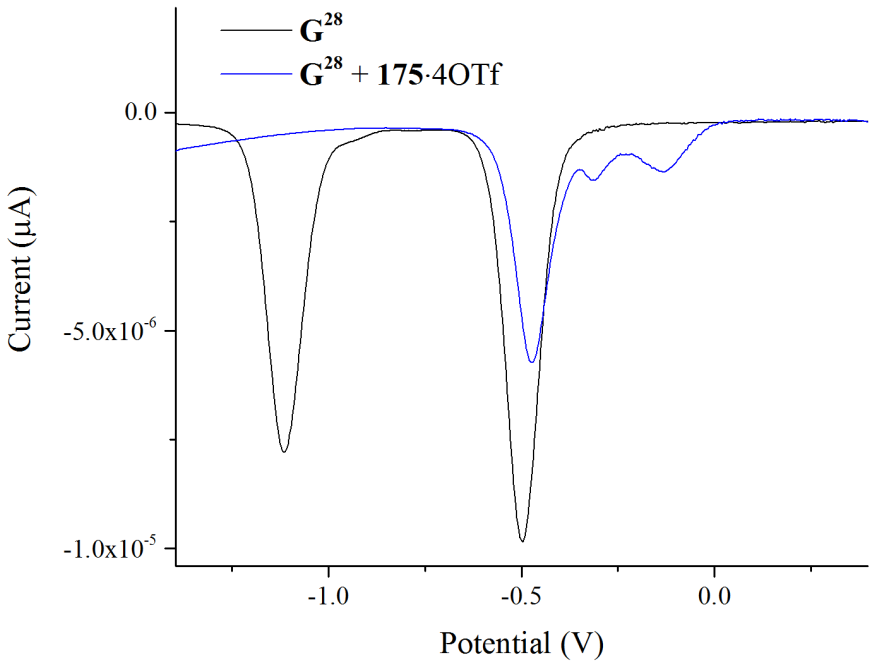

Figure 6.25: Differential Pulse Voltammetry of ***G*** ^{28} *before (black) and after the addition of* ***175***·*4OTf (blue).*

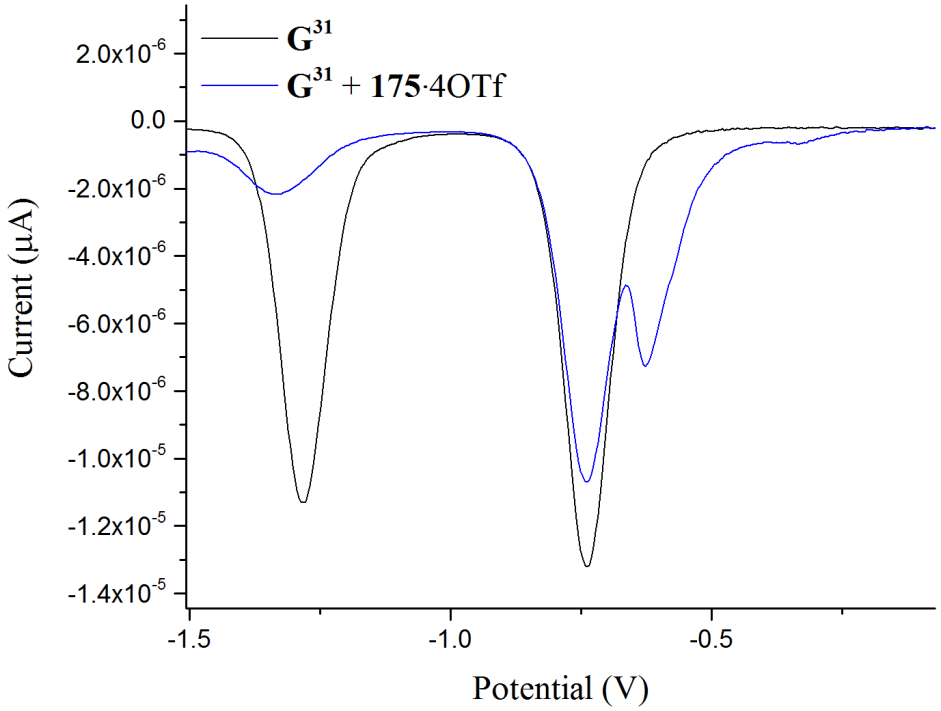

Figure 6.26: Differential Pulse Voltammetry of ***G*** ^{31} *before (black) and after the addition of* ***175****·4OTf (blue).*

6.8.7 Naphthoquinone Diels-Alder

Naphthoquinone (1.58 mg, 0.010 mmol) and freshly distilled cyclopentadiene (0.66 mg, 0.010 mmol) were dissolved in a solution of **175**·4OTf in CD_3CN (0.5 mL, 1 mM). The solution was left at room temperature and the reaction was monitored by timed ^1H NMR experiments (500 MHz, CD_3CN, 300 K). A control reaction was repeated without **175**·4OTf as a catalyst.

6.8.8 Identification of Host:Guest Interactions

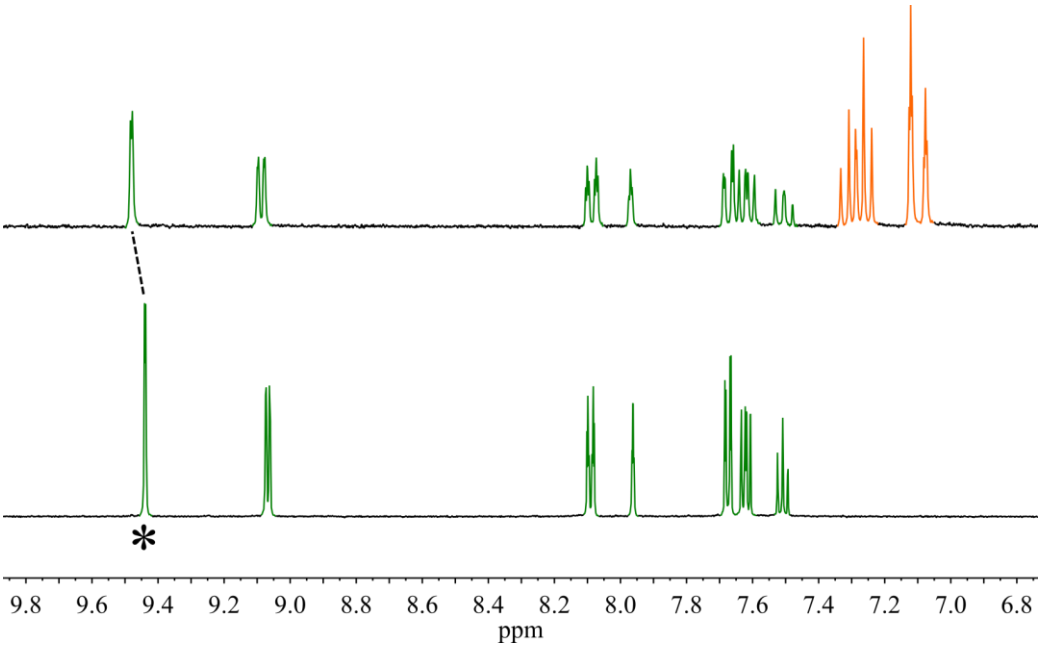

*Figure 6.27: ^{1}H NMR of **175**.4OTf (green) before (bottom) and after (top) the addition of 1-nitrohexene (orange). Inner pyridyl proton (*) gives the best indication of guest binding.*

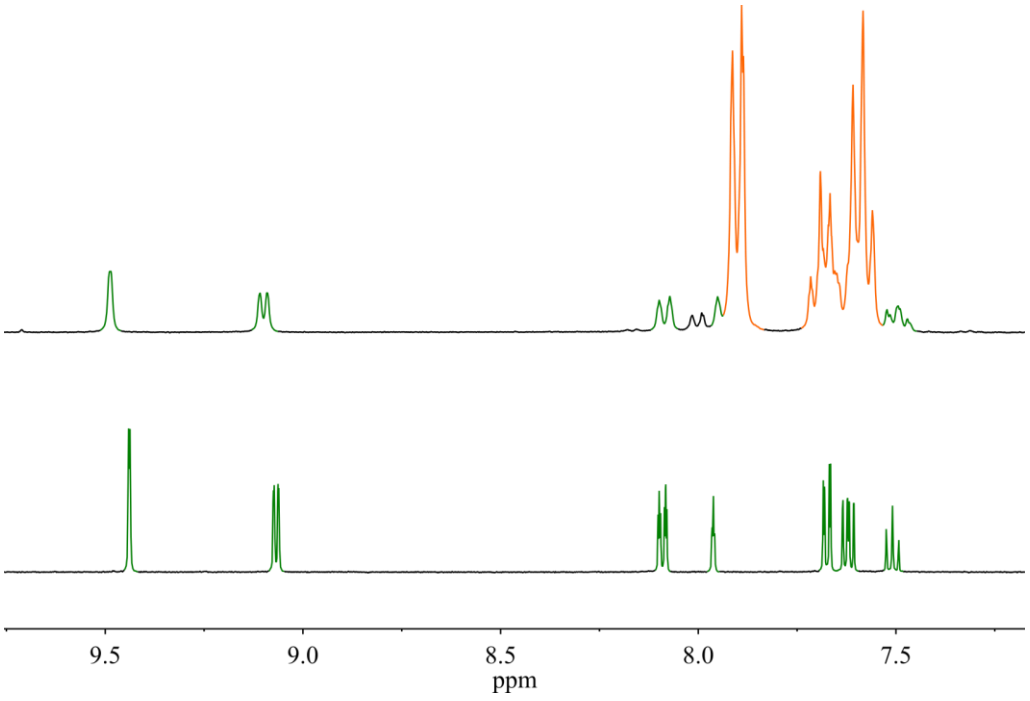

*Figure 6.28: ^{1}H NMR of **175**.4OTf (green) before (bottom) and after (top) the addition of benzaldehyde (orange).*

6.8.9 Oligomerisation of Cinnamyl Alcohol

Cinnamyl alcohol (0.81 mg, 6.0 µmol) was charged to a mixture of *p*-chloranil (1.48 mg, 6.0 µmol) and **175**·4BArF (2.87 mg, 10 mol%) in CD_2Cl_2 (0.6 mL). The reaction was kept at room temperature and monitored by ^1H NMR.

6.8.10 Friedel-Crafts Type Reactions

The following general method was used for all Friedel-Crafts reactions. An aromatic compound (6.0 µmol) was charged to a mixture of an alcohol (6.0 µmol), *p*-chloranil (1.48 mg, 6.0 µmol) and **175**·4BArF (2.87 mg, 10 mol%) in CD_2Cl_2 (0.6 mL). The reaction was kept at room temperature and monitored by ^1H NMR.

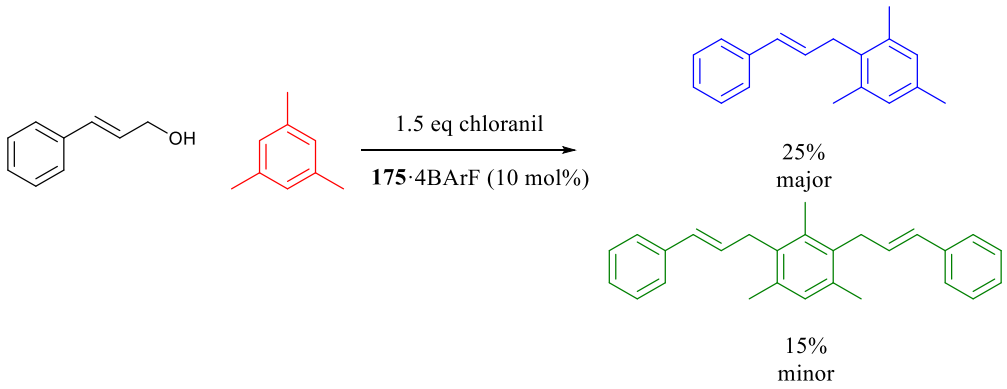

Scheme 6.13: A Friedel-Crafts type reaction between cinnamyl alcohol and mesitylene using a combination of p*-chloranil and* ***175****·4BArF.*

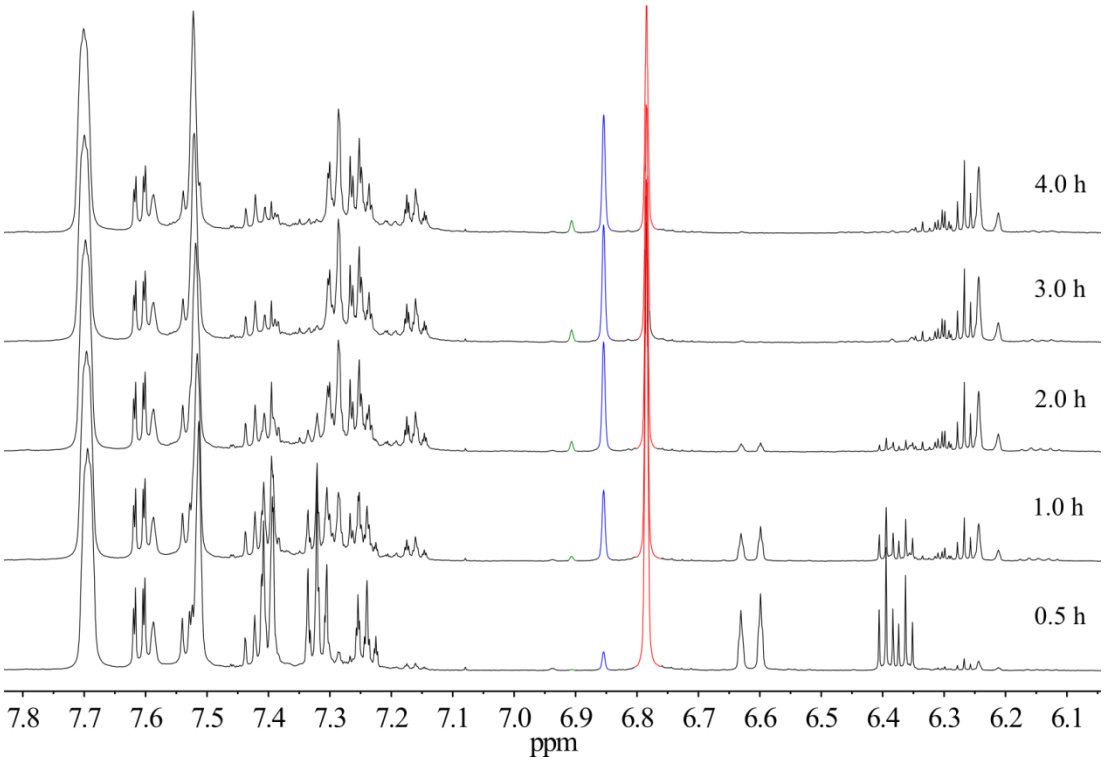

Figure 6.29: Partial ^{1}H NMR (500 MHz, CD_2Cl_2, 300 K) of cinnamyl alcohol/mesitylene reaction. The mesitylene aromatic singlet (red) functions as a useful indicator for the formation of the mono- (blue) and di-coupled (green) products.

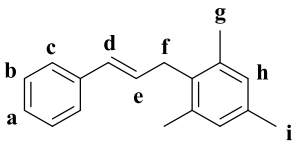

^{1}H NMR (500 MHz, $CDCl_3$) δ 7.36 – 7.32 (m, 2H, H_c), 7.32 – 7.27 (m, 2H, H_b), 7.23 – 7.18 (m, 1H, H_a), 6.92 (s, 2H, H_h), 6.36 – 6.24 (m, 2H, H_d, H_e), 3.56 (d, *J* = 4.3 Hz, 2H, H_f), 2.35 (s, 6H, H_g), 2.32 (s, 3H, H_i). ^{13}C NMR (126 MHz, $CDCl_3$) δ 137.81, 136.75, 135.66, 133.25, 130.03, 129.03, 128.55, 127.87, 127.01, 126.14, 32.71, 21.00, 20.03. *m/z* (EI) = 236 (M^+, 98%), 221 (100), 162 (38), 143 (43), 132 (75), 115 (68), 91 (48), 77 (47). *m/z* (HR-EI): 236.15530 (predicted [M] = 23615595).

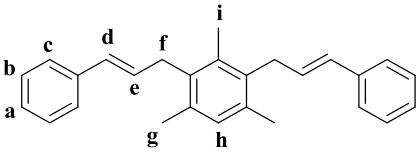

^{1}H NMR (500 MHz, $CDCl_3$) δ 7.34 – 7.29 (m, 4H, H_c), 7.29 – 7.24 (m, 4H, H_b), 7.21 – 7.15 (m, 2H, H_a), 6.94 (s, 1H, H_h), 6.36 – 6.22 (m, 4H, H_d, H_e), 3.59 (dd, *J* = 5.3, 1.2 Hz, 4H, H_f), 2.33 (s, 6H, H_g), 2.32 (s, 3H, H_i). ^{13}C NMR (126 MHz, $CDCl_3$) δ 137.83, 135.69, 134.72, 134.31, 130.13, 130.11, 128.56, 128.12, 127.02, 126.16, 33.44, 20.20, 15.83. *m/z* (EI) = 352 (M^+, 100%), 337 (20), 248 (38), 235 (85), 157 (59), 115 (27), 91 (31). *m/z* (HR-EI): 352.21882 (predicted [M] = 352.21855).

6.9 References

1 S. Horiuchi, T. Murase and M. Fujita, *Chem. – An Asian J.*, 2011, **6**, 1839–1847.

2 S. Horiuchi, Y. Nishioka, T. Murase and M. Fujita, *Chem. Commun.*, 2010, **46**, 3460–3462.

3 T. Murase, S. Horiuchi and M. Fujita, *J. Am. Chem. Soc.*, 2010, **132**, 2866–2867.

4 Y. Nishioka, T. Yamaguchi, M. Yoshizawa and M. Fujita, *J. Am. Chem. Soc.*, 2007, **129**, 7000–7001.

5 M. Yoshizawa, Y. Takeyama, T. Okano and M. Fujita, *J. Am. Chem. Soc.*, 2003, **125**, 3243–3247.

6 M. Yoshizawa, M. Tamura and M. Fujita, *Science*, 2006, **312**, 251–254.

7 D. Fiedler, R. G. Bergman and K. N. Raymond, *Angew. Chemie Int. Ed.*, 2004, **43**, 6748–6751.

8 D. Fiedler, H. van Halbeek, R. G. Bergman and K. N. Raymond, *J. Am. Chem. Soc.*, 2006, **128**, 10240–10252.

9 W. M. Hart-Cooper, K. N. Clary, F. D. Toste, R. G. Bergman and K. N. Raymond, *J. Am. Chem. Soc.*, 2012, **134**, 17873–17876.

10 W. M. Hart-Cooper, C. Zhao, R. M. Triano, P. Yaghoubi, H. L. Ozores, K. N. Burford, F. D. Toste, R. G. Bergman and K. N. Raymond, *Chem. Sci.*, 2015, **6**, 1383–1393.

11 C. J. Hastings, M. P. Backlund, R. G. Bergman and K. N. Raymond, *Angew. Chemie Int. Ed.*, 2011, **50**, 10570–10573.

12 C. J. Hastings, M. D. Pluth, R. G. Bergman and K. N. Raymond, *J. Am. Chem. Soc.*, 2010, **132**, 6938–6940.

13 M. D. Pluth, R. G. Bergman and K. N. Raymond, *J. Am. Chem. Soc.*, 2008, **130**, 11423–11429.

14 M. D. Pluth, R. G. Bergman and K. N. Raymond, *Acc. Chem. Res.*, 2009, **42**, 1650–1659.

15 M. D. Pluth, R. G. Bergman and K. N. Raymond, *Science*, 2007, **316**, 85–88.

16 A. G. Doyle and E. N. Jacobsen, *Chem. Rev.*, 2007, **107**, 5713–5743.

17 Y. Takemoto, *Org. Biomol. Chem.*, 2005, **3**, 4299–4306.

18 M. S. Taylor and E. N. Jacobsen, *Angew. Chemie Int. Ed.*, 2006, **45**, 1520–1543.

19 X. Yu and W. Wang, *Chem. - An Asian J.*, 2008, **3**, 516–532.

20 J. P. Malerich, K. Hagihara and V. H. Rawal, *J. Am. Chem. Soc.*, 2008, **130**, 14416–14417.

21 P. F. Gordon and P. Gregory, in *Organic Chemistry in Colour*, 1987.

22 H.-S. Bien, J. Stawitz and K. Wunderlich, in *Ullmann's Encyclopedia of Industrial Chemistry*, 2000.

23 T. D. Lash, *Chem. – A Eur. J.*, 1996, **2**, 1197-1200.

24 R. P. Linstead, *J. Chem. Soc.*, 1954, 3569-3574.

25 R. P. Linstead, *J. Chem. Soc.*, 1960, 3123–3132.

26 H. Naeimi and Z. Babaei, *J. Chinese Chem. Soc.*, 2015, **62**, 41–46.

27 C. B. Nielsen and F. C. Krebs, *Tetrahedron Lett.*, 2005, **46**, 5935–5939.

28 M. Mercha, *J. Chem. Phys.*, 1999, **110**, 9536-9546.

29 S. Kaur, A. Gupta, V. Bhalla and M. Kumar, *J. Mater. Chem. C*, 2014, **2**, 7356–7363.

30 P. De Marco, F. Bisti, F. Fioriti, M. Passacantando, C. Bittencourt, S. Lettieri, a. Ambrosio, P. Maddalena, S. Prezioso, S. Santucci and L. Ottaviano, *J. Appl. Phys.*, 2012, **112**, 1–5.

31 N. Li, L. Qi, J. Qiao and Y. Chen, *Anal. Chem.*, 2016, **88**, 1821–1826.

32 S. Karuppannan and J. C. Chambron, *Chem. - An Asian J.*, 2011, **6**, 964–984.

33 J. Duhamel, *Langmuir*, 2012, **28**, 6527–6538.

34 D. M. Ziegler, *Am. J. Clin. Nutr.*, 1961, **9**, 43–49.

35 A. Kroger and V. Dadak, *Eur. J. Biochem*, 1969, **11**, 328–340.

36 H. Nohl, W. Jordan and R. J. Youngman, *Adv. Free Radic. Biol. Med.*, 1986, **2**, 211–279.

37 F. Fringuelli, O. Piermatti, F. Pizzo and L. Vaccaro, *European J. Org. Chem.*, 2001, **2001**, 439–455.

38 U. Pindur, G. Lutz and C. Otto, *Chem. Rev.*, 1993, **93**, 741–761.

39 Y. Huang, T. Iwama and V. H. Rawal, *J. Am. Chem. Soc.*, 2002, **124**, 5950–5951.

40 S. Otto, F. Bertoncin and J. B. F. N. Engberts, *J. Am. Chem. Soc.*, 1996, **118**, 7702–7707.

41 E. J. Corey, *Angew. Chemie - Int. Ed.*, 2002, **41**, 1650–1667.

42 L. C. Dias, *J. Braz. Chem. Soc.*, 1997, **8**, 289–332.

43 H. B. Kagan, O. Riant and M. March, *Chem. Rev.*, 1992, **92**, 1007–1019.

44 G. Silvero, M. J. Arévalo, J. L. Bravo, M. Ávalos, J. L. Jiménez and I. López, *Tetrahedron*, 2005, **61**, 7105–7111.

45 Y. Huang and V. H. Rawal, *J. Am. Chem. Soc.*, 2002, **124**, 9662–9663.

46 S. Otto, W. Blokzijl and J. B. F. N. Engberts, *J. Org. Chem.*, 1994, **59**, 5372–5376.

47 P. M. Pihko, *Angew. Chemie Int. Ed.*, 2004, **43**, 2062–2064.

48 A. N. Thadani, A. R. Stankovic and V. H. Rawal, *Proc. Natl. Acad. Sci. U. S. A.*, 2004, **101**, 5846.

49 K. H. Jensen and M. S. Sigman, *Angew. Chemie - Int. Ed.*, 2007, **46**, 4748–4750.

50 P. Mal, B. Breiner, K. Rissanen and J. R. Nitschke, *Science*, 2009, **324**, 1697–1699.

51 J. M. Roberts, B. M. Fini, A. A. Sarjeant, O. K. Farha, J. T. Hupp and K. A. Scheidt, *J. Am. Chem. Soc.*, 2012, **134**, 3334–3337.

52 G. Talavera, E. Reyes, J. L. Vicario and L. Carrillo, *Angew. Chemie - Int. Ed.*, 2012, **51**, 4104–4107.

53 M. J. Narcis, D. J. Sprague, B. Captain and N. Takenaka, *Org. Biomol. Chem.*, 2012, **10**, 9134–6.

54 N. Gupta and H. Linschitz, *J. Am. Chem. Soc.*, 1997, **119**, 6384–6391.

55 P. S. Guin, S. Das and P. C. Mandal, *Int. J. Electrochem.*, 2011, **2011**, 1–22.

56 A. K. Turek, D. J. Hardee, A. M. Ullman, D. G. Nocera and E. N. Jacobsen, *Angew. Chemie - Int. Ed.*, 2015, 539–544.

57 B. Nepal and S. Scheiner, *J. Org. Chem.*, 2016, **81**, 4316-4324.

58 H. Matsubara, T. Maegawa, Y. Kita, T. Yokoji and A. Nomoto, *Org. Biomol. Chem.*, 2014, **12**, 5442–7.

59 R. Whetten and R. Sederoff, *Plant Cell*, 1995, **7**, 1001–1013.

60 J. Ralph, K. Lundquist, G. Brunow, F. Lu, H. Kim, P. F. Schatz, J. M. Marita, R. D. Hatfield, S. A. Ralph, J. H. Christensen and W. Boerjan, *Phytochem. Rev.*, 2004, **3**, 29–60.

61 T. Ito, R. Hayase, S. Kawai, H. Ohashi and T. Higuchi, *J. Wood Sci.*, 2002, **48**, 216–221.

62 P. Liao, B. W. Langloss, A. M. Johnson, E. R. Knudsen, F. S. Tham, R. R. Julian and R. J. Hooley, *Chem. Commun.*, 2010, **46**, 4932.

63 V. U. Pandit, S. S. Arbuj, U. P. Mulik and B. B. Kale, *Environ. Sci. Technol.*, 2014, **48**, 4178–83.

64 J. J. Mason and J. Bergman, *Org. Biomol. Chem.*, 2007, **5**, 2486–2490.

65 J. Barluenga, H. Fanlo, S. López and J. Flórez, *Angew. Chem. Int. Ed.*, 2007, **46**, 4136–40.

66 K. S. L. Chan, M. Wasa, X. Wang and J.-Q. Yu, *Angew. Chemie Int. Ed.*, 2011, **50**, 9081–9084.

Future Outlook

This work represents a significant advance in the areas of metallosupramolecular and photoredox catalysis. However, the overall aim of combining both fields with a single self-assembled system remains unaccomplished. In order to achieve those aims, future work will hopefully capitalise on the discoveries described herein, to design and synthesise modular systems that can incorporate photoactive building blocks into container compounds that also contain binding sites capable of activating substrates towards a range of potential reactions.

It is also hoped that the counter ion dependent guest binding discussed within will have wider reaching implications for a number of topical areas and potential supramolecular applications in years to come.